

Flexural Behaviour of Concrete Reinforced With Basalt Fibre Reinforcement Bars

An Experimental and Numerical Research

Kevin van der Lingen



Flexural Behaviour of Concrete Reinforced With Basalt Fibre Reinforcement Bars

An experimental and numerical research

by

Kevin van der Lingen

A thesis presented to obtain the degree of Master of Science
Faculty of Civil Engineering
Delft University of Technology
Defended publicly on Friday May 17th 2024 at 1:00 pm

Student number	4962265	
Project duration	November 14th, 2022 - May 17th, 2024	
Thesis committee	Dr. ir. M. Lukovic (chair)	TU Delft - Concrete Structures
	Prof.dr.ir. E. Schlangen	TU Delft - Materials and Environment
	Ir. H.J. Bezemer (daily supervisor)	TU Delft - Concrete Structures
	Ir. F. Leenders	van Hattum en Blankevoort

An electronic version of this thesis is available at <https://repository.tudelft.nl/>



Abstract

The emergence of innovative construction materials is dawning a new era of ambition within the civil engineering community. Among these innovative materials, Basalt Fibre Reinforced Polymer (BFRP) has recently surfaced with promising potential as a reinforcing material in concrete. Currently, in the Dutch concrete construction industry, the choice for reinforcement steel has remained unchanged for the past decades. However, the increasing availability of innovative alternatives could help the transition to a more sustainable concrete industry. Although BFRP has promising potential for application in concrete structures, the global application has not been established yet. One of the reasons for this limited research into the structural behaviour of concrete structures reinforced with BFRP-bars. Furthermore, the limited development of codes specifically designed for concrete reinforced with BFRP-bars and the modest availability compared to reinforcement steel also play into the unknowns about the material.

BFRP-bars contain certain qualities that reinforcement steel does not. One of the most prominent is resistance against corrosion due to environmental influences on concrete structures. This eliminates the requirement for the concrete cover to protect the reinforcement from corrosion. Hence, the concrete cover only serves its purpose to ensure effective bond action between the reinforcement bars and the concrete. This inherent quality of BFRP-bars eases the crack width control requirements in the codes for the design of structures reinforced with BFRP-bars to a range of 0.5 mm to 0.7 mm. Although this is a significant increase in comparison to the Eurocode for concrete structures (0.2 mm to 0.4 mm), the properties of BFRP-bars cause larger crack width development.

The aim of the experiment is to investigate the flexural behaviour of concrete beams reinforced with BFRP-bars as tensile reinforcement. The flexural behaviour of concrete structures reinforced with BFRP-bars is studied both experimentally and numerically. The research program contains 6 beams differing in reinforcement material, concrete covers, reinforcement ratio and bar diameters. To investigate the effects of the concrete cover, 2 beams are designed with concrete covers of 31 mm and 11 mm containing 3 BFRP-bars with a diameter of 8 mm in the tension zone. To compare the behaviour of these beams, 2 identical beams with reinforcement steel are designed. To determine the effects of the reinforcement bar diameter, 1 beam is designed with 2 bars with a diameter of 10 mm. The reinforcement ratio in beams remains approximately equal, hence the only changing parameter is the bar diameter. The effects reinforcement ratio is investigated by a beam designed with 2 bars with a diameter of 8 mm. By keeping the bar diameter and the concrete cover the same, the reinforcement ratio is the only changing parameter for this beam. By subjecting the beams to a 4-point bending test, a fully developed crack pattern can be established over a certain length. By using digital image correlation (DIC), the flexural behaviour is monitored and analysed. This includes both crack width development and overall pattern forming. The results are verified with linear variable differential transformers (LVDT's) and a laser measuring vertical displacements. This procedure is devised to evaluate the stiffness behaviour of the beams as well as the cracking behaviours. In addition, the experimental program includes a series of direct tensile tests with reinforcement bars to determine the stress-strain behaviour of the reinforcement bars themselves.

From the performed experiments, it is found that the flexural behaviour of concrete BFRP-reinforced beams differs compared to concrete beams reinforced with steel. Whereas steel-reinforced beams show a clear reinforcement yielding stage, the load-deflection behaviour of the beams containing BFRP-bars appears linear after the first cracks form. The measured deformation in the beams reinforced with BFRP-bars is generally significantly larger. Previous studies [Shamass and Cashell, 2020] indicate the reinforcements significantly lower Young's modulus causing the inferior stiffnesses of the beams reinforced with BFRP-bars. The load-deflection curves also show that the BFRP-reinforced beams show initial flexural cracking at lower load levels (9.82 kN to 13.00 kN). In contrast, the steel-reinforced beam's initial cracking phase starts at 15.11 kN and 17.69 kN respectively. From the cracking patterns, it is found that the BFRP-reinforced beams develop more cracks (7 to 8) in the constant bending moment zone compared to the steel-reinforced beams (5 and 7 respectively). The crack patterns also show the development of tensile splitting cracks at the reinforcement depth on the side of the beam for the BFRP-bars with a concrete cover of 31 mm. On the contrary, tensile splitting cracks on the side of steel-reinforced beams were not observed. The beam reinforced with BFRP-bars and a concrete cover of 11 mm also did not show tensile splitting cracks emerging at the side of the beam, however, this type of cracks did appear on the bottom surface. Tensile splitting of the concrete around the reinforcement reduces the bond strength of the reinforcement bar to the confining concrete, as suggested by Harajli [Harajli et al., 2004]. The emergence of tensile splitting cracks increases the crack spacing, which in turn increases the crack width. Based on the cracking patterns, it is found that lower reinforcement ratios in BFRP-beams correlate with larger tensile splitting crack development over the beam surface. On the contrary, larger bar diameters together with a larger bar spacing in the cross-section cause smaller tensile splitting crack development. From the crack width measurements, it is found that the beams reinforced with BFRP-bars show significantly larger crack width development compared to the steel-reinforced beams. Due to the inherent mechanical properties of the BFRP-bars, the crack width development is linear. This is contrary to the crack width development of the steel-reinforced beams, which exhibit a distinct yielding stage of the reinforcement. Although the maximum allowable crack width in the codes for BFRP-reinforced beams is considerably higher, the crack width measurements from the DIC-data show that the BFRP-beams reach the limits at earlier load levels than the steel-reinforced beams. When applying the lower bound limits (0.5 mm for BFRP-reinforced beams, 0.2 mm for steel-reinforced beams), it is found that the BFRP beams reach 0.5 mm crack widths at 14.11 kN to 29.08 kN, whereas the steel-reinforced beams reach 0.2 mm crack width at 28.04 and 37.57 kN respectively. This disparity is amplified even more when applying the upper bound crack width limits of 0.7 for BFRP-reinforced beams and 0.4 mm for steel-reinforced beams. The crack width limits are then reached at 21.90 kN to 38.21 kN for BFRP-beams, whereas the 0.4 mm limits for steel-reinforced beams are reached at 42.49 kN and 57.34 kN respectively. Based on the crack width models in the codes, it found that the BFRP-beams display larger crack widths than the theoretical curves, whereas the steel-reinforced beams generally adhere to the theoretical curves.

To conclude, the experimental study comparing the flexural behaviour of concrete BFRP-reinforced beams versus steel-reinforced beams reveals distinct differences in their structural responses to bending loads. While steel-reinforced beams exhibit an evident yielding stage, the BFRP-beams display a linear load-displacement behaviour post-initial cracking until failure. Additionally, BFRP-beams exhibit slightly earlier cracking. Contrary to the steel-reinforced beams, the BFRP-beams show a sensibility to tensile splitting crack, affecting the flexural crack formation. Despite a larger allowable crack width according to the codes, the BFRP-beams reach their limits at earlier load levels compared to steel-reinforced beams. Furthermore, the BFRP-beams display larger crack widths than predicted by the theoretical models in the codes. This is contrary to the steel-reinforced beams, which generally align to the theoretical curves. These findings underscore the necessity for design considerations to effectively accommodate the flexural behaviour of concrete structures reinforced with BFRP-bars.

Acknowledgements

I want to take this opportunity to express my heartfelt gratitude to the individuals and organisations who have played a significant role in the successful completion of this research project. Their unwavering support, guidance, and contributions have been invaluable and have greatly enriched the outcomes of my work.

First and foremost, I extend my sincere appreciation to Mladena Lukovic and Erik Schlangen from Delft University of Technology for their exceptional guidance and mentorship throughout this study. Their vast knowledge, expertise, and valuable insights have been instrumental in shaping the direction of my research and have inspired me to strive for excellence in my work. Their continuous encouragement and feedback have been pivotal in overcoming challenges and achieving my research goals.

Special recognition to PhD student Jelle Bezemer for his invaluable help during the preparation and execution of the experiment and the daily supervision. His knowledge, guidance, and support have been critical in refining my research methodology and analysing the results effectively. His contributions have significantly enriched the research process, and I am deeply grateful for his involvement.

My special thanks go to Felix Leenders and Eelco van der Weij from Hattum en Blankevoort for their dedicated guidance and mentorship throughout the project. Their extensive experience, practical insights, and continuous encouragement have motivated me to push the boundaries of my research and achieve meaningful results. Their guidance and involvement have been invaluable in ensuring the success of my endeavours.

I am deeply grateful to Rijkswaterstaat, particularly Sonja Fennis, for their generous financial support, which made it possible for me to conduct the experiments. Their belief in the importance of this research and their financial assistance have been instrumental in the successful execution of the project and the advancement of knowledge in this field. The support provided by Rijkswaterstaat has been crucial in driving my research forward and making a positive impact in the field of civil engineering.

I would like to acknowledge the significant contribution of Alexander Bobryshev from Orlimex Composites for providing the materials required for the experiment. Their generous support in supplying the necessary materials has been crucial in facilitating the experimental work and obtaining accurate results. Their collaboration has been a significant asset to my research, and I am truly grateful for their assistance.

I am also grateful to Albert Bosman and Ake Blom for their tireless efforts and assistance during the long and challenging hours spent in the concrete lab at the Faculty of Civil Engineering and Geosciences. Their technical expertise, valuable insights, and dedication have been paramount in ensuring the successful execution of the experimental work. Their unwavering commitment to help me has made a profound impact on the quality of my research.

Additionally, I extend my thanks to all the other individuals who have supported me in various ways throughout this journey. Your encouragement, understanding, and willingness to assist have been a source of motivation and inspiration, and I cherish the collaborative environment that you have fostered.

Acknowledgements

Last but not least, I want to express my sincere appreciation to my family, friends, and colleagues for their unwavering support and encouragement throughout this research endeavour. Your understanding, patience, and belief in my abilities have been invaluable, and I am truly grateful for your presence in my life.

In conclusion, the successful completion of this research project would not have been possible without the collective efforts and support of all those mentioned above. Their contributions have been instrumental in advancing my understanding of this field and have laid the foundation for future research endeavours. I am genuinely thankful for their support and look forward to continuing my journey with their encouragement in the pursuit of knowledge and innovation.

Kevin van der Lingen

Dordrecht, December 2023

Contents

Abstract	3
Acknowledgements	5
1 Introduction	21
1.1 Background and motivation	21
1.2 Scope and limitation of the research	23
1.3 Research objectives and methodology	23
1.4 Thesis outline	24
2 Literature study	25
2.1 Basalt fibre reinforcement bars	25
2.1.1 Constituent materials	25
2.1.1.1 Basalt fibres	25
2.1.1.2 Resin matrices	26
2.1.2 Production of reinforcement bars	27
2.1.2.1 Melting and crushing process	29
2.1.2.2 Continuous basalt fibre formation	29
2.1.2.3 Bar production through pultrusion	30
2.1.3 Determination of physical and mechanical properties	32
2.1.3.1 Physical properties	33
2.1.3.2 Short-term mechanical properties	33
2.1.3.3 Long-term mechanical properties	35
2.1.4 Characteristics of BFRP	36
2.1.4.1 Stress-strain behaviour	37
2.1.4.2 Longitudinal tensile strength	37

Table of Contents

2.1.4.3	Transverse strength	37
2.1.4.4	Young's modulus	38
2.1.4.5	Corrosiveness	38
2.1.4.6	Conductivity	38
2.1.4.7	Magnetic behaviour	38
2.1.4.8	On-site characteristics	39
2.2	Reinforced concrete structures with BFRP	39
2.2.1	Flexural behaviour	40
2.2.1.1	Influence of surface deformation	41
2.2.1.2	Cracking moment	41
2.2.2	Bond behaviour	41
2.2.2.1	Bond strength development	42
2.2.2.2	Bonding mechanism	44
2.2.2.3	Limitations in performed experimental studies	47
2.2.2.4	Ambiguity and discussions in bond strength	47
2.2.3	Cracking behaviour	47
2.2.3.1	Flexural cracks	47
2.2.3.2	Tensile splitting cracks	48
2.2.4	Crack width control	50
2.2.4.1	Crack width control to ACI440 [Busel, 2006]	51
2.2.4.2	Crack width control according to BRL0513	51
2.2.4.3	Crack width control according to JSCE	51
2.3	Sustainability	51
2.3.1	CO ₂ emission	52
2.3.2	Life cycle assessment	52
2.3.3	Environmental product declaration	54
2.3.4	ECI-calculation background	56
2.3.4.1	Influence of fibre content	57
2.3.5	Environmental cost indicator (ECI)	57
2.4	Costs	58
2.5	Design guidelines and regulations	58
2.5.1	Available guidelines	59
2.5.1.1	Fib model code for FRP-reinforced concrete (International)	59

2.5.1.2	ACI commission 440 (United States of America)	59
2.5.1.3	BRL0513 (the Netherlands)	59
2.5.1.4	Other guidelines	59
2.5.2	Forthcoming Eurocode 2	59
2.5.2.1	Partial factors	60
2.5.2.2	Materials	60
2.5.2.3	Durability and concrete cover requirements	62
2.5.2.4	Ultimate limit state analysis, special rules for FRP reinforcement	62
2.5.2.5	Serviceability limit state analysis, special rules for FRP reinforcement	63
2.6	Conclusions	66
3	Experimental study	69
3.1	Aim of the experimental research	69
3.2	Testing program	70
3.3	Direct tension test	70
3.3.1	Test specimen	70
3.3.1.1	Sample design and preparation	70
3.3.1.2	Capacity	71
3.3.1.3	Test setup	73
3.4	4-point bending test	74
3.4.1	Test specimens	74
3.4.1.1	Reinforcement configuration	75
3.4.1.2	Cross-sections	76
3.4.2	Resistance estimations	80
3.4.2.1	Bending moment capacity	81
3.4.2.2	Shear reinforcement	81
3.4.2.3	Crack width	83
3.4.2.4	Transfer length	84
3.4.3	Casting of the specimens	85
3.4.3.1	Concrete mixture	85
3.4.3.2	Casting and moulding conditions	86
3.4.3.3	Sampling of concrete	86
3.4.3.4	Results	90

3.4.4	Measuring techniques	91
3.4.4.1	Digital Image Correlation (DIC)	92
3.4.4.2	Crack width measurements from Digital Image Correlation data	93
3.4.4.3	Linear Variable Differential Transformer (LVDT)	93
3.4.4.4	Optical fibre strain gauges	94
3.4.4.5	Laser measuring vertical displacement at mid-span	96
3.4.5	Test setup	96
4	Results	98
4.1	Direct tension test	98
4.1.1	Results	98
4.1.2	Conclusion	100
4.2	4-point bending test	101
4.2.1	Performance indicators	101
4.2.2	Flexural behaviour	101
4.2.2.1	Load-deflection curves	101
4.2.2.2	Load-deflection stages	103
4.2.3	Cracking patterns	105
4.2.4	Emergence of tensile splitting cracks in beams reinforced with BFRP-bars	106
4.2.5	Maximum crack width	116
4.2.6	Conclusion	122
5	Discussion	124
6	Conclusions and recommendations	128
6.1	Conclusions	128
6.2	Recommendations for further research	131
	Bibliography	132
A	Parameter Study	136
A.1	Background and motivation	136
A.2	Assumptions	137
A.3	ECI and costs parameters	137
A.4	Structural parameters	149

A.5 Conclusions	167
B Graphs bending moment resistance parameter study	169
C Graphs Crack width parameter study	174
D Graphs crack spacing parameter study	179
E Results cube compression test	183
F Results cubes tensile splitting test	186
G Results prisms compression test	188
H Crack width development DIC-data	191
H.1 Results B-3r8-c31	192
H.2 Results B-2r10-c31	204
H.3 Results B-2r8-c31	212
H.4 Results B-3r8-c11	235
H.5 Results S-3r8-c31	244
H.6 Results S-3r8-c11	254

List of Figures

1.1	Principle of embedded fibres in polymer matrices [Erden and Ho, 2017]	21
1.2	Model of flexural crack width [Chiu et al., 2018]	22
2.1	Stress-strain curves of typical reinforcement fibres. a: High-modulus carbon, b: Low-modulus carbon; c: Aramid K49; d: S-glass; e: E-glass f: Basalt. [fib, 2007]	26
2.2	Simplified schematic overview of a continuous production line [Fiore et al., 2015] Basalt fibre manufacturing procedure illustrates the following steps: (1) crushed stone silo, (2) loading station, (3) transport system, (4) batch charging, (5) initial melting zone, (6) secondary heating zone with precise temperature control, (7) filament forming, (8) sizing applicator, (9) strand formation system, (10) fibre tensioning system, (11) automated winding system.	28
2.3	Pultrusion process scheme: (1): CBF's drawn from rovings. (2): CBF's impregnated with thermoset resin. (3): Impregnated CBF's are shaped with a hot mould, and resins are cured. (4): Products cut to the desired length. [Strauß et al., 2019]	28
2.4	Leakage plate nozzle (a) [Kelly et al., 1968] and CBF roving (b) [Jumaishing, 2022]	30
2.5	Drawn fibres from CBF rovings and typical resin bath [Vedernikov et al., 2021]	30
2.6	Closed injection versus open bath resin impregnation [Strauß et al., 2019]	31
2.7	Sand-coated FRP reinforcement bars [Nilforoush and Esfahani, 2012]	31
2.8	Stress strain relations of fibre reinforced polymer and constituent fibres and matrix [Zhang and Hsu, 2005]	32
2.9	Stress distribution of tensile stress in FRP-bars subjected to axial load [fib, 2000]	34
2.10	FRP reinforcement bar subject to a transverse shear force [fib, 2007]	35
2.11	typical strain history curve during creep deformation [fib, 2007]	36
2.12	Stress-strain diagram comparison [Shamass and Cashell, 2020]	37
2.13	experimental study by Shamass & Cashell [Shamass and Cashell, 2020]	40
2.14	Load-deflection curves experimental study by Shamass & Cashell [Shamass and Cashell, 2020]	40
2.15	Typical average bond stress versus bond-slip of FRP bars embedded in concrete [fib, 2000]	42
2.16	Radial component of the bond forces balanced against the tensile stress ring [fib, 2000]	43

2.17	Bond mechanism helical wrapping as surface deformation [Xiong et al., 2021]	44
2.18	Bond mechanism screw thread as surface deformation [Xiong et al., 2021]	45
2.19	Bond mechanism sand coating as surface deformation [Xiong et al., 2021]	45
2.20	Bond-slip test results bar diameter 10 mm with different surface deformations; (a) helical wrapping, (b) screw thread, (c) sand coating, (d) combined helical wrapping and sand coating [Xiong et al., 2021]	46
2.21	Stress distribution in concrete and reinforcement bonded reinforcement bars [Walraven, 2013]	48
2.22	Tensile stress distributions in elastic (1), partly cracked elastic (2) and plastic (3) stage [fib, 2007]	49
2.23	tensile splitting crack variations [Nagatomo et al., 1992]	49
2.24	Bond-slip model [Harajli et al., 2004]	50
2.25	Table 7.1N from Eurocode 2 [European Committee for Standardization, 2022]: Maximum allowable crack width	50
2.26	Stages of a life cycle assessment (LCA) [Pavlović et al., 2022]	53
2.27	Life cycle assessment stages [Pavlović et al., 2022]	54
2.28	ECI-calculation process [Ecochain, 2023]	57
2.29	Table R.1 from forthcoming Eurocode 2 [European Committee for Standardization, 2022], Annex R (NEN-EN-1992-1-1)	60
2.30	Stress-strain diagram for embedded FRP reinforcement from forthcoming Eurocode 2, Annex R (NEN-EN-1992-1-1)	61
2.31	Verification's, stresses and crack width limits for appearance from forthcoming Eurocode 2	64
2.33	Verification's, stresses and crack width limits for appearance from forthcoming Eurocode 2	66
3.1	Design drawing direct tensile test specimen	71
3.2	Direct tension test setup	73
3.3	4-point flexural bending test	74
3.4	Reinforcement configuration of the stirrups applied in the beam specimens	75
3.5	Reinforcement material designation	76
3.6	B-3r8-c31 sections A-A and B-B, (b)=BFRP-bar, (s)=Reinforcement steel bar	77
3.7	B-2r10-c31 sections A-A and B-B, (b)=BFRP-bar, (s)=Reinforcement steel bar	77
3.8	B-2r8-c31 sections A-A and B-B, (b)=BFRP-bar, (s)=Reinforcement steel bar	78
3.9	B-3r8-c11 sections A-A and B-B, (b)=BFRP-bar, (s)=Reinforcement steel bar	78
3.10	S-3r8-c31 sections A-A and B-B, (b)=BFRP-bar, (s)=Reinforcement steel bar	79
3.11	S-3r8-c11 sections A-A and B-B, (b)=BFRP-bar, (s)=Reinforcement steel bar	79
3.12	M-line and V-line beams experiment	80
3.13	Crack width prediction according to BRL0513 [CvD, 2015]	84

3.14	Freshly casted beams specimens 1&2 sealed with plastic layer	86
3.15	Cubes and prisms cast from concrete batch	87
3.16	Cycle for the determination of stabilized secant Young's modulus, method B according to NEN-EN-12390	88
3.17	Cubes and prisms subjected to respective tests	89
3.18	Schematic representation of correlation of the sub-images of deformed and un-deformed images on a two-dimensional deflection field [Shih and Sung, 2013]	92
3.19	Stochastic pattern applied to beam S-3r8-c31 during test preparation	93
3.20	LVDT-positioning on beam specimens	94
3.21	Optical fibres glued to reinforcement bar	95
3.22	Optical fibre strain gauges placement plan, side view	95
3.23	Laser device mounted to a beam specimen	96
3.24	4-point bending test setup	97
4.1	Test specimens after failure direct tension tests	99
4.2	Stress-strain relation direct tensile tests	100
4.3	Load-deflection curves of all tested beam specimen	102
4.4	Cracking stages comparison	104
4.5	Load-deflection curves comparison	104
4.6	Contour plots crack pattern from DIC-data comparison at load level ≈ 50 kN	105
4.7	Contour plots cracking from DIC-data comparison at load level ≈ 17 kN	106
4.8	Stresses and strains in a rectangular cross-section [Usingeurocode, 2023]	107
4.9	Strain in cross-section based on LVDT, tensile splitting crack emerging load levels	108
4.10	Tensile stress distribution in 1 elastic, 2 partly cracked elastic and 3 plastic stages	109
4.11	Bond stress resistance tensile splitting for each stage	110
4.12	Crack width propagation comparison B-3r8-c31 and B-2r10-c31	112
4.13	Crack width propagation comparison B-3r8-c31 and B-2r8-c31	113
4.14	Crack width propagation comparison B-3r8-c31 and B-3r8-c11	114
4.15	Contour plots cracking from DIC-data comparison at load level $F=50$ kN	115
4.16	tensile splitting crack variations [Nagatomo et al., 1992]	115
4.17	Tensile splitting cracks bottom side B-3r8-c11	116
4.18	Failed bar B-3r8-c11	116
4.19	Maximum crack width vs. force curves of all tested beam specimen	117
4.20	Maximum crack width vs. force curves of all tested beam specimen	117

4.21	Maximum crack width vs. force curves B-3r8-c31 and B-2r10-c31	118
4.22	Maximum crack width vs. force curves B-3r8-c31 and B-2r8-c31	119
4.23	Maximum crack width vs. force curves B-3r8-c31 and B-3r8-c11	119
4.24	Maximum crack width vs. force curves B-3r8-c31 and S-3r8-c31	120
4.25	Maximum crack width vs. force curves B-3r8-c11 and S-3r8-c11	120
4.26	Crack width comparison experimental versus codes	121
5.1	Load-deflection curve and maximum crack width curve comparison beam S-3r8-c31 with results Singh (2019) and Zhekang (2017)	125
5.2	Load-deflection curve and maximum crack width curve comparison beam S-3r8-c11 with results Zhekang (2017)	126
5.3	Contour plots crack pattern from DIC-data comparison at load level ≈ 50 kN	126
5.4	Overlapping of bond stress development zones	127
5.5	B-2r8-c31, Contour plots crack pattern from DIC-data comparison at load level ≈ 50 kN	127
6.1	Comparison of cracks and crack spacing beam specimen	129
6.2	Load level at maximum crack width limits are reached	130
A.1	Double reinforcement mesh slab reinforcement drawing	138
A.2	Costs and ECI comparison square metre slab $t=250$ mm, $b=1000$ mm, equal geometry	138
A.3	Impact categories scores of reinforcement materials in slabs with equal geometry	140
A.4	Crack width development for slab equal geometry	141
A.5	Crack width curves and ECI-score for adjusted for serviceability limit state	141
A.6	Costs and ECI comparison square metre slab $t=250$ mm, $b=1000$ mm, equal geometry with reduced cover of BFRP-reinforced slab	142
A.7	Crack width development for slab equal geometry (reduced cover for BFRP-reinforced slab	143
A.8	Crack width curves and ECI-score for adjusted for serviceability limit state, slab with reduced concrete cover	144
A.9	Single reinforcement mesh slab reinforcement drawing	145
A.10	Costs and ECI comparison square metre slab $t=250$ mm, $b=1000$ mm, equal geometry with reduced cover of BFRP-reinforced slab	146
A.11	Crack width development for a thin slab	147
A.12	Crack width curves and ECI-score for adjusted for serviceability limit state, thin slab	147
A.13	Determination reduction factor η_{Mrd} according to BRL0513 [CvD, 2015]	150
A.14	Bending moment diagrams for parameter A_{bfrp} for concrete classes C20/25, C30/37, C40/50 according to BRL0513	151

A.15	Strength reduction factor according to ACI440 [Busel, 2006]	152
A.16	Stress and strain distribution at ultimate conditions, Failure governed by concrete crushing failure (compression controlled) [Busel, 2006]	153
A.17	Stress and strain distribution at ultimate conditions, balanced failure (Transition zone) [Busel, 2006]	154
A.18	Stress and strain distribution at ultimate conditions, Failure governed by FRP rupture (tension controlled) [Busel, 2006]	154
A.19	Bending moment diagrams for parameter A_{bfrp} for concrete classes C20/25, C30/37, C40/50 according to ACI440	155
A.20	Ultimate bending moment diagrams for parameter A_g for concrete classes C20/25, C30/37, C40/50 according to Eurocode 2	156
A.21	Comparison bending moment resistance BRL0513, ACI440 and EC2 for C30/37, $d=250$ mm . . .	157
A.22	Favourability index BFRP according to BRL0513 and reinforcement steel according to Eurocode 2	158
A.23	Comparison ECI-value for BRL0513, ACI440 and EC2 for C30/37, bottom reinforcement first layer, $d=250$ mm, C30/37	158
A.24	Comparison ECI-value for BRL0513, ACI440 and EC2 for C30/37, bottom reinforcement first layer, $d=250$ mm, C30/37	159
A.25	Crack width development curves according to BRL0513 for various concrete cover c values, C20/25, $d=250$ mm, $A_{bfrp}=1500$ mm ² /m	161
A.26	Crack width development curves according to BRL0513 for various concrete cover c values with increased properties	162
A.27	Crack width development curves according to ACI440 for various concrete cover c values, C20/25, $d=250$ mm, $A_f=1500$ mm ² /m	163
A.28	Crack width development curves according to ACI440 for various concrete cover c values with increased properties	164
A.29	Crack width development curves according to Eurocode 2 for various concrete cover c values, C20/25, $d=250$ mm, $A_f=1500$ mm ² /m	165
A.30	Crack width development curves according to ACI440 for various concrete cover c values with increased properties	165
A.31	Crack width comparison with code limits	166
A.32	Bond factor crack spacing relation for $\varnothing_{bf}=12$ mm, $c=30$ mm	167
B.1	Bending moment diagrams comparison for varying effective heights and concrete strength classes	173
C.1	Crack width diagram comparison for various concrete covers, cross-sectional reinforcement area and concrete strength classes	178
D.1	Bond factor crack spacing relation for varying diameter, concrete cover, and bar diameter	182

H.1	B-3r8-c31, load-deflection curve versus maximum crack width measured from DIC-data	192
H.2	Crack widths contour plots B-3r8-c31 from DIC-data	202
H.3	B-3r8-c31: Load-displacement curves LVDT's and comparison with DIC-data	203
H.4	B-2r10-c31, load-deflection curve versus maximum crack width measured from DIC-data	204
H.5	Crack widths contour plots B-2r10-c31 from DIC-data	210
H.6	B-2r10-c31: Load-displacement curves LVDT's and comparison with DIC-data	211
H.7	B-2r8-c31, load-deflection curve versus maximum crack width measured from DIC-data	212
H.8	Combined crack widths contour plots B-2r8-c31 from DIC-data and corresponding strain graphs optical fibre from optical fibre data	232
H.9	Full optical fibre gauge length strain development beam B-2r8-c31	233
H.10	Full optical fibre gauge length stress development beam B-2r8-c31	233
H.11	B-2r8-c31: Load-displacement curves LVDT's and comparison with DIC-data	234
H.12	B-3r8-c11, load-deflection curve versus maximum crack width measured from DIC-data	235
H.13	Crack widths contour plots B-3r8-c11 from DIC-data	242
H.14	B-3r8-c11: Load-displacement curves LVDT's and comparison with DIC-data	243
H.15	S-3r8-c31, load-deflection curve versus maximum crack width measured from DIC-data	244
H.16	Crack widths contour plots S-3r8-c31 from DIC-data	252
H.17	S-3r8-c31: Load-displacement curves LVDT's and comparison with DIC-data	253
H.18	S-3r8-c11, load-deflection curve versus maximum crack width measured from DIC-data	254
H.19	Crack widths contour plots S-3r8-c11 from DIC-data	262
H.20	S-3r8-c11: Load-displacement curves LVDT's and comparison with DIC-data	263

List of Tables

2.1	Typical characteristics of single filament fibres [Nanni et al., 2014, Ji et al., 2009, Kumbhar, 2014, Li et al., 2018, fib, 2007]	26
2.2	Typical properties of resin matrices [Nanni et al., 2014, fib, 2007]	27
2.3	Typical properties of BFRP-bars compared to reinforcement steel, data from: [Nanni et al., 2014] [fib, 2007, Busel, 2006, Brózda et al., 2017]	34
2.4	Available literature on conducted experimental studies	39
2.5	Impact category values of BFRP and reinforcement steel per kg [Orlimex CZ s.r.o, 2022] [VWN, 2021]	55
2.6	Impact category values of BFRP and reinforcement steel per m ³ [Orlimex CZ s.r.o, 2022] [VWN, 2021]	55
2.7	A1 Impact category values and weight factor (€/unit) [Ecochain, 2023]	56
2.8	ECI-values comparison between BFRP and steel reinforcement bars in €/kg and €/m ³	58
2.9	Unit prices of reinforcement steel bar and BFRP-bars [Upadhyaya and Suntharavadivel, 2018, Barker, 2016, Colombo et al., 2012]	58
3.1	Beam specimen list	75
3.2	Materials and properties used in predictive calculations	80
3.3	Bending moment capacity estimations	81
3.4	Concrete mix design	85
3.5	Concrete cube compressive strength results	90
3.6	Concrete Young's modulus results	91
3.7	Tensile splitting strength cubes results	91
4.1	Combined Test Results	99
4.2	Performance summary of all tested beams	101
4.3	First crack load level, bending moment and corresponding vertical deflection	102
4.4	Force, deflection and tensile stress emergence tensile splitting cracks	106

4.5	Concrete compression zone height x analytical method and LVDT-data	108
4.6	Stress and strain in tensile reinforcement, analytical method and experimental values	108
4.7	Bond stress resistance tensile splitting for each stage	110
4.8	Bond stress τ_{bf} at tensile splitting crack emerging load level	111
4.9	Load level crack width limits according to ACI440, BRL0513 and Eurocode 2	118
A.1	Upper boundary values for ECI-values of concrete for 2029-2030 [Fennis, 2021]	137
A.2	Components of total ECI-score and costs per square metre slab $t=250$ mm, $b=1000$ mm, equal geometry	139
A.3	Adjusted ECI-score after adjusted for serviceability limit state	142
A.4	Components of total ECI-score and costs per square metre slab $t=250$ mm ($t=239$ mm for BFRP-reinforced slab), $b=1000$ mm, equal geometry	143
A.5	Adjusted ECI-score after adjusted for serviceability limit state	144
A.6	Components of total ECI-score per square metre slab minimum required thickness, $b=1000$ mm .	146
A.7	Components of total ECI-score per square metre slab minimum required thickness, $b=1000$ mm .	148
A.8	Required reinforcement and corresponding ECI-values and Costs slab $d=250$ mm for $M_{Rd}=75$ kNm and $M_{Rd}=200$ kNm	159
E.1	Concrete batch 1 cubes results	184
E.2	Concrete batch 2 cubes results	184
E.3	Concrete batch 3 cubes results	185
F.1	Concrete batch 2 cubes tensile splitting results	187
F.2	Concrete batch 3 cubes tensile splitting results	187
G.1	Concrete batch 1 prisms results	189
G.2	Concrete batch 2 prisms results	189
G.3	Concrete batch 3 prisms results	190
H.1	B-3r8-c31, summarized performance parameters	192
H.2	B-2r10-c31, summarized performance parameters	204
H.3	B-2r8-c31, summarized performance parameters	212
H.4	B-3r8-c11, summarized performance parameters	235
H.5	S-3r8-c31, summarized performance parameters	244
H.6	S-3r8-c11, summarized performance parameters	254

List of Abbreviations

AFRP	Aramid Fibre Reinforced Polymer
BFRP	Basalt Fibre Reinforced Polymer
CBF	Continuous Basalt Fibres
CFC	Chlorofluorocarbon
CFRP	Carbon Fibre Reinforced Polymer
CO₂	Carbon dioxide
DCB	Dichlorobenzene
DIC	Digital Image Correlation
ECI	Environmental Cost Indicator
EPD	Environmental Product Declaration
FRP	Fibre Reinforced Polymer
GFRP	Glass Fibre Reinforced Polymer
HFRP	Hybrid Fibre Reinforced Polymer
LCA	Life Cycle Assessment
LVDT	Linear Variable Differential Transformer
PO₄³⁻	Phosphate
Sb	Antimony
SO₂	Sulfur dioxide
SLS	Serviceability Limit State
ULS	Ultimate Limit State

Chapter 1

Introduction

1.1 Background and motivation

With recent concerns about climate change, the construction industry aims to make concrete structures more sustainable. Expanding on the sustainability of concrete involves delving into alternative materials and methods that can mitigate the environmental impact of traditional concrete production. One such avenue is exploring alternative binders, such as geopolymers, as a substitute for Portland cement. Geopolymer concrete offers promising potential for reducing carbon emissions associated with cement production. However, it is important to acknowledge the challenges it faces, including the availability of precursors like fly ash and blast furnace slag. While discussing this, it is crucial to address concerns raised about the complexity of the topic structure. Therefore, following the exposition of geopolymer concrete challenges, exploring alternative reinforcement avenues like Basalt Fibre Reinforced Polymer (BFRP) opens doors to advancing sustainability within the construction sector.

For the past centuries, steel has been the most widely used material to reinforce concrete structures. On the other hand, fibre reinforced polymer (FRP) bars have become commercially available since the late 1980's when the market demand for nonferrous reinforcement bars increased. The concept of fibre reinforced polymer composites originates from an old method of making a material better by combining two materials. FRP's are composed of a reinforcing phase (fibres) and a rigid resin matrix (polymer) where the fibres are embedded (figure 1.1).

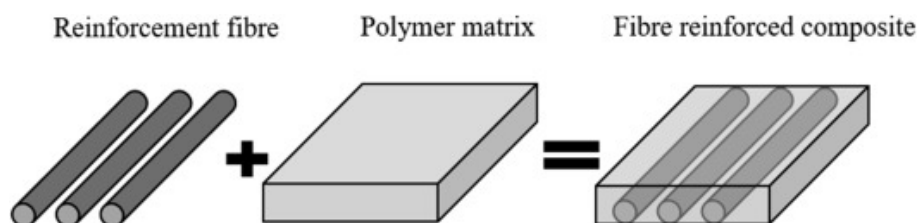


Figure 1.1: Principle of embedded fibres in polymer matrices [Erden and Ho, 2017]

The fibres used in FRP are formed from thin filaments. As fibre reinforced composites are a mixture of at least two different materials, the combination develops new and superior properties in relation to the individual materials. The opportunity of combining multiple materials into one brings the possibility of tailoring materials

to a specific desired application. An example of combining individual material properties is reinforced concrete. The concrete itself contains a relatively high compressive strength in relation to its tensile strength. Therefore, a reinforcing material with a high tensile strength (commonly reinforcement steel) is added to the area of the concrete structure where tensile stresses occur. Combining both materials results in properties that exceed those of the individual materials, making it superior.

In relation to reinforcement steel, FRP-bars generally contain higher tensile strengths, which could reduce the required cross-section surface in comparison to reinforcement steel [fib, 2007]. The application of reinforcement does have some challenges to be faced, especially from a durability point of view. Contrary to reinforcement steel, FRP-bars embedded in concrete are corrosion-resistant. FRP-bars do not significantly deteriorate when exposed to ingress of fluids due to weather influences and exposure to chemicals [Busel, 2006]. The emergence of commercially available FRP-bars also stems from the need to apply non-conductive material as reinforcement, which could be beneficial for concrete structures in the surrounding of MRI-equipment in hospitals [Busel, 2006]. FRP-bars also contain a limited transfer of heat in relation to reinforcement steel.

However, the application of BFRP-bars also comes with some challenges. For example, flexural cracking in concrete structures represents a critical concern in structural engineering. When reinforced with BFRP-bars, concrete structures exhibit different behaviour regarding flexural cracking in comparison to conventional reinforcement steel, such as larger crack width and larger displacements [Baena et al., 2013, Busel, 2006]. The cracking behaviour and crack width development, influenced by factors such as the Young's modulus of the reinforcement bars [Busel, 2006, fib, 2007], could significantly differ in BFRP-bar reinforced concrete structures due to their generally lower Young's modulus compared to steel (a factor of 3 to 4 [Busel, 2006]).

In addition, the bond behaviour between reinforcement steel and BFRP to the confining concrete could also vary due to the different characteristics and mechanical properties. Bond strength affects the spacing between the flexural cracks (noted as S_c in figure 1.2) emerging in a structure loaded in bending. Greater tensile reinforcement bonding correlates with reduced crack spacing in concrete structures.

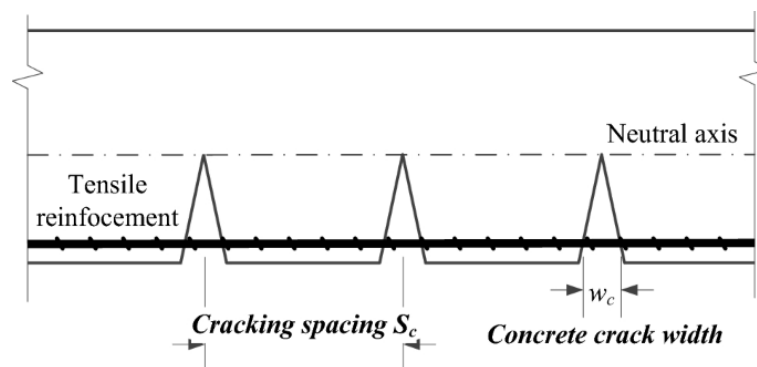


Figure 1.2: Model of flexural crack width [Chiu et al., 2018]

In conclusion, the extent to which each factor such as bond strength affects the flexural behaviour poses challenges. These challenges present a hurdle to take before the application of BFRP-bars in concrete becomes common practice. Hence, it is of utmost importance to gain an understanding of the flexural behaviour of concrete structures reinforced with BFRP-bars.

1.2 Scope and limitation of the research

Based on the preliminary but promising reports about BFRP-bars, Van Hattum en Blankevoort decided to initiate comprehensive research into the prospective substitution of traditional reinforcement steel in concrete structures. However, the research on the consequences of applying BFRP-bars in concrete on a structural and environmental level is limited. This study compares the performance of concrete structures reinforced with BFRP-bars versus reinforcement steel bars under bending loads. Notably, As BFRP has gained significant interest in the Dutch construction industry, this study focuses on BFRP and deliberately excludes other FRP types.

Based on an experiment on flexural behaviour, this study delves deeply into two key facets: the stiffness exhibited by these reinforced concrete structures and their flexural cracking behaviour. This examination aims to decipher and delineate the differences between concrete structures reinforced both with BFRP-bars and reinforcement steel bars loaded in bending. By scrutinizing stiffness and flexural cracking behaviours, the study seeks to elucidate the unique advantages and potential limitations of employing BFRP-bars as a substitute for traditional steel reinforcement within concrete structures, thereby contributing valuable insights to the realm of structural engineering and material science.

1.3 Research objectives and methodology

Exploring the potential of BFRP-bars as an alternative to reinforcement steel, the research delves into the impact on structural integrity, burden to the environment, and cost efficiency. Central to this inquiry is the fundamental research objective which is presented below. Through an experimental study, the aim is to unveil the tangible benefits and challenges of applying BFRP-bars in concrete, paving the way for a more informed and sustainable approach to construction methodologies.

To research the flexural behaviour of concrete reinforced with basalt fibre reinforcement bars

The main inquiry revolves around the efficacy of employing BFRP-bars in reinforced concrete structures, specifically assessing the structural behaviour in relation to concrete structures with reinforcement steel. This research unfolds through targeted objectives probing into the properties, comparative characteristics, structural behaviour, applicability, environmental footprint, and regulatory considerations of embedded BFRP-bars in concrete design. The research objectives are listed below.

- Compare the structural characteristics of BFRP-bars in relation to steel reinforcement, highlighting their differences and properties and the effects on structural behaviour;
- Research the structural behaviour variations between concrete structures reinforced with BFRP-bars and steel-reinforced concrete to establish any distinct structural behaviour differences;
- Address the environmental impact of concrete structures reinforced with BFRP-bars in comparison to those reinforced with steel bars;
- Review the existing guidelines and regulations governing the design principles of BFRP-reinforced concrete structures, outlining their applicability and implications in design practices.

In the research, the methodologies encompassed direct tension tests for assessing the tensile characteristics of BFRP-bars, alongside multiple 4-point bending tests to elucidate crack propagation and patterns. These investigations were complemented by techniques such as digital image correlation, providing comprehensive insights into material behaviour and structural responses.

1.4 Thesis outline

Chapter 2 revolves around the available literature on BFRP-bars. Apart from the production process, literature on the environmental consequences, the behaviour of concrete structures reinforced with BFRP-bars, and the physical and mechanical properties are addressed. Furthermore, research on applied design guidelines is conducted. Chapter 3 presents the motivation and approach of the experimental study conducted in the concrete lab at the Delft University of Technology. The experiments concern direct tensile tests with BFRP-bars to determine the mechanical properties and 4-point bending tests. The results of the experimental program are presented in Chapter 4. This chapter delineates two primary sections: the direct tensile test and the 4-point bending test. In Chapter 5, the results are discussed with respect to the expectations and previously performed experiments. Chapter 6 deals with the conclusions of the main research question and the objectives. This section provides recommendations for further research as well.

Chapter 2

Literature study

2.1 Basalt fibre reinforcement bars

Delving into the exploration of BFRP-bars involves a comprehensive analysis encompassing their composition, manufacturing process, and physical and mechanical properties. Grasping the intricate methodologies is essential for accurately determining these defining characteristics.

2.1.1 Constituent materials

The most commonly used fibre materials used are primarily glass, carbon, aramid and basalt [Fiore et al., 2015]. A matrix resin, when added to the fibres, collectively comprises the composite material. The constituent materials are discussed in this section.

2.1.1.1 Basalt fibres

Basalt is an igneous rock type, which can be molten in a furnace with a temperature of 1450 to 1500 °C [Nanni et al., 2014]. The production of basalt fibres uses the same technology as that of other types of fibres used in the production of FRP-bars, however, it requires less energy [Nanni et al., 2014]. Furthermore, the raw material basalt rock is available in abundance as approximately 33% of the earth is comprised of this rock type [Prasad and Talupula, 2018]. This is the largest base material abundance of all fibre types as the abundance of silica minerals in the earth's crust is second with 26% [Britannica, 2015].

From the commercially available fibre types (table 2.1), basalt fibres have the highest strength potential as the tensile strength of a single filament is the highest compared to other fibre types commonly applied as FRP-reinforcement bars in concrete [Li et al., 2018]. All properties of single fibre filaments of the four mentioned types are noted in table 2.1. Figure 2.1 presents the stress-strain relation of notable fibre types used in FRP-bars.

Table 2.1: Typical characteristics of single filament fibres [Nanni et al., 2014, Ji et al., 2009, Kumbhar, 2014, Li et al., 2018, fib, 2007]

Type of fibre	Density (kg/m ³)	Tensile strength (MPa)	Young's modulus (GPa)	Ultimate strain (%)
B500 reinforcement steel	7850	500-600	210	5.0
E-glass	2500	3100-3800	72.5-78	2.4
S-glass	2500	4020-4650	83-91	3.3
AR-glass	2250	1800-3550	70-80	2-3
High-modulus carbon	1950	2480-4000	300-600	0.5
Low-modulus carbon	1570	2500-3500	200-300	1.1
Aramid K29	1440	2760	70-125	4.4
Aramid K49	1440	3620	124-531	2.2
Aramid K149	1440	3550	124-151	1.4
Basalt	2800	3000-4840	79.3-93.1	3.1

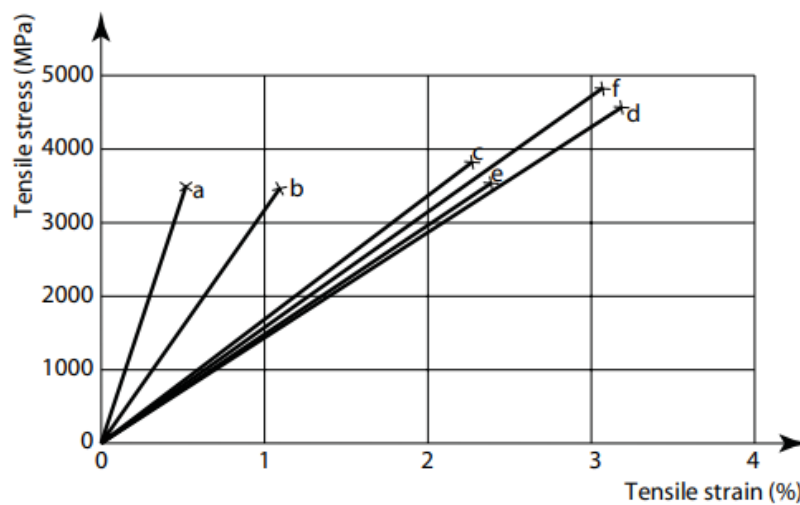


Figure 2.1: Stress-strain curves of typical reinforcement fibres. a: High-modulus carbon, b: Low-modulus carbon; c: Aramid K49; d: S-glass; e: E-glass f: Basalt. [fib, 2007]

2.1.1.2 Resin matrices

The resin matrix serves two primary functions: firstly, it binds the fibres utilized in the FRP-bars, and secondly, it safeguards both the individual fibres and the overall fibre structure of the bar [Nanni et al., 2014]. The matrices used in fibre reinforced polymers consist of thermoset polymeric resins. Thermoset resins are usually solids with a low-temperature melting point or liquids that are cured with a catalyst and/or heat. Once cured, thermoset resins cannot be reshaped or reverted to a liquid form. In the production of fibre reinforced polymers, three common types of matrices are used on an industrial level: epoxies, polyester and vinyl-esters. These 3 resin types are commonly applied due to their availability and cost-effectiveness, along with their mechanical properties. To

improve the mechanical properties of the resin, fillers and other additives are added. These added components also reduce the costs of the matrices [Nanni et al., 2014].

Epoxy is a type of thermosetting matrix containing at least one, but usually more epoxide groups in the molecule [Benmokrane et al., 2015]. Epoxies provide a high corrosion resistance and are less susceptible to damage from water or heat than the polyester and vinyl-ester. Epoxy however has a long required curing time and a relatively high cost. The use of epoxies is mainly in high-performance composites where good mechanical properties, corrosion resistance and low electricity conductivity are required. Epoxy is compatible with all fibre types used in the production of pultruded products, however its application is somewhat limited. Together with vinyl-ester, epoxies are applied in glass fibre reinforced polymers (GFRP's) [Fiore et al., 2015, Nanni et al., 2014].

Polyester resins provide a balanced set of chemical, mechanical and electrical properties, relatively low cost of production and good handling in the processing. By adjusting the components used in the production, polyester resins can be tailored chemically to meet various demands for different applications (flexibility, fire resistance, translucence, corrosion resistance, electrical insulation, heat resistance and UV-radiation resistance). The use of polyesters as a resin for the production of fibre reinforced polymer bars however is dissuaded because of the low chemical resistance in relation to the alternatives. Therefore, epoxies and vinyl-esters are applied more frequently [Nanni et al., 2014].

Vinyl-esters are the preferred choice amongst the matrices in the production of GFRP reinforcement as it has a good alkali resistance as well as bond with the glass fibres. Furthermore, vinyl-ester possesses the same advantageous properties as polyesters, as well as a better chemical resistance [Nanni et al., 2014] [Fiore et al., 2015].

Table 2.2 provides the mechanical properties of three commonly used resin matrices. The different resin types contain approximately the same density, however, vary slightly in their tensile strengths and moduli of elasticity. Note that, the physical and mechanical properties of the composite material also depend on the resin content and properties.

Table 2.2: Typical properties of resin matrices [Nanni et al., 2014, fib, 2007]

Type of matrix	Density (kg/m ³)	Tensile strength (MPa)	Young's modulus (MPa)
Epoxy	1186-1420	34.5-103.40	2070-3445
Polyester	1186-1420	38.2-130.90	2760-4130
Vinyl-ester	1130-1360	68.9-75.80	3000-3445

2.1.2 Production of reinforcement bars

The production of basalt fibre reinforcement bars is generally done using the pultrusion of continuous fibres. Pultrusion is a continuous production where fibres are pulled through a bath of heated resin matrix. The production process is schematically shown in figure 2.2. In each step of the production listed below, the corresponding number indication is mentioned.

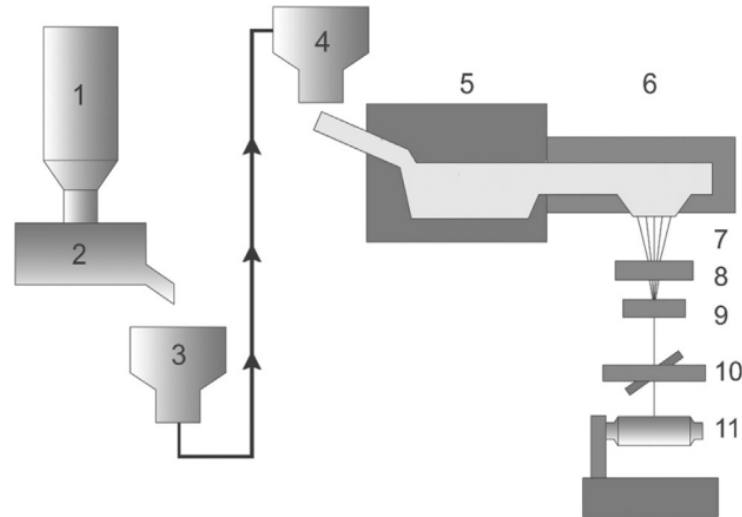


Figure 2.2: Simplified schematic overview of a continuous production line [Fiore et al., 2015] Basalt fibre manufacturing procedure illustrates the following steps: (1) crushed stone silo, (2) loading station, (3) transport system, (4) batch charging, (5) initial melting zone, (6) secondary heating zone with precise temperature control, (7) filament forming, (8) sizing applicator, (9) strand formation system, (10) fibre tensioning system, (11) automated winding system.

The production of basalt fibre reinforcement bars can roughly be distinguished into two main components. The first component is the production of the continuous fibres which are stored as coils, known as rovings. The second component is the production of the reinforcement bar itself out of the aforementioned semi-finished product.

Pultrusion offers a versatile method for creating a wide array of shapes, encompassing circular, H, L, U-profile sections, and more. The required length of the product is not limited by the pultrusion machine, but by the maximum transportable length of a pultruded product [Correia, 2013] [Nanni et al., 2014]. The process of pultrusion is schematically displayed in figure 2.3

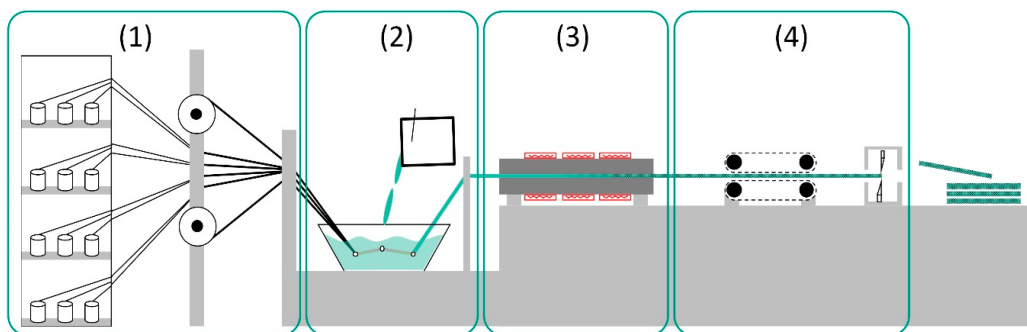


Figure 2.3: Pultrusion process scheme: (1): CBF's drawn from rovings. (2): CBF's impregnated with thermoset resin. (3): Impregnated CBF's are shaped with a hot mould, and resins are cured. (4): Products cut to the desired length. [Strauß et al., 2019]

2.1.2.1 Melting and crushing process

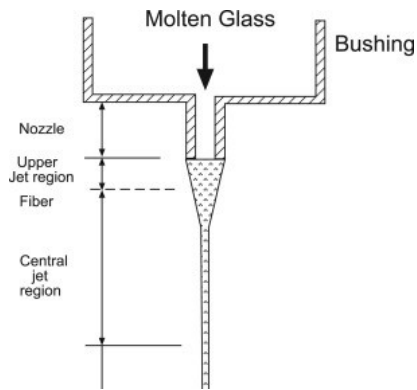
After the raw materials are screened, and the suitable rock types are selected for the production of CBF's, the raw material is ready to be melted. The process of melting basalt ore at a high temperature to a stable and homogeneous liquid is called basalt glass melting. The homogeneity and stability of liquid basalt glass influence the quality of the continuous basalt fibres and the drawing process.

The melting process of basalt can be divided into four stages [Wu et al., 2020]:

- Comminution (crushing) and homogenization of basalt ores: After crushing, the particle size is within a certain range to ensure a uniform mix of the basalt ore. This accelerates the melting of basalt and increases the quality and homogeneity of the liquid basalt glass melt. The required particle size for a good melting process should not be larger than 3 mm. For a quick melting process, the total surface area of the basalt rock particles must be as large as possible, hence the small rock particle size. A high melting speed is beneficial to the homogenization of the liquid basalt glass. To keep the mineral composition uniform, the crushed particles must be mixed evenly in size. A uniform mixture of particles is beneficial for ensuring the quality of CBF's and the physical properties of the desired end product. The crushing and homogenization of material is done in steps 1 and 2 respectively in figure 2.2.
- Basalt melt formation stage: For the basalt to melt, a continuous heating process is required. This means the heating of the basalt must be kept constant. At this stage, the basalt melt has a high viscosity, poor homogeneity and fluidity. At this point, the basalt is not yet liquified and is therefore heterogeneous in chemical and mineral composition. The temperature for the formation of liquid basalt is approximately 1250 up to 1450°C.
- Basalt melt stage of clarification and homogenization: With increasing temperature, the viscosity decreases and gasses in the rock such as carbonates and sulfates start to dissolve. To further reduce the viscosity, the molten basalt substance should be kept at a high temperature for a long time. The clarification and homogenization of the basalt melt happen in the range of approximately 1500 up to 1700°C. Steps 3 and 4 in figure 2.2 belong to this part of the production process.
- Basalt glass cooling stage: After homogenization, the liquid basalt glass is cooled to the forming temperature for the continuous basalt fibres. During cooling, crystallisation of the basalt glass should be prevented. The cooling stage is shown as steps 5 and 6 in figure 2.2.

2.1.2.2 Continuous basalt fibre formation

After melting and cooling down to a temperature suitable for continuous fibre formation. The liquid basalt glass is placed on a platinum-rhodium leakage plate. This plate contains leakage nozzles in a drop shape from where the liquid viscous basalt glass is drawn and solidified into a continuous basalt fibre (CBF) of the desired diameter. A cross-section of a nozzle is shown in figure 2.4a. The drawn continuous fibre (filament) is then caught by a wire drawing machine that is spinning at a continuous speed. The leakage plate determines the consistency of the diameter of the filaments. Next, the filaments are formed. These filaments are coiled to form a roving. An example of a roving is shown in figure 2.4b. The leaking plate and the formation of CBF's belong to steps 7 and 9 in figure 2.2. The winding of the rovings is shown in steps 10 and 11. These rovings are used in the pultrusion process.



(a) Cross-section nozzle of a leakage plate



(b) Roving containing basalt fibres

Figure 2.4: Leakage plate nozzle (a) [Kelly et al., 1968] and CBF roving (b) [Jumaishing, 2022]

2.1.2.3 Bar production through pultrusion

After the CBF rovings are produced, the necessary quantity of rovings is arranged in front of the pultrusion machine, depending on the bar diameter and the fibre content of the bar. The fibres are then drawn from the roving into the pultrusion machine (figure 2.5a), through a bath of resin matrices (figure 2.5b). These substances are hazardous to human health and the environment and require careful handling and storage. Exposure to elevated temperatures should be avoided in risk of fire [Correia, 2013] [Van de Velde and Kiekens, 2001].



(a) CBF are drawn from the rovings



(b) Typical open polymeric resin bath

Figure 2.5: Drawn fibres from CBF rovings and typical resin bath [Vedernikov et al., 2021]

The impregnation of the continuous fibres can be done using either an open resin bath or closed injection system, the latter is also called the 'straight through system'. The open bath process gives a slightly better result in terms of mechanical properties and dimensional accuracy of the final product, however, in most cases, this difference is negligible. Figure 2.6 shows the difference between the two methods. Subfigures a and b describe the process of the 'straight through' method and the open bath method, and subfigures c to f show the process variants of the closed injection system: c: teardrop, d: high-pressure, e: conical, f: siphon [Van de Velde and

Kiekens, 2001].

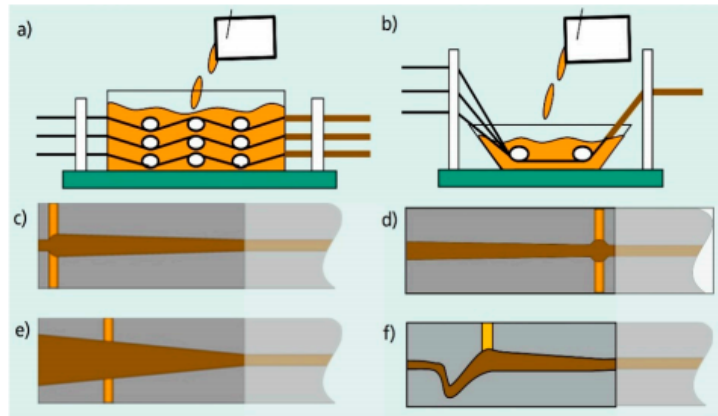


Figure 2.6: Closed injection versus open bath resin impregnation [Strauß et al., 2019]

The second phase starts by pulling the impregnated fibres through forming guides that shape the desired product. The filaments are pulled through a heated mould in the shape of the cross-section. The resin-impregnated filaments are then pulled through an oven when the polymeric resin is cured. Before entering this curing oven, helicoidal wraps are applied, as well as any desired coating. The applied coating forms both a protection for the bar against early damage of the fibre and resin structure as well as a surface deformation to form the bond mechanism to the concrete. In figure 2.7 the helicoidal wraps and the sand coating. The heat activates the resin curing, solidifying the polymeric matrices [Correia, 2013] [Nanni et al., 2014, Van de Velde and Kiekens, 2001]. After the thermoset resin is cured, the deformation capacity of the pultruded bar without causing damage is limited. Bending a bar after curing the resin leads to internal shear stresses causing delamination, and therefore weakening the fibre structure. This causes a loss of both strength and stability. After curing, the fibres cannot re-orientate within the resin anymore. The production speed of a pultrusion machine is approximately 900 mm of pultruded product per minute [Nanni et al., 2014].



Figure 2.7: Sand-coated FRP reinforcement bars [Nilforoush and Esfahani, 2012]

2.1.3 Determination of physical and mechanical properties

The mechanical properties of FRP-reinforcement are influenced by the mechanical and physical properties of the material. FRP-reinforcement can be tailored to meet specific requirements for the application in a structure. The composition and selection of the matrix play a role in the strength development of the composite reinforcement. The combination of the stress-strain relations of the constituent materials is shown in figure 2.8. Other relevant factors in the production are the bar diameter, production quality control and fibre orientation. The properties of the reinforcement are also influenced by the loading history, loading duration and factors such as temperature and humidity [fib, 2007].

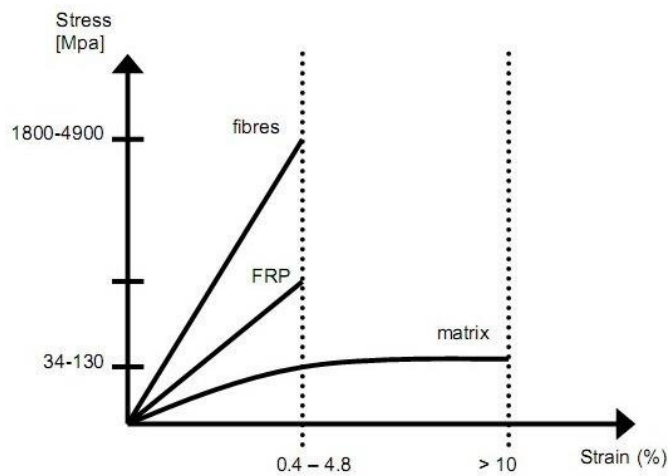


Figure 2.8: Stress strain relations of fibre reinforced polymer and constituent fibres and matrix [Zhang and Hsu, 2005]

An important element for the determination of the physical and mechanical properties is the characterization of the relative volume and mass content. The relative mass content is easier to determine because the mass of the fibres is generally better known than the volume. The relative volume (v_c) and mass (m_c) content of the constituent materials is determined in equations 2.1 and 2.2:

$$v_c = v_f + v_m \quad (2.1)$$

$$m_c = m_f + m_m \quad (2.2)$$

Note that, the subscripts f and m represent the fibres and the matrix respectively.

The volume (V_f , V_m) and mass (M_f , m_m) fractions can now be determined as well. These parameters are defined equation 2.3 to 2.7:

$$V_f = \frac{v_f}{v_c} \quad (2.3)$$

$$V_m = \frac{v_m}{v_c} \quad (2.4)$$

$$V_f + V_m = 1 \quad (2.5)$$

$$M_f = \frac{m_f}{m_c} \quad (2.6)$$

$$M_m = \frac{m_m}{m_c} \quad (2.7)$$

$$M_f + M_m = 1 \quad (2.8)$$

Note that, these fractions always have to add up to 1. If multiple types of fibre are used in the production of a bar, equations 2.9 and 2.10 apply. In this case, the reinforcement bar is called a Hybrid fibre reinforced Polymer bar (HFRP-bar).

$$V_{f,1} + V_{f,2} + \dots + V_m = 1 \quad (2.9)$$

$$M_{f,1} + M_{f,2} + \dots + M_m = 1 \quad (2.10)$$

From the fractions and the mechanical properties of the individual materials described in table 2.1, physical and mechanical properties can be derived.

2.1.3.1 Physical properties

2.1.3.1.1 Density The density of the composite reinforcement bar can be determined using the fractions of the volume or the mass. Equation 2.11 is used to determine the density of a reinforcement bar.

$$\rho_c = \rho_f V_f + \rho_m V_m \quad (2.11)$$

This formula uses the individual densities of the fibres and the matrix multiplied by the volume of fractions. In table 2.3 the densities for typical BFRP-bars are determined with a fibre content of 50% to 75% ($V_f=0.5-0.75$) and compared with reinforcement steel. Any deviations due to the weight of the selected resin matrix are taken into account, however, the differences are negligible [Nanni et al., 2014]. The density of BFRP-bars is 70% lower than that of reinforcement steel.

2.1.3.2 Short-term mechanical properties

2.1.3.2.1 Tensile properties The tensile properties of composite reinforcement depend mainly on the individual properties of the constituent materials. An analytical method derived from the works of Agarwal and Broutman [Agarwal and Broutman, 1990] gives the following expression for the longitudinal Young's modulus E_L (2.12) and subsequently, the longitudinal tensile strength f_{Lt} (2.13)

$$E_L = E_{fL} V_f + E_m V_m \quad (2.12)$$

Table 2.3: Typical properties of BFRP-bars compared to reinforcement steel, data from: [Nanni et al., 2014] [fib, 2007, Busel, 2006, Brózda et al., 2017]

	Steel	BFRP
Density (kh/m ³)	7850	2020-2420
Longitudinal Young's modulus (GPa)	200 50 to 78	
Longitudinal yielding tensile strength (MPa)	435	N/A
Longitudinal ultimate tensile strength (MPa)	500-600	1000 to 1800
Yielding tensile strain (%)	2.175	N/A
Rupture tensile strain (%)	5.0	2.0 to 2.6

$$f_{Lt} = f_{ft}V_f + \frac{E_m}{E_{fL}}V_m \quad (2.13)$$

A hybrid form can be adopted by combining two types of fibres within the same body of resin matrix. Equation 2.14 is used to determine the Young's modulus of two fibre types combined in a reinforcement bar. Indexes 1f and 2f denote the different types of fibre used.

$$E_L = E_{1fL}V_{1f} + E_{2fL}V_{2f} + E_m(1 - V_{1f} - V_{2f}) \quad (2.14)$$

Table 2.3 shows typical tensile strength and strain characteristics of common FRP-types. These values have been derived, assuming that an epoxy resin is applied.

Contrary to steel reinforcement, the maximum tensile force in FRP-reinforcement is not as clear-cut as multiplying the initial tensile strength with the area. Due to the shear-lag effect, the tensile strength of FRP-reinforcement decreases as the diameter of the bar increases [fib, 2000]. Figure 2.9 illustrates the shear lag effect. This makes the tensile strength dependent on the geometry of the bar. The shear lag effect is the decrease of strength due to a non-uniform stress distribution over the cross-section of the bar. This occurs due to the non-homogeneity of the cross-section. As the concrete is bonded to the outer fibres of the bar, the stresses are transferred gradually to the centre of the bar, inducing shear stresses between the individual fibres.

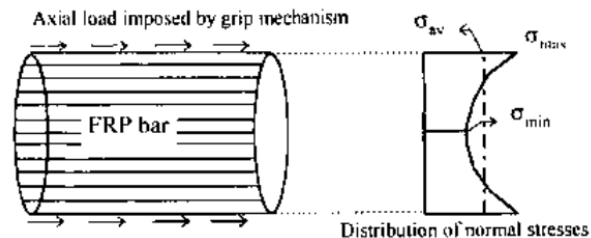


Figure 2.9: Stress distribution of tensile stress in FRP-bars subjected to axial load [fib, 2000]

2.1.3.2.2 Shear properties The main factor in the shear force resistance of a fibre reinforced polymer bar is the properties of the matrix. The domination shear force acting on FRP reinforcement bars is transverse rather than longitudinal. As the fibres are aligned perpendicular to the transverse shear force, the resistance

against transverse shear force primarily stems from the resin matrix's resistance. Transverse shear forces on the bar are shown in figure 2.10. The shear modulus $G_{\text{transverse}}$ can be determined with an equation derived from the works of Tsai [Tsai and Hahn, 1980]. This formula is noted in equation 2.15.

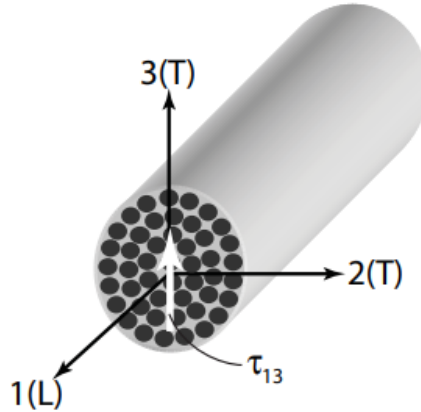


Figure 2.10: FRP reinforcement bar subject to a transverse shear force [fib, 2007]

$$G_{\text{transverse}} = G_m \frac{V_f + \eta_{\text{transverse}} V_m}{\eta_{\text{transverse}} V_m + V_f \frac{G_m}{G_f}} \quad (2.15)$$

where:

$$\eta_{\text{transverse}} = \frac{3 - 4v_m + \frac{G_m}{G_f}}{4(1 - c_m)} \quad (2.16)$$

Note that, the parameters G_f and G_m are the shear moduli of the fibres and the matrix respectively. Other parameters have been elaborated upon in previous equations.

In the case of interlaminar (transverse) shear force resistance, the shear strength of the matrix itself is the dominating factor. As this force acts perpendicular to the fibre direction, the fibres themselves do not contribute to the shear resistance of the reinforcement bar itself. This means that if the fibre volume V_f of the bar increases (and therefore the matrix volume V_m decreases), the shear force resistance of the bar reduces. Fibres have a negative effect on the force distribution within the reinforcement bar as they cause stress concentration in the matrix [fib, 2007, Barbero, 1999].

2.1.3.3 Long-term mechanical properties

The long-term properties of FRP-reinforcement differ significantly from that of reinforcement steel. The most prominent causes of loss of strength in the long-term mechanical properties are creep and relaxation of the FRP-bars [fib, 2007].

2.1.3.3.1 Creep and creep rupture Creep is the increase of tensile strain in the reinforcement under a constant loading of a long duration. Concerning creep, FRP's exhibit different behaviour compared to reinforcement steel. In concrete structures reinforced with steel bars, only the concrete shows creep behaviour. This is not the case for concrete structures reinforced with FRP-bars, as the FRP-bars also show creep behaviour.

Whereas the fibres exhibit no creep behaviour themselves, it is the FRP-composite as a whole that manifests creep behaviour, mostly governed by the properties of the resin matrix. The nature of FRP composites' creep behaviour often stems from the bonding properties at the interface of the fibres and the matrix resin [fib, 2007, Karbhari et al., 2003].

Figure 2.11 shows a typical strain history curve during creep deformation. This curve is comprised of two components. The first component is the initial elastic strain imposed directly after the load is applied at $t=0$. This component is not time-dependent. The second component consists of three stages of creep. In the first creep stage that starts at $t=0$, the strain grows rapidly over a short time, but the increment slope decreases gradually.

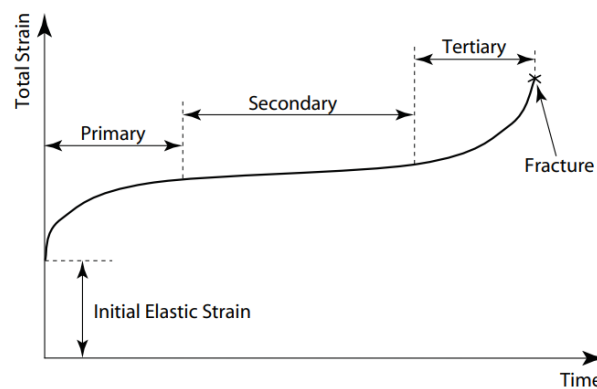


Figure 2.11: typical strain history curve during creep deformation [fib, 2007]

The secondary creep stage is defined by a continuous increment slope and concerns the period of the structure being in use. The Tertiary stage of creep is characterized by simultaneous accumulation of creep strain and material damage [fib, 2007]. The first component is the non-time-dependent part of the total strain. This initial elastic strain is dependent on the load applied and the tensile stress it imposes on the reinforcement, as well as the longitudinal Young's modulus. The initial elastic strain is determined with equation 2.17.

$$\varepsilon_0 = \frac{\sigma}{E_L} = \frac{\sigma}{E_{fL}V_f + E_mV_m} \quad (2.17)$$

The total time-dependent strain depends on the creep rate parameter, the parameter time t in hours and the initial elastic strain. The total strain including creep is determined by the formula noted in equation 2.18.

$$\varepsilon(t) = \beta \log(t) + \varepsilon_0 \quad (2.18)$$

2.1.4 Characteristics of BFRP

BFRP-bars have different characteristics when compared to reinforcement steel. These differences have some implications and consequences for designing concrete structures. The section elaborates on the characteristics of BFRP-bars and compares these characteristics to those of reinforcement steel [Busel, 2006].

2.1.4.1 Stress-strain behaviour

BFRP-bars contain a different stress-strain behaviour compared to reinforcement steel bars. Unlike reinforcement steel, BFRP-bars showcase a linear stress-strain response, characterized by their elastic behaviour until failure. The Young's modulus for BFRP remains consistent in the elastic region, providing predictable deformation patterns for the bar itself [Busel, 2006]. The stress-strain behaviour of both BFRP-bars and reinforcement steel is presented in figure 2.12.

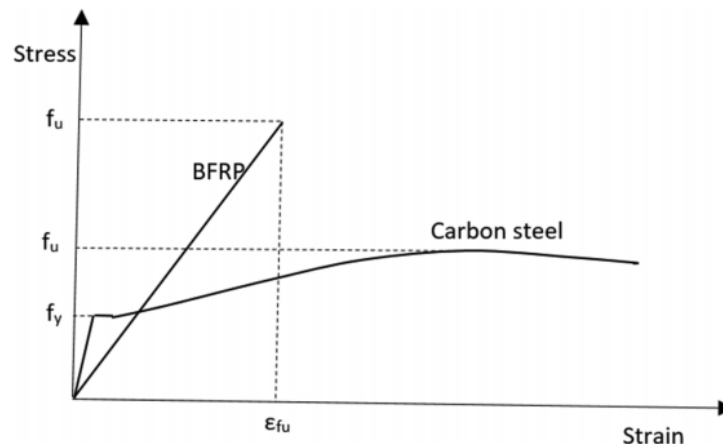


Figure 2.12: Stress-strain diagram comparison [Shamass and Cashell, 2020]

Up until the yielding stress (f_y in figure 2.12), the stiffness of reinforcement steel is generally larger than that of BFRP. However, when the yielding stress is exceeded, reinforcement steel enters its plastic deformation stage. In this stage, the strain increases rapidly, causing the stiffness to drop significantly as well. For BFRP-bars, there is no plastic deformation stage. As soon as the rupture stress and its corresponding yielding strain (f_u and ϵ_{fu} in figure 2.12 respectively) are reached, brittle failure occurs. As the BFRP-bars do not contain a plastic deformation stage, no irreversible deformation should occur after a load is removed [Shamass and Cashell, 2020, Busel, 2006].

2.1.4.2 Longitudinal tensile strength

In general, FRP has higher tensile strengths compared to common reinforcement steel. The characteristic tensile strength of BFRP is approximately 1000 to 1800 MPa, whereas B500 reinforcement steel has a characteristic tensile strength of 500 MPa. This difference implies that the cross-sectional area needed to achieve the required tensile force in the reinforcement is theoretically smaller for BFRP-bars than for reinforcement steel. However, this does not always apply, as serviceability limit state aspects such as crack width and deflection also play a role in structural design.

2.1.4.3 Transverse strength

The transverse strength of BFRP is relatively low. The transverse strength is dominated by the resin content of the bar, however, even with a high resin content (e.g. low fibre content), the transverse strength of BFRP-bars is still insignificant. BFRP-bars mostly serve a tensile reinforcement purpose. Consequently, the fibre content

is therefore between 70% and 85% to keep the tensile strength high. As a consequence, the resin content is lower, causing the transverse strength to be lower.

2.1.4.4 Young's modulus

The Young's modulus of BFRP is significantly lower than that of reinforcement steel. BFRP-bars typically have a Young's modulus of approximately 50 GPa. This is 3 to 4 times lower than that of reinforcement steel. This has some implications for concrete structures. For example, the lower Young's modulus causes concrete structures to be less stiff and therefore experience larger deformations at the same loads compared to concrete structures reinforced with steel bars.

2.1.4.5 Corrosiveness

Contrary to reinforcement steel, BFRP is not susceptible to corrosion. The corrosion resistance however is not limited to specifically BFRP reinforcement bars. Other types of FRP reinforcement, bars such as GFRP, have equal resistance against corrosion [Brózda et al., 2017]. This is significant because a commonly observed deterioration process in steel-reinforced concrete structures is the corrosion of the reinforcement steel. When steel corrodes, it forms expansive products that induce internal stress in the concrete, potentially leading to cracking and diminishing the structure's tensile bearing capacity. Applying non-corrosive reinforcement materials such as BFRP could represent a substantial enhancement in the durability of reinforced concrete structures.

2.1.4.6 Conductivity

Conductivity can be categorized into two types at most: electrical and thermal. BFRP-bars have a very low electrical conductivity as basalt fibres do not conduct electricity and the conductivity of the resin matrix is limited as well. As a result, structures reinforced with BFRP-bars do not create electrical pathways, reducing the risk of issues related to electrical conduction [Busel, 2006] [Ma et al., 2019]. In contrast, steel reinforcement bars are highly conductive. While this property is not necessarily a problem in most cases, it can lead to issues like corrosion in reinforced concrete structures due to the presence of chloride ions and moisture, especially in harsh environments or in the presence of stray electrical currents [Peet et al., 2011].

Of lesser importance in reinforced concrete is the lower thermal conductivity of BFRP-bars in relation to reinforcement steel. This characteristic could be advantageous in certain construction applications, especially where minimizing heat transfer or preventing temperature fluctuations is required, such as in structures subjected to extreme temperatures or environments sensitive to thermal changes [Busel, 2006] [Ashrafi et al., 2017, Peet et al., 2011].

2.1.4.7 Magnetic behaviour

BFRP is a nonmagnetic type of reinforcement. For some applications where nonmagneticity is required, BFRP-bars have an advantage over reinforcement steel, which is magnetic. On the other hand, this nonmagnetic property of BFRP makes it more difficult to separate reinforcement from concrete while recycling.

2.1.4.8 On-site characteristics

BFRP-bars have limited deformation capacities after production. If a bent bar is designed to be applied in a concrete structure, the reinforcement bar has to be produced in the required shape. Reinforcement steel can however be bent on site. BFRP-bars are approximately 4 times lighter than reinforcement steel bars of the same diameter. This is advantageous for the working conditions on site, as the workers have less burden to carry compared to steel reinforcement. For lifting by crane on site, reinforcement steel requires a crane with a larger lifting capacity.

2.2 Reinforced concrete structures with BFRP

The application of basalt fibre reinforced polymer bars in concrete alters the behaviour of reinforced concrete in comparison to reinforcement steel. BFRP-bars have different characteristics such as a lower Young's modulus and a higher tensile strength in comparison to reinforcement steel. The different characteristics of BFRP mean that the mechanics of BFRP-reinforced concrete differ from steel-reinforced concrete. Flexural behaviour under bending loads, bond behaviour, bond slip and cracking are among these influenced facets. Experimental studies provide insight into these topics. Available literature containing experimental studies with BFRP-bars is presented in table 2.4.

Table 2.4: Available literature on conducted experimental studies

Authors	Year of publication	Experiment topic
Huang et. al.	2021	Experimental and numerical study on concrete beams reinforced with Basalt FRP bars under static and impact loads [Huang et al., 2021].
Xiong et. al.	2021	Experimental study on the effects of glass fibres and expansive agent on the bond behaviour of glass/basalt FRP bars in seawater sea-sand concrete [Xiong et al., 2021].
Shamass & Cashell	2020	Experimental investigation into the flexural behaviour of basalt FRP reinforced concrete members [Shamass and Cashell, 2020].
Elgabbas et. al.	2016	Experimental testing of basalt-fiber-reinforced polymer bars in concrete beams [Elgabbas et al., 2016].
Pawłowski & Szumigala	2015	Flexural behaviour of full-scale basalt FRP RC beams – experimental and numerical studies [Pawłowski and Szumigala, 2015].
Beana et. al.	2013	Analysis of cracking behaviour and tension stiffening in FRP reinforced concrete tensile elements [Baena et al., 2013]
Tepfers & De Lorenzis	2003	Bond of FRP reinforcement in concrete - A challenge [Tepfers and De Lorenzis, 2003].
Kanakubo et. al.	1993	Bond splitting strength of concrete members reinforced with FRP bars kanakubo [Kanakubo et al., 1993].

2.2.1 Flexural behaviour

An experimental research by Shamass & Cashell [Shamass and Cashell, 2020] provides insight into the flexural behaviour of beams reinforced with BFRP-bars compared to the same beam reinforced with reinforcement steel. This experimental campaign contained 5 beams. In one of the beams, reinforcement steel was applied, whereas the remaining 4 beams were reinforced with BFRP-bars. The experiment investigates the impact of surface deformation. To achieve this, 2 beams were coated with sand while the other 2 contained ribs, formed through helical wrapping, on their surfaces. The beams were subjected to a 4-point bending test (2.13). The concrete class used in the experiment is C30/37.

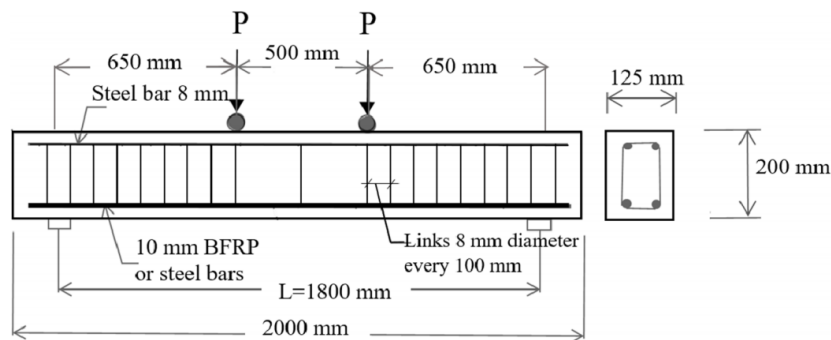


Figure 2.13: experimental study by Shamass & Cashell [Shamass and Cashell, 2020]

Beams labeled "SA" feature sand-coated BFRP-bars, "R" denotes ribbed bars with helical wrapping, and "S" indicates steel reinforcement. Each beam type is identified by the abbreviation followed by "B10" for beam type and 10 mm for bar diameter, with a serial number denoting the variation. Beams are intended to fail in the concrete compression zone. Load-deflection curves are depicted in Figure 2.14.

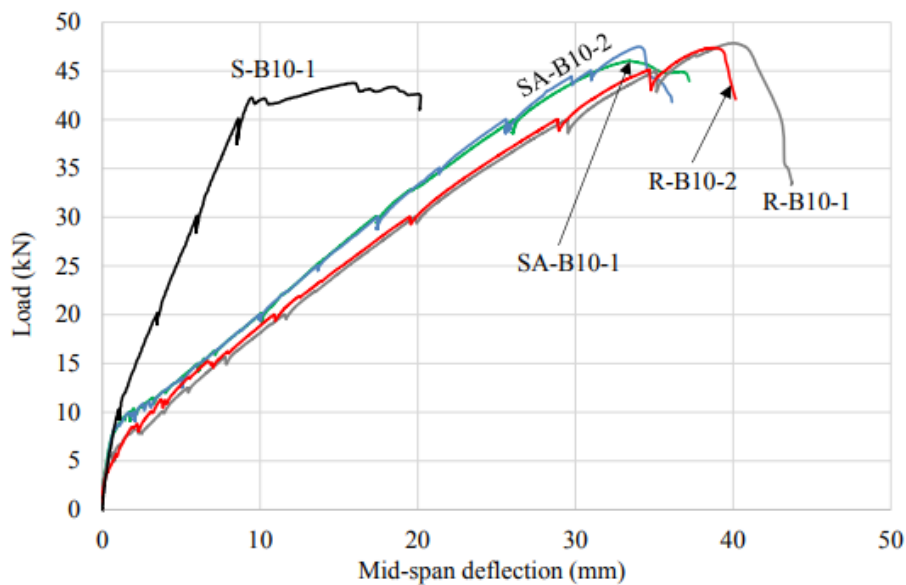


Figure 2.14: Load-deflection curves experimental study by Shamass & Cashell [Shamass and Cashell, 2020]

After the first crack appears, all beam types reinforced with BFRP-bars show significantly more vertical deflection compared to the beam reinforced with steel. According to Shamass & Cashell, this is caused by the differing Young's modulus of the reinforcement bars. Material tests before the 4-point bending test show that the BFRP-bars used in beams contain a Young's modulus of 54 to 56 GPa, whereas the reinforcement steel contains a Young's modulus of 200 GPa. After the initial cracking phase, the load-deflection patterns of beams reinforced with BFRP-bars display an almost linear trend until the concrete compression zone starts to fail. This behaviour contrasts with that of concrete beams reinforced with steel bars, where there is a plastic deformation stage notable in the load-deflection curve. The deflection curve (see figure 2.14) indicates noticeable plastic deformation of the reinforcement steel around 40 kN. This plastic strain in the reinforcement causes a significant drop in beam stiffness and a substantial increase in beam deformation. However, the deflection magnitude observed in the BFRP-reinforced beams is never attained. An experimental study on the flexural behaviour of BFRP-reinforced beams by Pawlowski & Szumigala in 2015 [Pawlowski and Szumigala, 2015] presents similar load-deflection behaviour of beams loaded in bending. All beams failed within the concrete compression zone, aligning with the intended design outcome.

2.2.1.1 Influence of surface deformation

The beams with sand-coated bars demonstrate a slightly higher stiffness than those with ribbed BFRP-bars, possibly because the sand-coated bars exhibit a superior bond strength development, as noted by Shamass & Cashell in their experimental study [Shamass and Cashell, 2020]. Since both types of bars have similar Young's moduli, this difference is likely to have a minimal impact on the beams' stiffness.

2.2.1.2 Cracking moment

Shamass & Cashell also claim the cracking moment M_{cr} is slightly higher for beams reinforced with steel bars. This is due to the higher Young's modulus of reinforcement steel, influencing the moment of inertia of the beams. A higher Young's modulus causes the centre of gravity to shift slightly more to the bottom of the cross-section, requiring a larger load to reach the tensile strength of the concrete and initiating a crack.

2.2.2 Bond behaviour

Bond behaviour is defined as the way the reinforcement bonds to the concrete. The bonding of concrete to the reinforcement influences the cracking behaviour of the concrete structure in the zones of structures subjected to tension. Factors that influence the bond behaviour of reinforcement, in general, are listed below [Al-Azzawi et al., 2018] [Walraven, 2013] [fib, 2000].

- The aggregate size in the concrete;
- The applied concrete strength class defines the tensile strength of the concrete;
- The detailing of the reinforcement bars;
- The diameter of the applied reinforcement bars;
- The applied concrete cover.

The application of FRP-bars has some implications on the bond behaviour. In addition to the influences listed above, factors that specifically apply to concrete reinforced with FRP-bars are:

- The surface deformation of the bar to provide bond strength with the confining concrete. The degree and type of the deformation, either through a sand-coating, helical wrapping or screw thread, provides friction

or interlocking with the concrete [Sólyom et al., 2018]. When anchoring reinforcement steel bars, the bond strength is developed through chemical bond and through interlocking. In FRP's, the bond strength is developed through chemical bond and friction, especially with sand-coated bars [Busel, 2006].

- The shear stiffness of fibre reinforced polymer is significantly lower than that of reinforcement steel. In FRP-bars, the bond stress is transferred through the resin matrix of the reinforcement bar. If the bond stress oversteps the shear strength of the matrix resin, bond-shear failure occurs in the bar, causing the adhesion between the concrete and the FRP-bar to break down and therefore reducing the bond strength [Busel, 2006];

In the following paragraphs, the influences on the bonding mechanisms are further elaborated upon.

2.2.2.1 Bond strength development

The bond strength development of FRP bars is described by the bond law, which is the relation of the loaded end slip of the bars versus the bond stress. The bond behaviour develops in stages that depend on the bar diameter, the concrete class, the properties and detailing of the reinforcement material and the type of surface shapes and surface deformation of the bar [fib, 2000]. The stages of bond stress development are shown in figure 2.15. The stages of bond strength development are described below.

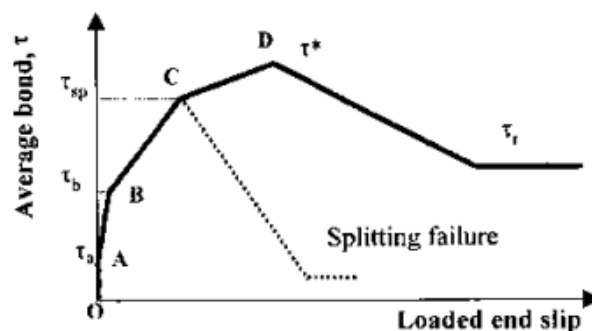


Figure 2.15: Typical average bond stress versus bond-slip of FRP bars embedded in concrete [fib, 2000]

Tepfers [fib, 2000] has derived a multi-linear model for the bond-slip curve of FRP-bars, presented in figure 2.15. This model is divided into several sections with different characteristics in the bond strength development.

Section OA: As the bond stress increases, the first stage does not show any measurable slip of the reinforcement. The main bond mechanism at this stage is the chemical bonding of the concrete to the reinforcement.

Section AB: At a certain point in the load increment, the chemical bonding starts to fail and the mechanical interlocking or friction mechanisms begin to take up shear stress. A slope in the graph is now noticeable, which means the bond stiffness gradually decreases. Deformations in the bars and micro-cracks in the concrete now start to emerge. Compared to steel reinforcement, the formation of cracks in concrete is delayed because the FRP bars are more susceptible to local deformation of the bars. At this stage, FRP-reinforcement generally has better bond properties than ribbed steel reinforcement of equal diameters. [Tepfers and Karlsson, 1997]

Section BC: At this stage of the bond stress development, bearing stresses in the surrounding concrete increase to concrete splitting level τ_{sp} . The principle direction of the bearing stresses is assumed to be under an angle (α) shown in figure 2.16. The value of angle (α) depends on the properties of both the concrete and the reinforcement

bars, such as the Young's modulus of the bar, the concrete shear strength and the shape and surface deformation of the bar surface. The radial component of the total bond force is balanced against the ring of tensile stress developed in the surrounding concrete.

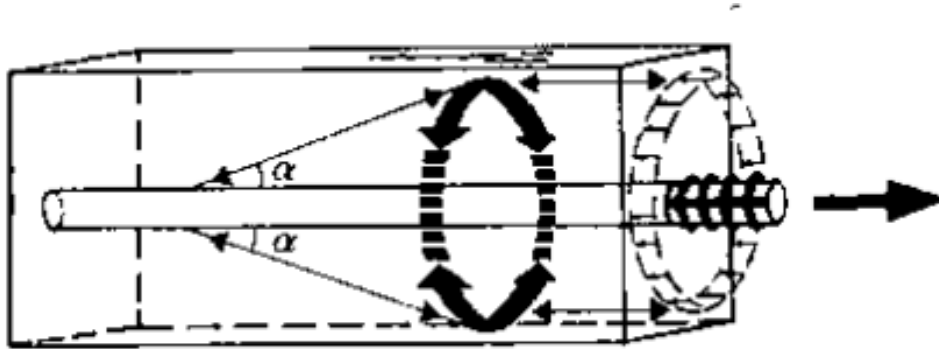


Figure 2.16: Radial component of the bond forces balanced against the tensile stress ring [fib, 2000]

At this stage, the concrete's splitting resistance is key. The ultimate cracking pattern exercises the minimum splitting resistance and therefore determines the anchoring capacity. The main influences on the splitting resistance are the confinement by the concrete mass, applied transverse reinforcement (for example stirrups in beams), and externally applied pressure in the anchoring zone. If the concrete confinement is not sufficient, the force in the bar is not properly distributed over the full circumference of the bar, causing the hoop forces to exceed the tensile strength of the concrete. Cracks will therefore appear over the length of reinforcement.

Section CD: After the concrete splitting stress τ_{sp} is reached, the bond stiffness decreases significantly. If sufficient resistance to splitting can be reached by the confining concrete mass, the maximum bond strength τ^* can be achieved. At this stage in the bond development process, a total of four bond failure modes may occur.

- Shearing off part of or all the surface deformation of the bar: The bond strength is not governed by the concrete strength in this failure mode, but either by the laminar shear strength between the fibres or by the shear strength of the bar deformations. Contrary to steel, an increase in concrete strength will not lead to a higher bond strength for this failure mode, because it's not governing for this particular failure mode. This bond failure mode will yield the highest possible bond strength from the bar.
- Concrete shear failure: Failure occurs in the concrete rather than on the surface of the bar. This bond failure mode is similar to that of deformed steel reinforcement bars. The concrete is crushed at the bar deformation due to localized peak stresses. For this bond failure mode, the bond strength is mainly dependent on the concrete shear strength.
- Combined failure mode: A combination of the above-mentioned failure modes. This is likely to occur for intermediate concrete classes.
- Squeeze through: Due to the low transverse stiffness of FRP bars, the bars could squeeze through the concrete. Bond strength is provided by friction through wedging the bar surface deformation on the confining concrete. The failure mode is therefore ductile, as it concerns the shear resistance of the FRP-ribs. The bond strength development heavily depends on the geometry of the FRP-bar surface. Bars with larger deformations such as ribs are therefore less prone to squeeze through bond failure than sand-coated bars.

Beyond point D: After the peak bond stress is reached, the mechanism that ensures bond strength progressively loses integrity. The residual bond stress comes from friction τ_r due to the roughness of the interface of

the bond failure.

2.2.2.2 Bonding mechanism

In flexural cracking, the manner of bonding and bond strength development plays a considerable role. Research by Xiong [Xiong et al., 2021] has pointed out the differences in surface deformation type. In general, BFRP-bars have 4 options in terms of surface deformation. These varieties are listed and elaborated upon below.

- Helical wrapping;
- Screw thread;
- Sand coating;
- Combined helical wrapping and sand coating.

Helical wrapping: Bond behaviour is dominated by mechanical interlocking with the surrounding concrete. By casting the concrete, ribs form in the cavities of the wrapping. When slip occurs, the ribs of the bar containing the wrapping fibres and the concrete ribs ensure the interlocking. For this type of surface shape, the main failure modes are the shear failure of the concrete ribs and the deformation of the helical wrapping fibre ribs of the BFRP-bar. Figure 2.17 presents the bonding mechanism of this surface deformation [Xiong et al., 2021].

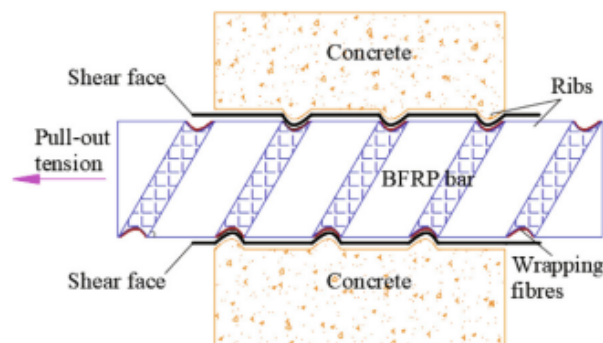


Figure 2.17: Bond mechanism helical wrapping as surface deformation [Xiong et al., 2021]

Screw thread: Bond behaviour is mostly dominated by mechanical interlocking as well. The difference in shape with the helical wrapping is the smaller width of the ribs of the bars. This makes the concrete less susceptible to shear failure but makes the ribs of the bars more susceptible to failure. The failure modes of this type of surface shape and surface deformation remain the same as for the helical wrapping. Figure 2.18 presents the bonding mechanism of this surface deformation [Xiong et al., 2021].

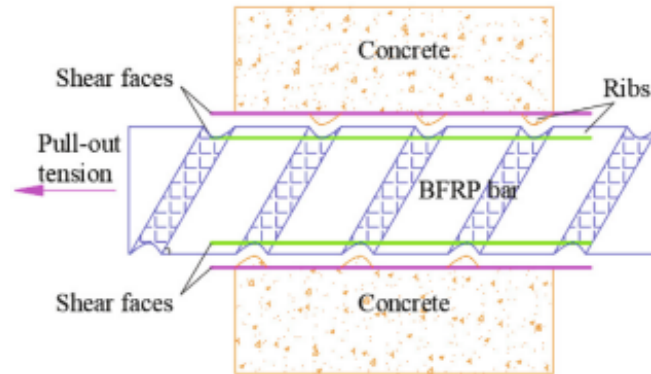


Figure 2.18: Bond mechanism screw thread as surface deformation [Xiong et al., 2021]

Sand coating: The primary bonding mechanism for the sand coating is friction. By applying a sand coating, 2 shear faces occur. The first shear face is located at the interface of the bar and the sand coating. The second shear face concerns the bond of the sand coating to the surrounding concrete. Note that, this type of bar has an even surface without screw threads, and therefore does not bond by mechanical interlocking. The main failure modes are shear failure of the sand coating at its interface with the bar, and shear failure of the sand coating at its interface with the concrete. Figure 2.19 presents the bonding mechanism of this surface deformation [Xiong et al., 2021].

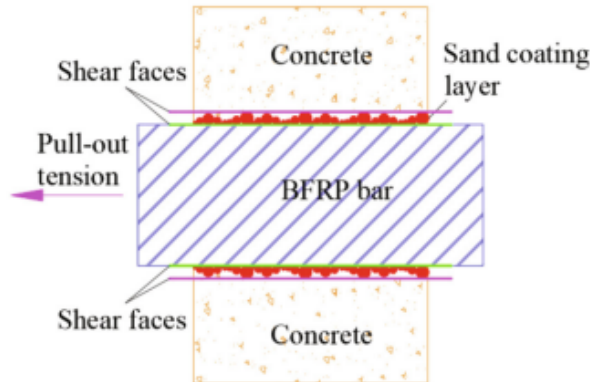


Figure 2.19: Bond mechanism sand coating as surface deformation [Xiong et al., 2021]

Screw thread and sand coating combination: This shape incorporates the combined properties of the surface deformation discussed earlier. A report by Xiong [Xiong et al., 2021] claims the bond behaviour is similar to the sand-coating without a helical wrapping and is therefore dominated by friction. Failure is therefore likely to occur in the helical wrapping.

Figure 2.20 shows results from a slip versus bond stress test. The highest bond stresses are reached by the bars produced with helical wrapping (subfigure 2.20a) and the screwed thread (subfigure 2.20b). The curves of the helical wrapped and the screwed thread bars initially exhibit elastic characteristics, until the stiffness goes to zero at the first peak of the curve. This point in the curve signifies the peak value of bond strength. After the peak is reached, the described failure modes start to occur along the length of the bar and residual bond strength comes from friction. After the slip distance reached approximately the centre-to-centre distance of the ribs, new

interlocking arises, hence the second increase in stiffness. This new interlocking, however, does not reach the same peak bond strength as the initial peak bond strength and is therefore inadvisable to rely on. Figure 2.20a includes a proposed model curve that does not include the second bond strength development phase. This proposed model curve shows similarities with the bond stress development curve in figure 2.15 [Xiong et al., 2021].

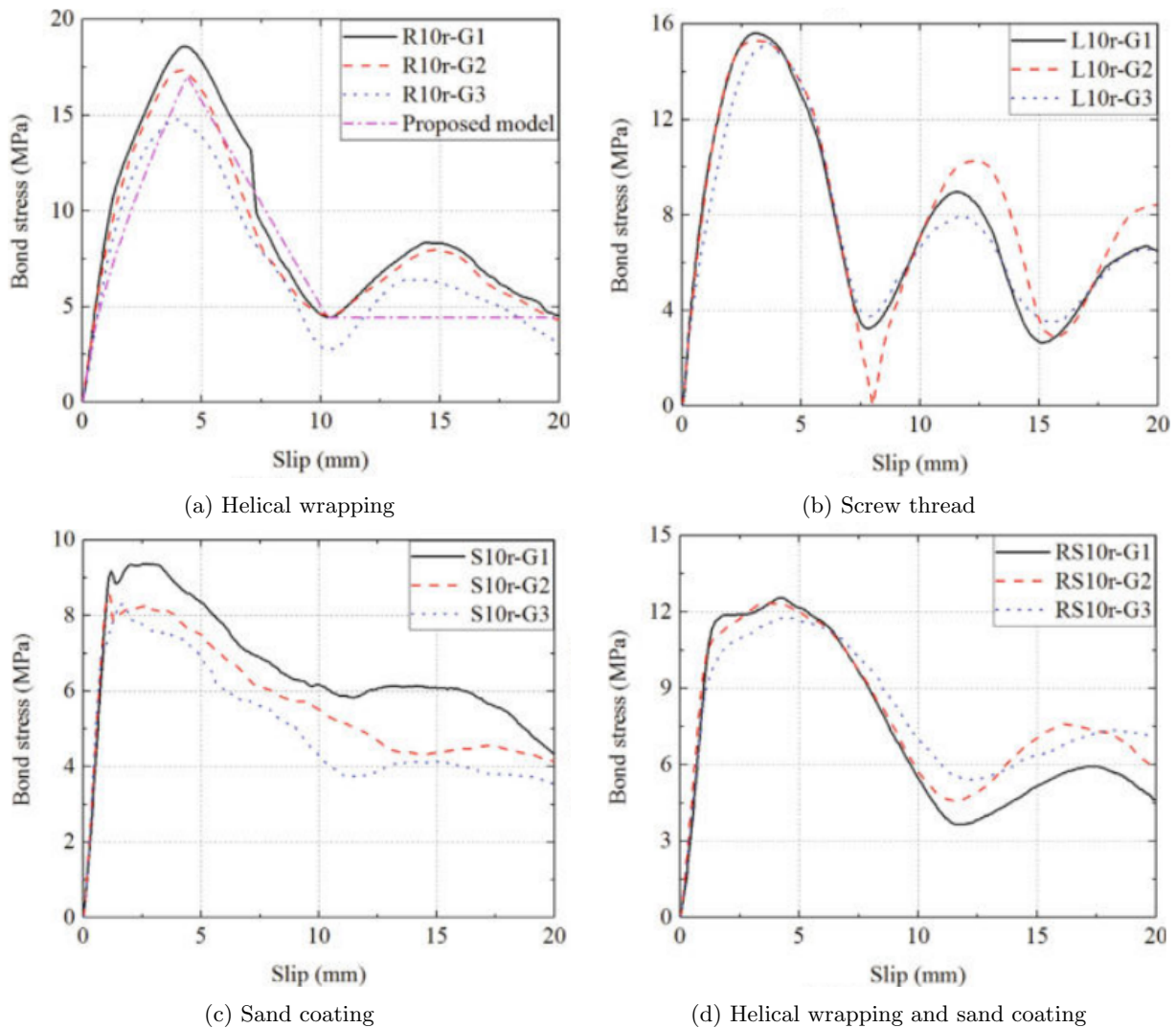


Figure 2.20: Bond-slip test results bar diameter 10 mm with different surface deformations; (a) helical wrapping, (b) screw thread, (c) sand coating, (d) combined helical wrapping and sand coating [Xiong et al., 2021]

The bond-slip curve of the sand-coated bar specimen is friction-dominated due to the absence of ribs on the bars. Because of this absence, a second bond stress development due to new interlocking is therefore limited or non-existent. In the first stage of the bond stress development, stiffness remains relatively constant due to the limited slip. As the curve reaches its peak, local shear faces are formed over the length of the bar, and the bond strength reaches a short plateau where the slip increases. According to [Xiong et al., 2021], the surface

deformation starts to fail due to the internal interaction of the shear force in the reinforcement bar. Lastly, the curve descends due to the described failure modes emerging in the sand coating and the concrete.

The specimen with the helical wrapping and the sand coating shows features of the curves of the individual surface shapes and surface deformation. The steep inclination is a characteristic of the sand coating, as well as the plateau at the peak stress. As the slip increases, the bond stress decreases after the plateau, but due to new interlocking, the bond stress increases again. This characterizes the ribs of the helical wrapping.

2.2.2.3 Limitations in performed experimental studies

The performed experimental research does however has limitations. Whereas Pawlowski & Szumigala [Pawlowski and Szumigala, 2015] and Shamass & Cashell [Shamass and Cashell, 2020] did load-deflection behaviour of beams reinforced with BFRP-bars, an extensive analysis of cracking patterns and a comparison with steel-reinforced beams is not performed. Elgabbas [Elgabbas et al., 2016] however does investigate the cracking patterns, but does not include the effects of the concrete cover. The research by Huang et. al. [Huang et al., 2021] does contain extensive investigation into cracking patterns, but is more aimed at shear crack development. However, as a 3-point bending test is performed, a fully developed cracking pattern over a certain length can not be established.

2.2.2.4 Ambiguity and discussions in bond strength

Extensive research has been performed in the matter of bond strength of FRP-bars to concrete and reinforcement steel to concrete. However, there is no consensus on whether the ribbed reinforcement steel bars contain better bond strength than FRP-bars. Some research into bond strength has shown that steel reinforcement develops a bond strength superior to that of FRP [Benmokrane et al., 1996, Larralde and Silva-Rodriguez, 1993] [Al-Zahrani et al., 1999, Chaallal and Benmokrane, 1993, Castel et al., 2007]. Other research suggests that the bond strength of FRP is generally higher than that of ribbed steel reinforcement [S. Solyom, 2017, Nanni et al., 2014, Nanni et al., 1995, Freimanis et al., 1998].

2.2.3 Cracking behaviour

Bending loads exercised on concrete structures cause various forms of cracking. Concerning the bond characteristics of longitudinal reinforcement, it is pertinent to investigate flexural cracks and tensile splitting cracks. Vertical flexural cracks tend to appear in spots where the tensile strength of the concrete is exceeded. As the longitudinal reinforcement is located at the bottom, perpendicular to the direction of the crack, these bars control the flexural crack width. Tensile splitting cracks emerge parallel to the longitudinal tensile reinforcement. These cracks tend to appear due to excessive bond stresses at the surface of the reinforcement. This causes tensile stresses in the concrete, leading to cracking. Excessive formation of tensile splitting cracks could cause spalling of the concrete cover [Huang et al., 2021].

2.2.3.1 Flexural cracks

As sand-coated BFRP-bars contain higher bond strength than reinforcement steel, more cracks should appear over the same distance compared to beams reinforced with steel bars [Shamass and Cashell, 2020]. As sand-coated BFRP-bars contain a high bond strength, the required transfer length (denoted as $l_{s,max}$ in figure 2.21) for the tensile force from the bar to the concrete should be smaller. At the location of the cracks, the tensile stress peaks, where the stress in the concrete is zero. This is shown in subfigures 2.21(b) and 2.21(c). If the bond

strength of BFRP-bars is higher, the flexural cracks should occur closer to each other over the length of the beam compared to steel-reinforced concrete beams. This allows for a larger number of flexural cracks to appear over the length of a beam, allowing further reduction of the stiffness of the beam. In figure 2.21, the steel, concrete and bond stress distributions in the cracked area of a deformed concrete member are shown [Walraven, 2013].

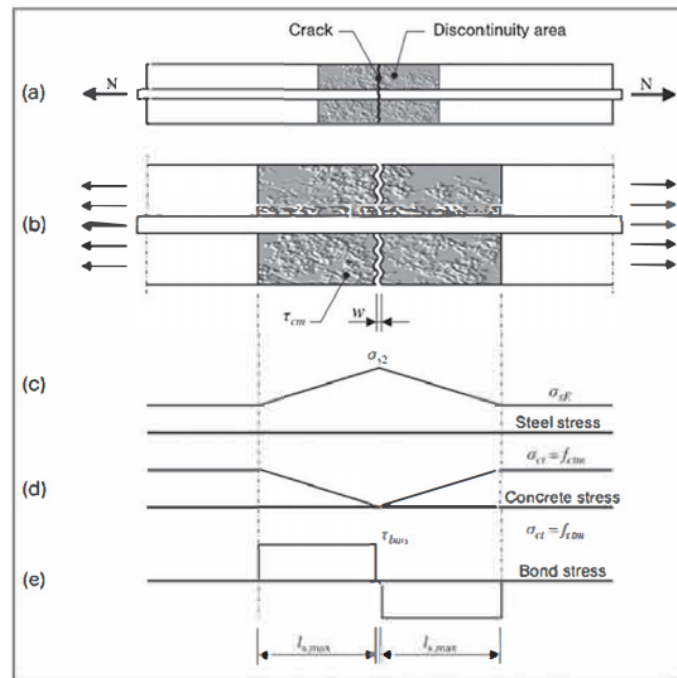


Figure 2.21: Stress distribution in concrete and reinforcement bonded reinforcement bars [Walraven, 2013]

2.2.3.2 Tensile splitting cracks

A study conducted by Tepfers & De Lorenzis in 2003 [Tepfers and De Lorenzis, 2003] claims concrete structures reinforced with BFRP-bars containing rough surface deformations are more likely to develop tensile splitting cracks. The rough surface deformation ensures higher bond strength, however, this increases the risk of tensile splitting cracks. Figure 2.22 presents the bond stress development in the concrete. Cracks start to appear as the bond stress development exceeds the tensile strength of the concrete. The surface at which the tensile splitting crack appears depends on the concrete cover to the individual faces of the concrete structure [fib, 2007].

Figure 2.23 presents 3 typical tensile splitting crack shapes common in reinforced concrete structures. A small cover to the bottom face of the structure likely leads to side-splitting, which can cause spalling of the concrete cover [Huang et al., 2021]. This failure mode encompasses all reinforcement bars in the tensile reinforcement layer. Failure modes pertaining to single bars are the V-notch splitting and the corner splitting. Corner splitting is likely to happen if the cover to either of the faces is not significantly larger than the other [Nagatomo et al., 1992].

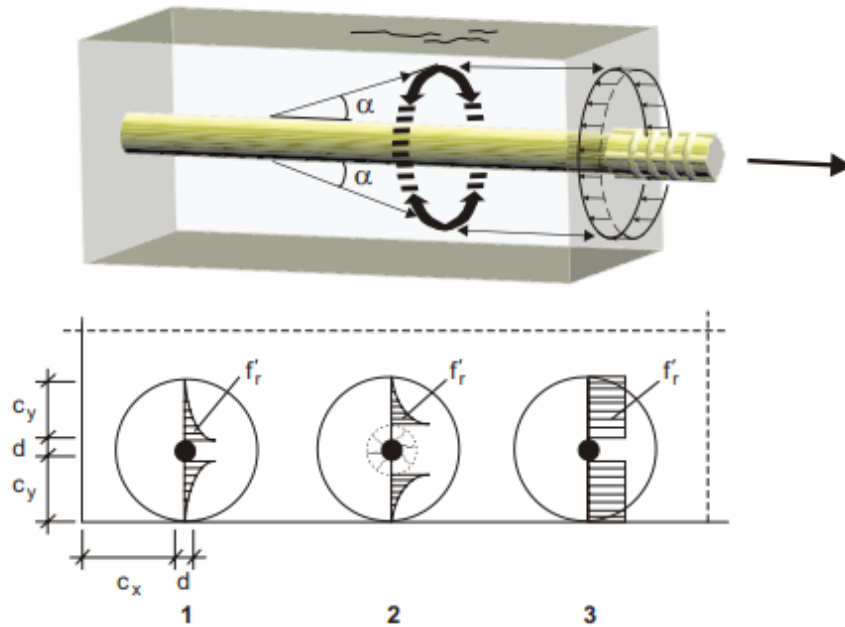


Figure 2.22: Tensile stress distributions in elastic (1), partly cracked elastic (2) and plastic (3) stage [fib, 2007]

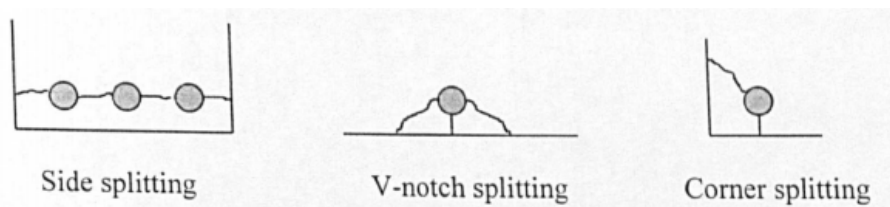


Figure 2.23: tensile splitting crack variations [Nagatomo et al., 1992]

According to a bond-slip model derived by Harajli [Harajli et al., 2004] (figure 2.24), the effect of tensile splitting is considerable. This bond-slip model presents 3 curves. The curve labelled "Plain concrete with splitting failure" does not apply to reinforced concrete structures. However, the other two curves illustrate variations in bond strength based on whether tensile splitting occurs or not. In cases of splitting failure, the bond strength decreases sharply with increasing load and slip, leading to a significant increase in the required transfer length of the reinforcement. In instances where tensile splitting does not occur, the predominant failure mode is pull-out failure.

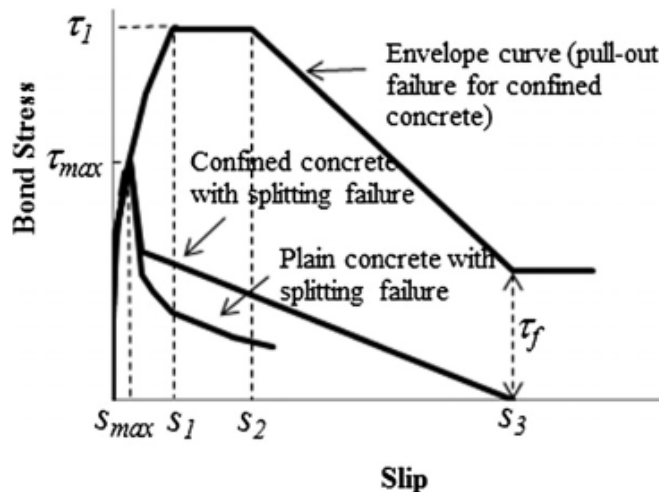


Figure 2.24: Bond-slip model [Harajli et al., 2004]

2.2.4 Crack width control

As BFRP is corrosion resistant, a larger crack width is allowed than Eurocode 2 [European Committee for Standardization, 2022] prescribes for concrete structures reinforced with steel bars. For this reason, design codes ACI440 [Busel, 2006] and BRL0513 [CvD, 2015] allow for larger crack widths. These maximum crack widths are limited for aesthetic reasons. However, it is important to consider that codes could be subject to updates in the future due to ongoing research addressing durability and fire concerns in this area. Figure 2.25 shows table 7.1N from Eurocode 2 where the maximum allowable crack width ranged from 0.2 mm to 0.4 mm depending on the exposure class, the type of loading and the reinforcement type.

Exposure Class	Reinforced members and prestressed members with unbonded tendons	Prestressed members with bonded tendons
	Quasi-permanent load combination	Frequent load combination
X0, XC1	0,4 ¹	0,2
XC2, XC3, XC4	0,3	0,2 ²
^{AC2} XD1, XD2, XD3, XS1, XS2, XS3 ^{AC2}		Decompression
<p>Note 1: For X0, XC1 exposure classes, crack width has no influence on durability and ^{AC1}this limit is set to give generally acceptable appearance. In the absence ^{AC1} of appearance conditions this limit may be relaxed.</p> <p>Note 2: For these exposure classes, in addition, decompression should be checked under the quasi-permanent combination of loads.</p>		

Figure 2.25: Table 7.1N from Eurocode 2 [European Committee for Standardization, 2022]: Maximum allowable crack width

2.2.4.1 Crack width control to ACI440 [Busel, 2006]

The recommended maximum crack width is 0.7 mm for interior exposure and 0.5 mm for exterior exposure conditions. According to the ACI440 [Busel, 2006] guideline for the design and construction of structural concrete with FRP bars, the maximum probable crack width can be determined using equations 2.19 to A.30. [Busel, 2006]

$$w = 2 \frac{f_f}{E_f} \beta k_b \sqrt{d_c^2 + \left(\frac{s}{2}\right)^2} \quad (2.19)$$

The parameter s is the bar spacing, and f_f is the tension in the reinforcement bars. For the factor k_b , which is the bond coefficient, a value of 1.4 is recommended. The parameter d_c is the thickness of the concrete cover measured from the bottom of the beam to the centre of the tensile reinforcement bar. The parameter β is the ratio of the distance from the neutral axis to the extreme tension fibre to the centre of the tensile reinforcement. The parameter k is the ratio of the depth of the neutral axis to the depth of the reinforcement. The crack width formulae according to the ACI440 are elaborated upon in the parameter study.

2.2.4.2 Crack width control according to BRL0513

According to Dutch model code BRL0513 [CvD, 2015], which is a guideline code for concrete structures with GFRP reinforcement bars, the maximum allowed crack width should not exceed 0.5 mm. Depending on the characteristics of the BFRP-reinforced concrete structure, stricter crack width limits may be applied, for example for aesthetics or waterproofing. The verification method of crack width control according to the BRL0513 closely resembles the Eurocode 2 [European Committee for Standardization, 2022] method of crack width control. The crack width formulae according to the BRL0513 are elaborated upon in the parameter study.

2.2.4.3 Crack width control according to JSCE

According to Japanese modelling code JSCE 1997, a crack width of at most 0.5 mm is allowed.

2.3 Sustainability

Sustainable design has become a more prevalent topic in the recent years. The construction sector account for approximately 38% of global CO₂ emissions [M Sobota, 2022, Bijleveld et al., 2013]. The Dutch Betonakkoord is an initiative by the Dutch government, suppliers, manufacturers and contractors to collectively work towards a more sustainable construction sector. One of the goals is to reduce CO₂ emission by 30% in 2030 compared to 1990, and aim to reduce by 49% in the long term [Betonakkoord, 2017].

A study on the environmental impact is performed in Appendix A Parameter Study. The analysis is focused on comparing the burden on the environment of concrete structures reinforced with BFRP-bars in relation to reinforcement steel bars.

2.3.1 CO₂ emission

The carbon dioxide emission (CO₂) for the production of BFRP reinforcement is 2.96 kg of CO₂ per tonne of reinforcement (for $V_f=80\%$). This is significantly higher compared to the emission attributed to the production of steel reinforcement, which is 992 kg of CO₂ per tonne. The production per kg of reinforcement steel is environmentally more favourable, however, BFRP weighs considerably less than steel. Steel reinforcement weighs 7850 kg/m³, whereas BFRP weighs approximately 2000 kg/m³. The production of a cubic metre of reinforcement steel equates to 18370 kg of CO₂, whereas the production of BFRP equates to 5200 kg of CO₂. The production of BFRP therefore has a 71.7% lower emission than the production of steel reinforcement [Inman et al., 2017].

The largest contribution to the CO₂ is the matrix resin with a contribution of approximately 86.8% of the total emission. The remaining 13.2% is comprised of energy consumption (6.7%), mining of basalt ores (6.3%) and transport (0.1%). The epoxy resin is proportional to the amount of CO₂ emission from production. A higher resin content in the BFRP reinforcement bar leads to higher CO₂ emissions [Inman et al., 2017] [Pavlović et al., 2022].

2.3.2 Life cycle assessment

A life cycle assessment is a mostly standardized tool to determine and compare the ecological impact of the production, use and disposal of production in the construction sector. The framework of the life cycle assessment is built up of four interrelated stages: goal and scope definition, inventory analysis, impact assessment and interpretation. This concept is shown in figure 2.26.

A life cycle analysis considers all stages in the service life of the material. Considering all stages is referred to as a cradle-to-grave analysis. This starts at the gathering and supply of the raw constituent materials (cradle), the production, the assembly, transport up to the installation, recycling and the end of service life (grave). For all stages in the LCA, natural resources are consumed and emissions are released into the environment. For each product that has been analyzed, the consumption of natural resources and the emission (input and output) are quantified for numerous categories such as acidification and global warming potential. There are two main types of LCA's [Pavlović et al., 2022]:

- Attributional LCA
- Consequential LCA

An attributional life cycle assessment aims to describe the environmentally physical flows (such as transport of materials, energy and emissions throughout the life cycle of the product or material) to and from its life cycle. The goal for this type of LCA is to assess what the global impacts are that belong to this product. A consequential life cycle assessment has the aim to describe how environmentally relevant flows will change in response to possible decisions. Its goal is to assess the influence of the product on the global environmental impact. This subtle difference in aim and goal has consequences for the overall analysis [Ekvall et al., 2016].

When conducting an LCA, the stages of the examined product to be included can be taken into consideration. Modules A1 to A3 (figure 2.27) only take into account the production of the product itself. If a life cycle analysis is conducted with only these modules, it is called a Cradle-to-Gate analysis. The life cycle analysis of the product stops after production is completed. Modules A4 and A5 are the stages of construction. This includes transport from the factory to the construction site. Stage B is the use phase of the material within the building. This includes maintenance, repair, replacement and refurbishment. This phase is often ignored in structural building materials such as reinforcement because the aimed lifetime of the materials is designed

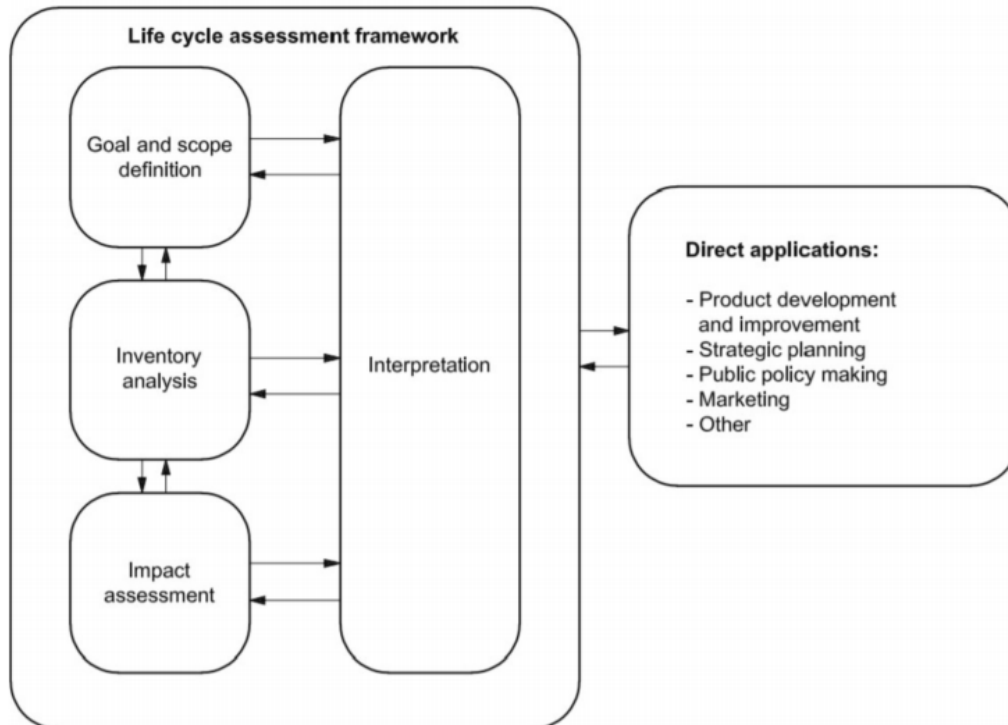


Figure 2.26: Stages of a life cycle assessment (LCA) [Pavlović et al., 2022]

the same as the intended lifetime of the building. Stage C is the end-of-life phase of the product. This includes the demolishing of the building, transport, waste processing and the disposal of the material. If an LCA is conducted by taking modules A1 to C4 into account, this is called a Cradle-to-Grave analysis. In addition to the first 3 phases, stage D focuses on the recovery, reusability and recycle-ability of the disposed material. If all stages are taken into account in the LCA, this is called a Cradle-to-Cradle analysis. Figure 2.27 shows the life cycle analysis chart used in the LCA [Pavlović et al., 2022].

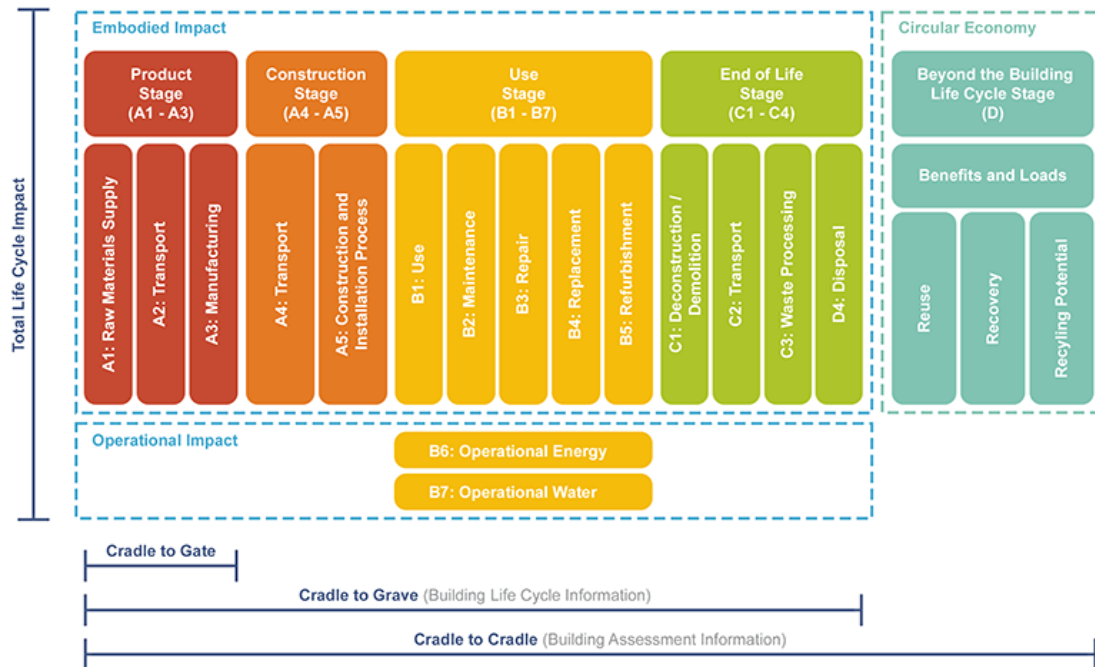


Figure 2.27: Life cycle assessment stages [Pavlović et al., 2022]

2.3.3 Environmental product declaration

An Environmental product declaration (EPD) is a declaration in which the quantification of environmental information on the life cycle of a product is declared. One of the goals of an EPD is to enable comparisons between products that fulfil the same function. The methodology EPD is based on and follows from the life cycle assessment as described in ISO14040.

As the BFRP and steel reinforcement bars fulfil the same purpose, EPD's can be compared. Listed in table 2.5, the values for the aforementioned 11 impact categories are compared. These EPD incorporate only the production stage of the reinforcement bars themselves, which are stages A1 to A3. Transport is excluded (stage A4 in figure 2.27). This is also known as 'Cradle-to-Gate'. The EPD for BFRP reinforcement bars come from Orlimex based in the Czech Republic [Orlimex CZ s.r.o, 2022]. Values are based on an 8 mm bar diameter. Some small variations between the values are noticeable depending on the bar diameter, which can lead to slight inaccuracies. However, the differences are negligible. The values per impact category for steel reinforcement come from an EPD for "Wapeningsstaal voor toepassingen in gewapende betonconstructies" from the Dutch reinforcement steel corporation [VWN, 2021].

Table 2.5: Impact category values of BFRP and reinforcement steel per kg [Orlimex CZ s.r.o, 2022] [VWN, 2021]

Impact category	Unit	BFRP	Steel
ADPE	kg Sb. eq.	2.14E-5	9.66E-6
ADPF	kg Sb. eq.	2.18E-2	7.50E-3
GWP	kg CO ₂ eq.	2.69E+0	9.92E-1
ODP	kg CFC 11 eq.	2.85E-7	8.87E-8
POCP	kg ethene eq.	1.40E-3	1.03E-3
AP	kg SO ₂ eq.	9.96E-3	4.62E-3
EP	kg PO ₄ ³⁻ eq.	1.45E-3	6.42E-4
HTP	kg DCB eq.	1.23E+0	6.24E-1
FAETP	kg DCB eq.	1.63E-1	2.19E-2
MAETP	kg DCB eq.	8.13E+1	4.21E+1
TETP	kg DCB eq.	6.28E-3	6.01E-2

Note that, the emissions per kg are significantly less for reinforcement steel than for BFRP reinforcement bars. However, the steel reinforcement has a density approximately 3.93 times higher. When converted to volumetric units instead of weight, the advantage of BFRP reinforcement bars is significant, which is shown in table 2.6. Note that, this is just on an individual product comparison base. Application in design is not incorporated. This would be needed to assess the sustainability of reinforced concrete structures as LCA's prescribe to perform the analysis on an inclusive level.

Table 2.6: Impact category values of BFRP and reinforcement steel per m³ [Orlimex CZ s.r.o, 2022] [VWN, 2021]

Impact category	Unit	BFRP	Steel
ADPE	kg Sb. eq.	4.28E-2	7.58E-2
ADPF	kg Sb. eq.	4.36E+1	5.89E+1
GWP	kg CO ₂ eq.	5.38E+3	7.79E+3
ODP	kg CFC 11 eq.	5.70E-4	6.96E-4
POCP	kg ethene eq.	2.80E+0	8.09E+0
AP	kg SO ₂ eq.	1.99E+1	3.63E+1
EP	kg PO ₄ ³⁻ eq.	2.90E+0	5.04E+0
HTP	kg DCB eq.	2.46E+3	4.90E+3
FAETP	kg DCB eq.	3.26E+2	1.72E+2
MAETP	kg DCB eq.	1.63E+5	3.30E+5
TETP	kg DCB eq.	1.26E+1	4.72E+2

Abbreviations of 11 impact categories:

ADPE	Abiotic Depletion Potential for non-fossil resources
ADPF	Abiotic Depletion Potential for fossil resources
GWP	Global Warming Potential
ODP	Depletion potential of the stratospheric ozone layer
POCP	Formation potential of tropospheric ozone photochemical oxidants
AP	Acidification Potential of land and water
EP	Eutrophication Potential
HTP	Human Toxicity Potential
FAETP	Freshwater aquatic ecotoxicity potential
MAETP	Marine aquatic ecotoxicity potential
TETP	Terrestrial ecotoxicity potential

2.3.4 ECI-calculation background

The Environmental Cost Indicator (ECI) calculation offers insight into the hidden expenses imposed on the environment by a manufactured material or product. It serves as an estimated monetary representation, denominated in euros, illustrating the environmental toll exacted during the production of a specific material or product. This calculation relies on predefined impact categories to ascertain the shadow cost incurred per unit of the material or product. Figure 2.28 presents a representation of how an ECI-calculation comes to fruition.

Table 2.7: A1 Impact category values and weight factor (€/unit) [Ecochain, 2023]

Impact category	Unit	weight factor (€/unit)
ADPE	kg Sb. eq.	€0,16
ADPF	kg Sb. eq.	€0,16
GWP	kg CO ₂ eq.	€0,05
ODP	kg CFC 11 eq.	€30,00
POCP	kg ethene eq.	€2,00
AP	kg SO ₂ eq.	€4,00
EP	kg PO ₄ ³⁻ eq.	€9,00
HTP	kg DCB eq.	€0,09
FAETP	kg DCB eq.	€0,03
MAETP	kg DCB eq.	€0,0001
TETP	kg DCB eq.	€0,06

Each impact category is weighed differently with a specific attributed value. This attributed value of the direct reflection of the severity of the impact category on the environment. The attributed weighing value for each impact category is noted in table 2.7. The ECI-value per unit (kg or m³) of the material or product used is the summation of the total ECI-values of the impact categories.

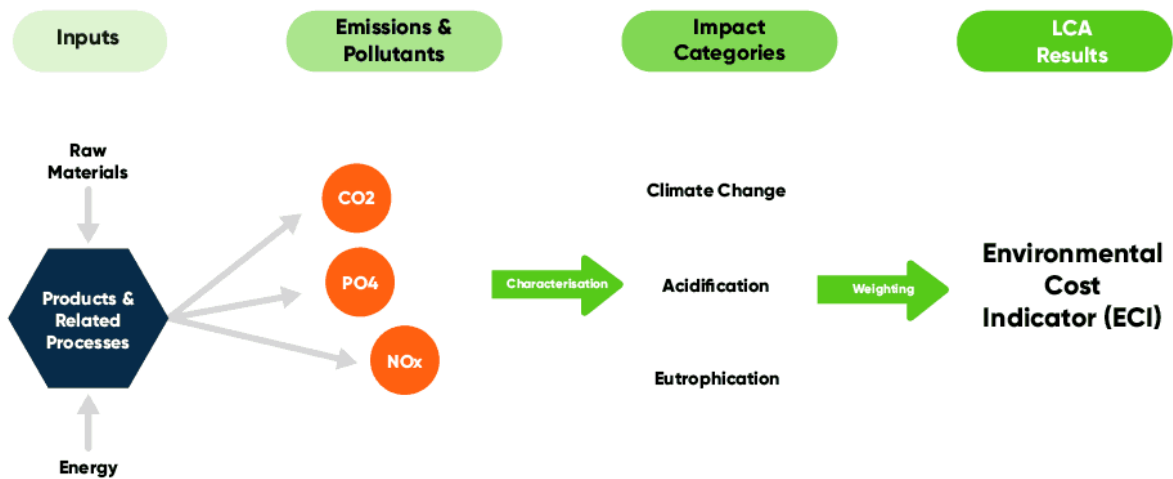


Figure 2.28: ECI-calculation process [Ecochain, 2023]

Even though the ECI-value per unit of the material is calculated using the method described above, some Environmental Product Declarations (EPD's) already provide their values on the certificate.

2.3.4.1 Influence of fibre content

A study conducted among the above-mentioned 11 categories shows the influence of the fibre content present in the reinforcement [Pavlović et al., 2022]. The fibre content may vary between producers of BFRP reinforcement bars but is likely to be between 70% and 85%. As the fibre content and the resin content cumulatively should be equal to 100%, the resin content varies between 15% as a lower bound and 30% as an upper bound. From this research, it's concluded that higher fibre contents, and therefore lower resin content, reduce the score in all impact categories.

2.3.5 Environmental cost indicator (ECI)

An ECI-score (in Dutch: MKI, Milieukostenindicator) is a single-score indicator expressed in euro. The value expressed in euro represents the shadow cost of the product or material 'costs' for the environment. The greater the ECI-value, the heavier the burden on the environment due to the production and use of a product or material. A comparison between the ECI-values is shown in table 2.8.

Table 2.8: ECI-values comparison between BFRP and steel reinforcement bars in €/kg and €/m³

Material	ECI (€/m ³)	ECI (€/kg)
BFRP reinforcement bars	640,00	0.320
Steel reinforcement bars	1114.70	0.142

2.4 Costs

The cost of a type of reinforcement plays a substantial role in the choice of application. Table 2.9 shows the costs per kilogram of BFRP reinforcement bars in comparison to reinforcement steel.

Table 2.9: Unit prices of reinforcement steel bar and BFRP-bars [Upadhyaya and Suntharavadivel, 2018, Barker, 2016, Colombo et al., 2012]

	Steel	Basalt (BFRP)
Price (€/per kg)	0.43	2.31-2.50

Initially, the cost of BFRP-bars per kilogram is significantly higher, which could be a disadvantage. However, these are the costs solely for the production and the transport. With the rapidly growing demand for a sustainable building sector and the rise in climate change awareness, BFRP-bars could provide a discount in the tender phase or funding for sustainability. In Appendix A Parameter Study, an analysis including costs is presented.

2.5 Design guidelines and regulations

For reinforced concrete structures with FRP reinforcement bars, there is currently no effectual Eurocode available. However, there are national design codes, which allow the application of FRP. The available national guidelines apply to all reinforced concrete structures with FRP reinforcement bars. The materials used in the production (eg. glass, basalt, aramid, carbon or hybrid variations) are not of influence as these codes generalize around the use of FRP-bars regardless of the fibre type [Pilakoutas et al., 2011, Rehman and Michler, 2022].

A study on the prominent and effectual codes related to the Dutch concrete market is performed in Appendix A Parameter Study. The analysis is focused on comparing the design of concrete structures along these codes for concrete structures reinforced with BFRP-bars and drawing a comparison with concrete structures reinforced with steel bars according to Eurocode 2. As this thesis focuses on flexural and cracking behaviour, this part of Appendix A Parameter Study focuses on bending moment capacity and crack width control in the design codes.

2.5.1 Available guidelines

The most prominent guidelines used are the international fib model code bulletin 40 by the Federation for Structural Concrete and the guideline for FRP reinforced concrete by ACI (American Concrete Institute) commission 440 [Busel, 2006]. Other nationally effectual guidelines are available, however, the use of these guidelines is limited to the country of origin.

2.5.1.1 Fib model code for FRP-reinforced concrete (International)

Task group 9.3 of the International Federation for Structural Concrete published a guideline for FRP-reinforced concrete structures in 2007. The report published by fib in bulletin 40 encompasses all aspects of the design of reinforced concrete with FRP bars and shows resemblances with Eurocode [fib, 2007].

2.5.1.2 ACI commission 440 (United States of America)

ACI Commission 440 produced a design guide for reinforced concrete structures. This design guide does not only prescribe calculation methodology but also elaborates upon conducted research and overall documentation of state-of-art research [Busel, 2006].

2.5.1.3 BRL0513 (the Netherlands)

Dutch BRL0513 [CvD, 2015] is an assessment guideline from the Netherlands which is aimed primarily at the design of reinforced concrete structures with glass fibre reinforcement bars. As the currently effectual Eurocode 2 [European Committee for Standardization, 2022] does not provide guidelines for concrete structures reinforced with FRP bars, BRL0513 provides guidance to design FRP-reinforced concrete structures. However, this code is focused on the design of reinforced concrete structures with GFRP reinforcement bars. For the moment, the applicability for BFRP reinforced concrete is limited [CvD, 2015].

2.5.1.4 Other guidelines

Other guidelines and model codes of note are:

- JSCE guideline for FRP reinforced concrete structures (Japan, 1992, 1993 and 1997)
- CSA guideline for FRP reinforced concrete structures (Canada, 1996)
- NS3473 design guideline (Norway, 2003)
- British Institution of Structural Engineers (BISE) design guideline (United Kingdom, 2015)

2.5.2 Forthcoming Eurocode 2

The forthcoming version of Eurocode 2 [European Committee for Standardization, 2022] (NEN-EN-1992-1-1), includes guidelines for the design of concrete structures with embedded FRP reinforcement bars. The new Eurocode 2 however is not yet available to the public. The following themes are noted in Annex R of the pending Eurocode 2 code.

2.5.2.1 Partial factors

Table R.1 of Annex R of the forthcoming Eurocode 2 [European Committee for Standardization, 2022] shows the partial factors for embedded FRP reinforcement applied in concrete structures. This table is shown in figure 2.29. The partial factor γ_{FRP} for ultimate limit state analysis is 1.5 for FRP reinforcement types. For reinforcement steel, this remains 1.15 in ULS. A partial factor designated to the design of shear and punching resistance for concrete structures without shear reinforcement is determined to be 1.5 as well for ULS. The partial factors for accidental action design situations differ between 1.10 and 1.15 respectively depending on the type of force. For serviceability limit state analysis, only a partial factor of 1.0 for γ_{FRP} needs to be taken into account.

Table R.1 (NDP) — Partial Factors for FRP Reinforcing

Design Situation	γ_{FRP}	γ_v for shear and punching resistance without shear reinforcement
Ultimate Limit States (Persistent and transient design situation)	1,50	1,50
Accidental Actions	1,10	1,15
Serviceability	1,00	--

Figure 2.29: Table R.1 from forthcoming Eurocode 2 [European Committee for Standardization, 2022], Annex R (NEN-EN-1992-1-1)

2.5.2.2 Materials

Annex R provides limits for the materials used as embedded reinforcement. These limits are determined to be the following:

- Minimum Young's modulus: $E_{FRP} \geq 40000$ MPa;
- Ratio of $f_{tk,100a}/E_{FRP} \geq 0.005$;
- Characteristic compressive strength of concrete $f_{ck} \geq 20$ MPa;
- $\rho_{1f} \leq 0.05$.

A maximum longitudinal reinforcement ratio of 5% indicates the preferred failure mode in reinforced concrete structures under bending loads: failure in the compression zone instead of failure in the tensile reinforcement as sudden failure of the tensile reinforcement ought to be avoided. The required Young's modulus of the tensile FRP-bar reinforcement implies a minimum desired stiffness of the reinforced concrete structure. Conducted experiments by Shamass & Cashell in 2020 [Shamass and Cashell, 2020] on the flexural behaviour of concrete structures reinforced with BFRP-bars and other FRP types of reinforcement bars show significantly larger deflection compared to steel-reinforced counterparts.

The design tensile strength of embedded FRP reinforcement bars is determined according to equation 2.20.

$$f_{ftd} = \frac{f_{ftk,100a}}{\gamma_{FRP}} \quad (2.20)$$

Where:

$f_{ftk,100a}$ is the design tensile strength which can either be specified from the product data or determined using equation 2.21.

$$f_{ftk,100a} = C_t C_C C_e f_{ftk,0} \quad (2.21)$$

C_t is a factor considering the effects of temperature. The following values for C_t can be applied;

- $C_t = 1.0$ for indoor and underground environments;
- $C_t = 0.8$ for members if heating due to solar radiation cannot be excluded.

Further detailed information for the determination of C_t can be found in fib Bulletin 40 [fib, 2007].

C_C is the coefficient between the strength under sustained load and the strength under short-term load. For GFRP, this factor is determined to be 0.35. For CFRP, this value is determined to be 0.8. Other values can be taken in case these values are accurately determined according to ISO-10406-1. Note that, this factor considers creep within the reinforcement bar itself.

C_e is the coefficient described by the forthcoming Eurocode 2 as the coefficient between the strength before and after ageing. This pertains to the long-term strength in relation to the short-term strength. The value for C_e must be taken as 0.7 unless more accurate values are determined. This value can be determined according to the test concept noted in ISO 10406-1.

The stress-strain diagram constitutional relation for embedded FRP reinforcement should be taken as displayed in figure 2.30. Note that, the material does not enter a plastic stage as soon as the maximum strain is reached.

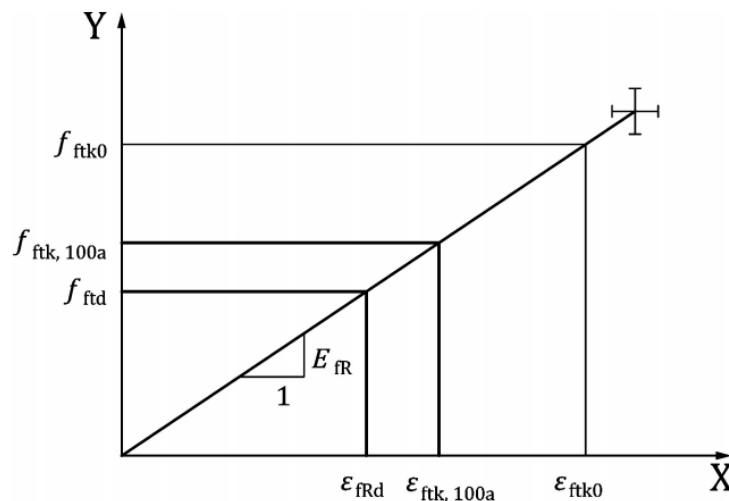


Figure 2.30: Stress-strain diagram for embedded FRP reinforcement from forthcoming Eurocode 2, Annex R (NEN-EN-1992-1-1)

2.5.2.3 Durability and concrete cover requirements

The determination of the concrete cover in the effectual Eurocode 2 consists of a minimum cover (c_{\min}) and an allowance in design for deviation (Δc_{dev}). The summation of these components determines the nominal concrete cover in the design of reinforced concrete structures. The minimum concrete cover is determined as shown in equation 2.22.

$$c_{\min} = \max(c_{\min,b}; c_{\min,dur} + \Delta c_{dur,\gamma} - \Delta c_{\min,dur} - \Delta c_{dur,add}; 10\text{mm}) \quad (2.22)$$

In the forthcoming Eurocode 2, the requirement for $c_{\min,dur}$ is eliminated and may be assumed to be zero. By taking this value as zero, the exposure classes do not have an influence anymore on the required concrete cover.

The bond component ($c_{\min,b}$) of the equation for the minimum nominal concrete cover in the effectual Eurocode 2 is dependent on the bars being bundled or separated, as well as the maximum aggregate size. In the forthcoming Eurocode 2, the requirement for ($c_{\min,b}$) solely depends on the bar diameter. If there is no test data available, this value should be taken as $c_{\min,b} \geq 2\varnothing$. If there is test data available, the minimum required value is $c_{\min,b} \geq 1.5\varnothing$, with a lower limit value $c_{\min,b} \geq 10$ mm. This only applies to concrete structures reinforced with FRP-bars.

The forthcoming Eurocode also states from a durability perspective, direct contact between carbon FRP (CFRP) bars with reinforcement steel ought to be avoided as corrosion of the reinforcement steel bar is accelerated. However, as this clause specifically mentions CFRP, this does not apply to BFRP-bars.

2.5.2.4 Ultimate limit state analysis, special rules for FRP reinforcement

Annex R of the forthcoming Eurocode 2 specifies additional rules for the design of members in bending and with or without axial forces. These rules contain the following:

- Tensile strain in FRP reinforcement shall be limited to the design rupture strain ε_{fRd} ;
- FRP reinforcement cannot be applied as compression reinforcement;
- Unless more rigorous analysis is undertaken, the benefit of the confining effect of FRP reinforcement should be reduced by the ratio E_{fR}/E_s .

For members loaded in shear, the forthcoming Eurocode 2 also specifies certain rules and formulae. These rules contain the following most notable changes:

- For concrete members reinforced with longitudinal FRP-bars and no shear reinforcement, the minimum shear resistance may be taken as shown in equation 2.23.

$$\tau_{Rdc,\min} = \frac{11}{\gamma_v} \sqrt{\frac{f_{ck}}{f_{tk0}} \frac{E_{fR}}{E_s} \frac{d_{dg}}{d}} \quad (2.23)$$

- The determination of ρ_1 in section 8.2.2 of the forthcoming Eurocode 2 should be reduced by the ratio E_{fR}/E_s .
- The expression for the angle of inclination of the compressive field $\cot(\theta)$ should be replaced with a fixed value of 0.8.
- The shear resistance for members requiring shear reinforcement may be determined by using expressions 2.24 to 2.26.

$$\tau_{Rd,f} = \tau_{Rd,f} + \rho_w f_{fwRd} \leq 0.17 f_{cd} \quad (2.24)$$

Where:

$$f_{fwRd} = \frac{f_{fwk,100a}}{\gamma_{FRP}} \leq \varepsilon_{fwRd} E_{fwR} \quad (2.25)$$

$$\varepsilon_{fwRd} = 0.0023 + \frac{1}{15} E_{fFR} A_{fR} (0.8d)^2 10^{-15} \leq 0.007 \quad (2.26)$$

A_{fR} = longitudinal reinforcement considering for slabs of a width of 1 metre .

Among the changes and provisions listed above, changes to verify punching shear and torsion are included in Annex R of the forthcoming Eurocode 2 as well.

2.5.2.5 Serviceability limit state analysis, special rules for FRP reinforcement

In the forthcoming version of Eurocode 2, Annex R provides 2 tables (R.2 and R.3) that replace tables 9.1 (NDP) and 9.2 (NDP). Figure 2.31 shows table 9.2 (subfigure 2.31a) in the main section of the Eurocode 2, as well as replacement table R.2 (subfigure 2.31b) for concrete design with embedded FRP reinforcement. These tables contain verification limits for stress and crack width for appearance.

Figure 2.33 shows table 9.3 (subfigure 2.32a) from the main section of the forthcoming Eurocode 2 as well as table R.3 (subfigure 2.33a) from Annex R. Note that, for embedded FRP reinforcement, the allowable crack width can be relaxed up to 0.7 mm, which is in accordance with other guidelines such as the ACI commission 440 design guideline. Note that, the table for steel-reinforced concrete is significantly more complicated due to the various exposure classes that need to be taken into account.

Table 9.1 (NDP) — Verifications, stress and crack width limits for appearance

Verification	Calculation of minimum reinforcement according to 9.2.2	Verification of crack width according to 9.2.3	Verification of reinforcement stresses to avoid yielding at SLS
Combination of actions for calculating σ_s	Cracking forces according to 9.2.2	Quasi-permanent combination of actions	Characteristic combination of actions
Limiting value of crack width $w_{lim,cal}$ or stress σ_s	$\sigma_s \leq f_{yk}$	$w_{lim,cal} = 0,4 \text{ mm}$ $\sigma_s \leq f_{yk}$	$\sigma_s \leq 0,8f_{yk}$ $\sigma_p \leq 0,8f_{pk}$
NOTE Crack widths are verified at the member surface unless the National Annex gives a different location.			

(a) Table 9.1(NDP) from forthcoming Eurocode 2

Table R.2 — Verifications, stress and crack width limits for appearance

Verification	Calculation of minimum reinforcement according to 9.2.2	Verification of crack width according to 9.2.3	Verification of reinforcement stresses to avoid failure at SLS
Combination of actions for calculating σ_f	Cracking forces according to 9.2.2	Quasi-permanent combination of actions	Characteristic combination of actions
Limiting value of crack width $w_{lim,cal}$ or stress σ_f	$\sigma_f \leq f_{td}$	$w_{lim,cal} = 0,4 \text{ mm}$ $\sigma_f \leq f_{td}$	$\sigma_f \leq 0,8f_{td}$

(b) Table R.2 from forthcoming Eurocode 2, Annex R

Figure 2.31: Verification's, stresses and crack width limits for appearance from forthcoming Eurocode 2

Table 9.2 (NDP) — Verifications, stress and crack width limits for durability

Exposure Class	Reinforced members and prestressed members without bonded tendons and with bonded tendons with Protection Levels 2 or 3 according to 5.4.1(4)		Prestressed members with bonded tendons with Protection Level 1 according to 5.4.1(4) and pretensioned members.		
	combination of actions		combination of actions		
	quasi-permanent	characteristic	quasi-permanent	frequent	characteristic
X0, XC1	-	-	-	$w_{lim,cal} = 0,2 \text{ mm} \cdot k_{surf}$	-
XC2, XC3, XC4	$w_{lim,cal} = 0,3 \text{ mm} \cdot k_{surf}$		Decompression ^b	$w_{lim,cal} = 0,2 \text{ mm} \cdot k_{surf}$	
XD1, XD2, XD3 XS1, XS2, XS3		$\sigma_c \leq 0,6f_{ck}^{a,c}$	-	Decompression ^b	$\sigma_c \leq 0,6f_{ck}^{a,c}$
XF1, XF3 XF2, XF4	-				

NOTE 1 Crack widths are verified at the member surface unless the National Annex gives a different location.

NOTE 2 The factor k_{surf} considers the difference between an increased crack width at the member surface and the required mean crack width according to durability performance of the minimum cover: $1,0 \leq k_{surf} = c_{act}/(10 \text{ mm} + c_{min,dur}) \leq 1,5$.

c_{act} is a specified actual cover $\geq c_{nom}$ due to detailing or execution reasons.

^a This limitation in serviceability conditions is not necessary for stresses under bearings, partially loaded areas and plates of headed bars.

^b The decompression limit requires that all parts of the bonded tendons or duct lie at least 25 mm within concrete in compression. The decompression check is only relevant in the direction of the prestressed reinforcement.

^c The compressive stress σ_c may be increased to $0,66f_{ck}$ if the cover is increased by 10 mm or confinement by transverse reinforcement is provided.

(a) Table 9.1(NDP) from forthcoming Eurocode 2

Table R.3 — Verifications, stress and crack width limits for durability

Exposure Class	Concrete members with FRP reinforcement	
	combination of actions	
	quasi-permanent	characteristic
XC, XF, XD	$w_{lim,cal} = 0,4 \text{ mm}^c$	$\sigma_c \leq 0,6f_{ck}^{a,b}$
^a No limitation in serviceability conditions is necessary for stresses under bearings, partially loaded areas and plates of headed bars. ^b The compressive stress σ_c may be increased to $0,66f_{ck}$ if the cover is increased by 10 mm or confinement by transverse reinforcement is provided. ^c In absence of appearance conditions, fasteners, punctual wheel pressure, lap splice or freeze thaw this limit may be relaxed to values up to 0,7 mm.		

(a) Table R.2 from forthcoming Eurocode 2, Annex R

Figure 2.33: Verification's, stresses and crack width limits for appearance from forthcoming Eurocode 2

2.6 Conclusions

BFRP reinforcement bars deviate notably from traditional steel bars in several key characteristics, fundamentally impacting the design approach for concrete structures. Their distinct traits include exceptionally high longitudinal tensile strength, ranging between 1000 to 1800 MPa compared to the 500 MPa of B500 steel reinforcement. The transverse strength of BFRP, influenced by resin content, maintains a delicate balance between tensile strength and lower transverse strength, typically kept at 70% to 85%. With a significantly lower modulus of approximately 50 to 70 GPa compared to steel, BFRP causes reinforced concrete structures to be less stiff, leading to increased deformations and larger crack widths. Unlike steel's ductile behaviour, BFRP exhibits a linear elastic behaviour until reaching rupture strain, resulting in a brittle failure mode. Moreover, BFRP's resistance to corrosion, low thermal and electrical conductivity, nonmagnetic behaviour, and lighter weight compared to steel offer both advantages and challenges in various construction scenarios. Understanding these physical and mechanical properties, influenced by factors like loading history, composition, and environmental conditions, is crucial for effectively utilizing BFRP in structural design. Beyond their mechanical properties, BFRP-bars also present distinctive on-site attributes. They cannot be bent on-site, requiring precise pre-fabrication to match design specifications. Furthermore, the significant reduction in mass of BFRP compared to steel not only simplifies on-site handling but also requires less lifting capacity during crane operations, thus enhancing construction logistics.

Determining BFRP's physical and mechanical properties involves understanding matrix composition, loading history, production factors, and environmental influences like temperature and humidity. The reinforcement's density, tensile, shear, and compressive properties are essential considerations. Creep, fatigue, and long-term behaviour influenced by factors like load duration and environmental exposure, impact BFRP's integrity and durability. Understanding these properties is vital for their effective application in structural design.

The financial aspect possibly impacts the selection of reinforcement types. If the cost of BFRP-bars significantly surpasses that of steel and any potential discounts during the tender process fail to offset the disparity becomes questionable. The considerable price difference, as indicated by market rates, portrays a potential challenge in the widespread adoption of BFRP reinforcement in construction projects.

The application of basalt fibre reinforced polymer (BFRP) bars in concrete significantly alters the behaviour

of reinforced concrete in comparison to traditional reinforcement steel. BFRP exhibits distinct characteristics, including a lower Young's modulus and higher tensile strength, fundamentally influencing various mechanical aspects like bond behaviour, bond slip, and cracking in BFRP-reinforced concrete. The bond behaviour, crucial for concrete-reinforcement interaction, diverges between BFRP and steel reinforcement. While factors like aggregate size, concrete class, reinforcement bar detailing, diameter, and concrete cover affect general reinforcement bonding, BFRP introduces factors like lower Young's modulus, shear stiffness, and thermal expansion, influencing bonding mechanisms.

Bond strength development in FRP bars follows distinct stages: initial chemical bonding, gradual transition to mechanical interlocking, and eventual split and bond failure modes. The phases display varying bonding mechanisms influenced by surface shapes and deformations. Surface deformations, like helical wrapping or sand coating, influence friction, mechanical interlocking, and shear failures, impacting bond strength development. Regarding cracking behaviour, higher bond strengths in BFRP-bars potentially result in a smaller flexural crack spacing along concrete beams compared to steel reinforcement, impacting the beam's stiffness and crack spacing. Crack width control differs based on standards like Eurocode, ACI440, BRL0513, and JSCE, with variations in maximum allowable crack widths, ranging between 0.2 mm and 0.7 mm, and specific parameters influencing crack width calculations.

In the pursuit of sustainable construction practices, the discourse around sustainable design has gained significant traction in recent years. The imperative to address the construction sector's substantial contribution of approximately 38% to global CO₂ emissions has spurred initiatives like the Dutch Betonakkoord. This collaborative effort, involving the Dutch government, suppliers, manufacturers, and contractors, aims to curtail CO₂ emissions by 30% by 2030 compared to 1990 levels, with a long-term ambition of reducing emissions by 49%. Central to this movement is the utilization of life cycle assessments (LCAs) in the construction sector, offering a standardized framework to evaluate and compare ecological footprints. LCAs, comprising stages from goal definition to impact assessment, delineate the complete journey of materials from production to disposal. They enable nuanced examinations, such as the distinction between attributional and consequential LCA's, elucidating the global impacts and environmental consequences.

A critical case study within this discourse examines the environmental implications of BFRP-bars versus traditional steel reinforcement. Despite BFRP's significantly higher CO₂ emissions per unit of weight compared to steel, the notably lower density unveils a more favourable environmental impact in volumetric terms. Environmental Product Declarations (EPD's) and Environmental Cost Indicators (ECI) offer valuable insights, showcasing nuanced comparisons across various impact categories and economic assessments. These findings underscore the multifaceted nature of sustainability assessments in construction materials. While CO₂ emissions stand out as a crucial factor, considerations about volumetric efficiency, broader environmental impacts, and economic implications are pivotal in making informed decisions for sustainable construction materials. The journey toward sustainable design continues to demand comprehensive assessments, considering diverse parameters to foster environmentally conscious choices in the construction sector.

The realm of reinforced concrete structures employing FRP reinforcement bars lacks a unified and comprehensive Eurocode design standard. Instead, it relies on diverse national guidelines, each serving specific contexts. These guidelines, irrespective of the FRP materials used (like glass, basalt, aramid, carbon, or hybrids), are predominantly applied within respective countries' boundaries. Prominent globally used guidelines include the fib model code bulletin 40 by the International Federation for Structural Concrete and the ACI commission 440's guideline for FRP reinforced concrete. While other national guidelines exist, their applicability extends only within their country of origin, limiting their widespread use.

The forthcoming version of Eurocode 2 (NEN-EN-1992-1-1) is anticipated to address the lack of standardised FRP reinforcement guidelines. Annex R of this pending Eurocode delineates various aspects such as partial factors, material limitations, durability criteria, and design specifics for FRP reinforcement in concrete struc-

tures. Notable changes include the specification of partial factors for different design situations, criteria for materials used as embedded reinforcement, and rules for ultimate and serviceability limit state analyses. These forthcoming provisions in Eurocode 2 mark a significant step towards a standardised and comprehensive framework for designing concrete structures reinforced with FRP bars. The annexed regulations encompass diverse considerations, aiming to ensure structural safety, durability, and serviceability while navigating the intricacies of employing FRP reinforcements.

Chapter 3

Experimental study

The main objective of the experimental research of this thesis is to uncover the differences in the structural behaviour of concrete structures reinforced with BFRP-bars in comparison to reinforcement steel bars. To establish this beams with different reinforcement configurations, concrete cover, bar diameters, and reinforcement materials are designed and subjected to a 4-point bending test. The study also aims to explore the contrasting cracking and flexural behaviour between BFRP-bars and steel reinforcement bars in reinforced concrete structures, providing an understanding of the interplay between these materials in concrete structures.

3.1 Aim of the experimental research

The main points of interest are the cracking behaviour and the bond strength of BFRP-bars in concrete concrete structures. The investigation aims to research the effect of the above-mentioned characteristics. The objectives are:

- To investigate the tensile behaviour of BFRP-bar and compare it to that of reinforcement steel bars;
- To investigate the flexural behaviour of concrete beams reinforced with BFRP-bars in comparison to reinforcement steel;
- To investigate the crack development and cracking pattern of concrete flexural members reinforced with basalt fibre reinforcement bars;
- To investigate the influence of the bar diameter;
- To investigate the effects of the reinforcement ratio of BFRP in concrete members in bending;
- To investigate the effect of the concrete cover;

The objectives outlined above aim to investigate both the behaviour of BFRP-bars independently and their performance as tensile reinforcement within concrete structures subjected to bending loads. These objectives collectively address the primary research goal.

3.2 Testing program

The program of the experimental testing consists of 2 parts:

- Direct tensile tests with a single reinforcement bar; To determine the properties of the applied BFRP-bar and compare their behaviour to reinforcement steel, a number of 3 BFRP reinforcement bars are tested in uniaxial tension;
- 4-point bending tests with reinforced concrete beams; A total of 6 beams, different by reinforcement configuration, diameter and concrete cover are subjected to a 4-point bending test to establish a fully developed cracking pattern.

3.3 Direct tension test

The direct tension test applies an incremental axial tensile load on a single bar to determine the relevant properties of the reinforcement bar. By determining the characteristic properties, more accurate estimates can be made in terms of capacity for the beams in the 4-point bending tests. One of the properties to be determined is the force at failure for a single reinforcement. By determining the maximum force, and therefore the maximum tensile stress, the bending moment capacity for a beam loaded in bending can be determined. Secondly, the strain development during the experiment is monitored. By measuring the strain in the single reinforcement bar, the Young's modulus is determined using the constitutive relations of materials. For both serviceability and ultimate limit state calculations of structural elements within the scope of the experimental study, these properties are vital to know.

3.3.1 Test specimen

For the determination of the tensile properties of any type of FRP-bar, the American Concrete Institute (ACI) published a test standard. This test standard (ACI440.3R [American Concrete Institute, 2012]) provides design guidelines for the specimen as well as guidelines for the testing procedure. The test specimen design (figure 3.1) consists of 2 tubes in which a BFRP-bar is inserted with sufficient overlapping at both ends. The tubes are then filled with 2-component epoxy adhesive glue to ensure a stiff connection with the bar.

3.3.1.1 Sample design and preparation

The design of the test specimens consists of 2 tubes of sufficient length in which a BFRP-bar with a diameter of 8 mm is anchored with an epoxy adhesive. To prevent the bar and the body of epoxy adhesive from sliding out of the tube, a circular plate with a hole of 10 mm is welded to the tube. The hole is slightly oversized as the sand cover is not included in the 8 mm diameter.

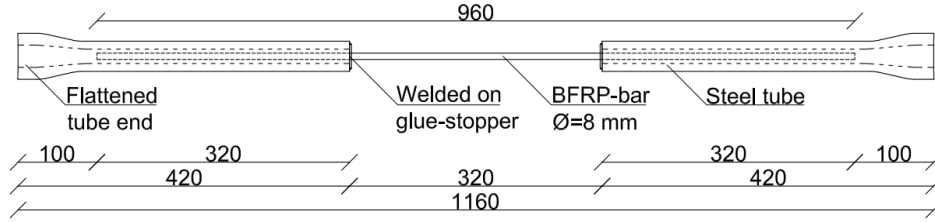


Figure 3.1: Design drawing direct tensile test specimen

Before subjecting the specimen to a tensile force, the tubes have been flattened at the ends. The flattened ends of the tubes are clamped by the beaks of the tensile test machine. The force from the beaks does therefore not interfere with the tensile force from the direct tensile test. As the steel tube itself has sufficient tensile force capacity, the weak part remains the BFRP-bar.

As this specimen is designed according to the guidelines of ACI440.3R, the free length between the anchoring tubes is equal to $40\phi_{\text{bfrp}}$ to allow proper failure to occur in the exposed part of the bar, rather than inside the tubes. For an 8 mm diameter bar, this equates to 320 mm (figure 3.1).

3.3.1.2 Capacity

The projected tensile strength of the reinforcement bar ($\phi 8$) is expected to be at least 1000 MPa. The specimens ought to be designed in such a manner that the weakest point in the specimen is the exposed part of the bar (figure 3.1). A brittle failure is desirable to occur in this location to deduce the maximum stress and strain at rupture. To determine the tensile stress at rupture, other failure mechanisms have to be prevented. These failure mechanisms include but are not limited to:

- Failure in steel tube;
- Bond failure of the bar;

The minimum required resistance is determined to be as follows in equation 3.1.

$$F_{\text{rupture,min}} = A_{\text{bfrp}} \sigma_{\text{bfrp}} = \frac{\pi}{4} * 8^2 * 1000 = 50.27 \text{ kN} \quad (3.1)$$

To prevent the other failure modes, a safety factor of 1.5 is applied. Therefore, the failure load to be taken into account is 75.40 kN. The minimum resistance for the unfavoured failure loads should therefore be larger than 75.40 kN.

The steel tubes used in the direct tension test specimens consist of S355-grade steel. Externally, the diameter of the steel tube is 38 mm. The internal diameter changes halfway from 22 mm to 18 mm. The governing internal diameter is therefore the former. The governing cross-section surface is therefore (equation 3.2):

$$A_{\text{tube}} = \frac{\pi}{4} (D_{\text{ext}}^2 - D_{\text{int}}^2) = \frac{\pi}{4} (38^2 - 22^2) = 753.98 \text{ mm}^2 \quad (3.2)$$

The design yield stress (σ_s) of steel grade S355 is 355 MPa, therefore the tensile capacity of the steel tubes is determined as follows (equation 3.3):

$$F_{\text{tube}} = A_{\text{tube}}\sigma_s = 753.98 * 355 = 267.66 \text{ kN} > 75.40 \text{ kN} \quad (3.3)$$

The tensile force capacity of the tubes is significantly higher than the projected force required for a brittle failure of the bar in tension. Therefore, yielding and subsequent failure of the steel tube is unlikely to occur.

Bond failure in the bar is prevented by the length of the tube. If the tube length is increased, the average bond stress over the length of the overlap with the tube decreases. Earlier bond stress testing by Sólyom [Sólyom, 2017] has shown results of at least 17.39 MPa. Assuming the upper boundary rupture force of 75.40 kN, the required tube length is determined in equation 3.4.

$$L_{\text{tube,min}} = \frac{F_{\text{rupture,max}}}{D_{\text{bar}}\pi\tau_{\text{bond}}} = \frac{75.40 * 1000}{8 * \pi * 17.39} = 172.52 \text{ mm} < 320 \text{ mm} \quad (3.4)$$

A tube length of 320 mm is sufficient for the upper boundary force to be applied. Even though 320 mm overlap is conservative, the process of applying the epoxy adhesive in the tube cannot be controlled very well, which might lead to air pockets in the tube. Therefore, a 320 mm overlap is applied.

3.3.1.3 Test setup

The specimens are inserted into a machine that exerts one-dimensional tension on the item placed (figure 3.2a). The specimen is subjected to a prescribed velocity of 1.0 mm/min (0.0167 mm/sec). To accurately measure the strain in the bar only, an extensometer is applied to the exposed portion of the bar (figure 3.2b). The extensometer measures the strain over a distance of 50 mm in the BFRP-reinforcement bar. As BFRP is linear elastic up to failure, applying the constitutive laws is allowed to determine the Young's modulus.



(a) Specimen loaded in direct tension testing machine



(b) Extensometer applied to the exposed part of the specimen

Figure 3.2: Direct tension test setup

3.4 4-point bending test

The proposed test is a 4-point bending test, where insights into the structural behaviour of beam specimens loaded in bending are provided. The emergence and propagation of cracks will be monitored, as well as the total vertical deflection of the loaded beams. The setup for the 4-point bending test is shown in figure 3.3.

A 4-point bending test is selected because a fully developed crack pattern can be established.

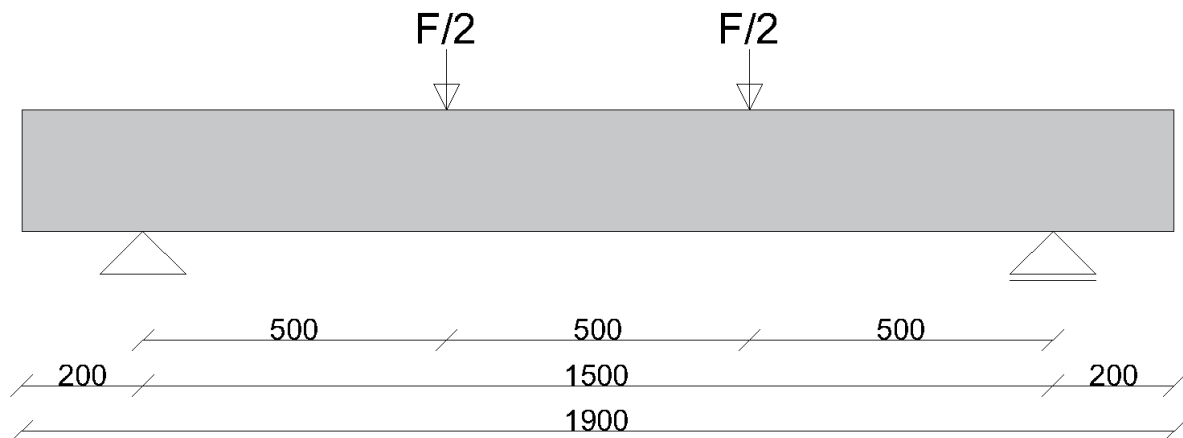


Figure 3.3: 4-point flexural bending test

3.4.1 Test specimens

6 different beam specimens are included in the test. The beam length, width and height are fixed to be 1900x150x200 (lxbxh). 4 out of 6 beams contain BFRP-bars as their longitudinal reinforcement. The remaining 2 beam specimens contain reinforcement steel in the longitudinal direction. Please note that shear capacity and shear crack formation are not included in the scope of this research, hence the stirrups are comprised of reinforcement steel for all 6 beam specimens.

The beam specimens are abbreviated by their reinforcement material, longitudinal reinforcement composition and concrete cover. The formulation of the abbreviations is as follows: [Reinforcement material]-[Longitudinal reinforcement composition]-[Concrete cover]. The reinforcement material is BFRP (B) or reinforcement steel (S). The longitudinal reinforcement composition is noted with the number of bars in the cross-section followed by the diameter in millimetres, for example, 3 longitudinal bars with a diameter of 8 mm is denoted as 3r8. The concrete cover is noted with the value in millimetre, preceded by the letter c. A beam with BFRP-bars as its reinforcement, containing 3 bars with a diameter of 8 millimetres and a concrete cover of 31 millimetres is therefore named: B-3r8-c31. Note that the concrete cover is taken from the constant bending moment zone and does therefore not include the stirrups. Table 3.1 shows a list of the tested specimens. Figure 3.4 shows the reinforcement configuration of the stirrups applied in the beam specimens, as well as the location of sections A-A and B-B.

Table 3.1: Beam specimen list

Specimen	Reinforcement material	Reinforcement	Cover
B-3r8-c31	BFRP	3Ø8	31 mm
B-2r10-c31	BFRP	2Ø10	31 mm
B-2r8-c31	BFRP	2Ø8	31 mm
B-3r8-c11	BFRP	3Ø8	11 mm
S-3r8-c31	Reinforcement steel	3Ø8	31 mm
S-3r8-c11	Reinforcement steel	3Ø8	11 mm

For each specimen, only one parameter is changed. B-3r8-c31 has a flexural reinforcement of 3Ø8 ($A_{bfrp,1} \approx 151 \text{ mm}^2$). In B-2r10-c31, the flexural reinforcement is 2Ø10, which is approximately the same cross-section area ($A_{bfrp,1} \approx 157 \text{ mm}^2$). For B-3r8-c31 and B-2r10-c31 $A_{bfrp,1} \approx A_{bfrp,2}$ applies, therefore the changing parameter is the bar diameter. B-2r8-c31 is designed with flexural reinforcement 2Ø8 ($A_{bfrp,1} \approx 100 \text{ mm}^2$). In relation to B-3r8-c31, the number of bars and subsequently the reinforcement percentage is changed. B-3r8-c31, B-2r10-c31 and B-2r8-c31 all have an applied concrete cover of 31 mm. B-3r8-c11 however incorporates the same reinforcement as B-3r8-c31, but with a smaller concrete cover of 11 mm as its differing parameter. Lastly, beam specimens S-3r8-c31 and S-3r8-c11 have the same geometry as B-3r8-c31 and B-3r8-c11 respectively, however, the reinforcing material is changed from BFRP-bars to reinforcement steel bars. These beam specimens serve the purpose of comparison with a steel-reinforced concrete structure.

The beam designs are based on experimental studies conducted at the concrete laboratory of Delft University of Technology. Data from prior experiments is utilized to validate the results of the current experimental study conducted for this master's thesis. Consequently, concrete covers of 31 mm and 11 mm were selected for incorporation into the beam design, taking into account the impact of reduced concrete cover. The validation process involves referencing the theses authored by Singh in 2019 and Zhekan in 2017.

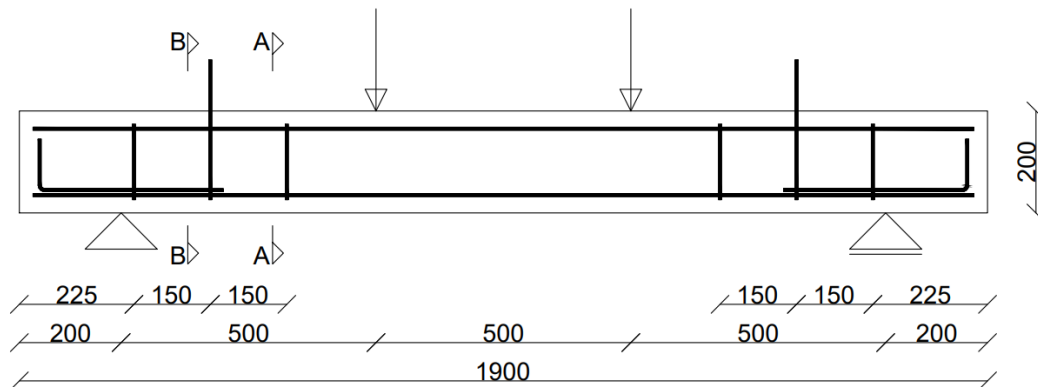


Figure 3.4: Reinforcement configuration of the stirrups applied in the beam specimens

3.4.1.1 Reinforcement configuration

As shown in 3.4, stirrups will only be placed between the supports and the loading application points. As the experimental research is focused on flexural cracking behaviour, the zone of interest is where the bending moment is constant, which is the part between the loading points. The shear force between the loading points

is theoretically equal to zero with this test setup, which means any stirrups for shear force resistance would be unnecessary.

For the top longitudinal reinforcement in the beam specimen, reinforcement steel is used since the simply supported beam does not include a hogging bending moment, hence is no need for the top reinforcement to be comprised of BFRP-bars. Since the shear force resistance of stirrups is not a point of interest in this research, there is no requirement for the stirrups to be BFRP-bars as well. In figure 3.5 every bar is marked with an "s" or a "b" (reinforcement steel (s) and BFRP (b)). The splices located at the ends of the bottom longitudinal reinforcement are required as BFRP-bars are hard to bend. The added reinforcement provides improved anchoring for the BFRP-bars. The overlapping of the longitudinal BFRP-bars with the additional L-shaped bars is 500 mm, which is presented in figure 3.5. To account for the bond strength development, L-shaped bars are placed on top of the longitudinal bars, rather than between the longitudinal bars.

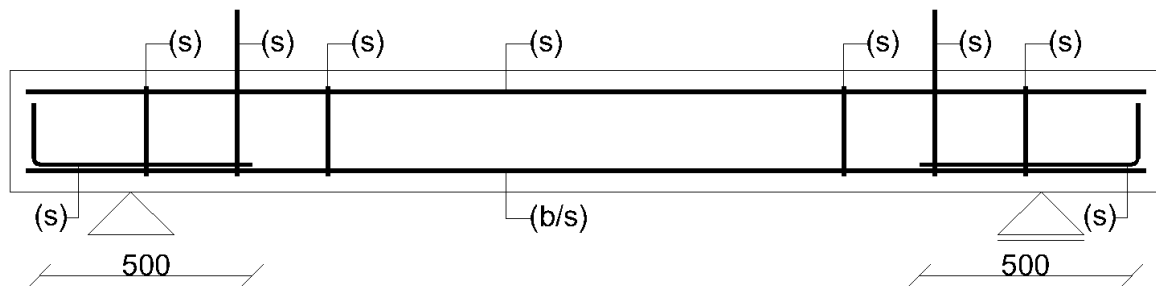


Figure 3.5: Reinforcement material designation

Based on Eurocode 2 [European Committee for Standardization, 2022], a transfer length of 384 mm is required. As $500 \text{ mm} > 384 \text{ mm}$, the provided transfer length is sufficient. The calculation according to Eurocode 2 for the transfer length is provided in the section "resistance estimation."

3.4.1.2 Cross-sections

In figures 3.6 up to and including 3.11, cross-sections A-A and B-B of the beam specimen are shown. Note that the reinforcement material is indicated in the respective figures. The beam specimens are too heavy to be lifted manually, therefore stirrups protrude from the top surface and can be used as anchorage for the crane.

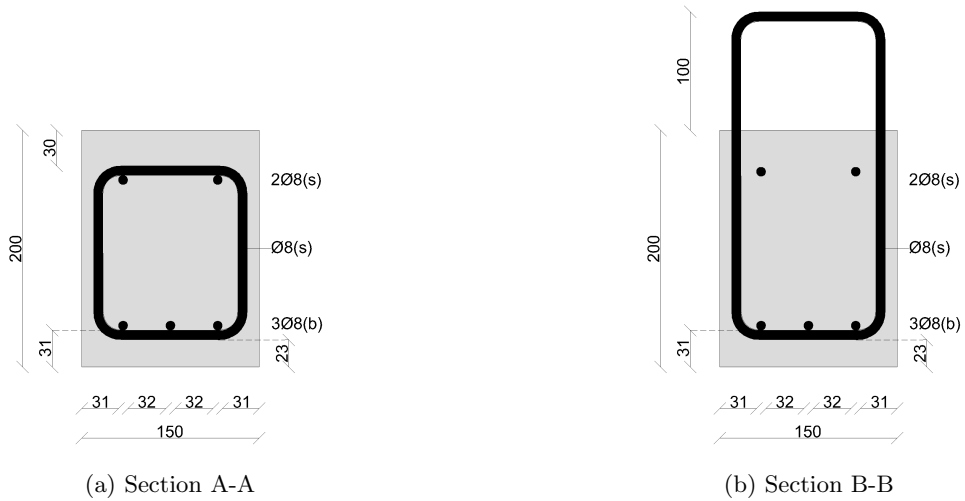


Figure 3.6: B-3r8-c31 sections A-A and B-B, (b)=BFRP-bar, (s)=Reinforcement steel bar

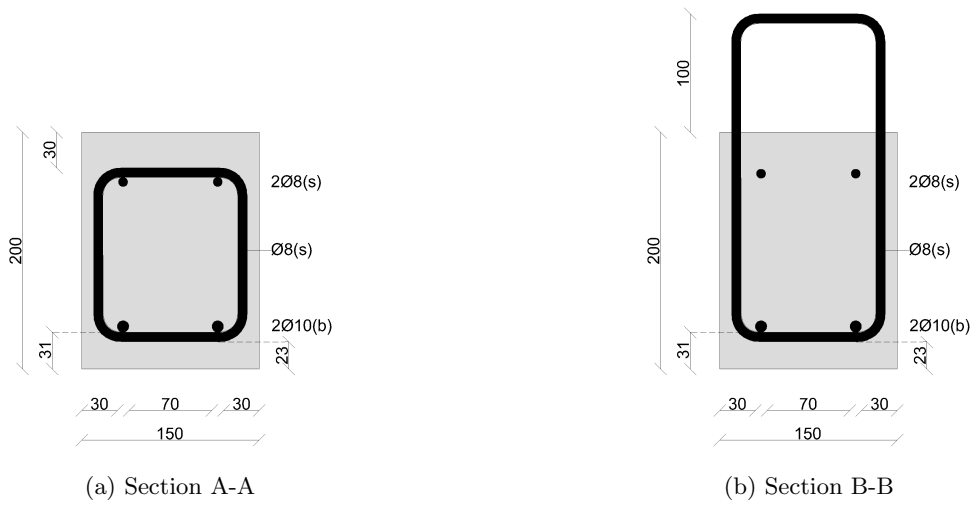


Figure 3.7: B-2r10-c31 sections A-A and B-B, (b)=BFRP-bar, (s)=Reinforcement steel bar

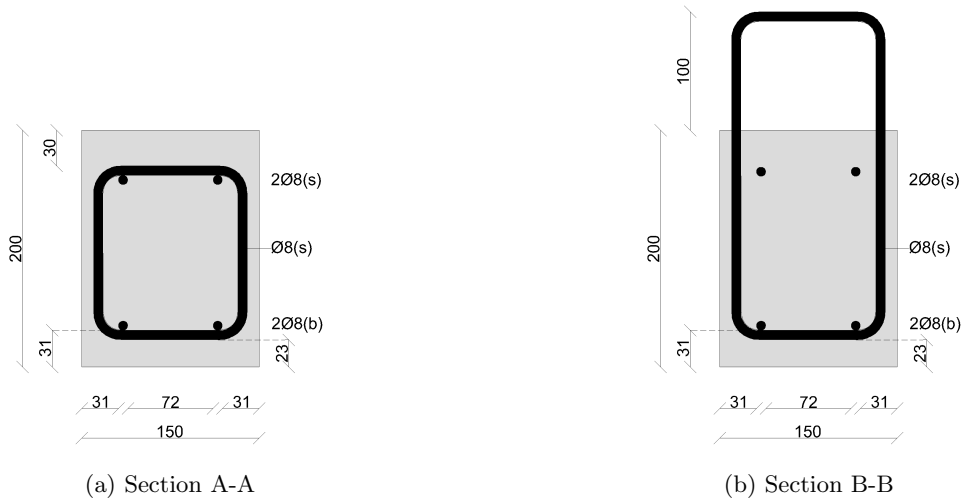


Figure 3.8: B-2r8-c31 sections A-A and B-B, (b)=BFRP-bar, (s)=Reinforcement steel bar

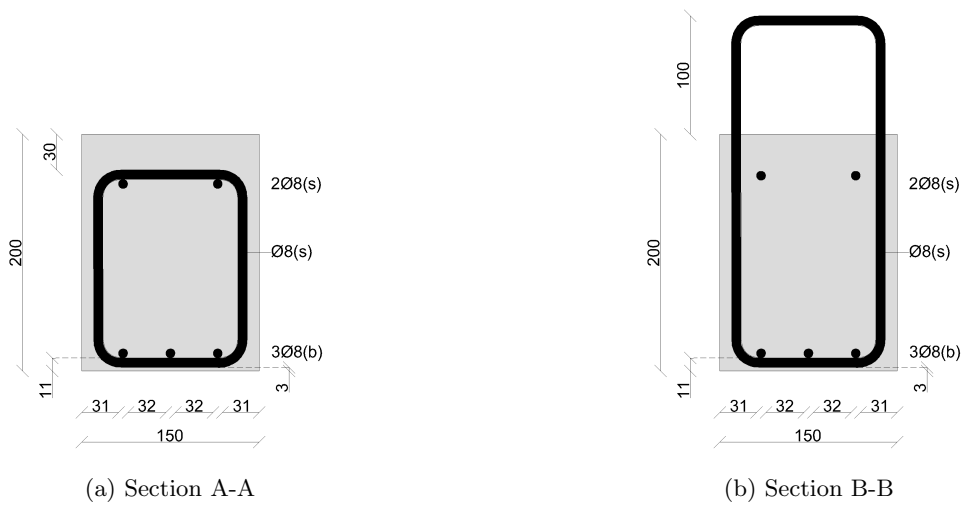


Figure 3.9: B-3r8-c11 sections A-A and B-B, (b)=BFRP-bar, (s)=Reinforcement steel bar

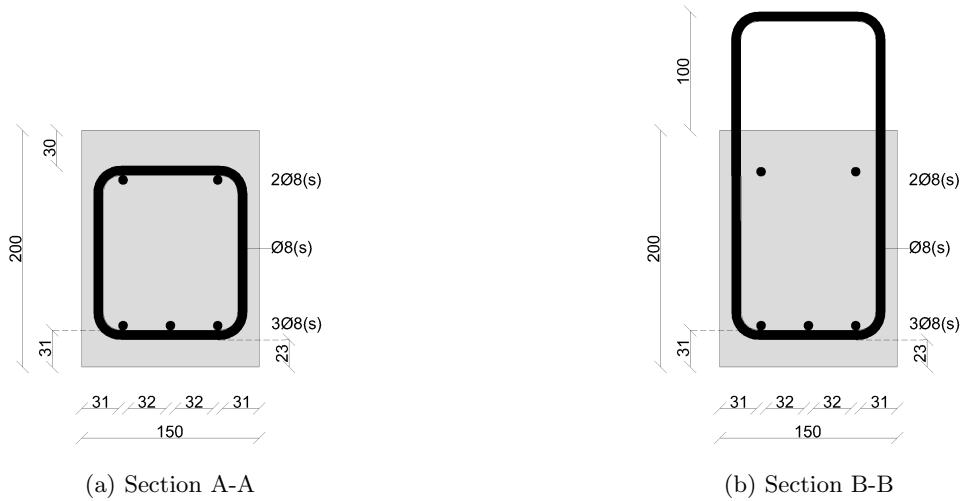


Figure 3.10: S-3r8-c31 sections A-A and B-B, (b)=BFRP-bar, (s)=Reinforcement steel bar

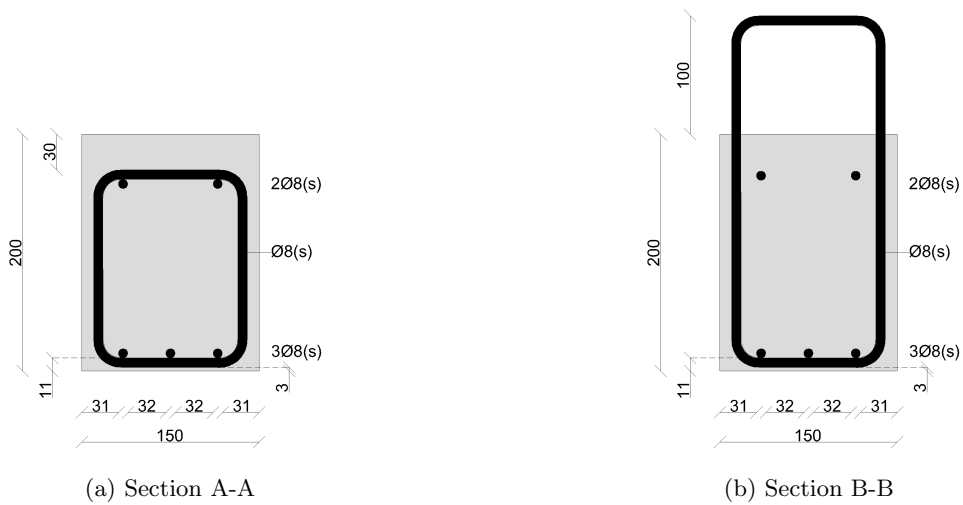


Figure 3.11: S-3r8-c11 sections A-A and B-B, (b)=BFRP-bar, (s)=Reinforcement steel bar

3.4.2 Resistance estimations

With the properties of the constituent material known, an estimation of the bending moment resistance and the shear resistance can now be made. Figure 3.12 presents the mechanical schematization of the 4-point bending test, as well as the M-line and the V-line.

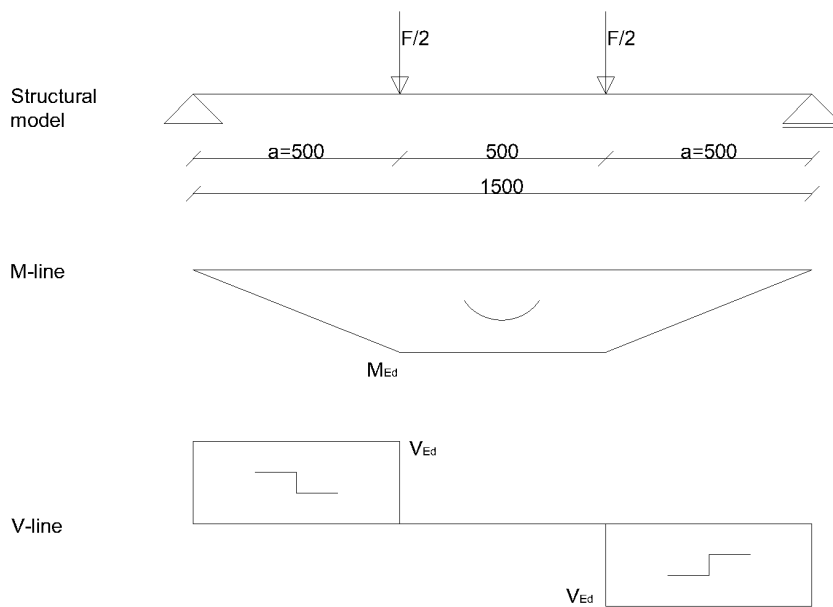


Figure 3.12: M-line and V-line beams experiment

Note that the material properties used for the construction of the crack width development prediction curves are presented in table 3.2. These assumptions are made because, at this point in the research, the strength properties were not known.

Table 3.2: Materials and properties used in predictive calculations

Material	Strength class/property
BFRP-bars:	
Tensile strength	1000 MPa
Young's modulus	50 GPa
Rupture strain	2.0%
Reinforcement steel	B500
Concrete	C30/37

3.4.2.1 Bending moment capacity

The estimated bending moment capacity M_{Rd} of the beam specimens can be determined by applying the ACI440 [Busel, 2006] and BRL0513 [CvD, 2015] codes formulae for the bending moment resistance. Another way of estimating the bending moment resistance is by determining the internal lever arm under the assumption that the ultimate height of the concrete compression zone x_u is reached. Equation 3.5 and 3.6 are used to determine the bending moment resistance by determining the internal lever arm. Note that long-term properties were not taken into account as the beams were tested 28 days after casting. Material factors, partial factors, load factors and environmental factors pertaining to the BRL0513, ACI440 and Eurocode respectively are not taken into account. From the tested materials, the mean values are used.

$$x_u = \frac{A_{bfrp}\sigma_{bfrp}}{0.75bf_c} \quad (3.5)$$

$$M_{Rd} = A_{bfrp}\sigma_{bfrp}\left(d - \frac{7}{18}x_u\right) \quad (3.6)$$

For the determination of the respective bending moment resistances, equations provided in Chapter 3 parameter study are used. The bending moment resistance according to the BRL0513 is determined using equations A.2 to A.6. The ACI440 used equation A.14 to A.17 in Appendix A to determine bending moment capacity. Table 3.3 presents bending moment resistance estimations succeeded by the corresponding maximum force in parentheses. The maximum force in kilonewtons is then used in the following subsection to determine the required shear force.

Table 3.3: Bending moment capacity estimations

	ACI440	BRL0513	Internal lever arm
B-3r8-c31	12.03 kNm (48.10 kN)	11.93 kNm (47.73 kN)	24.71 kNm (98.85 kN)
B-2r10-c31	11.99 kNm (47.96 kN)	11.93 kNm (47.73 kN)	24.71 kNm (98.85 kN)
B-2r8-c31	9.57 kNm (38.30 kN)	10.03 kNm (40.12 kN)	17.00 kNm (67.98 kN)
B-3r8-c11	14.24 kNm (56.95 kN)	14.20 kNm (56.79 kN)	27.49 kNm (109.97 kN)
S-3r8-c31	-	-	13.51 kNm (54.04 kN)
S-3r8-c11	-	-	15.32 kNm (61.28 kN)

The upper bound projected required force is 109.97 kN, which is required to reach the ultimate bending moment resistance M_{Rd} of beam specimen B-3r8-c31. This force is used to determine the required shear reinforcement.

3.4.2.2 Shear reinforcement

Since the point of interest is cracking behaviour, failure should be designed to occur in the constant bending moment zone of the beam, which is located between the point of load application. Flexural failure should be governing. The projected maximum force F applied is equal to 109.97 kN on the beam with the highest capacity

(beam B-3r8-c11). To avoid shear failure, the beam has to be reinforced accordingly. Figure 3.12 presents the M-line and the V-line for the experimental setup.

The shear force V_{Ed} is determined as follows:

$$V_{Ed} = \frac{F}{2} = 54.96 \text{ kN} \quad (3.7)$$

The shear stress on the section v_{Ed} is dependent on the effectual height of the reinforcement and is equal to:

$$d = h - c - \frac{\varnothing}{2} = 200 - 11 - \frac{8}{2} = 185 \text{ mm} \quad (3.8)$$

$$v_{Ed} = \frac{V_{Ed}}{b_w d} = \frac{54.96 * 10^3}{150 * 185} = 1.98 \text{ MPa} \quad (3.9)$$

The shear resistance for the concrete section $v_{Rd,c}$ is determined as follows:

$$v_{Rd,c} = 0.12k(100\rho_1f_{ck})^{\frac{1}{3}} = 0.12 * 2(100 * 0.00145 * 30)^{\frac{1}{3}} = 0.392 \text{ MPa} \quad (3.10)$$

Where: ρ_1 is the longitudinal reinforcement ratio. For beam B-3r8-c11, this is determined in equation 3.11. As a concrete class of C30/37 is assumed, f_{ck} equals 30 MPa.

$$\rho_1 = \frac{E_{bfrp}A_{bfrp}}{E_s b d} = \frac{53.46 * 10^3 * 150.80}{200 * 10^3 * 150 * 185} = 0.00145 \leq 0.02 \quad (3.11)$$

$$k = 1 + \sqrt{\frac{200}{d}} = 1 + \sqrt{\frac{200}{185}} \leq 2,00 \quad (3.12)$$

For the parameter k, a maximum value of 2.00 is taken into account. As $v_{Rd,c} < v_{Ed}$, shear reinforcement is required to prevent shear failure. The shear crack angle θ is determined (equation 3.13):

$$\theta = \frac{1}{2} \text{Arcsin}\left(\frac{2V_{ed}}{\alpha_{cw} v f_{cd} b_w z}\right) \quad (3.13)$$

Where $\alpha_{cw}=1.00$. $f_{cd}=20$ MPa. The lever arm between the centres of the concrete compression zone and the tensile reinforcement is equal to 159.85 mm. The parameter v is determined as follows (equation 3.14):

$$v = 0.7\left(1 - \frac{f_{cd}}{250}\right) = 0.7\left(1 - \frac{20}{250}\right) = 0.644 \quad (3.14)$$

The shear crack angle is determined as follows (equation 3.15):

$$\theta = \frac{1}{2} \text{Arcsin}\left(\frac{2 * 54.96 * 10^3}{1 * 0.644 * 20 * 150 * 159.85}\right) = 10.49^\circ \quad (3.15)$$

Since the calculated crack angle θ is smaller than the limiting value of 21.8° , θ is assumed to be 21.8° (0.3805 RAD).

The required steel area per millimetre is determined in equation 3.16. For the yielding stress f_{ywd} of the reinforcement steel of the stirrups, 500 MPa is taken as it is determined as the yielding stress f_y in the tensile test of the reinforcement bar presented in figure 4.2.

$$\frac{A_{sw}}{s} = \frac{V_{Ed}}{f_{ywd}z\cot(\theta)} = \frac{54.96 * 10^3}{500 * 159.85 * \cot(0.3805)} = 0.2751 \text{ mm}^2/\text{mm} \quad (3.16)$$

For a centre-to-centre distance of $s=150$ mm, the required cross-section of steel A_{sw} of the stirrups is equal to 41.27 mm^2 . With 3 2-leg stirrups in each shear zone of the beam specimens, with a diameter is 8 mm, the total cross-section surface is equal to 301.59 mm^2 . This is sufficient to prevent shear failure.

Since the crack angle is assumed to be 21.8° , the required distance for the crack to appear is equal to $z\cot(\theta)=384.34 \text{ mm} > 300 \text{ mm}$. Therefore, all stirrups will fall within this distance. The shear capacity is determined as follows (equation 3.17):

$$V_{Rd,s} = A_s f_{ywd} = 301.59 * 500 = 150.80 \text{ kN} > 54.96 \text{ kN} \quad (3.17)$$

3.4.2.3 Crack width

The bending moment at which cracking occurs M_{cr} depends primarily on the properties of the concrete and the geometry of the beam. As concrete usually has a lower tensile strength than compressive strength, the tensile strength of the concrete is dominant for the cracking bending moment. equation 3.18 is used to determine the cracking bending moment of the beams. The assumed tensile strength of the assumed concrete strength class C30/37 is 2.90 MPa.

$$M_{cr} = \frac{1}{6} h^2 b f_{ctm} = \frac{1}{6} * 200^2 * 150 * 2.90 = 2.90 \text{ kNm} \quad (3.18)$$

This equates to an applied force of 11.60 kN. At this point, the first crack should emerge in the concrete beams. Figure 3.13 presents a prediction of the crack width development according to the cracking models of the BRL0513 and ACI440 for the beams reinforced with BFRP-bars in relation to the force. In the same figure, the crack width curves for the beams reinforced with steel bars are presented according to Eurocode 2. Note that the Young's modulus after yielding of the reinforcement steel is taken into account, which results in a significant increase in the slope of the curves for the crack width prediction of the beams reinforced with steel bars.

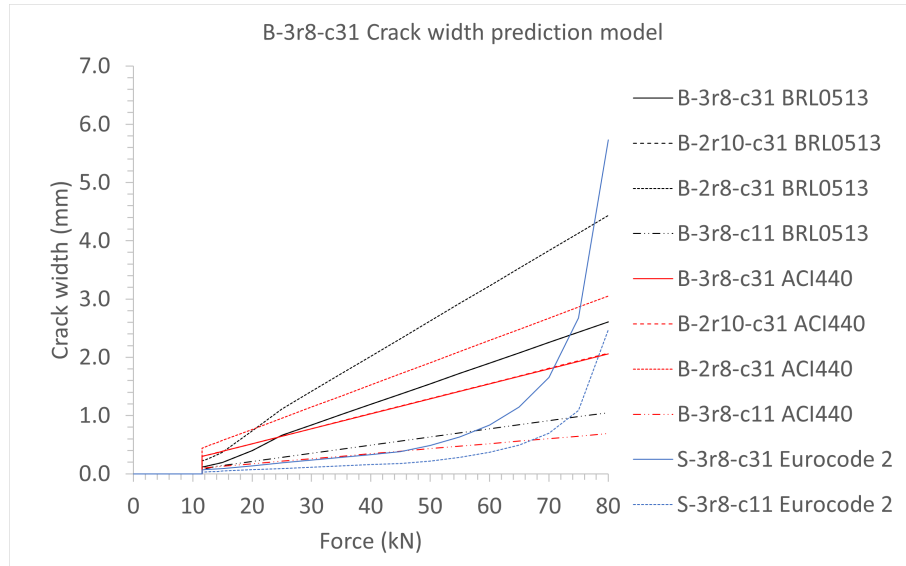


Figure 3.13: Crack width prediction according to BRL0513 [CvD, 2015] and ACI440 [Busel, 2006] (BFRP) and Eurocode 2 [European Committee for Standardization, 2022].

This approach is based on a rectangular concrete section and neglects the influence of the reinforcement in the concrete. Using this method, the neutral axis is assumed to be in the centre of the cross-section. In a more thorough approach, the influence of the reinforcement and its Young's modulus is included in the determination of the moment of inertia I_g of the gross cross-section. The cracking bending moment M_{cr} is determined using equation 3.19.

$$M_{cr} = \frac{I_g}{y_t} f_{ctm} \quad (3.19)$$

In this equation, y_t is the distance from the neutral axis of the gross cross-section to the extreme tension fibres in the cross-section. As BFRP generally contains a significantly lower Young's modulus in relation to reinforcement steel, the neutral axis in the cross-section containing BFRP-bars is expected to be closer to the centre of the cross-section. Therefore y_t is likely slightly larger. Cross-sections containing BFRP-bars are therefore likely to have a slightly smaller cracking moment M_{cr} the beams with reinforcement steel, which is also claimed by Shamass and Cashell [Shamass and Cashell, 2020].

3.4.2.4 Transfer length

To ensure proper force transfer from the BFRP-bar to the reinforcement steel bars in the beam designs, the length of the overlap has to be sufficient. The provided overlapping length is equal to 500 mm. Based on the methods of determining the minimum required transfer length in Eurocode 2, the base transfer length $l_{b,rqd}$ is determined according to equations 3.20 and 3.21.

$$l_{b,rqd} = \frac{\sigma_{sd}}{4 f_{fb}} \quad (3.20)$$

Where:

$$f_{bd} = 2.25\eta_1\eta_2f_{ctm} \quad (3.21)$$

The factors η_1 and η_2 are taken as 1. As the force transfer concerns the bottom reinforcement, good bond conditions are assumed, therefore η_1 is equal to 1. η_2 is also equal to 1 as the bar diameter is smaller than 32 mm. For the experiment, the mean tensile strength of concrete f_{ctm} is assumed. For concrete strength class C30/37, f_{ctm} is equal to 2.90 MPa

$$f_{bd} = 2.25 * 1 * 1 * 2.90 = 6.525 \quad (3.22)$$

Based on an assumed conservative value of 1000 MPa for the tensile stress in the tensile reinforcement bars and the largest applied diameter of 10 mm, the base transfer length is determined in equation 3.23

$$l_{b,reqd} = \frac{10}{4} * \frac{1000}{6.525} = 384 \text{ mm} < 500 \text{ mm} \quad (3.23)$$

As the base transfer length is sufficient, any reduction due to factors such as bar geometry and concrete cover, which is possible according to Eurocode 2, is not necessary.

3.4.3 Casting of the specimens

3.4.3.1 Concrete mixture

The beam specimens are cast with three concrete batches of 165 litres. The utilized concrete is a CEM I concrete with sand and gravel aggregates of various grain sizes and superplasticizers and water. The mix design and its ingredients are listed in table 3.4. The batches of concrete are created by firstly mixing the dry sand and gravel aggregates in order to ensure an equal distribution of the aggregates. After this, the cement is added to the dry substance and the mixing continues until a uniform mix is achieved. The superplasticizers are mixed with the water and added to the dry mixture of cement and aggregates. The concrete mixture is further mixed until all liquids are mixed with the dry substances until a uniform concrete mix is accomplished and ready to be cast into the moulds. The first batch of 165 litres is used to cast beam specimens B-3r8-c31 and B-2r10-c31. Subsequently, the second and third batches are used to cast the remaining beams.

Table 3.4: Concrete mix design

Component	Dry weight (kg/m ³)
CEM I 52.5R	260
Sand 0.125-0.25 mm	78.83
Sand 0.25-0.5 mm	256.20
Sand 0.5-1 mm	256.20
Sand 1-2 mm	157.66
Sand 2-4 mm	98.54
Gravel 4-8 mm	394.15
Gravel 8-16 mm	729.18
Water	156
Super-plasticizer	0.26

3.4.3.2 Casting and moulding conditions

2 beams are cast per casting day. As the concrete is poured in parts, a vibrating needle is used to compact the concrete. After the moulds are filled to the top, the surface is levelled with a putty knife. As all the required concrete is in, the beam specimens are sealed off with a plastic foil layer (figure 3.14) to retain a moist environment. After 28 days, the beams are demoulded and prepared for testing the day after.



Figure 3.14: Freshly casted beams specimens 1&2 sealed with plastic layer

3.4.3.3 Sampling of concrete

To verify the material properties of the concrete, additional smaller samples are cast. These smaller samples consist of several cubes and prisms cast from the same batch. Firstly, the moulds for the cubes and prisms are cleaned and oiled in. After filling up the beam specimen moulds, the remainder of the concrete is poured into the prepared moulds and compacted on a vibration table (figure 3.15) to release entrapped air bubbles. The relevant properties of the concrete batches are the concrete compressive cube strength, the Young's modulus and the tensile strength of the concrete.



Figure 3.15: Cubes and prisms cast from concrete batch

For the first batch of concrete, 3 concrete cubes of 150x150x150 mm have been cast, as well as an equal number of prisms of 100x100x400 mm. As for the second and third batches, the remaining concrete volume after the casting of the beam specimens allowed for 6 cubes where cast, as well as 3 prisms. The excess cubes of batches 2 and 3 are used to determine the tensile splitting strength and subsequently the tensile strength of the concrete. After 29 days, the cubes and prisms were tested to determine the compressive strength and the Young's modulus of the concrete.

The cubes are used to determine the compressive cube strength of the concrete batch according to NEN-EN-12390-3 [Nederlands Normalisatie-instituut, 2019a]. When compressing the cubes from the top and the bottom sides (Figure 3.17a), the other sides are free to deform. The cubes are subjected to an increasing compression force with an increment rate of 13.5 kN/s, which equals the prescribed 0.6 MPa/s. The test is stopped when the concrete cube fails.

The prisms however are used to determine the Young's modulus according to the NEN-EN-12390-13 [Nederlands Normalisatie-instituut, 2020]. By compressing the prisms cyclically between σ_a and σ_b , which is 10% to 33% of the compressive strength respectively (figure 3.16) and measuring the strain with LVDT's, the Young's modulus can be derived. After the loading cycle is completed, the prisms are compressed to failure to determine the prisms' strength from which 10% and 33% compressive strengths are taken. The determination of the Young's modulus utilizes the mean differences of the applied stress and the strain measured by LVDT's (equation 3.24)

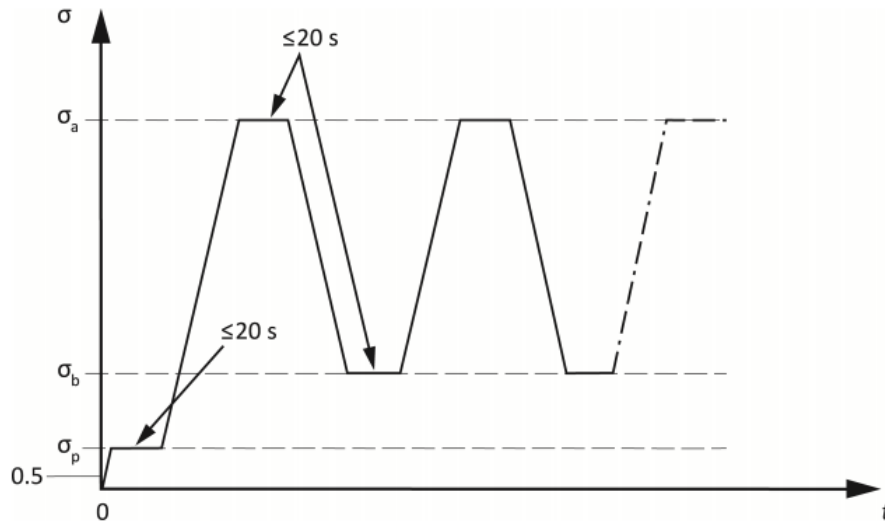


Figure 3.16: Cycle for the determination of stabilized secant Young's modulus, method B according to NEN-EN-12390

$$E_{c,s} = \frac{\sigma_a^m - \sigma_b^m}{\varepsilon_{a,3} - \varepsilon_{b,2}} \quad (3.24)$$

To measure the strain uniformly over the full cross-section, all 4 sides of the prisms are equipped with LVDT's with a range of 135 mm (Figure 3.17b).



(a) Cube subjected to compression test

(b) Prism subjected to compression test

(c) Cube subjected to tensile splitting test

Figure 3.17: Cubes and prisms subjected to respective tests

The tensile strength of the concrete can be derived by determining the splitting strength first. Batches 2 and 3 produced 3 cubes that are used to determine the splitting strength according to the NEN-EN-12390-6 [Nederlands Normalisatie-instituut, 2019b]. The required loading rate (R) for the tensile splitting is determined by using equation 3.25

$$R = \frac{s\pi Ld}{2} \quad (3.25)$$

Where the parameters L and d are the length and depth of the concrete sample used in the test. The stress rate s is advised to be between 0.04 MPa/s and 0.06 MPa/s. The upper boundary of 0.06 MPa/s is used, resulting in a loading rate of 2.12 kN/s. The tensile splitting strength is determined using equation 3.26. The parameter F represents the maximum load applied to the sample. Figure 3.17c shows one of the concrete cubes in the compression machine.

$$f_{ct,sp} = \frac{2F}{\pi Ld} \quad (3.26)$$

Section 3 of the NEN-EN 1992-1-1 provides a method of determining the axial tensile strength from the tensile splitting strength (equation 3.27). Taking the mean value out of 3 cubes, f_{ctm} is determined.

$$f_{ct} = 0,9f_{ct,sp} \quad (3.27)$$

For the tensile strength of the first batch, formulae provided by Eurocode 2 are used to determine the tensile strength derived from the compressive cube strength.

3.4.3.4 Results

The properties collected are the concrete cubes' strength (table 3.5), the concrete Young's modulus (table 3.6), and lastly the tensile splitting strength (table 3.7). For the batches to be considered valid, the coefficient of variation should not exceed 10% for each testing group. Further detailed results are shown in Appendix E, F, and G respectively. The characteristic cube strength f_{ck} is determined by subtracting 1.48σ (Standard deviation) from the average concrete cube compressive strength (equation 3.28), which is a method provided in NEN-EN-206+A2 [Nederlands Normalisatie-instituut, 2016]. The factor 1.48 may be applied if the sample size exceeds 15 cubes. As this concrete mixture has been used numerously in similar experiments at the TU Delft, and it's a well-known mixture within the concrete industry, the sample size tested over the years using this mixture can be assumed to exceed the threshold of 15 cubes. Therefore, the factor of 1.48 is valid to use.

The cube dimensions used in the test are 150x150x150 mm, which are the standard dimensions for the test. The measure averages in the test are 44.5, 51.5 and 51.2 MPa (table 3.5).

$$f_{ck} = f_{cm} - 1.48\sigma \quad (3.28)$$

Table 3.5: Concrete cube compressive strength results

Cube sample	Batch 1	Batch 2	Batch 3
Cube 1	39.9 MPa	50.5 MPa	53.1 MPa
Cube 2	46.6 MPa	54.2 MPa	48.7 MPa
Cube 3	46.9 MPa	49.7 MPa	52.0 MPa
Average cube strength	44.5 MPa	51.5 MPa	51.2 MPa
Standard deviation	3.9 MPa	2.4 MPa	2.3 MPa
Coefficient of variation	8.88%	4.63%	4.46%

The characteristic values for the compressive cube strength of the respective concrete batches are 38.6, 47.9 and 47.9 MPa after applying equation 3.28. The compressive cylindrical strength of the concrete is determined by applying the relation in equation 3.29.

$$f_{ck,cylinder} = 0.82f_{ck,cube} \quad (3.29)$$

The average compressive cylindrical strength $f_{ck,cylinder}$ of the respective concrete batches are 31.7, 39.3 and 39.2 MPa respectively after applying equation 3.29. Note that the concrete force first batch has a significantly lower concrete compressive strength than the second and third batches. As the coefficient of variation is within 10%, and the strength is within the designed concrete strength class, the effects on the structural behaviour are expected to be insignificant. As all concrete batches meet the benchmark for the average compressive cylindrical strength of at least 30 MPa, The concrete batches are classified as C30/37 based on the compressive strength properties.

The Young's modulus of the concrete batches is tested 29 days after each batch is cast (table 3.6). All full results are shown in Appendix G. The average moduli of elasticity are 39463 MPa (batch 1), 36106 MPa (batch 2) and 37591 MPa (batch 3). All three concrete batches have significantly larger moduli of elasticity in relation to their strength classification based on the compressive strength properties.

Table 3.6: Concrete Young's modulus results

Prism sample	Batch 1	Batch 2	Batch 3
Prism 1	37727 MPa	36681 MPa	38426 MPa
Prism 2	39950 MPa	36818 MPa	37686 MPa
Prism 3	40390 MPa	35232 MPa	38716 MPa
Average Young's modulus	39355 MPa	36244 MPa	38276 MPa
Standard deviation	1684.58 MPa	878.34 MPa	531 MPa
Coefficient of variation	4.28%	2,42%	1.39 %

The tensile strength of the concrete of batch 1 is determined using the empirical relations provided in Eurocode 2, which is based on the characteristic concrete compressive cube strength. For concrete classes lower than C50/60, the tensile strength is determined using equation 3.30.

$$f_{ctm} = 0.3f_{ck}^{\frac{2}{3}} \quad (3.30)$$

By applying equation 3.30 over the characteristic concrete compressive cube strength of batch 1, the concrete tensile strength is determined to be 3.43 MPa. For batches 2 and 3, the tensile strength is determined by the procedure described in the previous section. The average tensile splitting strengths are 3.94 MPa (batch 2) and 3.79 MPa (batch 3), which is shown in table 3.7. This leads to a concrete tensile strength of 3.55 MPa (batch 2) and 3.41 MPa (batch 3) after applying equation 3.27.

Table 3.7: Tensile splitting strength cubes results

Cube sample	Batch 1	Batch 2	Batch 3
C2.4	-	3.98 MPa	3.71 MPa
C2.5	-	3.73 MPa	3.84 MPa
C2.6	-	4.13 MPa	3.81 MPa
Average tensile splitting strength	-	3.94 MPa	3.79 MPa
Standard deviation	-	0,20 MPa	0.067 MPa
Coefficient of variation	-	5.10%	1.78%

Note that for batch 1, no cubes were made for testing on tensile splitting strength.

3.4.4 Measuring techniques

To measure the cracking behaviour of the beam specimen subjected to the 4-point bending test, the following measuring techniques and equipment are used:

- Digital Image Correlation (DIC)

- Crack width measurements from Digital Image Correlation data
- Linear Variable Differential Transformer (LVDT)
- Optical fibres

3.4.4.1 Digital Image Correlation (DIC)

With Direct Image Correlation, deflections and strain can be identified on a two-dimensional plane. By comparing and correlating data captured by a camera setup at a prescribed distance, the relations between the consecutive images can be identified. The DIC-system correlates 2 images by overlapping and dividing the overlapping images into sub-images (figure 3.18). The DIC-system then assigns coordinates to the overlapped sub-images. The deflection and subsequently the strain are found by correlation of the reference image with the sub-image [Shih and Sung, 2013].

The correlation of the images is done by determining the correlation coefficient (COF). The correlation coefficient is the ratio between the sum of the grayscale in a sub-image (\tilde{g}_{ij}) in relation to the grayscale in the reference image (g_{ij}). The calculation of the correlation coefficient is provided in equation 3.31.

$$COF = \frac{\sum g_{ij} \tilde{g}_{ij}}{\sqrt{\sum g_{ij}^2 \sum \tilde{g}_{ij}^2}} \quad (3.31)$$

For the correlation process of the sub-images and the reference image or the sub-image with the sub-images, the plane to which the camera is aimed should have a unique pattern which should be recognisable by the software. This pattern can be established by spraying a random dot speckle on a plain white background on the side of the beam specimen. The dots in the pattern should be sized appropriately. Dots of insignificant size will not be recognized as such by the software. If the dots exceed the appropriate size, data inaccuracy and loss of data occur. The area of interest for this experiment is the constant bending moment zone between the point of load application, the stochastic pattern is only applied to this area.

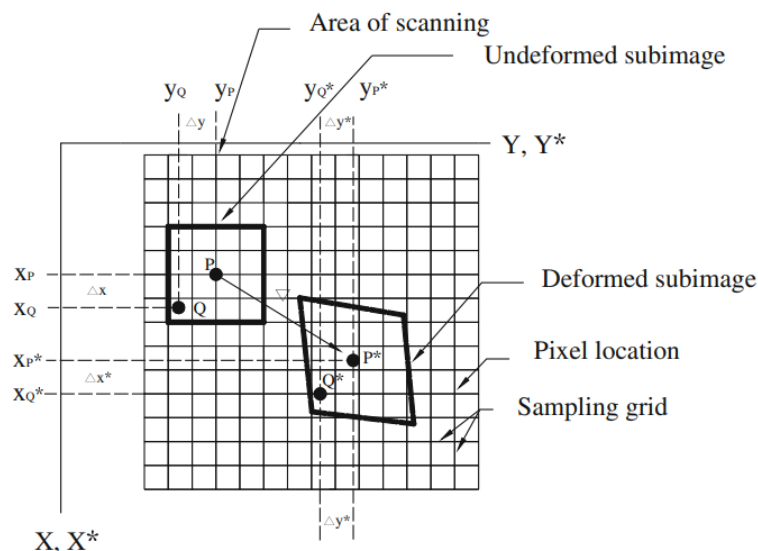


Figure 3.18: Schematic representation of correlation of the sub-images of deformed and un-deformed images on a two-dimensional deflection field [Shih and Sung, 2013]

Since Digital Image Correlation is an optical instrument, its accuracy depends on the lighting conditions in the surrounding area and also on the stability of the camera. The camera uses flashes to condition the images taken. By limiting the camera opening through which the image is taken, the influence of the light in the room is limited. The DIC-system is set up by placing a camera at a certain distance which is operated remotely. Since the camera has to be in the same position for the full duration of the test, a perimeter is put in place around the camera. The application of the stochastic pattern to a beam specimen is shown in figure 3.19.



Figure 3.19: Stochastic pattern applied to beam S-3r8-c31 during test preparation

3.4.4.2 Crack width measurements from Digital Image Correlation data

DIC is used to gather deflections and strains from the stochastic pattern in the images taken by the camera. This deflection and strain field can be analysed and measured over a defined section in the images. This section in the DIC-images is drawn close to the bottom surface of the beam (approximately 2 mm) to measure the width of the primary flexural cracks. By determining the principle of Von Mises stresses over the length of the section, the x-coordinate of the peak values should coincide with the location of the cracks. To eliminate noise from the data gathered in the section, a threshold of 0.5% is enforced.

The width of the cracks in the section can be determined by calculating the difference in horizontal displacement in the x-coordinate of the first and the last point in the crack width interval (equation 3.32), which are denoted as x_1 and x_2 respectively.

$$w(x) = |dx_1 - dx_2| \quad (3.32)$$

The crack widths are calculated using a MATLAB script. To verify the output of the MATLAB script, crack widths are manually calculated over the length of the section using the program GOM-correlate as well.

3.4.4.3 Linear Variable Differential Transformer (LVDT)

In addition to Digital Image Correlation, strain measurements using strain gauges are used to validate the data. These strain gauges in the form of Linear Variable Data Transformers (LVDT's) are used to measure the

displacement between 2 defined locations on the beam specimens. Depending on the relative displacements of these points on the beam specimens, a spring is either compressed or extended. The change in the length of the spring induces a change in resistance in an electrical circuit. This change in resistance generates a voltage in the system, which is used to measure the displacement. LVDT's are positioned on the beam specimens in positions relevant to the research goals (figure 3.20).

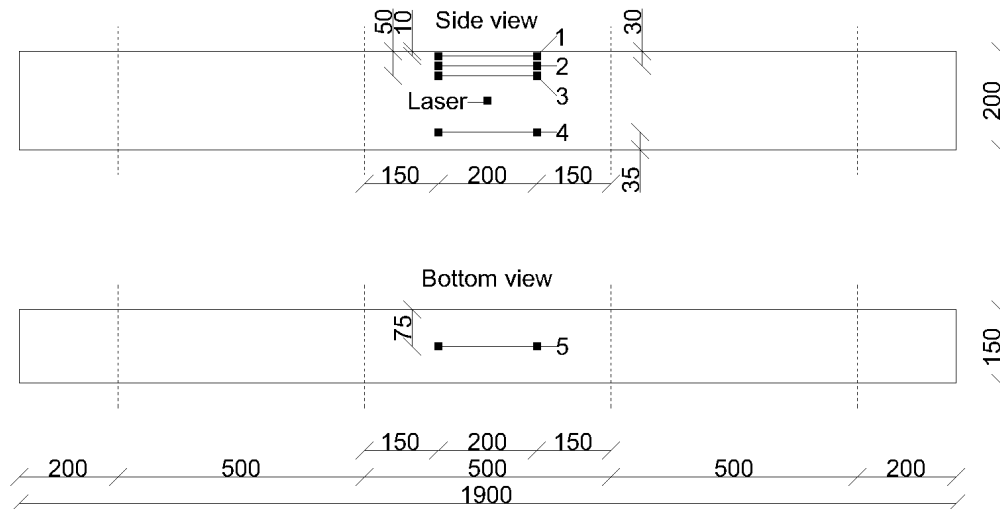


Figure 3.20: LVDT-positioning on beam specimens

3.4.4.4 Optical fibre strain gauges

Whereas LVDT's measure the strain in the concrete externally, Continuous strain measurement by distributed fibre optical sensors measures the strain in the reinforcement bars internally. Before casting, optical fibre strain gauges are glued to the bottom side of the bottom reinforcement (figure 3.21). Each beam has 1 optical fibre strain gauge attached to 1 bar in the bottom reinforcement layer.



Figure 3.21: Optical fibres glued to reinforcement bar

The length of the glued part of the optical fibre strain gauge spans the constant bending moment zone of the beam with some excess length (figure 3.22). The advantage of applying this system to the reinforcement bars is the direct measurement of the strain in the reinforcement.

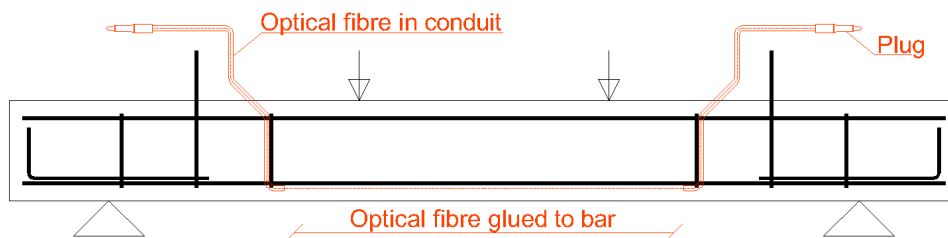


Figure 3.22: Optical fibre strain gauges placement plan, side view

During preparation, the conduits were glued to the bottom of the reinforcement bar and guided upwards along the innermost stirrups to stick out of the beam at the top surface after casting (figure 3.22). The optical fibre is then inserted into one of the conduits and pushed through to the exit of the conduit at the bottom section of the beam. Tensioning the constant bending moment zone, the fibre is inserted into the second conduit and pushed through the end of the conduit at the opposite side of the beam. The optical fibre is glued to the bottom side of the reinforcement bar with a thin layer of CN glue. Before applying the glue, the bottom surface of the BFRP-bar is processed with sandpaper and cleaned using acetone. At the bottom of the reinforcement bar, the optical fibre is pulled straight to be parallel to the bar and glued to the reinforcement bar at the ends. This caused a slight pretension to be present in the optical fibre. Finally, the optical fibre spanning the constant bending moment zone is carefully glued to the bar to ensure a constant bond for accurate strain measurement.

After casting, plugs are installed at the ends of the fibres to be inserted into a computer with software to translate the measured data.

3.4.4.5 Laser measuring vertical displacement at mid-span

To measure the vertical displacement of the concrete beam specimen at mid-span, a laser device is installed. The laser is mounted to a wooden joist that is supported above the concrete beams support at half-height (figure 3.23). The laser is aimed at a steel plate glued to the bottom of the beam, measuring its relative distance. The purpose of the laser is to measure the mid-span deflection without the influence of the supports or initial settlements. As the test is started, the measured displacement is reset to zero and the displacement is measured as the load increases. To eliminate force in the wooden joist, one side is free to slide horizontally.



Figure 3.23: Laser device mounted to a beam specimen

3.4.5 Test setup

The force required is generated by a hydraulic press with a force capability of 400 kN. The press is attached to an overarching steel frame (figure 3.24). The force is applied to an intermediate beam, that splits the force over the desired length of the constant bending moment zone (500 mm). The loading surface of the load spreader beams is connected to the beam specimens by the loading plates. Of these loading plates, one is a fixed hinge, whereas the other is a free hinge. The supports of the beam specimens consist of rolling hinges with limited horizontal movement capacity.

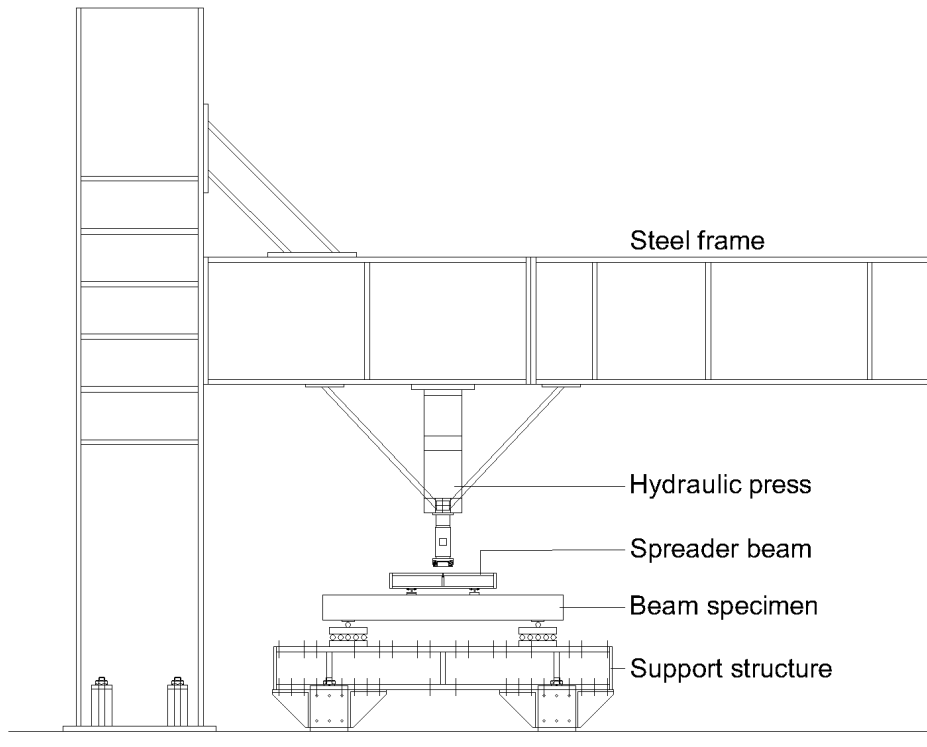


Figure 3.24: 4-point bending test setup

Chapter 4

Results

4.1 Direct tension test

This section presents the results of the performed direct tension test. The results of this test are used to outline the difference in structural behaviour between BFRP-bars and reinforcement steel. Also, the relevant properties are presented for further incorporation into predictive calculations. The failure modes of the specimens are presented as well.

4.1.1 Results

From the tensile test, the properties of the BFRP-bars can be determined. These properties are listed below. The guideline used for determining the relevant properties is the ACI440.3R [American Concrete Institute, 2012] and the ACI440.1R [American Concrete Institute, 2015]. For the determination of the average properties such as the Young's modulus and the average tensile strength and the statistical meaning of the test results, the ACI440.3R provides methods. For the determination of the characteristic values of the properties, the ACI440.1R is used. The extracted properties from the direct tensile tests are listed below:

- Force at failure
- Tensile stress at failure
- Strain at failure
- Young's modulus

Testing guideline ACI440.3R mentions 2 ways of determining the properties of the BFRP-bar. Method 1 is based on the composite area that takes into account the gross cross-sectional area of the bar. Method 2 is based on the fibre content of the composite and does not take into account the resin content of the BFRP-bar. As the resin content does contribute to the tensile strength of the BFRP-bar, method 1 is selected (composite area). The ACI440.3R requires the average, standard deviation and coefficient of variation to be determined for the properties listed above. From the maximum tensile force, the tensile strength can be derived.

Table 4.1: Combined Test Results

Parameter	Force at failure	Tensile stress at failure	Strain at failure	Young's modulus
Specimen 1	55.90 kN	1112.15 MPa	2.09%	54.16 GPa
Specimen 2	53.85 kN	1071.26 MPa	1.87%	54.86 GPa
Specimen 3	62.23 kN	1238.00 MPa	2.39%	51.44 GPa
Average	57.33 kN	1140.51 MPa	2.12%	53.49 GPa
Standard deviation	3.57 kN	71.01 MPa	0.21%	1.47 GPa
Coefficient of variation	6.23%	6.23%	9.94%	2.75%

The failed specimens (figure 4.1) all show the same failure mode, which is the disintegration of the exposed part of the bar into smaller bundles of fibres. As the maximum projected force during the direct tensile tests is approached, individual fibres and small bundles start to fail. As the force increased, more smaller bundles of fibres failed and the cross-section surface decreased further. At last, the final remaining fibres fail as well causing the force to decrease.



Figure 4.1: Test specimens after failure direct tension tests

The results of the direct tensile tests show a spread in the stress-strain relation (figure 4.2), which is noticeable in the standard deviation. As a spread in the rupture strain and the maximum tensile stress cause a larger standard deviation, this is unfavourable for the determination of the guaranteed properties according to the ACI440.1R [American Concrete Institute, 2012] as the standard deviation is subtracted 3 times. The slight deviation may be attributed to intrinsic material imperfections or faulty alignment during the preparation of the test. From the same batch as the reinforcement steel applied in the beam specimens, one bar is subjected to a direct tension test. The yielding stress f_y is equal to 520 MPa, with a corresponding yielding strain of approximately 0.26%. The ultimate strength f_u of this bar is measured at approximately 600 MPa, with a corresponding strain of 2.70%. The stress-strain relation is shown in figure 4.2, along with the results from the direct tensile tests conducted with the BFRP-bars.

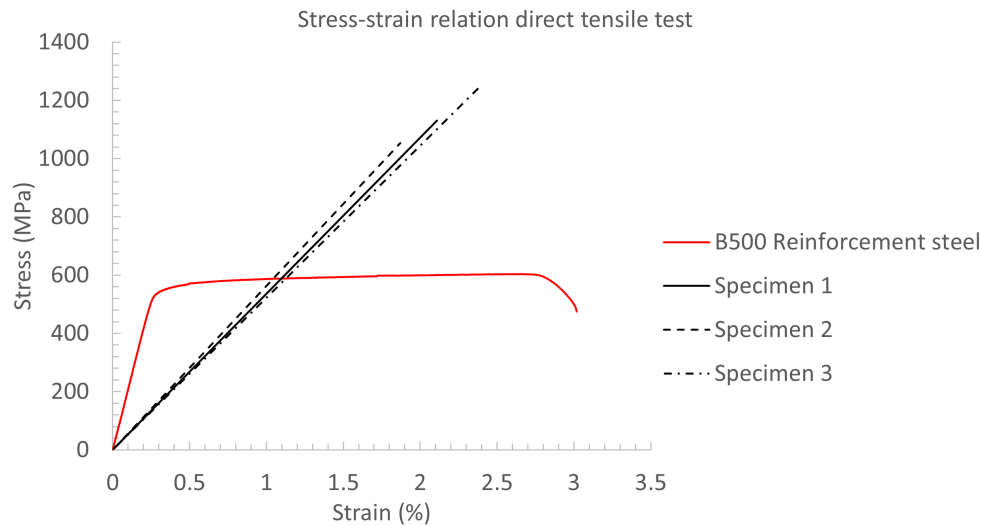


Figure 4.2: Stress-strain relation direct tensile tests

4.1.2 Conclusion

Direct tensile testing of BFRP-bars indicates an average tensile strength of 1140 MPa. Contrary to reinforcement steel, the basalt fibre reinforcement bar shows a linear elastic behaviour throughout the entire tensile tests up to the moment of failure. The failure occurred at an average tensile strain of 2.12%. The average Young's modulus of the BFRP-bars used in the experimental study is determined to be 53.46 GPa. During testing, the BFRP-bars show linear elastic behaviour up to the failure load, which is consistent with the literature.

4.2 4-point bending test

During the experiment, the load-deflection behaviour of the beams is monitored, as well as the cracking behaviour extracted from DIC-data. This section presents the results of the 4-point bending with the 6 tested beams. The results of the individual beams are presented in Appendix H. This includes the load-deflection curves, the chronological cracking development of the constant bending moment zone and the data from the LVDT's.

4.2.1 Performance indicators

Table 4.2 presents performance indicators for all beams tested in the experimental study. The maximum loads and corresponding deflections are presented, as well as the maximum measured deflection of the beams. The number of cracks and the corresponding average crack spacing were measured over the constant bending moment zone.

Table 4.2: Performance summary of all tested beams

	B-3r8-c31	B-2r10-c31	B-2r8-c31	B-3r8-c11	S-3r8-c31	S-3r8-c11
Maximum load	61.89 kN	65.17 kN	59.96 kN	71.05 kN	59.38 kN	64.77 kN
Mid-span vertical deflection at maximum load	25.64 mm	25.47 mm	32.16 mm	21.90 mm	17.17 mm	17.47 mm
Maximum vertical deflection at mid-span	46.83 mm	25.47 mm	37.76 mm	21.90 mm	21.76 mm	23.87 mm
Number of cracks in constant bending moment zone	7	7	7	8	5	7
Average crack spacing	71.43 mm	71.43 mm	71.43 mm	62.5 mm	100 mm	71.43 mm

The beams containing a concrete cover of 31 mm fail at a load of approximately 60 to 65 kN, whereas the failure mode of the beams with the smaller concrete cover, and therefore a larger internal lever arm, reach a failure load of approximately 65 to 70 kN.

With the the exception of B-2r8-c31 and B-3r8-c11, failure of all concrete beams is dictated by the crushing of the concrete compression zone, as intended by the design. Beam B-2r8-c31 failed in the shear zone of the beam due to a faulty stirrup. Even though the failure mode was not as expected, the force at which B-2r8-c31 failed is comparable to the beams that failed in compression. Beam B-3r8-c11 failed in the tensile reinforcement, which was not expected to occur.

4.2.2 Flexural behaviour

4.2.2.1 Load-deflection curves

A significant distinction of the load-deflection curves is noticeable between the beams according to their respective reinforcement materials. The load-deflection curves of all tested beams are presented in figure 4.3. The red curves, which depict the beams reinforced with steel bars, show a significantly higher stiffness up to approximately 17 kN. The blue curves (beams reinforced with BFRP-bars) show an earlier reduction in stiffness that starts at approximately 12 kN. This part of the load-deflection curves is presented in a close-up in figure 4.3. The load level at which the cracking emerges primarily depends on the properties of the concrete. However, the reinforcement material and its respective Young's modulus influence the initial crack formation as well.

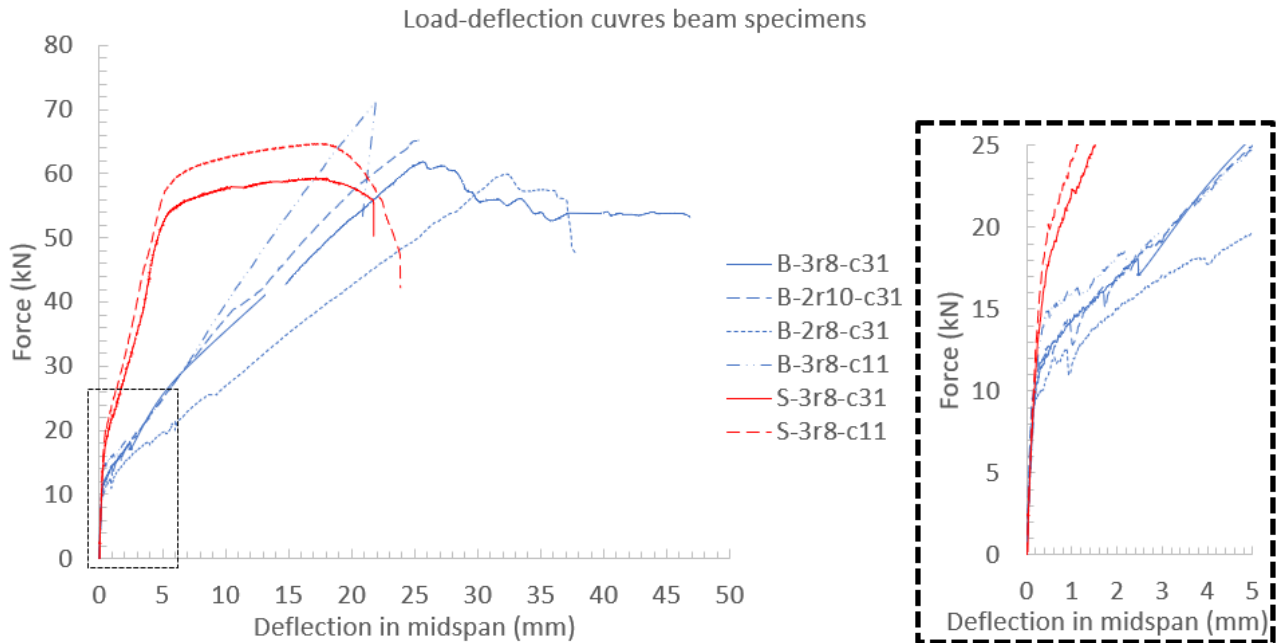


Figure 4.3: Load-deflection curves of all tested beam specimen

From the DIC-data, the deflection level at which the first crack emerges can be determined. The corresponding load level and bending moment are then determined using the test data from the load-deflection curves. Table 4.3 presents the load level, bending moment and vertical deflection at which the first crack appears in each beam.

Table 4.3: First crack load level, bending moment and corresponding vertical deflection

Beam	Force	Bending moment	Vertical deflection
B-3r8-c31	10.55 kN	2.64 kNm	0.2335 mm
B-2r10-c31	10.90 kN	2.73 kNm	0.2055 mm
B-2r8-c31	9.82 kN	2.46 kNm	0.2532 mm
B-3r8-c11	13.00 kN	3.25 kNm	0.2955 mm
S-3r8-c31	15.11 kN	3.78 kNm	0.3269 mm
S-3r8-c11	17.69 kN	4.42 kNm	0.3499 mm

The beams containing BFRP-bars show earlier initial cracking due to their lower Young's modulus as hypothesized by Shamass & Cashell [Shamass and Cashell, 2020]. The beams with the largest reinforcement depth show the latest cracking in the loading cycle for both reinforcement materials, at the neutral axis is shifted downwards to most. The earliest cracking in the loading cycle is found in beam B-2r8-c31, as its reinforcement ratio is the lowest, causing the neutral axis to be shifted downwards the least. Based on the predicted cracking bending moment of 2.90 kNm with a corresponding force of 11.60 kN appeared to be generally accurate for the beam containing BFRP-bars, but conservative for the beam reinforced with steel bars. Other deviations may

be attributed to the real concrete tensile strength of the mixture as this calculation was made with an assumed concrete class of C30/37.

4.2.2.2 Load-deflection stages

Once cracking initiates, the reinforcement becomes engaged, absorbing the tensile force that was initially borne by the uncracked concrete. Following cracking, the deflection at the mid-span of steel-reinforced beams is notably less compared to beams reinforced with BFRP-bars at similar points. This points to a reduction in stiffness post-cracking in the beam, which is shown in figure 4.3. The beams reinforced with reinforcement steel show 5 stages in the load-deflection curves. These stages in chronological order are the following:

1. Uncracked stage
2. Crack formation stage
3. Stabilized cracking stage
4. Yielding stage
5. Concrete crushing

These stages are noted in order of occurrence in subfigure 4.4a.

The first stage is the uncracked stage for which the deflection is relatively minimal. The stiffness of the beam is the largest in this stage, hence a relatively steep slope in the load-deflection curve compared to the other stages. After the first crack appears, the crack formation stage starts. In this stage, cracks form over the length of the constant bending moment zone. As all cracks have been formed, the stabilized cracking stage starts. In this stage, the existing cracks will propagate in depth and width. No new cracks emerge in this stage. The next stage for the beams reinforced with reinforcement steel is the yielding of the reinforcement which causes the largest drop in stiffness relative to the previous stages. In this stage, the reinforcement steel enters the plastic deformation stage, causing larger strains and therefore larger and irreversible deformations. The steep drop in stiffness is visible in figure 4.3 for beam specimens S-3r8-c31 and S-3r8-c11 as at approximately 6 mm in vertical deflection for both beams. In this stage, the force barely increases with the imposed deformation. At the end of the stage, the concrete compression zone failed for both beam specimens and the force decreased while the mid-span deflection was still increasing. As the concrete crushing strain in the compression zone is reached, the beams start to fail. In this stage, crack width still increases.

For the beams reinforced with BFRP-bars, there is no yielding of the reinforcement, as the reinforcement material does not have a plastic deformation stage. This makes the order of chronological cracking stages in the load-deflection curve in subfigure 4.4b as follows:

1. Uncracked stage
2. Crack formation stage
3. Stabilized cracking stage
4. Concrete crushing

Therefore, the beams reinforced with BFRP-bars do not have a yielding stage. The concrete crushing in the compression zone follows directly after the stabilized cracking stage. Figure 4.4 presents the differences in

cracking stages between beams containing different reinforcement materials. Note that for the load-deflection curve of B-3r8-c31, the cycle of unloading and reloading has been removed in subfigure 4.4b.

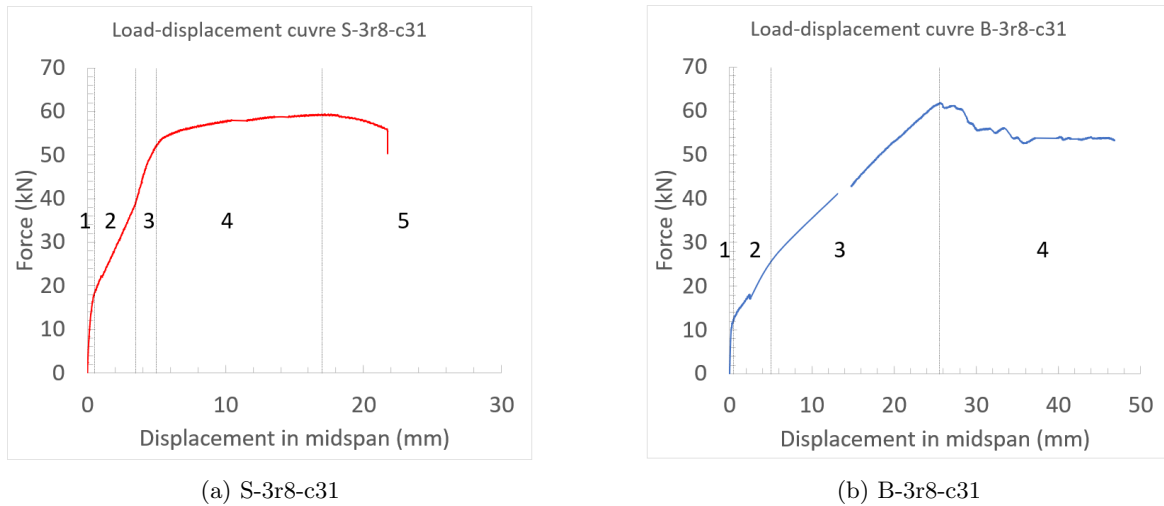


Figure 4.4: Cracking stages comparison

The load-deflection curves of the beam specimens where the reinforcement material is changed are compared to their respective counterparts. Overlays of the load-deflection curve of beams specimens B-3r8-c31 and S-3r8-c31 (subfigure 4.5a) as well as B-3r8-c11 and S-3r8-c11 (subfigure 4.5b).

A notable difference in the load-deflection curves is the larger vertical deflection starting from the end of the crack formation stage at the same load level. This significant increase in deflection might, at least to some extent, be attributed to the lower Young’s modulus compared to reinforcement steel. However, the concrete stiffening effect might contribute to this as well.

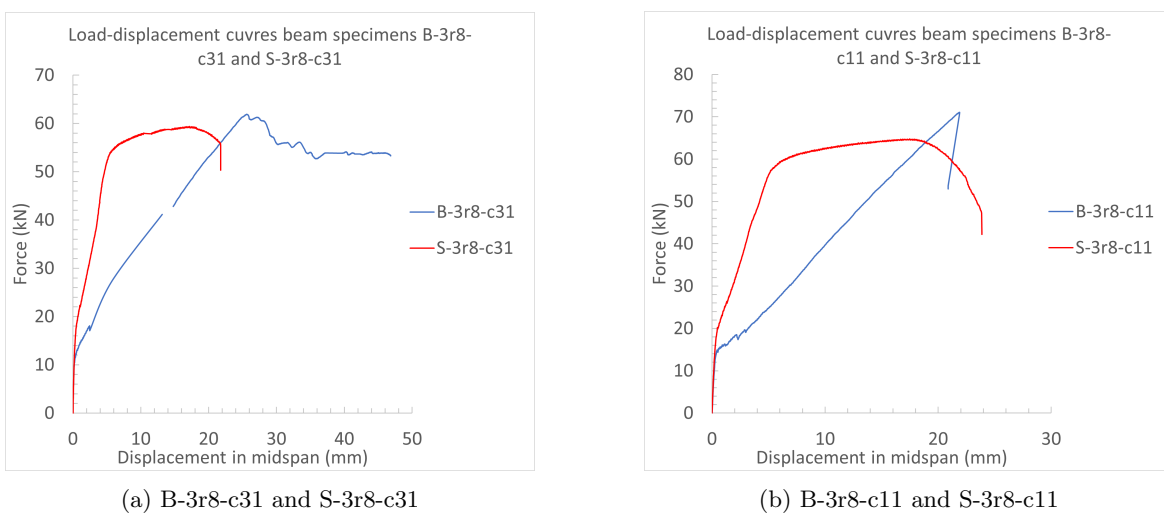


Figure 4.5: Load-deflection curves comparison

Due to the formation of secondary cracks, it is difficult to estimate the decrease in tension stiffening [Brown and Bartholomew, 1993]. The vertical deflection at the start of the concrete crushing in beam specimen B-3r8-c31 is approximately 25 mm, which is significantly more than its counterpart at approximately 17 mm.

4.2.3 Cracking patterns

At a load level of approximately 50 kN (figure 4.6), the crack patterns have established in the beams' constant bending moment zones. Cracks in the beams reinforced with BFRP-bars (subfigures 4.6a, 4.6b, 4.6c and 4.6d) have a significantly larger crack width than their steel reinforced counterparts (subfigures 4.6e and 4.6f). This might be caused by the lower Young's modulus of the BFRP. Furthermore, secondary cracks branching of the primary flexural cracks form for the beams with a concrete cover of 31 mm (subfigures 4.6a, 4.6b, 4.6c). The crack formation of beam B-3r8-c11 (subfigure 4.6d) does not show this behaviour.

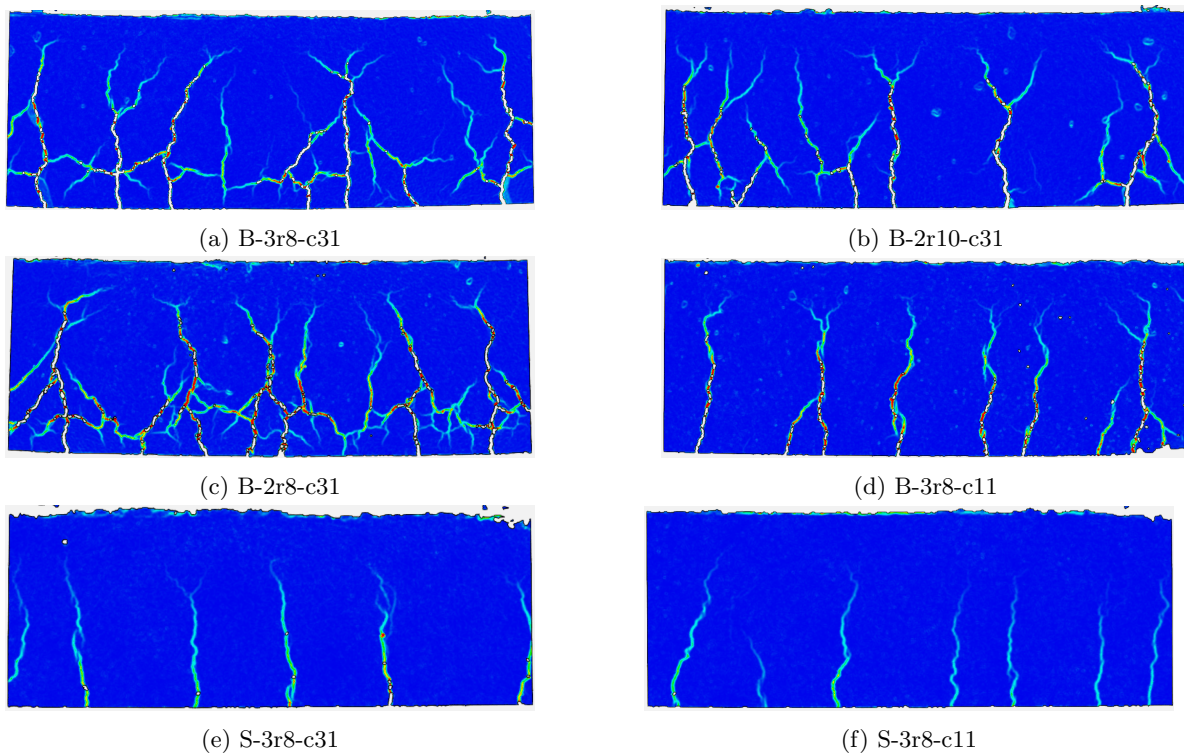


Figure 4.6: Contour plots crack pattern from DIC-data comparison at load level ≈ 50 kN

Another difference in crack formation is the emergence of tensile splitting cracks on the side surface of beams with a concrete cover of 31 mm, which does not emerge in beam B-3r8-c11. As the concrete cover of B-3r8-c11 is significantly smaller, tensile splitting cracks are more like to appear on the bottom surface. Tensile splitting cracks also do not appear in the crack width development of S-3r8-c31 and S-3r8-c11.

4.2.4 Emergence of tensile splitting cracks in beams reinforced with BFRP-bars

Tensile splitting cracks emerge when the bond stress of the reinforcement bar exceeds the tensile strength of the confining concrete [fib, 2007]. Insufficient development length is unlikely as well as the bars are not spliced within the constant bending moment zone. The bars are however spliced in the ends of the beam with $\varnothing 8$ steel reinforcement bars bending upwards (figure 3.5 in Chapter 3 Experimental Study) to provide anchorage to the BFRP-bar in the neutral zone of the concrete.

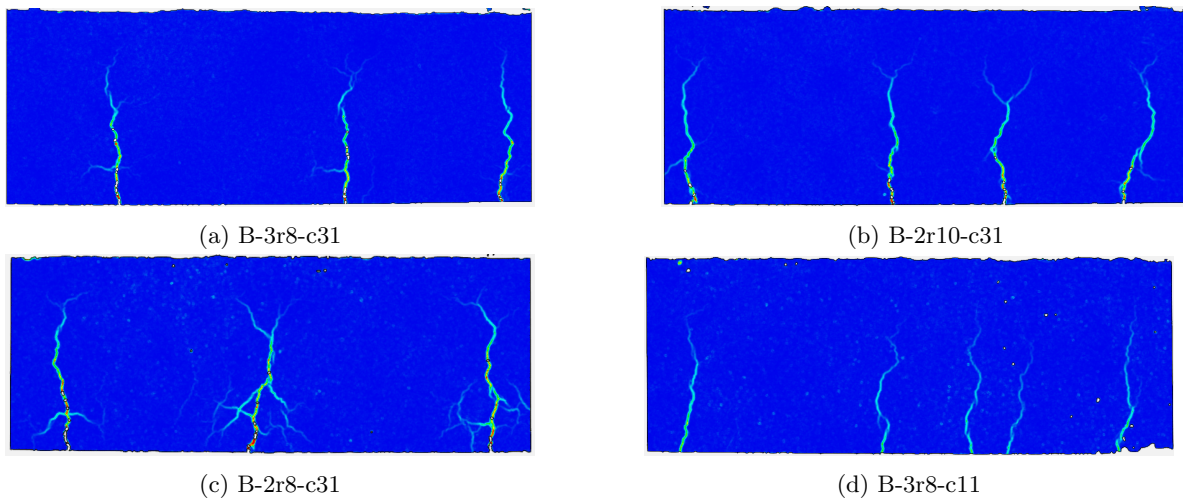


Figure 4.7: Contour plots cracking from DIC-data comparison at load level ≈ 17 kN

At early load stages, tensile splitting cracks emerge in 3 out of 4 beams reinforced with BFRP-bars. These cracks appear at the depth of the reinforcement in the cross-section. The 3 beam specimens where the tensile splitting crack emerges are the ones with a concrete cover of 31 mm. Beam specimen B-3r8-c11 does not show this cracking behaviour on the side of the beam. However, these cracks might have formed at the bottom surface of this beam.

The contour plots of the crack patterns at a load level of approximately 17 kN for the beam specimens reinforced with BFRP-bars are presented in figure 4.7. At this load level, the tensile splitting cracks are significantly visible in the contour plots for each beam type. Upon further inspection of the DIC-data, the tensile splitting cracks emerge at the load levels indicated in table 4.4. The corresponding vertical deflections at which these cracks occur are presented as well in table 4.4.

Table 4.4: Force, deflection and tensile stress emergence tensile splitting cracks

Beam specimen	Force	Vertical deflection
B-3r8-c31	15.16 kN	1.374 mm
B-2r10-c31	15.44 kN	1.405 mm
B-2r8-c31	13.18 kN	1.295 mm

The emergence of tensile splitting cracks in beam B-3r8-c11 cannot be determined since these cracks occurred on the bottom surface of the beam, which was not monitored with DIC-data.

The tensile stress in the reinforcement bars at which the tensile splitting cracks emerge can be determined using both a fully analytical approach and a hybrid approach using data from the experiment and an analytical model.

The fully analytical method is based on 2 equilibria of bending moments around a set point and horizontal forces. The point taken for the moment equilibrium is the top of the cross-section. These equilibria are presented in equations 4.1 and 4.2. The unknowns in the equations are the height of the concrete compression zone x and the compressive strain at the top of the cross-section ε_c . As the number of unknowns equals the number of equations, the system is solvable. A visualisation of the analytical approach is presented in figure 4.8. In this figure, the influence of the top reinforcement in the cross-section is outlined as well, however, this influence is neglected in the equilibrium formulation.

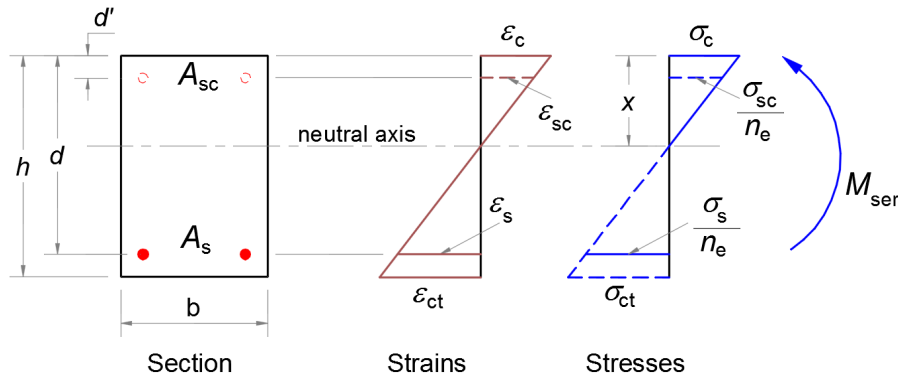


Figure 4.8: Stresses and strains in a rectangular cross-section [Usingeurocode, 2023]

$$\sum F_h = 0 \rightarrow \frac{d-x}{x}bx\varepsilon_c E_{cm} - \frac{1}{2}A_{bf}\varepsilon_c E_{bf} = 0 \quad (4.1)$$

$$\sum M = 0 \rightarrow M_{ser} + \frac{d-x}{x}bx\varepsilon_c E_{cm}d - \frac{1}{2}A_{bf}\varepsilon_c E_{bf}\frac{x}{3} = 0 \quad (4.2)$$

Having identified the values for x and ε_c , the next step involves determining the tensile strain in the reinforcement using equation 4.3. Subsequently, this tensile strain is utilized to calculate the corresponding stress in the reinforcement layer, as outlined in equation 4.4.

$$\varepsilon_{bf} = \frac{d-x}{x}\varepsilon_c \quad (4.3)$$

$$\sigma_{bf} = \varepsilon_{bf}E_{bf} \quad (4.4)$$

The fully analytical approach estimates the height of the concrete compression zone x based on equilibrium. However, this is a theoretical value which is possibly inaccurate. To verify the accuracy of the estimated concrete compression zone height, the data from the LVDT's can be utilized. By plotting the strain values based on the

LVDT's over the height of the depth of the cross-section (figure 4.9), the height of the concrete compression zone can be determined more accurately instead of an estimation.

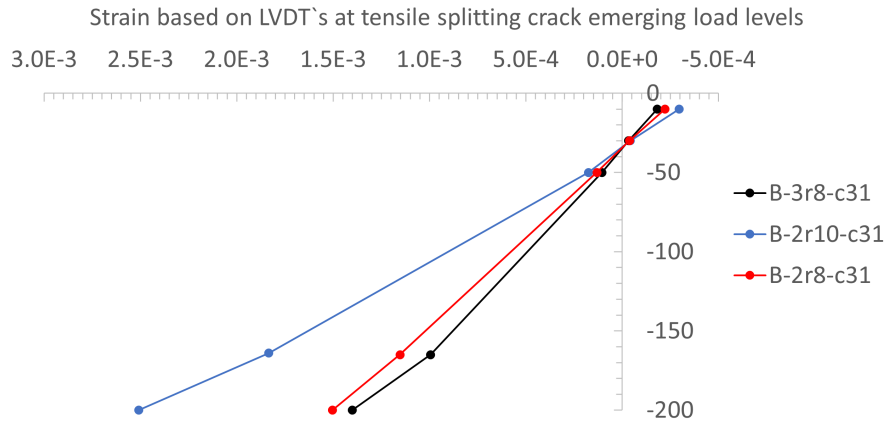


Figure 4.9: Strain in cross-section based on LVDT, tensile splitting crack emerging load levels

The intersection of the curves with the y-axis outlines the height of the concrete compression zone. This approach eliminates the unknown value for the concrete compression zone height x . Therefore, only 1 equation is required to solve for the concrete compressive strain at the top of the cross-section ε_c . The remaining equation to determine this unknown is the moment equilibrium (equation 4.2). Table 4.5 presents the values for the concrete zone height according to the analytical method and from the LVDT-data.

Table 4.5: Concrete compression zone height x analytical method and LVDT-data

Beam specimen	Analytical method	Based on LVDT-data
B-3r8-c31	20.743 mm	34.795 mm
B-2r10-c31	21.073 mm	33.886 mm
B-2r8-c31	16.709 mm	34.401 mm

Estimating the concrete compression zone height based on the analytical method considerably underestimates the value for x compared to the approach based on the LVDT-data. The tensile strains and stresses based on both approaches are presented in table 4.6.

Table 4.6: Stress and strain in tensile reinforcement, analytical method and experimental values

Beam specimen	Strain analytical	Stress analytical	Strain experimental	Stress experimental
B-3r8-c31	0.296%	158.99 MPa	0.363%	195.07 MPa
B-2r10-c31	0.291%	156.54 MPa	0.346%	186.28 MPa
B-2r8-c31	0.382%	205.58 MPa	0.555%	298.48 MPa

Fib bulletin 40 [fib, 2007] provides a predictive model by Tepfers about the tensile splitting resistance of concrete reinforced with FRP-bars. The equations used to describe the predictive model depend on the tensile strength of the concrete f_{ct} , the bar diameter denoted as d , the concrete cover to either the side surface or the bottom surface of the beam c_y or c_x (whichever one is decisive), and an angle α which describes the angle under which the bond stress is distributed to the surrounding concrete (figure 4.10). Fib bulletin 40 [fib, 2007] mentions an angle of 45° to be assumed for sand-coated GFRP-bars, which is assumed for this analysis. Equation 4.5 is used for the tensile splitting resistance in the elastic stage of the concrete. At this stage, the concrete has not shown cracking due to bond stress in the surrounding concrete.

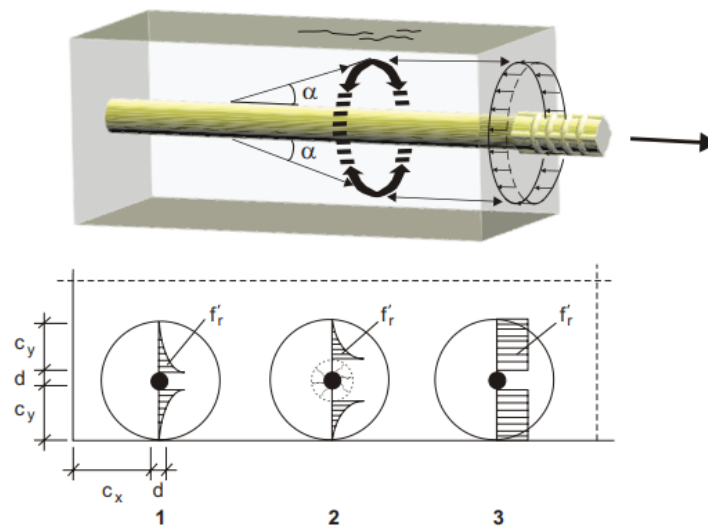


Figure 4.10: Tensile stress distribution in 1 elastic, 2 partly cracked elastic and 3 plastic stages

Equation 4.6 describes the partly cracked elastic stage, in which the concrete directly surrounding the bar starts to show cracking. Equation 4.7 presents the plastic stage in which cracks have surfaced. Figure 4.10 presents the stress distributions of each stage.

$$\tau = \frac{1}{\tan(\alpha)} \frac{(c_y + \frac{d}{2})^2 - (\frac{d}{2})^2}{(c_y + \frac{d}{2})^2 + (\frac{d}{2})^2} f_{ct} \quad (4.5)$$

$$\tau = \frac{c_y + \frac{d}{2}}{1.664d \tan(\alpha)} f_{ct} \quad (4.6)$$

$$\tau = \frac{2c_y}{d \tan(\alpha)} f_{ct} \quad (4.7)$$

Based on equations 4.5 to 4.7, the tensile splitting resistances of each stage are presented in figure 4.11 and table 4.7. Note that for all beams, the concrete cover to the side surface c_x is equal to 31 mm.

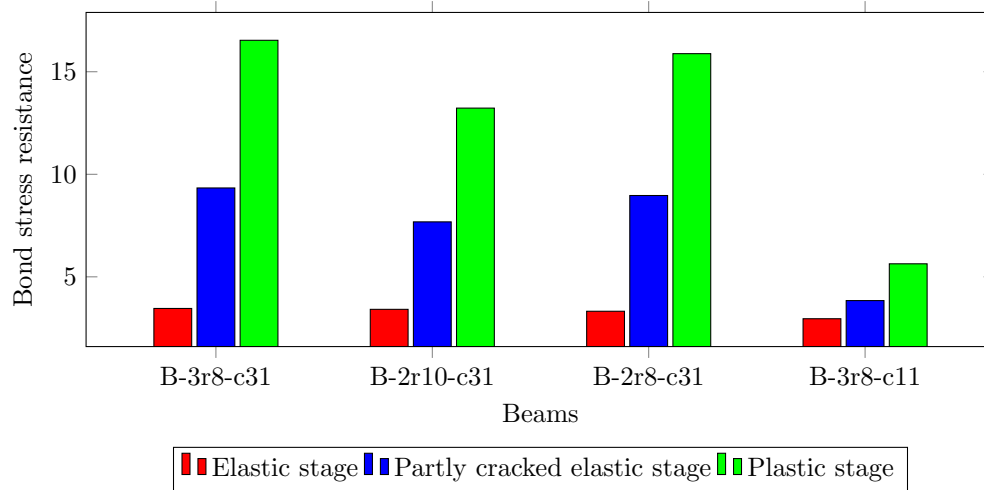


Figure 4.11: Bond stress resistance tensile splitting for each stage

Table 4.7: Bond stress resistance tensile splitting for each stage

Beam	Elastic stage τ_{el}	Partly cracked elastic stage τ_{pc}	Plastic stage τ_{pl}
B-3r8-c31	3.458 MPa	9.334 MPa	16.534 MPa
B-2r10-c31	3.416 MPa	7.680 MPa	13.227 MPa
B-2r8-c31	3.322 MPa	8.966 MPa	15.881 MPa
B-3r8-c11	2.957 MPa	3.842 MPa	5.636 MPa

According to the predictive model, a bar larger diameter results in a slightly smaller resistance to tensile splitting. The resistance to tensile splitting should approximately be the same for beams B-3r8-c31 and B-2r8-c31. However, as the concrete constitutes different batches, the tensile strength f_{ct} differs slightly, which is the only differing parameter. As beam B-2r8-c31 contains a smaller reinforcement ratio, the bond stress at which cracking starts is reached earlier. The most prominent influence on the predictive model is the concrete cover c_y or c_x , as the bond stress resistance to tensile splitting is considerably smaller for beam B-3r8-c11 compared to the other beams.

Based on the number of cracks and the average crack spacing s_{ave} from the DIC-data and the tensile stress in the reinforcement bars, the bond stress can be determined. Equation 4.8 is used to determine the bond stress.

$$\tau = \frac{\sigma_{bf} A_{bf}}{nd\pi s_{ave}} \quad (4.8)$$

Where parameter n is the number of bars, d is the bar diameter, σ_{bf} is the tensile stress in the reinforcement and A_{bf} is the reinforcement area in the cross-section. According to equation 4.8, the bond stress at the load level of the emerging tensile splitting crack is outlined in table 4.8.

Table 4.8: Bond stress τ_{bf} at tensile splitting crack emerging load level

Beam	Bond stress
B-3r8-c31	5.468 MPa
B-2r10-c31	6.520 MPa
B-2r8-c31	8.357 MPa

For beams B-3r8-c31, B-2r10-c31 and B-2r8-c31 applies $\tau_{el} < \tau_{bf} < \tau_{pc}$ at the load level on which the tensile splitting cracks start to emerge at the surface. As the bond stress exceeds the elastic bond stress resistance, tensile splitting cracks are expected to appear according to the predictive model.

Given the relatively low tensile splitting resistance of beam B-3r8-c11, the possibility exists that theoretically, tensile splitting cracks should appear in an earlier loading stage than the flexural cracking. Based on the load level of the crack (13.00 kN for B-3r8-c11), the concrete compression zone height can be determined from the LVDT-data. Right after cracking, the concrete compression zone height is equal to 88.66 mm. Using equation 4.2, the tensile stress σ_{bf} in the reinforcement is equal to 30.051 MPa based on equation 4.8. This equates to a bond stress τ_{bf} of 0.962 MPa, which is below the elastic stage bond stress resistance τ_{el} . Therefore, tensile splitting cracks are unlikely to emerge before flexural cracks. Due to the small concrete cover to the bottom surface c_y , tensile splitting cracks are likely to emerge at the bottom. Using the predictive models, the tensile splitting resistance to the side surface of the beam is similar to that of B-2r8-c31, as the cover to the side surface c_x is equal to the other beams. The concrete of these beams belongs to the same concrete batch (batch 3).

After emerging, the tensile splitting cracks propagate further over the length of the beams. Figures 4.12 to 4.14 present crack pattern development comparisons of the beams reinforced with BFRP-bars at different load levels. Note that for comparison containing beam B-3r8-c31, contour plots for load levels 30 kN and 40 kN are absent as no valid DIC-data was captured for this load level.

Figure 4.12 outlines a comparison between B-3r8-2r10. For this beam, the reinforcement ratio is similar, however the applied bar diameter differs. Based on the results captured in figure 4.11, beam B-2r10-c31 should have more propagation over the length of the beam. However, the length of the developed tensile splitting cracks stays limited on higher load levels. Considering the smaller total circumference of 2 bars with a diameter of 10 mm in comparison to 3 bars with a diameter of 8 mm, the bond stress should be higher. Based on the DIC-data, this is contrary to the predictive model presented by Burgoyne [fib, 2007].

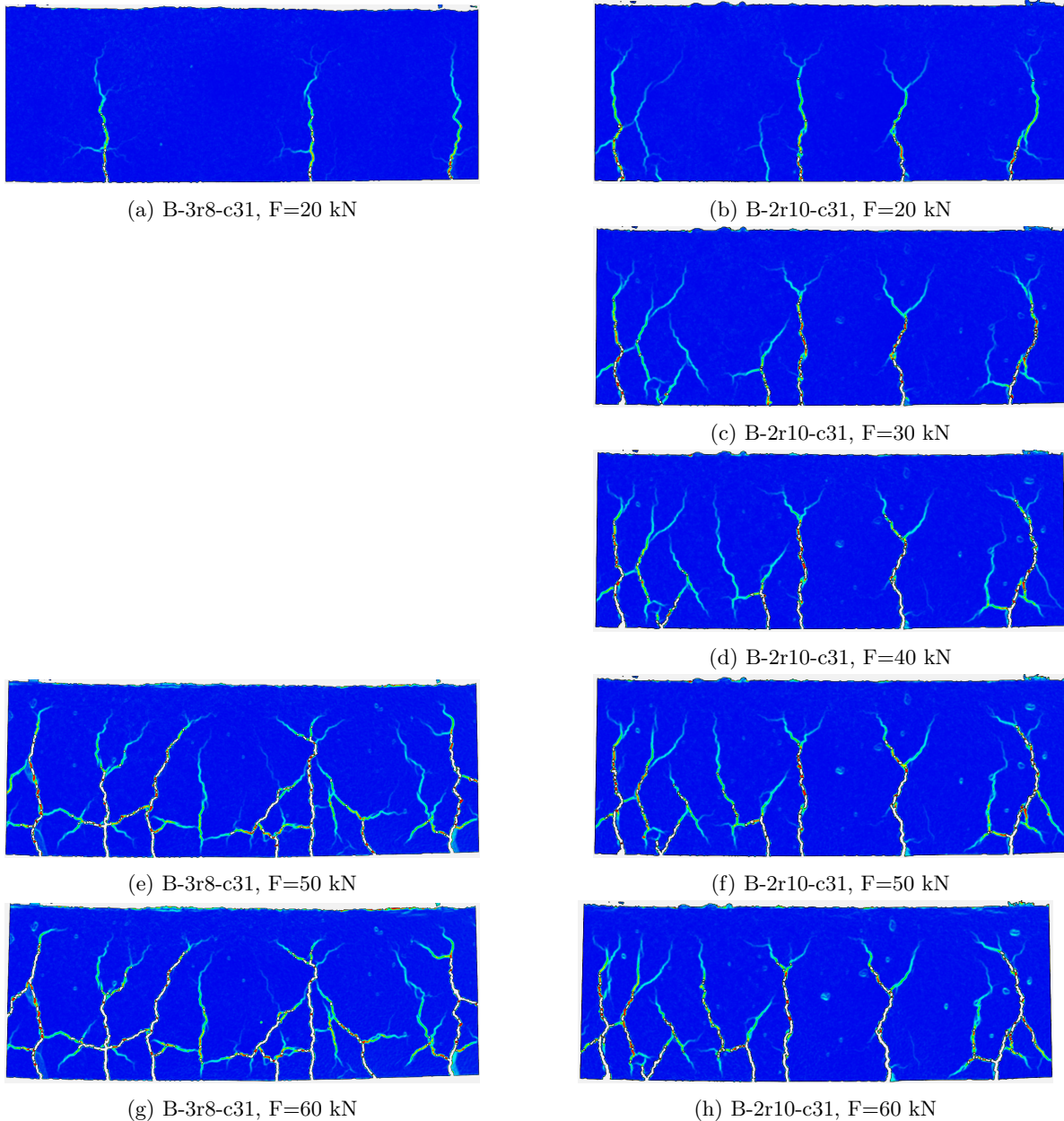


Figure 4.12: Crack width propagation comparison B-3r8-c31 and B-2r10-c31

A comparison between B-3r8-c31 and B-2r8-c31 in figure 4.13 illustrates the difference in reinforcement ratio while maintaining the same bar diameter. The higher tensile stress in B-2r8-c31, due to its smaller reinforcement ratio, leads to increased bond stress between the reinforcement bar and surrounding concrete. This elevated bond stress suggests that tensile splitting cracks may propagate further. As seen in figure 4.13, these cracks have fully propagated along the constant bending moment zone, forming a long single crack, which is less evident in B-3r8-c31. The results are consistent with the predictive model, anticipating further propagation in B-2r8-c31.

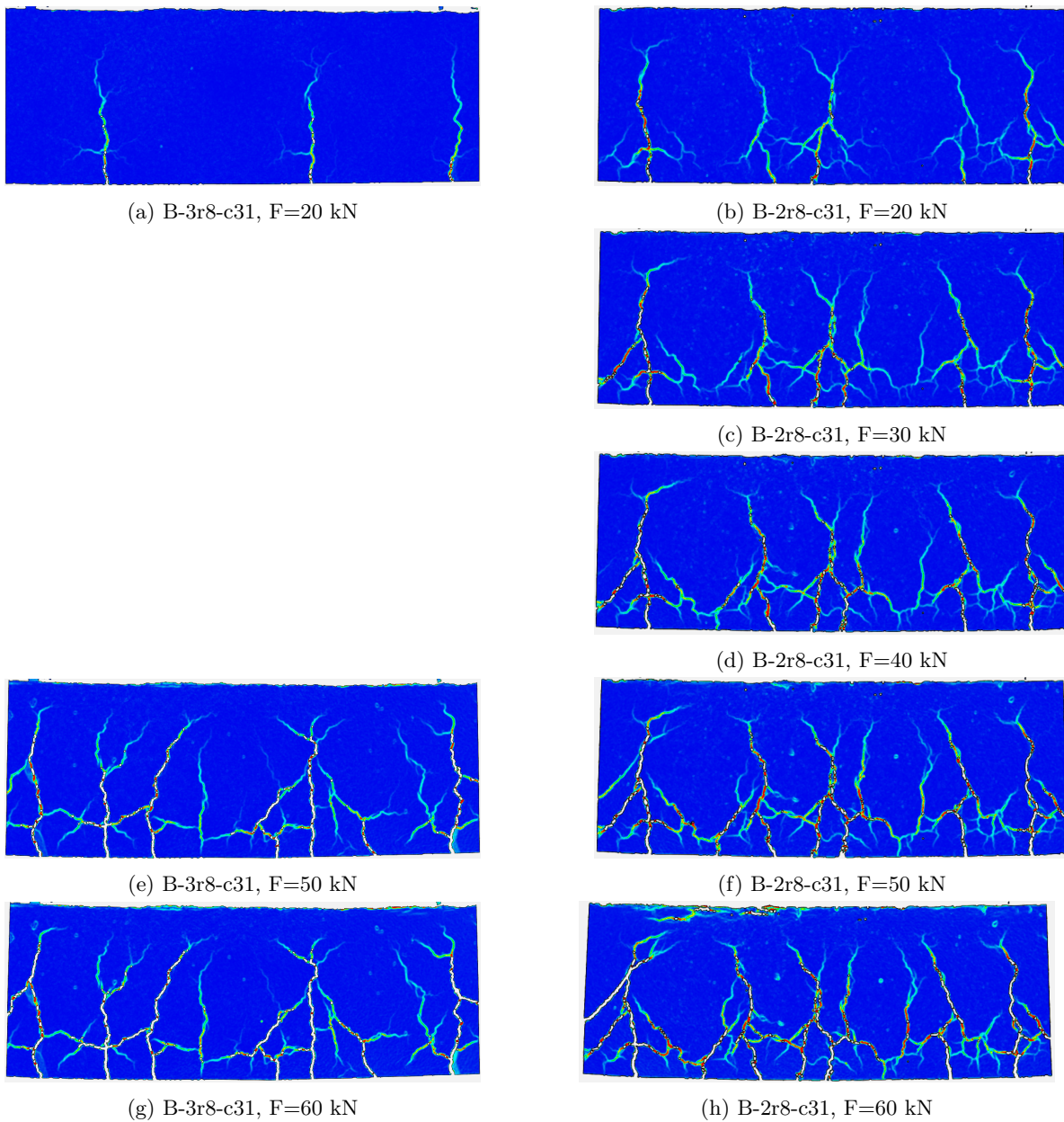


Figure 4.13: Crack width propagation comparison B-3r8-c31 and B-2r8-c31

Figure 4.14 presents a comparison between B-3r8-c31 and B-3r8-c11, outlining the effects of a smaller concrete cover. Based on the DIC-data, the contour plots show little to no tensile splitting crack to the side surface of beam B-3r8-c11. At higher load levels, limited tensile splitting cracks start to emerge. Based on the predictive model, this is expected to happen, as the tensile splitting resistance of the bottom surface is considerably smaller.

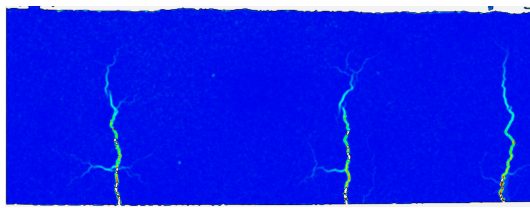
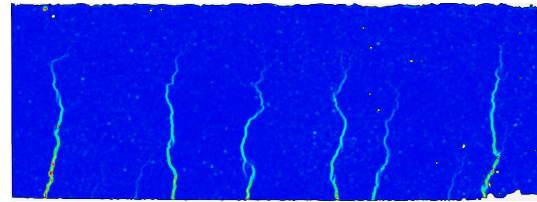
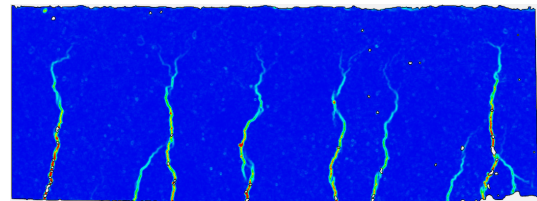
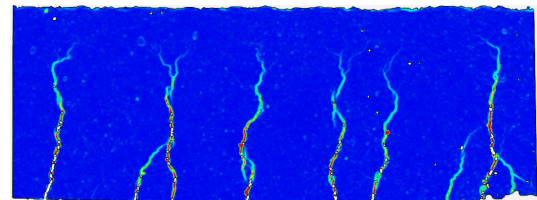
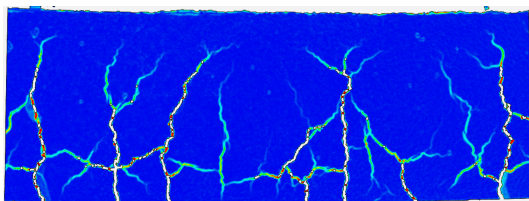
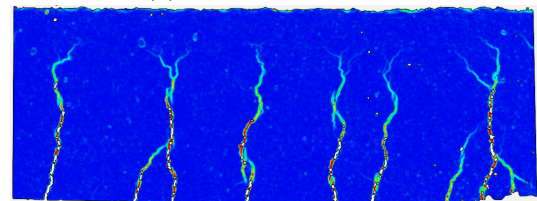
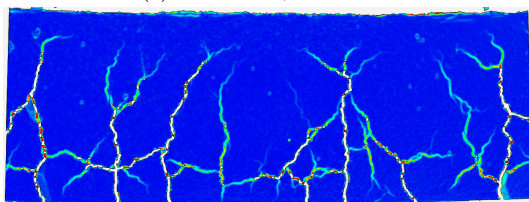
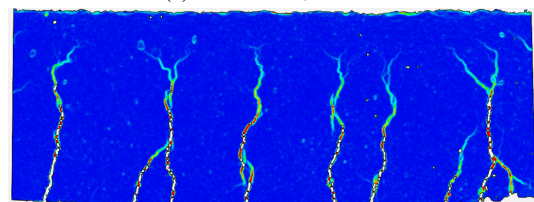
(a) B-3r8-c31, $F=20$ kN(b) B-3r8-c11, $F=20$ kN(c) B-3r8-c11, $F=30$ kN(d) B-3r8-c11, $F=40$ kN(e) B-3r8-c31, $F=50$ kN(f) B-3r8-c11, $F=50$ kN(g) B-3r8-c31, $F=60$ kN(h) B-3r8-c11, $F=60$ kN

Figure 4.14: Crack width propagation comparison B-3r8-c31 and B-3r8-c11

At a load level of approximately 50 kN, the tensile splitting cracks have propagated on the side surface of the beam specimen with cover 31 mm (subfigures 4.15a, 4.15b, 4.15c respectively). Beam specimen B-3r8-c11 (subfigure 4.15d) however has not developed these types of cracks on the side surface of the beam. The propagation of the tensile splitting cracks is relatively minimal in beam B-2r10-c31 (subfigure 4.15b) compared to beams B-3r8-c31 and B-2r8-c31. This may be caused by the required transfer length of the different bar diameters. The tensile splitting cracks in beams B-3r8-c31 (subfigure 4.15a) and B-2r8-c31 (subfigure 4.15c) form an almost continuous crack over the length of the constant bending moment zone.

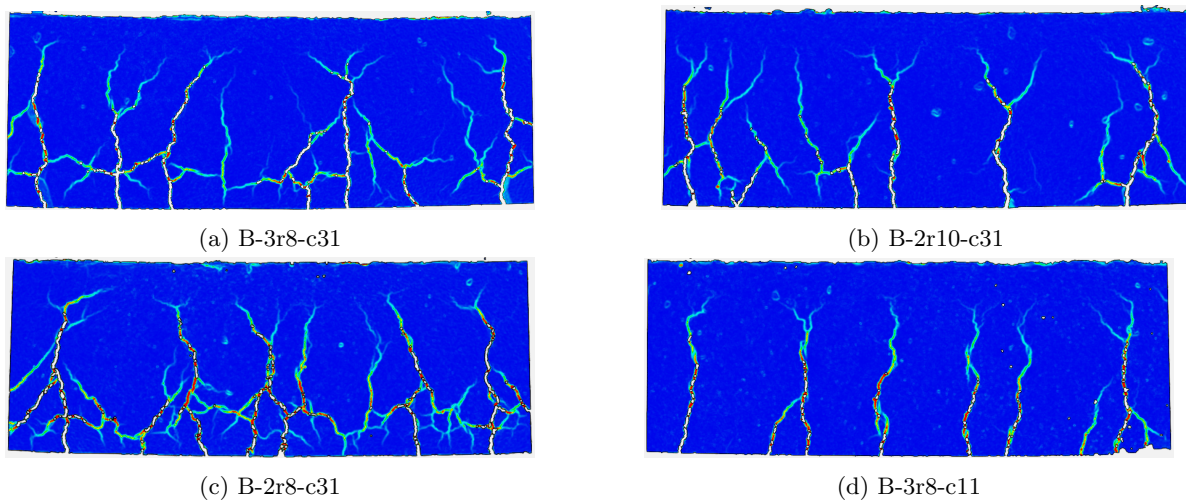


Figure 4.15: Contour plots cracking from DIC-data comparison at load level $F=50$ kN

Upon inspection after the failure of the beam, it became apparent tensile splitting cracks did occur in beam B-3r8-c11. However, the cracking occurred mostly on the bottom side of the beam (figure 4.17). Note that corner-splitting cracks (highlighted in blue) and v-notch-splitting cracks (red) appear on the beam. Figure 4.16 presents the principles of these types of tensile splitting cracks in a cross-section [fib, 2007]. Note that the cracking occurred specifically on one side of the bottom surface. These tensile splitting cracks are located at the bar that failed in tension. After the beam failed, the concrete cover of beam B-3r8-c11 at the cracking was removed to see the failed bar (figure 4.18).

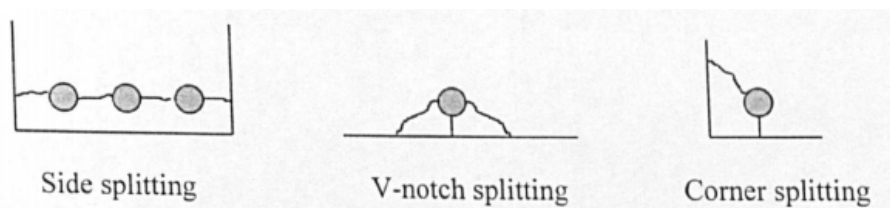


Figure 4.16: tensile splitting crack variations [Nagatomo et al., 1992]



Figure 4.17: Tensile splitting cracks bottom side B-3r8-c11

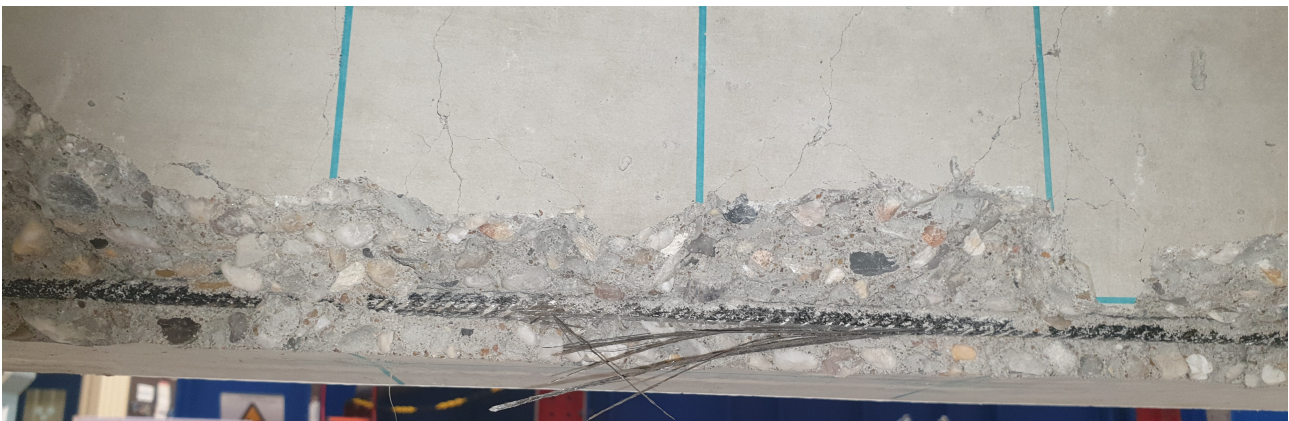


Figure 4.18: Failed bar B-3r8-c11

4.2.5 Maximum crack width

As the studied literature suggested, the crack width development in beams reinforced with BFRP-bars is generally larger compared to beams reinforced with reinforcement steel. The maximum crack width measured from DIC-data is projected in figure 4.19. Generally speaking, the maximum crack width of the beams reinforced with BFRP-bars does indeed exceed its steel-reinforced counterparts. The dots projected in figure 4.19 present the crack width measurements from the DIC-data. Beam specimens S-3r8-c31 and S-3r8-c11 initially develop smaller crack widths. The crack width development in the beams reinforced with reinforcement steel increases significantly when the yielding stage is reached. As the reinforcement steel reaches the plastic stage, it experiences increased strain, leading to more significant deformations. This is noticeable in figure 4.19 with increased slopes of the curves of beams S-3r8-c31 and S-3r8-c11. These kinks coincide with the stiffness drops noticeable in the load-deflection curves of the beams.

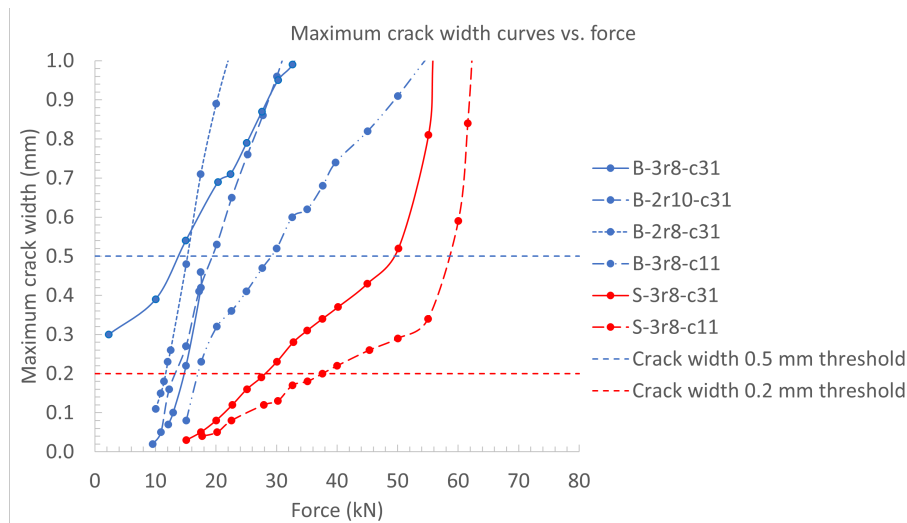


Figure 4.19: Maximum crack width vs. force curves of all tested beam specimen

The crack width limits shown in Figure 4.19 demonstrate the strictest crack width limits as per Eurocode 2 (0.2 mm) for concrete structures reinforced with steel bars. Additionally, the most strict crack width limits (0.5 mm) outlined by BRL0513 and ACI440 for concrete structures reinforced with BFRP bars are presented. Upon comparing the maximum crack width curves in relation to the crack width limits, the beams containing BFRP-bars reach the 0.5 mm limit at an earlier load level compared to the beams with reinforcement steel.

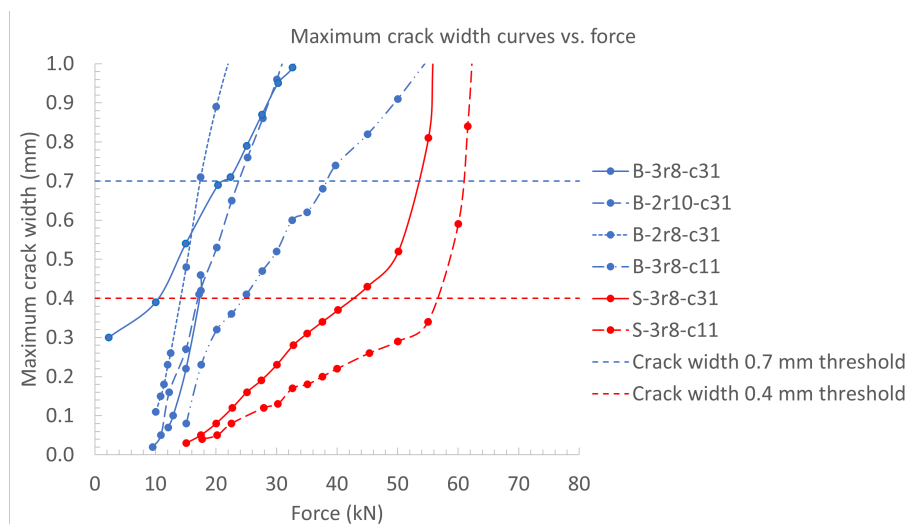


Figure 4.20: Maximum crack width vs. force curves of all tested beam specimen

If the least strict crack width limit is allowed according to Eurocode 2 (0.4 mm) for reinforcement steel and BRL0513 and ACI440 (0.7 mm) for BFRP-bars, the difference in load level becomes more apparent. The crack width curves of S-3r8-c31 and S-3r8-c11 and the crack width limits intersect at an even higher load level relative to the beams containing BFRP-bars. The load levels at which the crack width limits are presented in figures

4.19 and 4.20 are presented in table 4.9.

Table 4.9: Load level crack width limits according to ACI440, BRL0513 and Eurocode 2

Beam	Lower limits		Upper limits	
	0.2mm (EC2)	0.5mm (BRL0513/ACI440)	0.4mm (EC2)	0.7mm (BRL0513/ACI440)
B-3r8-c31		14.11 kN		21.90 kN
B-2r10-c31		19.16 kN		24.53 kN
B-2r8-c31		15.37 kN		17.41 kN
B-3r8-c11		29.08 kN		38.21 kN
S-3r8-c31	28.04 kN		42.49 kN	
S-3r8-c11	37.57 kN		57.34 kN	

By comparing beam specimens B-3r8-c31 and B-2r10-c31, approximately the same amount of reinforcement in the cross-section is utilized, however, the number of bars is different (figure 4.21). Until the crack width limits are reached, the crack width development is mostly the same and differences are barely noticeable. However, after these limits are exceeded, the crack width development in beam specimen B-3r8-c31 slows down whereas the development of beam B-2r10-c31 stays continuous. This might be due to tensile splitting crack propagation and the type of tensile splitting cracks, which is relatively smaller in beam B-2r10-c31 compared to beam B-3r8-c31.

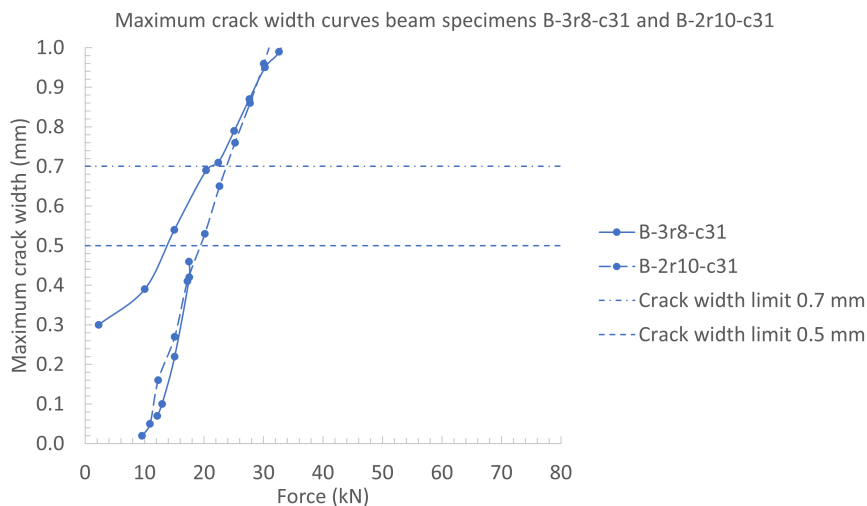


Figure 4.21: Maximum crack width vs. force curves B-3r8-c31 and B-2r10-c31

By comparing beam specimens B-3r8-c31 and B-2r8-c31, the differing parameter in the beams is the reinforcement ratio. Based on the force-maximum crack width curves presented in figure 4.22, the crack width limit of B-2r8-c31 is reached at a load level of 17.41 kN. The curves of B-3r8-c31 intersect the 0.7 mm crack width limit at 21.90 kN. Based on the loading history of B-3r8-c31, a comparison at a crack width limit of 0.5 mm is not fair. Under normal loading circumstances, the curve of B-2r8-c31 is likely to reach the 0.5 mm crack width at an earlier load level than B-3r8-c31.

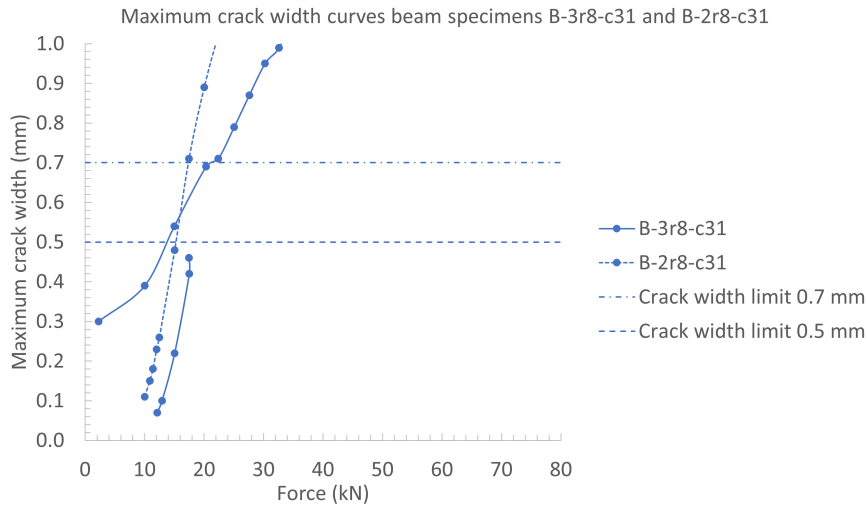


Figure 4.22: Maximum crack width vs. force curves B-3r8-c31 and B-2r8-c31

Within the model of the BRL0513 and ACI440 codes, the concrete cover plays a significant role in the crack width control. By comparing B-3r8-c31 and B-3r8-c11, the same reinforcement configuration is utilized in the cross-section, however the cover differs by 20 mm. The effects of the difference in concrete cover are presented in figure 4.23.

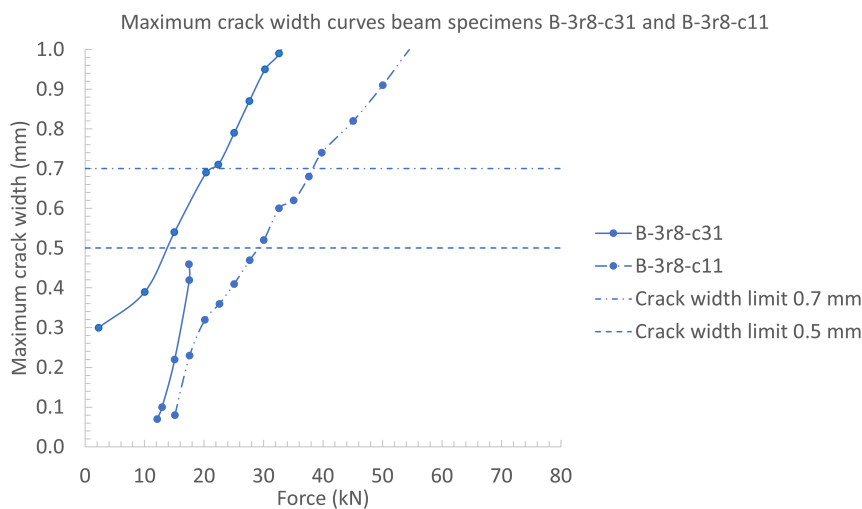


Figure 4.23: Maximum crack width vs. force curves B-3r8-c31 and B-3r8-c11

Figures 4.24 and 4.25 present comparisons between beams where the reinforcement materials differ. As the crack width development of the beams with a concrete cover of 11 mm is slower (figure 4.25), the differences in load level to reach the crack width limits are significantly more favourable for the beam reinforced with reinforcement steel bars. It's important to note that the bottom side of the beam was not monitored, hence the crack and pattern on the bottom were not checked, potentially influencing the overall assessment.

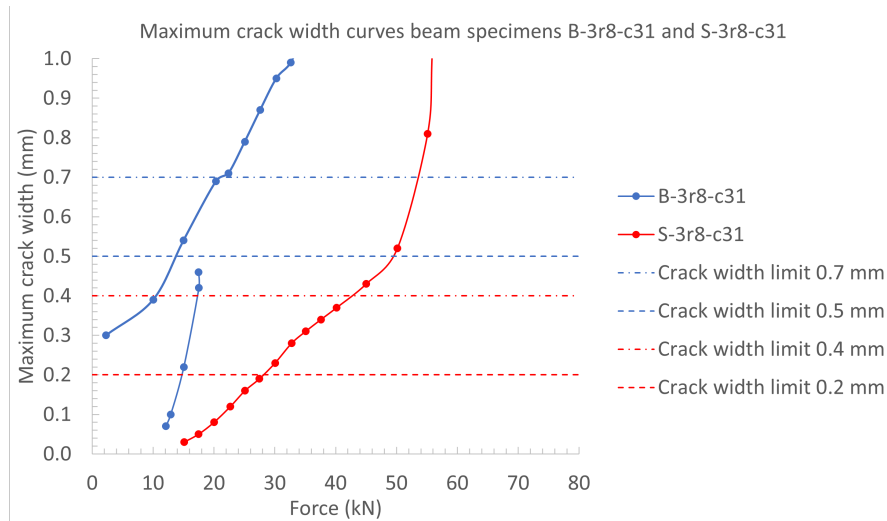


Figure 4.24: Maximum crack width vs. force curves B-3r8-c31 and S-3r8-c31

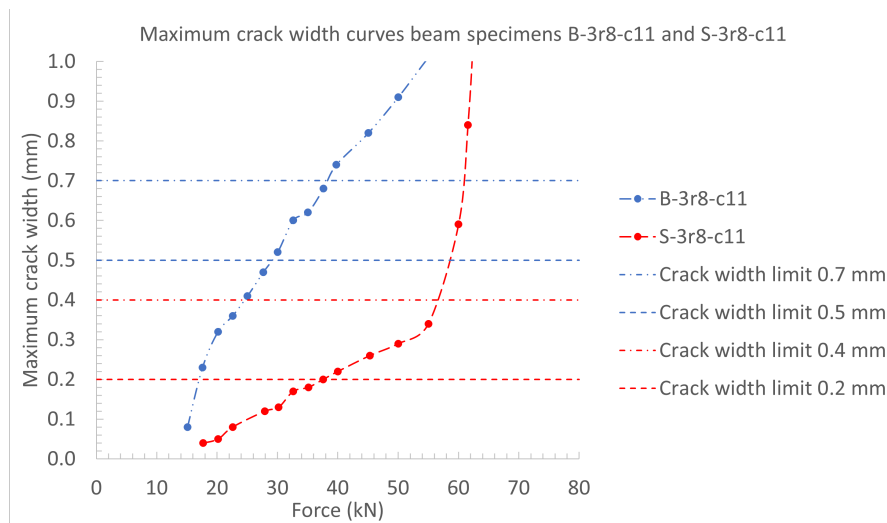
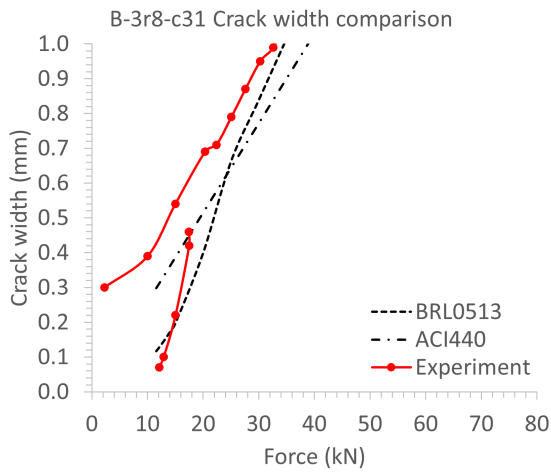
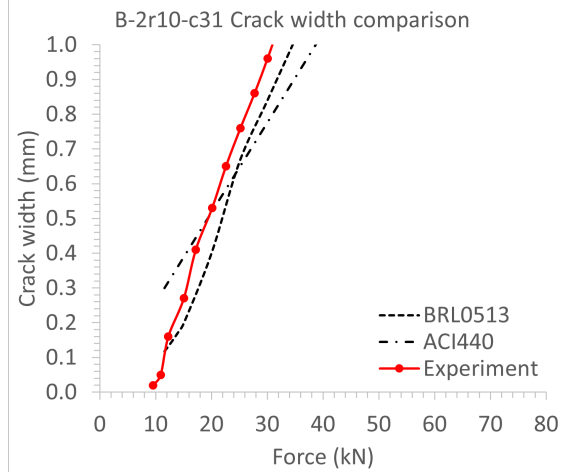


Figure 4.25: Maximum crack width vs. force curves B-3r8-c11 and S-3r8-c11

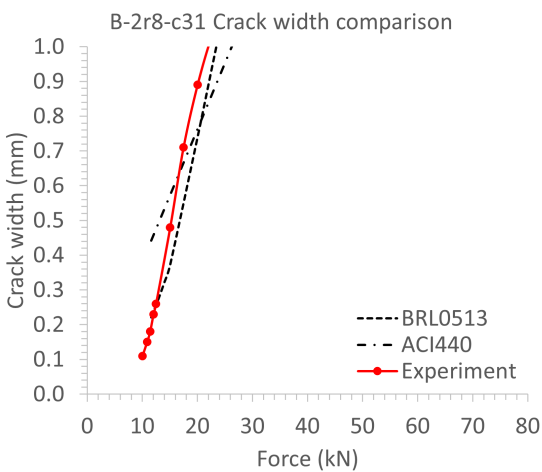
A comparison to the theoretical models is presented in figure 4.26 to put the crack width curves into perspective. As the models in codes are conservative estimations, the measured crack widths from the experiment should be consistent with the theoretical curves. The crack width development curves of the experiment of the beams reinforced with BFRP-bars (subfigures 4.26a tot 4.26d) show superior crack width development in relation to the theoretical curves, whereas the beams reinforced with reinforcement steel (subfigures 4.26e and 4.26f) are consistent with their respective theoretical curves.



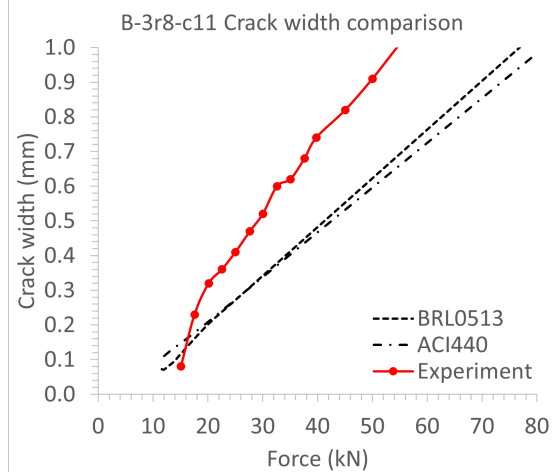
(a) B-3r8-c31



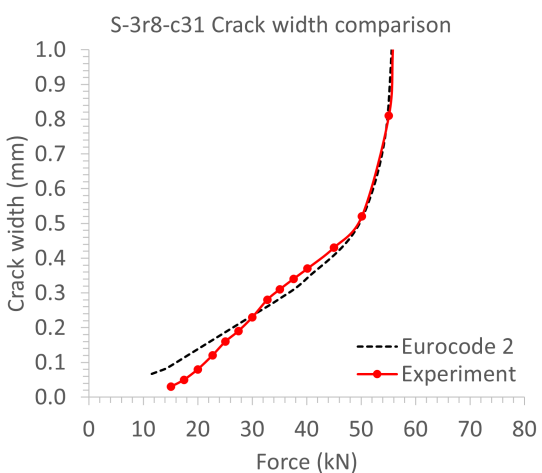
(b) B-3r8-c31



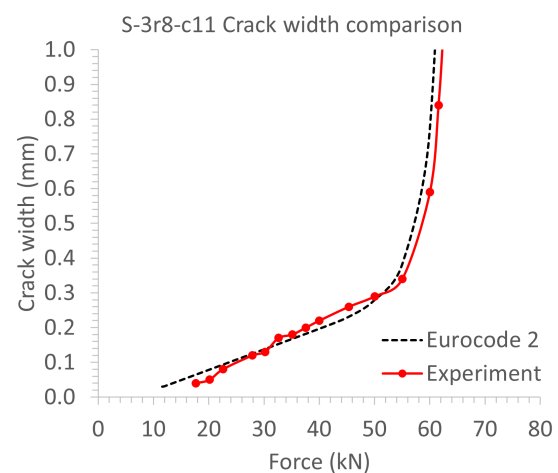
(c) B-3r8-c31



(d) B-2r10-c31



(e) B-2r8-c31



(f) B-3r8-c11

Figure 4.26: Crack width comparison experimental versus codes

The beams reinforced with BFRP-bars have in common that the first few crack width measurements do not exceed their respective theoretical curve's values. However, after the first tensile splitting cracks appear, the crack width development oversteps the theoretical curves. Based on the principles of Harajli (figure 2.24), the appearance of tensile splitting cracks leads to a decrease in bond strength and therefore an increase in crack spacing due to a larger required transfer length. This causes the crack width, at least to some extent, to develop more quickly.

Beam B-3r8-c11 (4.26d) shows the largest disproportion compared to its theoretical curves according to BRL0513 and ACI440 respectively. As this beam type has the smallest concrete cover, it is most prone to tensile splitting cracks emergence, according to Tepfers' model (figure 4.11 and table 4.7). The tensile splitting cracks should develop the most for this beam, amplifying the decrease in bond strength of the reinforcement bar to the concrete.

Note that, contrary to figure 3.13, the material properties of the concrete and the reinforcement material tested before the experiments are used for the construction of the theoretical crack width development curves (figure 4.26) according to BRL0513, ACI440 and Eurocode 2 respectively.

4.2.6 Conclusion

The beams reinforced with basalt fibre reinforcement bars show significantly more vertical deflection after the first cracks start to appear. This is caused by the difference in Young's modulus of the reinforcement material. As the BFRP-bars do not display plastic deformation, the vertical deflection has a linear character up to the moment of failure, as outlined by Shamass & Cashell [Shamass and Cashell, 2020] and Pawlowski and Szumigala [Pawlowski and Szumigala, 2015]. This is contrary to the behaviour of steel-reinforced beams, which do show an abrupt decrease in stiffness as the reinforcement steel starts to yield.

The cracking patterns recorded with DIC-data show significant differences in cracking patterns. The beams reinforced with BFRP-bars show tensile splitting cracks emerging in an early stage of loading, whereas these cracks are absent in the steel-reinforced beams. Upon emerging and propagation of tensile splitting cracks, debonding of the concrete cover seems to appear. Based on the principles of Harajli [Harajli et al., 2004] and Tepfers [fib, 2000], the emergence of tensile splitting cracks causes the bond strength development to decrease.

The number of flexural cracks appearing in the constant bending moment zone however does not seem to differ significantly between the beams. Although studies report higher bond strength for sand-coated BFRP-bars, the number of cracks over the constant bending moment zone does not significantly differ in comparison to beams reinforced with steel bars. As the crack spacing, and therefore the number of cracks, is related to the bond strength of the reinforcement, the absence of more flexural cracks might be attributed to the tensile splitting.

Based on the predictive model by Tepfers presented in fib bulletin 40 [fib, 2007], a larger bar diameter should result in a lower tensile splitting resistance. However, the propagation of the tensile splitting crack in beam B-2r10-c31 suggests otherwise in comparison to B-3r8-c31.

The reinforcement ratio does not directly influence the tensile splitting resistance, as it is based on the geometry and the tensile strength of the concrete. A lower reinforcement ratio however results in more tensile stress, causing the tensile splitting cracks to propagate quicker through the loading cycle. Therefore, the propagation of the tensile splitting cracks in beam B-2r8-c31 exceeds that of B-3r8-c31 significantly.

The influence of the concrete cover on the predictive model is severe as the tensile splitting strength of B-3r8-c11 is considerably lower compared to the beams with a concrete cover of 31 mm. Therefore, beam B-3r8-c11 was more prone to tensile splitting cracking to the bottom surface than to the sides, as the side surface maintains a cover of 31 mm. At higher load levels, tensile splitting cracks emerge in a limited capacity to the side of the beam.

Larger crack widths are recorded for the beams reinforced with BFRP-bars, caused by the lower Young's modulus of BFRP-bars. As the cracks propagate to larger widths in the beams reinforced with BFRP-bars, the stiffness decreases faster, causing larger vertical deflections.

Based on a comparison of the most strict crack width limits (e.g. 0.2 for steel bars, 0.5 for BFRP-bars), the beams containing BFRP-bars reach the crack width limit at an earlier load level. When comparing the curves to the least strict limits based on the researched codes (e.g. 0.4 for steel bars, 0.7 for BFRP-bars), the difference becomes even larger. The difference in crack width development becomes smaller as the reinforcement steel enters the plastic deformation stage, causing the crack width to develop rapidly.

Whereas the bar diameter does not influence to a large extent as the reinforcement area in the cross-section is approximately equal, the reinforcement ratio displays its effect as the maximum crack width curve of B-2r8-c31 shows a steeper slope compared to the other beams containing BFRP-bars. The concrete cover of B-3r8-c31 illustrates a significant influence on crack width control. Compared to B-3r8-c31, the curve of B-3r8-c11 shows a more gentle slope, indicating a slower crack width development, which is expected according to the crack width models presented in the ACI440 and BRL0513.

Upon comparison with the theoretical models for crack width calculation in the codes BRL0513, ACI440 and Eurocode 2, it shows the influence of the tensile splitting crack emergence, at least to some extent, is noticeable. This is likely caused by the decrease in bond strength following tensile splitting crack formation, therefore increasing the required transfer length of the reinforcement bar to the concrete. Therefore, less flexural cracks can form over the length of the bending moment zone of the beam, causing the existing cracks to develop larger widths.

Chapter 5

Discussion

In preparation of the concrete batches for the experimental study, concrete batch 1 used an insufficient volume of water in the mixture. This caused the concrete to be more porous. During the determination of the mechanical properties of this concrete batch, the cubes subjected to compression tests failed at an earlier load stage than concrete batches 2 and 3, likely due to the porosity and incomplete hydration due to insufficient water content in the mixture. The measured value of the Young's modulus is higher, indicating a higher concrete compressive strength of this batch. In addition to this, if less water is used, the proportion of the other components in the mixture becomes relatively larger. As aggregates are considerably stiffer than cement paste, proportion-wise, a higher Young's modulus is expected compared to mixtures containing more water.

As the concrete beam with a concrete cover of 11 mm to the bottom surface of the beam, in further research pertaining to cracking behaviour, DIC-data collection from the bottom surface of the beams could provide insights into tensile splitting crack development. The development of cracks emerging in this surface was not monitored in this experimental study, causing the cracks to be noticed after the failure of the beam.

To validate the results of the 4-point bending tests, a comparison of the results of beams with the same design and concrete mix is performed. The results of beams S-3r8-c31 are compared with the results of the same design from the experimental study conducted by Singh in 2019 and Zhekan in 2017. Figure 5.1 compares the results of beam S-3r8-c31 and data provided by the thesis from Singh in 2019 and Zhekan in 2017.

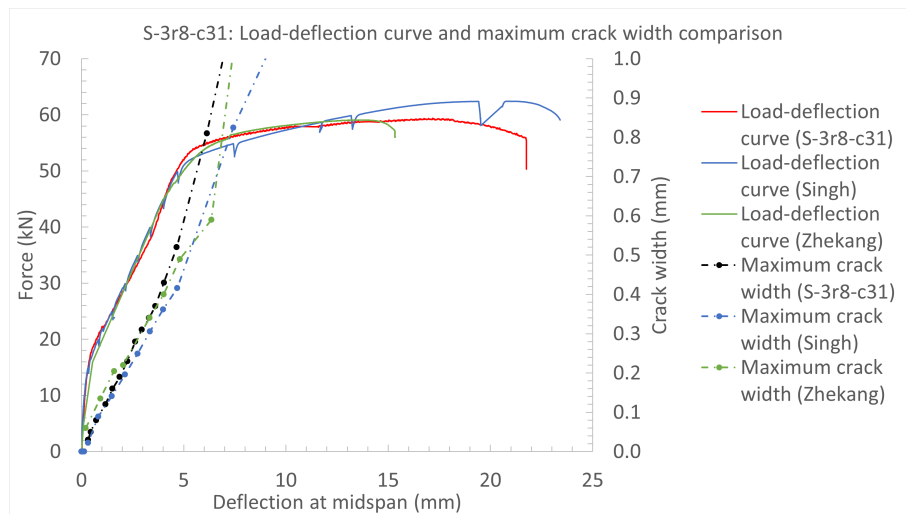


Figure 5.1: Load-deflection curve and maximum crack width curve comparison beam S-3r8-c31 with results Singh (2019) and Zhekang (2017)

The data from the thesis of Singh is provided in blue in figure 5.2. The load-deflection curve of beam S-3r8-c31 generally follows the same trajectory as the experimental results provided by Singh. The maximum crack width of beam S-3r8c31 is slightly higher. Upon inspection of the DIC-data provided in Singh's thesis, 6 cracks appear, which is 1 more crack that appears in beam S-3r8-c31. This could be an explanation for a slightly larger maximum crack width in S-3r8c31.

The load-deflection curve and the maximum crack widths from the thesis of Zhekang (2017) are plotted in figure 5.1 in green. The data provided show the same stiffness behaviour, however, the beam failed with a smaller vertical displacement. The maximum crack width development is comparable to the beams tested for this research, as well as that of the beams tested by Singh in 2019. As the results are generally in accordance with each other, the results are considered valid.

Zhekang (2017) tested a beam with a reinforcement configuration of $3\varnothing 8$ and a concrete cover of 11 mm. Figure 5.2 presents the load-deflection curves and maximum crack width curves of both S-3r8-c11 and the beam tested by Zhekang. The same concrete mix has been used for this beam as well. The stiffness behaviour of the beam is, at least for the most part, the same. The maximum load of beam S-3r8-c11 (64.77 kN) is comparable to that of the beam tested by Zhekang (63.93 kN). At approximately 60 kN, a small drop in stiffness is measured, which is likely due to the rapid emergence and opening of a newly formed crack. This is also noticeable in the maximum crack width curve at the same deflection level, where a small reduction in maximum crack width is measured.

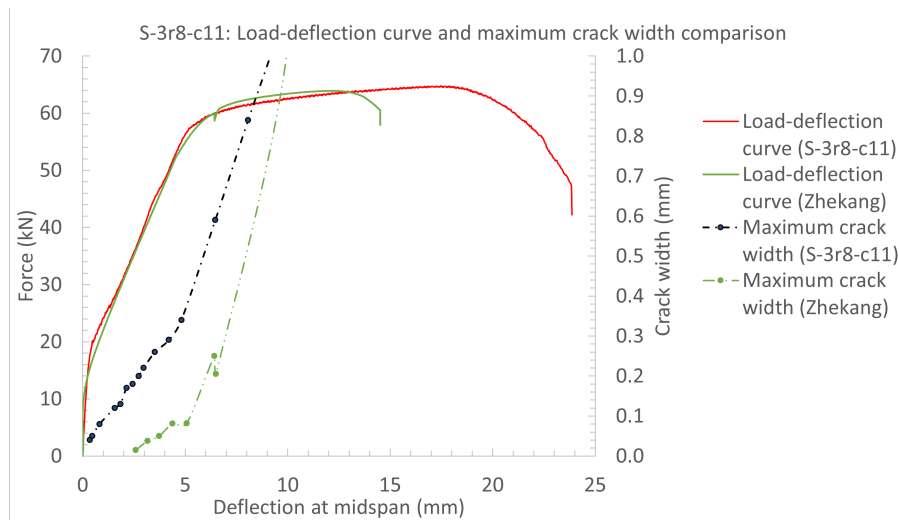


Figure 5.2: Load-deflection curve and maximum crack width curve comparison beam S-3r8-c11 with results Zhekang (2017)

However, there is a disparity in the maximum crack width development. The maximum crack width in S-3r8-c11 is considerably smaller throughout the loading. Upon reviewing the DIC-data from the beam Zhekang tested, more cracks seem to appear over the full length of the beam than in beam S-3r8-c11. As more cracks appear, the maximum crack widths remain smaller, which could be an explanation for this difference. As the results are generally in accordance with each other, the results are considered valid.

Based on the model devised by Tepfers for tensile splitting cracks, beam B-2r8-c31 should show faster tensile splitting crack development as its resistance to tensile splitting cracks is lower (figure 4.11 and table 4.7). This, however, is not the case, as the development of tensile splitting cracks in B-3r8-c31 exceeds that of B-2r10-c31 (figure 5.3).

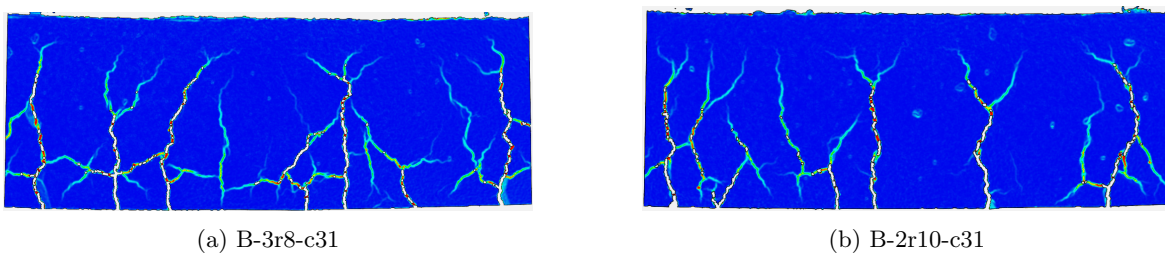


Figure 5.3: Contour plots crack pattern from DIC-data comparison at load level ≈ 50 kN

A possible explanation for this phenomenon can be found in the development pattern of the bond stress in the reinforcement bar as illustrated in figure 4.10. The Tepfers model does not consider the bar spacing and assumes the areas of influence do not interfere with each other. Upon applying the Tepfers model to the cross-sections of the beams (figure 5.4), the bond stress development zones of B-3r8-c31 (figure 5.4a) do interfere with each other as equation 5.1 applies.

$$c_y + \frac{d}{2} < \frac{s}{2} \quad (5.1)$$

Where the bar spacing and the bar diameter are denoted as parameters s and d respectively. To beam B-2r10-c31, equation 5.1 does not apply as the radius of the development zone does not exceed half the bar spacing (figure 5.4b). The interference of the bond stress development zones in the cross-section could cause the cracking stages described by the Tepfers model to not develop uniformly around the reinforcement bar. Therefore, the development of tensile splitting cracks could have been accelerated in beam B-3r8-c31.

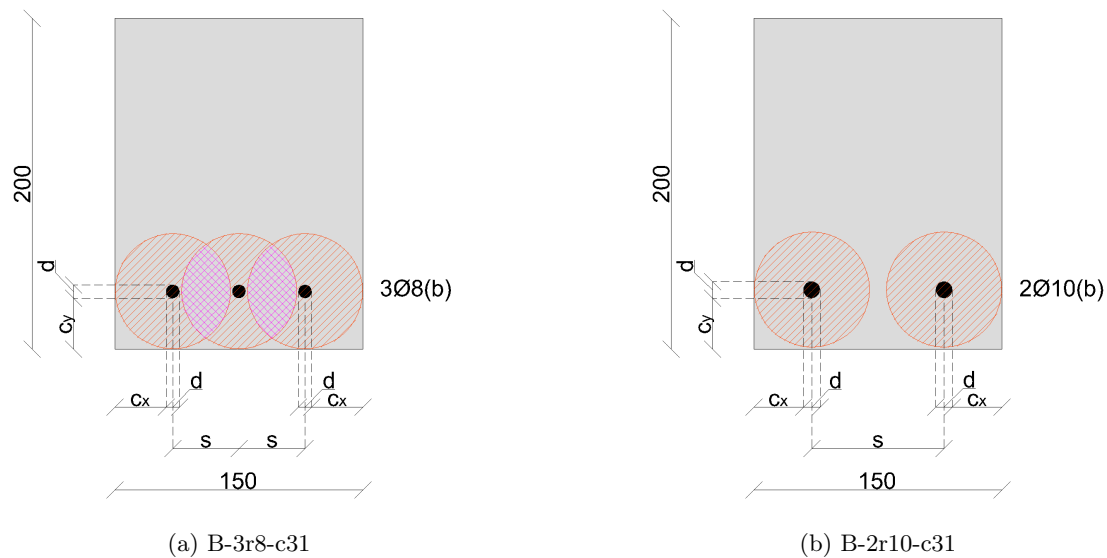


Figure 5.4: Overlapping of bond stress development zones

Although beam B-2r8-c31 (figure 5.5) has bond stress development zones that do not interfere with each other (figure 5.4b), the rapid development of tensile splitting cracks is more likely due to the reinforcement ratio. This beam type has a considerably lower reinforcement ratio compared to beams B-3r8-c31 and B-2r10-c31.

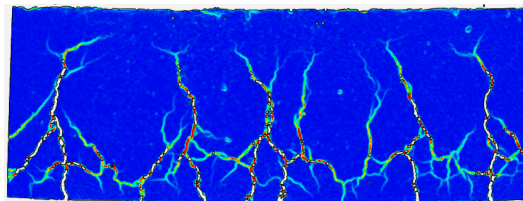


Figure 5.5: B-2r8-c31, Contour plots crack pattern from DIC-data comparison at load level ≈ 50 kN

This causes the tensile stress in the reinforcement bars to increase more quickly, which in turn increases the bond stress. The rapid development can therefore not be attributed to interference, but more likely a consequence of the lower reinforcement ratio of the beam.

Chapter 6

Conclusions and recommendations

This chapter provides an overview of the obtained findings. It formulates a response to the primary research question based on these findings and also offers recommendations for future research endeavours.

6.1 Conclusions

The main research objective is to determine to which extent BFRP-bars can contribute to the design of reinforced concrete structures. To reiterate, the main research objective is presented below.

To research the flexural behaviour of concrete reinforced with basalt fibre reinforcement bars

Based on the numerical study and experimental research, the findings are summarised as follows:

- Concrete structures reinforced with BFRP bars show significantly larger vertical deflection under bending loads and a lower cracking bending moment compared to concrete structures reinforced with steel bars. This could, at least to some extent, be attributed to the Young's modulus of the reinforcement bars. The linear elastic tensile behaviour of BFRP-bars results in a linear load-deflection curve after the first cracks have emerged. On the other hand, the studied steel reinforced beams showed a linear load-deflection behaviour as well until the stress in the reinforcement steel reaches the yielding strength. From this point, plastic deformations in the reinforcement are reached, causing larger vertical deflections.
- As the studied literature suggests, the bond strength of sand-coated BFRP bars is higher. This should be visible in the number of emerging cracks in the beams. A higher bond strength should lead to a smaller crack spacing as the length required to transfer stresses from the tensile reinforcement to the confining concrete. However, the experimental study supports this assertion, at least to some extent. The beams reinforced with BFRP-bars contain a smaller average crack spacing, and therefore more cracks, over the length of the constant bending moment zone (figure 6.1). The emergence and propagation of tensile splitting cracks at early loading stages prevent the development of bond strength in the sand-coated BFRP bars, thereby limiting the number of flexural cracks in the bending moment zone. Consequently, this contributes (along with the lower Young's modulus) to the larger crack widths in the flexural cracks that do emerge. The emergence of tensile splitting cracks is influenced by the bar diameter. It is observed from the experimental study that a larger bar diameter limits the propagation of tensile splitting cracks over the length of the reinforcement bar. The influence of the concrete cover on the emergence of tensile

splitting is considerable as well. It is observed that the reduced concrete cover results in a smaller resistance against tensile splitting cracks, which is confirmed by predictive models. The reinforcement ratio does not play a role in the tensile splitting resistance; however, a reduced reinforcement ratio results in higher bond stresses, causing larger propagation of tensile splitting cracks. No tensile splitting cracks were observed on the beams containing reinforcement steel.

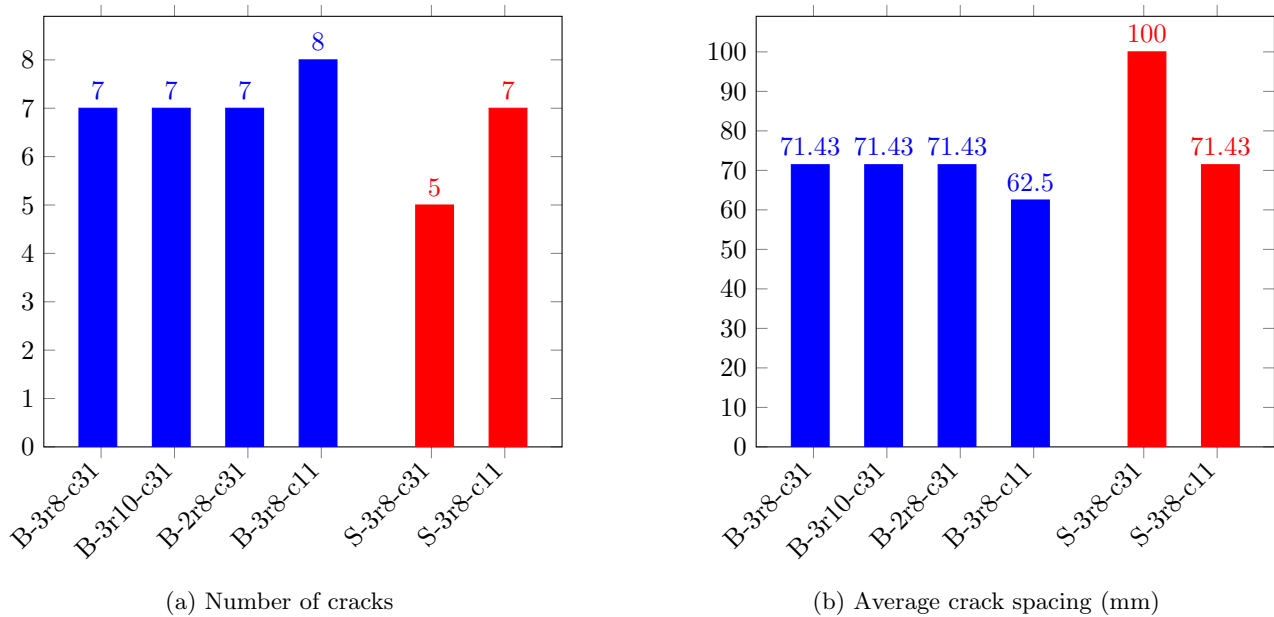


Figure 6.1: Comparison of cracks and crack spacing beam specimen

- Concrete structures reinforced with BFRP-bars show a considerably larger crack width under bending load concerning steel-reinforced concrete structures. When comparing the maximum crack width in beams reinforced with BFRP-bars to the crack width limits specified in BRL0513 and ACI440 for BFRP-reinforced beams, as well as Eurocode 2 for steel-reinforced concrete structures, it is observed that concrete structures with BFRP-bars reach these crack width limits at an earlier load level. This holds for both the most and least strict crack width limits dictated by the codes. Based on this, it can be concluded that a larger permissible crack width does not automatically imply favourability towards the application of BFRP-bars in concrete. The load levels at which the maximum crack widths are reached are presented in figure 6.2.

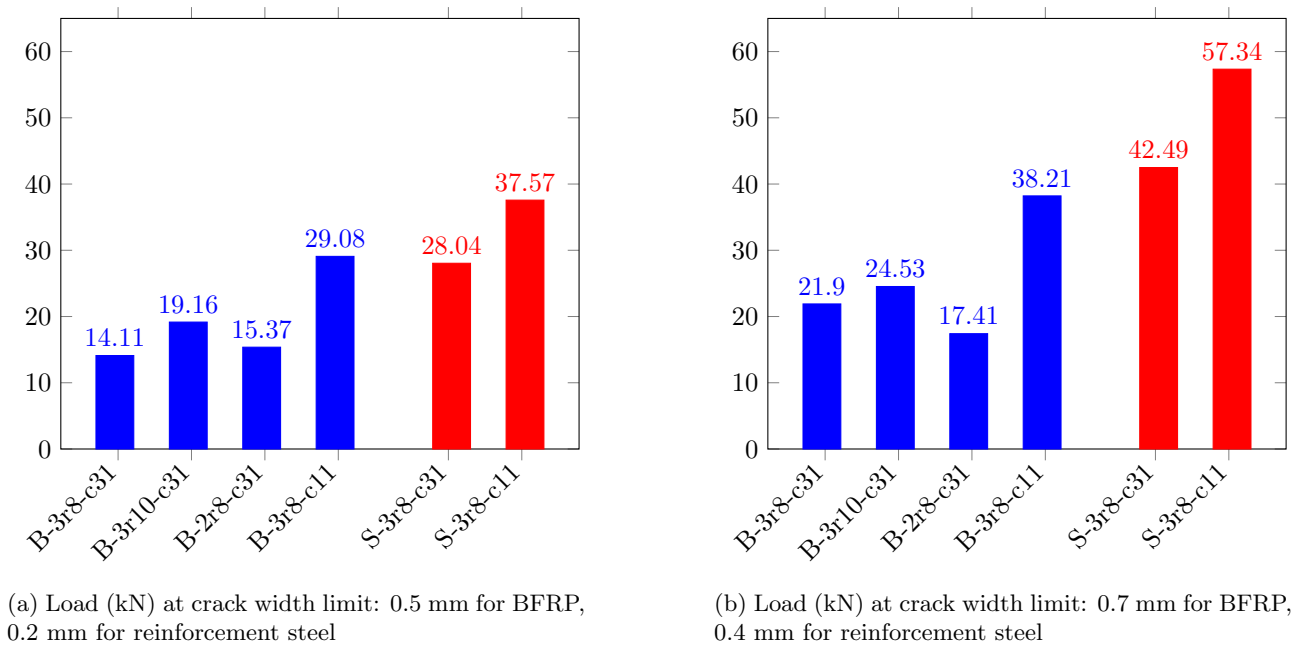


Figure 6.2: Load level at maximum crack width limits are reached

- In analyzing the use of basalt fibre reinforcement (BFRP) versus steel in slabs of similar design, the Environmental Cost Indicator (ECI) emerges as a pivotal factor. Despite the higher upfront costs linked to BFRP implementation, its consistently lower ECI across various setups stands out prominently. This reduction in environmental impact, particularly concerning concrete utilization and global warming potential, is significant. The adjustment of concrete cover thickness notably influences both ECI and costs in BFRP-reinforced slabs; however, it also increases the tendency for tensile splitting crack development. Reducing the cover to 1.5 times the BFRP bar diameter not only amplifies the ECI advantage but also narrows the cost gap between BFRP and steel reinforcement. Remarkably, in concrete structures where minimal thickness suffices for non-structural purposes, BFRP emerges as superior in both ECI and potential cost savings. These findings underscore the environmental advantages of BFRP, emphasizing its ability to curtail concrete usage and diminish environmental impact despite initial higher expenses.

In conclusion, the tensile behaviour of BFRP-bars is predominantly linear elastic, contrasting with steel reinforcement's plastic deformation stage. Concrete structures reinforced with BFRP-bars exhibit earlier cracking and larger deflections due to the lower Young's modulus of the bar, at least to some extent. Despite the propensity for larger crack widths under bending loads, BFRP-bars offer environmental advantages over reinforcement steel, highlighted by its consistently lower Environmental Cost Indicator and potential cost savings, especially when the concrete cover can be minimized. Minimising the concrete cover, however, causes an increasing probability of the emergence of tensile splitting cracks.

6.2 Recommendations for further research

From the conclusions, the following recommendations for research for future studies are made:

- As the parameter study is primarily focused on the BFRP-bars as a replacement for reinforcement steel, a comparison between the other types of FRP reinforcement bars such as CFRP and GFRP could give insight into the performance of BFRP-bars compared to these FRP types. This study should include but is not limited to costs, ECI-calculations and implications for structural behaviour of concrete structures reinforced with FRP-bars.
- As tensile splitting cracks emerged in the early loading stages, further research into the causes of the emergence of these cracks might provide insight into this phenomenon. This research should also include the effects on the bond strength of sand-coated FRP-bars for loads increased to SLS-level. In addition, further research into the tensile splitting cracks, and the effects of transversal reinforcement in the constant bending moment zone should be researched.
- In this experiment centred on BFRP-bars for flexural reinforcement, the potential of BFRP-bars in shear reinforcement remains unexplored. Investigating BFRP's efficacy in shear aspects aims to reveal its potential comprehensively. While its promise in shear reinforcement is yet uncertain, this study serves as a starting point to gauge its potential beyond flexural applications.
- The experimental section of the thesis focuses on exploring the immediate effects of BFRP-bars in concrete structures. However, it is crucial to recognize that a comprehensive understanding of the structural performance demands an examination of the long-term implications associated with the use of BFRP-bars.
- One aspect that is untouched upon in this thesis is the consideration of the long-term effects of BFRP-bars themselves, particularly concerning the phenomenon of creep in the resin. Creep, the gradual deformation of a material under sustained loading over time, can significantly impact the structural behaviour of concrete elements reinforced with BFRP-bars. Investigating the extent of creep in the resin, and its subsequent influence on the overall behaviour of the structure, is required for a complete assessment of BFRP-bars as an alternative for reinforcement steel.
- This thesis has not delved into the flexural and cracking behaviour of concrete structures reinforced with BFRP-bars under cyclic loading conditions. Cyclic loading introduces a dynamic element to the assessment, presenting challenges and responses that may differ from those observed under static loading conditions. Understanding how concrete structures containing BFRP-bars respond to cyclic loading, especially in terms of flexural strength and crack formation, is essential for predicting their performance in applications where structures experience varying and dynamic loads.

Bibliography

- Agarwal, B. and Broutman, L. (1990). *Analysis and performance of fiber composites Second edition*. John Wiley & Sons.
- Al-Azzawi, M., Yu, T., and Hadi, M. N. (2018). Factors affecting the bond strength between the fly ash-based geopolymer concrete and steel reinforcement. In *Structures*, volume 14, pages 262–272. Elsevier.
- Al-Zahrani, M. M., Al-Dulaijan, S. U., Nanni, A., Bakis, C. E., and Boothby, T. E. (1999). Evaluation of bond using frp rods with axisymmetric deformations. *Construction and Building Materials*, 13(6):299–309.
- American Concrete Institute (2012). ACI 440.3R-12: Guide Test Methods for Fiber-Reinforced Polymers (FRPs) for Reinforcing or Strengthening Concrete Structures. Technical Report ACI 440.3R-12, American Concrete Institute, Farmington Hills, MI.
- American Concrete Institute (2015). ACI 440.1R-15: Guide for the Design and Construction of Structural Concrete Reinforced with Fiber-Reinforced Polymer (FRP) Bars. Technical Report ACI 440.1R-15, American Concrete Institute, Farmington Hills, MI.
- Ashrafi, H., Bazli, M., Najafabadi, E. P., and Oskouei, A. V. (2017). The effect of mechanical and thermal properties of frp bars on their tensile performance under elevated temperatures. *Construction and building materials*, 157:1001–1010.
- Baena, M., Torres, L., Turon, A., and Miàs, C. (2013). Analysis of cracking behaviour and tension stiffening in frp reinforced concrete tensile elements. *Composites Part B: Engineering*, 45(1):1360–1367.
- Barbero, E. J. (1999). Introduction to composite materials design.
- Barker, C. (2016). The feasibility of fibre reinforced polymers as an alternative to steel in reinforced concrete. *Dechief*.
- Benmokrane, B., Elgabbas, F., Ahmed, E. A., and Cousin, P. (2015). Characterization and comparative durability study of glass/vinylester, basalt/vinylester, and basalt/epoxy frp bars. *Journal of Composites for Construction*, 19(6):04015008.
- Benmokrane, B., Tighiouart, B., et al. (1996). Bond strength and load distribution of composite gfrp reinforcing bars in concrete. *Materials Journal*, 93(3):254–259.
- Betonakkoord (2017). Betonakkoord: Samenwerken aan Duurzaam Beton. Retrieved from <https://www.betonakkoord.nl/>.
- Bijleveld, M. M., Bergsma, G. G., and van Lieshout, M. M. (2013). Milieu-impact van betongebruik in de nederlandse bouw. *Delft: CE Delft Report*.
- Britannica, E. (2015). Silica mineral. <https://www.britannica.com/science/silica-mineral>. Accessed on February 13, 2024.
- Brown, V. L. and Bartholomew, C. L. (1993). Frp reinforcing bars in reinforced concrete members. *Materials Journal*, 90(1):34–39.
- Brózda, K., Selejda, J., and Koteš, P. (2017). Analysis of properties of the frp rebar to concrete structures. *Appl. Eng. Lett*, 2:6–10.
- Busel, J. (2006). *Guide for the Design and Construction of Structural Concrete Reinforced with FRP Bars*. American Concrete Institute, Indianapolis, Indiana, United States of America.

- Castel, A., François, R., Tourneur, C., et al. (2007). Effect of surface pre-conditioning on bond of carbon fibre reinforced polymer rods to concrete. *Cement and Concrete Composites*, 29(9):677–689.
- Chaallal, O. and Benmokrane, B. (1993). Pullout and bond of glass-fibre rods embedded in concrete and cement grout. *Materials and structures*, 26:167–175.
- Chiu, C.-K., Chi, K.-N., and Ho, B.-T. (2018). Experimental investigation on flexural crack control for high-strength reinforced-concrete beam members. *International Journal of Concrete Structures and Materials*, 12(1):1–20.
- Colombo, C., Vergani, L., and Burman, M. (2012). Static and fatigue characterisation of new basalt fibre reinforced composites. *Composite structures*, 94(3):1165–1174.
- Correia, J. R. (2013). Pultrusion of advanced fibre-reinforced polymer (frp) composites. In *Advanced Fibre-Reinforced Polymer (FRP) Composites for Structural Applications*, pages 207–251. Elsevier.
- CvD (2015). *Glasvezelstaven voor toepassing als wapening in beton*. KIWA, Gouda, Netherlands.
- Ecochain (2023). Environmental Cost Indicator (ECI). <https://ecochain.com/blog/environmental-cost-indicator-eci/>.
- Ekvall, T., Azapagic, A., Finnveden, G., Rydberg, T., Weidema, B. P., and Zamagni, A. (2016). Attributional and consequential lca in the ilcd handbook. *The International Journal of Life Cycle Assessment*, 21:293–296.
- Elgabbas, F., Vincent, P., Ahmed, E. A., and Benmokrane, B. (2016). Experimental testing of basalt-fiber-reinforced polymer bars in concrete beams. *Composites Part B: Engineering*, 91:205–218.
- Erden, S. and Ho, K. (2017). Fiber reinforced composites. In *Fiber Technology for Fiber-Reinforced Composites*, pages 51–79. Elsevier.
- European Committee for Standardization (2022). Eurocode 2: Design of concrete structures - Part 1-1: General rules and rules for buildings (NEN-EN 1992-1-1). Brussels, Belgium: European Committee for Standardization.
- Fayomi, G., Mini, S., Fayomi, O., and Ayoola, A. (2019). Perspectives on environmental co2 emission and energy factor in cement industry. In *IOP Conference Series: Earth and Environmental Science*, volume 331, page 012035. IOP Publishing.
- Fennis, Sonja Diemel, V. (2021). Rtd 1033 verduurzaming beton. *Rijkswaterstaat Centre for Infrastructure, Report RTD*, 5749:2021(1.1):18.
- fib (2000). fib bulletin 10: Precast concrete.
- fib (2007). fib bulletin 40: Frp reinforcement in rc structures. *International Federation for Structural Concrete*.
- Fiore, V., Scalici, T., Di Bella, G., and Valenza, A. (2015). A review on basalt fibre and its composites. *Composites Part B: Engineering*, 74:74–94.
- Freimanis, A., Bakis, C., Nanni, A., and Gremel, D. (1998). A comparison of pull-out and tensile behaviors of frp reinforcement for concrete. In *Second International Conference on Composites in Infrastructure National Science Foundation*, volume 2.
- Harajli, M. H., Hamad, B. S., and Rteil, A. A. (2004). Effect of confinement of bond strength between steel. *ACI Structural Journal*, 101(5):595–603.
- Huang, Z., Chen, W., Tran, T. T., Pham, T. M., Hao, H., Chen, Z., and Elchalakani, M. (2021). Experimental and numerical study on concrete beams reinforced with basalt frp bars under static and impact loads. *Composite Structures*, 263:113648.
- Inman, M., Thorhallsson, E. R., and Azrague, K. (2017). A mechanical and environmental assessment and comparison of basalt fibre reinforced polymer (bfrp) rebar and steel rebar in concrete beams. *Energy Procedia*, 111:31–40.
- Ji, S., Wang, Q., and Salisbury, M. H. (2009). Composition and tectonic evolution of the chinese continental crust constrained by poisson’s ratio. *Tectonophysics*, 463(1-4):15–30.
- Jumaishing (2022). Basalt fiber spray-up roving. <https://www.basaltfiber-cn.com/products/basalt-fiber-spray-up-roving>. 2022.

- Kanakubo, T., Yonemaru, K., Fukuyama, H., and Sonobe, Y. (1993). Bond splitting strength of concrete members reinforced with frp bars. *Transactions of the Japan Concrete Institute*, 15:305–318.
- Karbhari, V., Chin, J., Hunston, D., Benmokrane, B., Juska, T., Morgan, R., Lesko, J., Sorathia, U., and Reynaud, D. (2003). Durability gap analysis for fiber-reinforced polymer composites in civil infrastructure. *Journal of composites for construction*, 7(3):238–247.
- Kelly, A., Zweben, C. H., and Chou, T.-W. (1968). Fiber reinforcements and general theory of composites. (*No Title*).
- Kumbhar, V. P. (2014). An overview: basalt rock fibers-new construction material. *Acta Engineering International*, 2(1):11–18.
- Larralde, J. and Silva-Rodriguez, R. (1993). Bond and slip of frp rebars in concrete. *Journal of Materials in Civil Engineering*, 5(1):30–40.
- Li, Z., Ma, J., Ma, H., and Xu, X. (2018). Properties and applications of basalt fiber and its composites. In *IOP Conference Series: Earth and Environmental Science*, volume 186, page 012052. IOP Publishing.
- M Sobota, I Driessen, M. H. (2022). Carbon-based design onderzoek naar de milieu-impact van de woningbouw. *CITYFOSTER*.
- Ma, G., Huang, Y., Aslani, F., and Kim, T. (2019). Tensile and bonding behaviours of hybridized bfrp-steel bars as concrete reinforcement. *Construction and Building Materials*, 201:62–71.
- Nagatomo, K., Matsubara, S., and Kaku, T. (1992). Bond strength of deformed bars under lateral stress. yokohoko oryoku sayo ka ni okeru ikei tekkin no fuchaku kyodo ni kansuru kenkyu. *Doboku Gakkai Ronbunshu;(Japan)*, 451.
- Nanni, A., Al-Zaharani, M., Al-Dulajjan, S., Bakis, C., and Boothby, I. (1995). 17 bond of frp reinforcement to concrete-experimental results. In *Non-metallic (FRP) Reinforcement for Concrete Structures: Proceedings of the Second International RILEM Symposium*, volume 29, page 135. CRC Press.
- Nanni, A., De Luca, A., and Zadeh, H. (2014). *Reinforced concrete with FRP bars*. Taylor and Francis group.
- Nederlands Normalisatie-instituut (2016). *NEN-EN 206+A2: Concrete - Specification, performance, production, and conformity*. Nederlands Normalisatie-instituut, Delft, Netherlands. EN standard.
- Nederlands Normalisatie-instituut (2019a). *NEN-EN 12390-3: Testing hardened concrete - Part 3: Compressive strength of test specimens*. Nederlands Normalisatie-instituut, Delft, Netherlands. EN standard.
- Nederlands Normalisatie-instituut (2019b). *NEN-EN 12390-6: Testing hardened concrete - Part 6: Tensile splitting strength of test specimens*. Nederlands Normalisatie-instituut, Delft, Netherlands. EN standard.
- Nederlands Normalisatie-instituut (2020). *NEN-EN 12390-13: Testing hardened concrete - Part 13: Determination of secant modulus of elasticity in compression*. Nederlands Normalisatie-instituut, Delft, Netherlands. EN standard.
- Nilforoush, R. and Esfahani, M. S. (2012). *Numerical Evaluation of Structural Behavior of the Simply Supported FRP-RC Beams*. Kungl. Tekniska Högskolan.
- Orlimex CZ s.r.o (2022). Environmental Product Declaration (EPD) for Basalt Fibre Reinforced Polymer Rebar. Technical Report.
- Pavlović, A., Donchev, T., Petkova, D., and Staletović, N. (2022). Sustainability of alternative reinforcement for concrete structures: Life cycle assessment of basalt frp bars. *Construction and Building Materials*, 334:127424.
- Pawłowski, D. and Szumigala, M. (2015). Flexural behaviour of full-scale basalt frp rc beams—experimental and numerical studies. *Procedia Engineering*, 108:518–525.
- Peet, M., Hasan, H., and Bhadeshia, H. (2011). Prediction of thermal conductivity of steel. *International Journal of Heat and Mass Transfer*, 54(11-12):2602–2608.
- Pilakoutas, K., Guadagnini, M., Neocleous, K., and Matthys, S. (2011). Design guidelines for frp reinforced concrete structures. *Proceedings of the Institution of Civil Engineers-Structures and Buildings*, 164(4):255–263.
- Prasad, V. V. and Talupula, S. (2018). A review on reinforcement of basalt and aramid (kevlar 129) fibers. *Materials Today: Proceedings*, 5(2):5993–5998.

- Rehman, M. S. N. U. and Michler, I. H. (2022). Existing codes and guidelines for durability design of frp reinforcement. *Proceedings of the Institution of Civil Engineers-Structures and Buildings*.
- S. Solyom, M. Di Benedetti, G. B. (2017). *Effect of Surface Characteristics of FRP Bars on Bond Behavior in Concrete*. Budapest University of Technology and Economics, Faculty of Civil Engineering Department of Construction Materials and Technologies.
- Shamass, R. and Cashell, K. (2020). Experimental investigation into the flexural behaviour of basalt frp reinforced concrete members. *Engineering Structures*, 220:110950.
- Shih, M.-H. and Sung, W.-P. (2013). Application of digital image correlation method for analysing crack variation of reinforced concrete beams. *Sadhana*, 38:723–741.
- Sólyom, S., Di Benedetti, M., and Balázs, G. L. (2018). Effect of surface characteristics of frp bars on bond behavior in concrete. *Aci Sp*, 327:41–1.
- Strauß, S., Senz, A., and Ellinger, J. (2019). Comparison of the processing of epoxy resins in pultrusion with open bath impregnation and closed-injection pultrusion. *Journal of Composites Science*, 3(3):87.
- Sólyom, S. (2017). *Bond test results of PMB Composite FRP bars*. Budapest University of Technology and Economics, Faculty of Civil Engineering Department of Construction Materials and Technologies.
- Tepfers, R. and De Lorenzis, L. (2003). Bond of frp reinforcement in concrete—a challenge. *Mechanics of composite materials*, 39:315–328.
- Tepfers, R. and Karlsson, M. (1997). Pull-out and tensile reinforcement splice tests using frp c-bars. In *Third International Symposium on Non-metallic (FRP) Reinforcement for Concrete Structures, Sapporo 14-16 October 1997*, pages 357–364.
- Tsai, S. and Hahn, H. (1980). Introduction to composite materials, technomic publ. Co., Westport.
- Upadhyaya, V. and Suntharavadiel, T. (2018). Advances in frp ret part-ii: Developmen mineral com. *Technology*, 9:13.
- Usingeurocode (2023). Eurocode 2 design - bending at serviceability limit state.
- Van de Velde, K. and Kiekens, P. (2001). Thermoplastic pultrusion of natural fibre reinforced composites. *Composite structures*, 54(2-3):355–360.
- Vedernikov, A., Nasonov, Y., Korotkov, R., Gusev, S., Akhatov, I., and Safonov, A. (2021). Effects of additives on the cure kinetics of vinyl ester pultrusion resins. *Journal of Composite Materials*, 55(21):2921–2937.
- VWN (2021). Environmental product declaration (epd) for reinforcing steel in reinforced concrete structures. Technical Report.
- Walraven, J. (2013). fib model code for concrete structures 2010: mastering challenges and encountering new ones. *Structural Concrete*, 14(1):3–9.
- Wu, Z., Wang, X., Liu, J., and Chen, X. (2020). Mineral fibres: basalt. In *Handbook of Natural Fibres*, pages 433–502. Elsevier.
- Xiong, Z., Wei, W., Liu, F., Cui, C., Li, L., Zou, R., and Zeng, Y. (2021). Bond behaviour of recycled aggregate concrete with basalt fibre-reinforced polymer bars. *Composite Structures*, 256:113078.
- Zhang, Z. and Hsu, C.-T. T. (2005). Shear strengthening of reinforced concrete beams using carbon-fiber-reinforced polymer laminates. *Journal of composites for construction*, 9(2):158–169.

Appendix A

Parameter Study

This section contains research into applicable regulations. By adjusting certain parameters in the design of concrete structures subject to bending, the effects of those parameters can be measured. The section is split up into ECI-value and cost parameters, as well as structural parameters. As structural parameters will influence the ECI-value, a comparison in retrospect is made to determine the overall advantages and disadvantages.

A.1 Background and motivation

This parameter study aims to comprehensively evaluate and compare the performance of BFRP-bars against reinforcement steel bars concerning various parameters encompassing cost, environmental impact, and structural considerations such as bending moment resistance, crack width, and crack spacing.

The background for this study is rooted in the growing interest and utilization of alternative materials like BFRP-bars in concrete structures due to their potential advantages mentioned in the literature study. Notably, ongoing research focuses on understanding the precise effects of parameters within the formulas provided by these design codes on structural behaviour.

By conducting a thorough comparison, the aim is to illustrate the strengths and limitations of both materials under the purview of different design codes used in distinct regions. The comparison will be executed using three design codes to ensure a comprehensive analysis. The ACI 440 [Busel, 2006], originating from the United States of America and utilized globally, serves as a benchmark for structures incorporating Fibre Reinforced Polymer (FRP) bars. The BRL0513 [CvD, 2015], specific to the Dutch concrete market, provides insights tailored to the Netherlands' conditions, particularly for FRP bars in concrete structures. Lastly, Eurocode 2 [European Committee for Standardization, 2022], a prominent standard for concrete structures reinforced with reinforcement steel bars, offers a basis for comparison against the reinforcement steel bars.

This study aims to assess parameters such as cost-effectiveness, environmental sustainability, and structural performance in terms of bending moment resistance, crack width, and crack spacing. The effects of these parameters within the design formulas will be considered to ensure a more understanding of their impact. The findings will contribute valuable insights for engineers, policymakers, and stakeholders in the construction industry, aiding informed decision-making towards more sustainable and efficient infrastructure development.

A.2 Assumptions

The ECI-value for concrete is determined according to RTD1033 version 1.1 "Verduurzaming beton" [Fennis, 2021], which provides upper boundary values put out by the Dutch government for concrete. The values used depend on the concrete class used in the design as well as the time and date. For the research to be future-proof, the upper boundary values used for this parameter study are those of the years 2029-2030. These upper boundary values are noted in table A.1 in €/m³.

Table A.1: Upper boundary values for ECI-values of concrete for 2029-2030 [Fennis, 2021]

	C12/15	C20/25	C30/37	C35/45	C45/55	C55/67	C70/85	C90/105
€/m ³	12.10	13.90	14.70	16.20	18.30	25.20	27.60	28.90

For the price of concrete, €170 per cubic metre is assumed. Note that the price of concrete is dependent on the market and therefore fluctuates. Furthermore it is assumed concrete has a CO₂ emission of 0.9 kg per 1 kg of concrete [Fayomi et al., 2019]

A.3 ECI and costs parameters

This section evaluates and compares the environmental footprint of reinforced concrete structures utilizing BFRP-bars and steel bars, along with cost considerations. The focus of the assessment is on slabs due to their ease of parameterization on a per-square-metre basis. Notably, slabs typically do not necessitate shear reinforcement, in contrast to beams. Since shear force and shear reinforcement fall outside the scope of this research, they are excluded from consideration.

Equal geometry, slab with top and bottom reinforcement

A direct comparison between 2 slabs of equal geometry and reinforcement configuration gives insight into the cost difference and the ECI of a direct replacement of steel reinforcement with basalt fibre reinforcement. A slab with a thickness of 250 mm with $\varnothing 16-100$ in both the first layers is used for the comparison. Distribution reinforcement in both second layers is $\varnothing 10-100$. The reinforcement configuration is shown in figure A.1. A concrete class of C30/37 is assumed to account for the cost and ECI-values of the concrete volumes. The applied cover on both sides of the slab is 35 mm. A comparison of costs and ECI-value for this structure is shown in figure A.2.

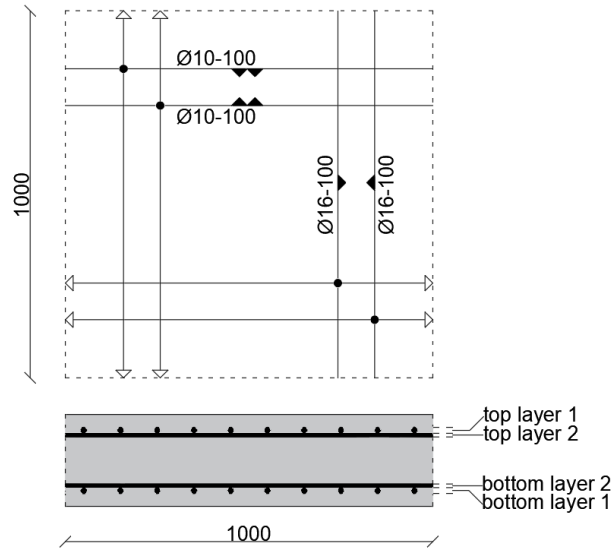


Figure A.1: Double reinforcement mesh slab reinforcement drawing

A slab with the same geometry reinforced with BFRP-bars gets a total ECI value of €7.25, whereas the same slab reinforced with reinforcement steel results in an ECI value of €9.91. Applying the same bar diameters and spacing in all layers of reinforcement results in an ECI-value difference of €2.66 per square metre of concrete slab, which is a reduction of 23.8% (including the concrete part). Table A.2 shows the components of the total ECI-value and the costs. The construction costs for the identical slab are €9.94 higher when BFRP-bars are utilized.

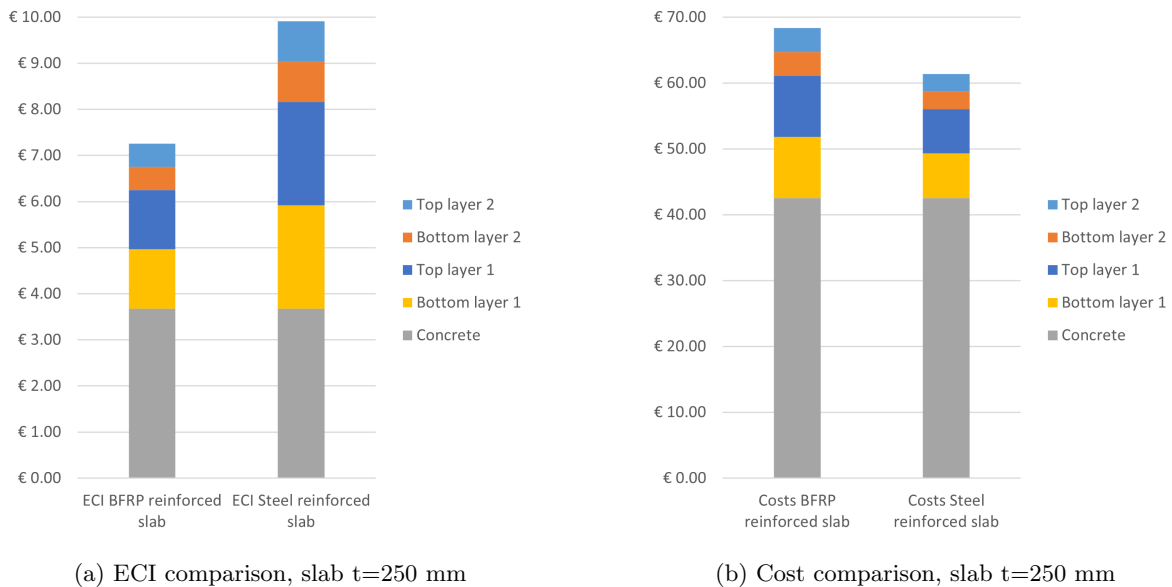
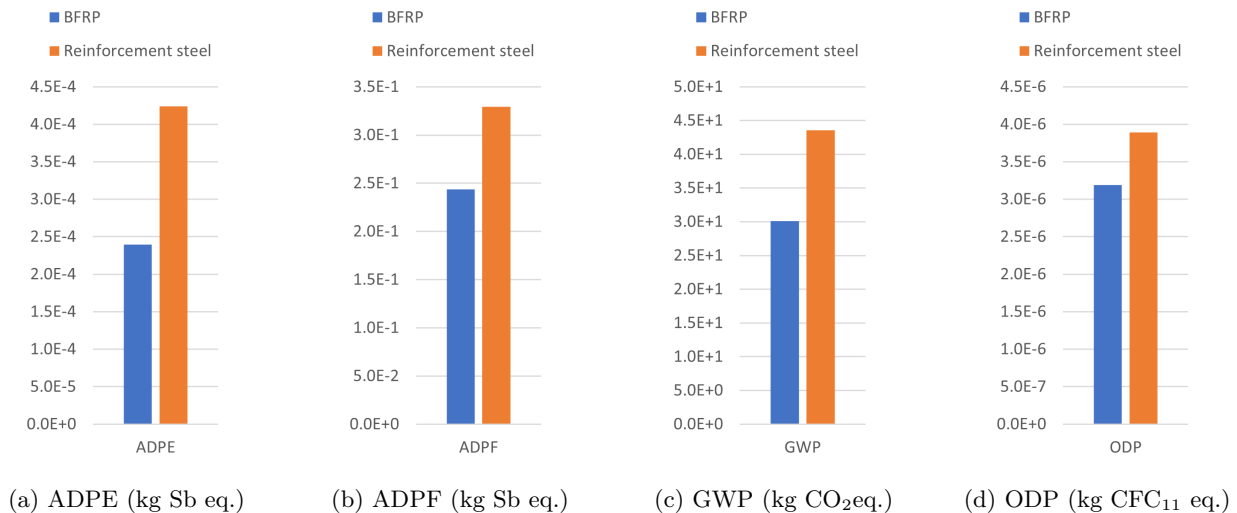


Figure A.2: Costs and ECI comparison square metre slab t=250 mm, b=1000 mm, equal geometry

Table A.2: Components of total ECI-score and costs per square metre slab t=250 mm, b=1000 mm, equal geometry

Reinforcement	Bottom layer 1	Bottom layer 2	Top layer 1	Top layer 2	Concrete	Total
ECI-score BFRP-bars	€1.29	€0.50	€1.29	€0.50	€3.68	€7.25
ECI-score Reinforcement steel	€2.24	€0.88	€2.24	€0.88	€3.68	€9.91
ECI-score difference						€2.66
Costs BFRP-bars	€9,29	€3.63	€9,29	€3.63	€42,50	€68.34
Costs Reinforcement steel	€6.79	€2.65	€6.79	€2.65	€42,50	€61.36
Costs difference						€6.98

Note how the concrete part is the majority of both the ECI-value and the costs. In the next paragraph. By reducing the concrete part, a further reduction in ECI-value and costs is still possible. The impact categories used for the calculations are noted in table 2.5 in Chapter 2 Literature Study. When looking at the impact categories of BFRP-bars compared to reinforcement steel, in all categories except for freshwater aquatic ecotoxicity potential (FAETP) BFRP-reinforcement bars have a lower score, hence the lower ECI-value for equal diameter and geometry. One of the most notable impact categories is the global warming potential (GWP). For this impact category, the reinforcement steel applied in the slab described above, the score is 43.55 kg CO₂ eq. whereas the same reinforcement layout in BFRP has a 30.91 kg CO₂ eq. This is a difference of 13.46 kg CO₂ eq. which is a reduction of 30.9%. All scores on the 11 impact categories comparing BFRP and reinforcement steel are presented in figure A.3.



Appendix A – Parameter Study

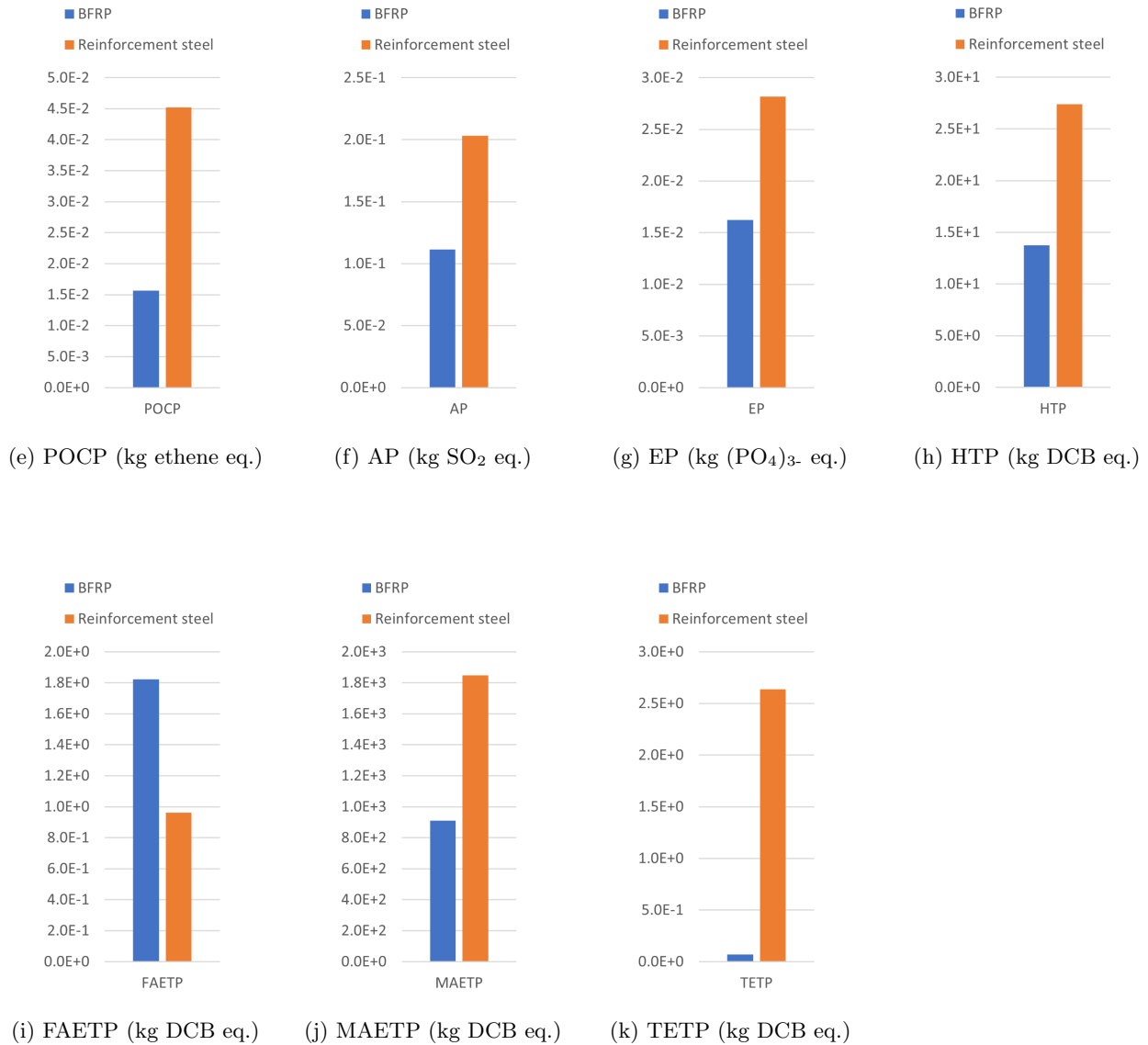


Figure A.3: Impact categories scores of reinforcement materials in slabs with equal geometry

The magnitude of each impact category is measured in the conversion to the ECI-value. A high score of a product on one of the impact categories does not automatically result in a high contribution to the ECI-score. Note that the weight factor for each impact category is always subject to change as environmental concerns are growing rapidly. Most notably the weight factor for Global Warming Potential (GWP) is likely to increase over the coming years. The weight factors are presented in table 2.7 in Chapter 2 Literature Study.

This however is not the whole story. The serviceability limit state (crack width control in this case) can not be left out of the equation to adjust for structural parameters. Based on the crack width models in BRL0513, ACI440 and Eurocode 2, the crack width curves are constructed (figure A.4). The crack width limits used are 0.5 for a BFRP-reinforced slab and 0.2 for a steel-reinforced slab. Herein is shown that the crack width limit of

0.2 is reached at 137 kNm. As the BFRP-reinforced slabs show an earlier exceeding of the 0.5 mm crack width limit, the serviceability limit state performance is not equal.

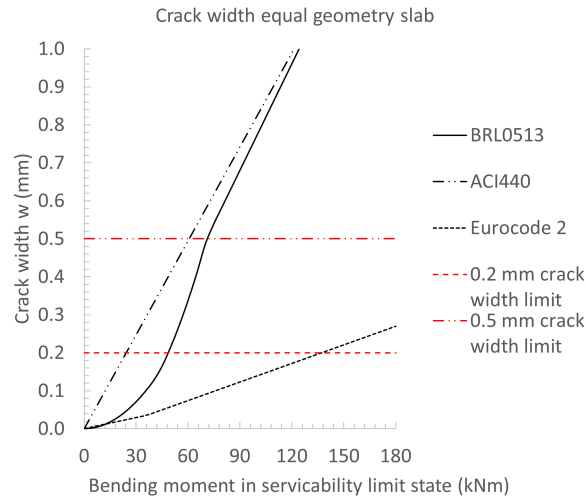


Figure A.4: Crack width development for slab equal geometry

To adjust for this, the reinforcement configuration of the BFRP-reinforced slab needs to be changed. To reach a 0.5 mm crack width limit in the BFRP-reinforced slab, the centre-to-centre distance of the BFRP-bars is adjusted. Using the BRL0513 model, a centre-to-centre distance of 53 mm is required, where 42 mm is required according to ACI440. The effects of this adjustment are shown in figure A.5 and table A.3

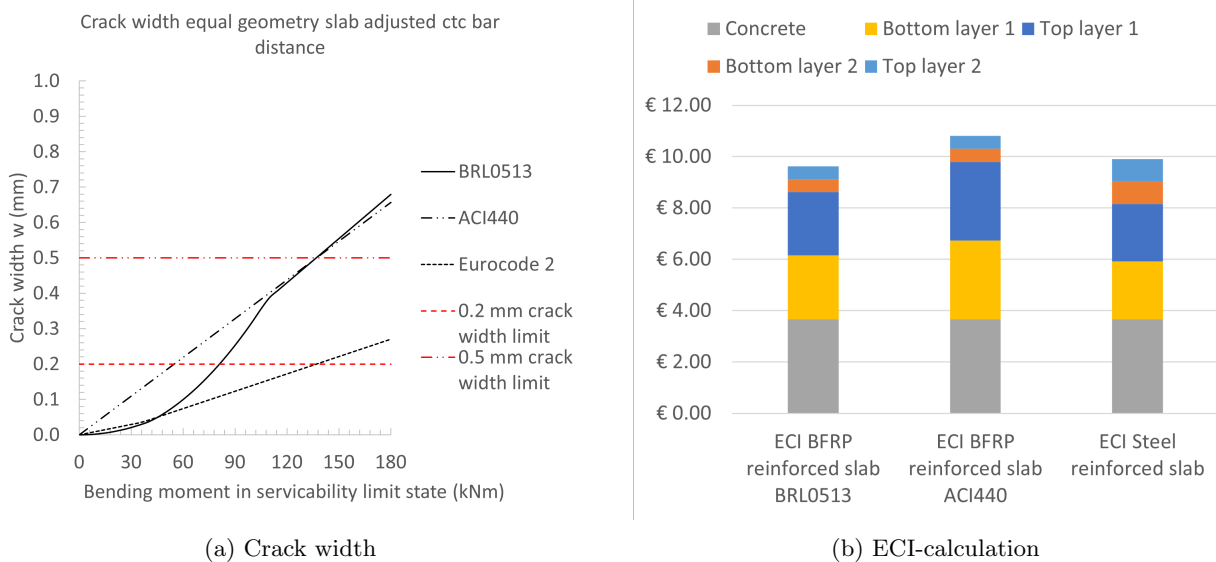


Figure A.5: Crack width curves and ECI-score for adjusted for serviceability limit state

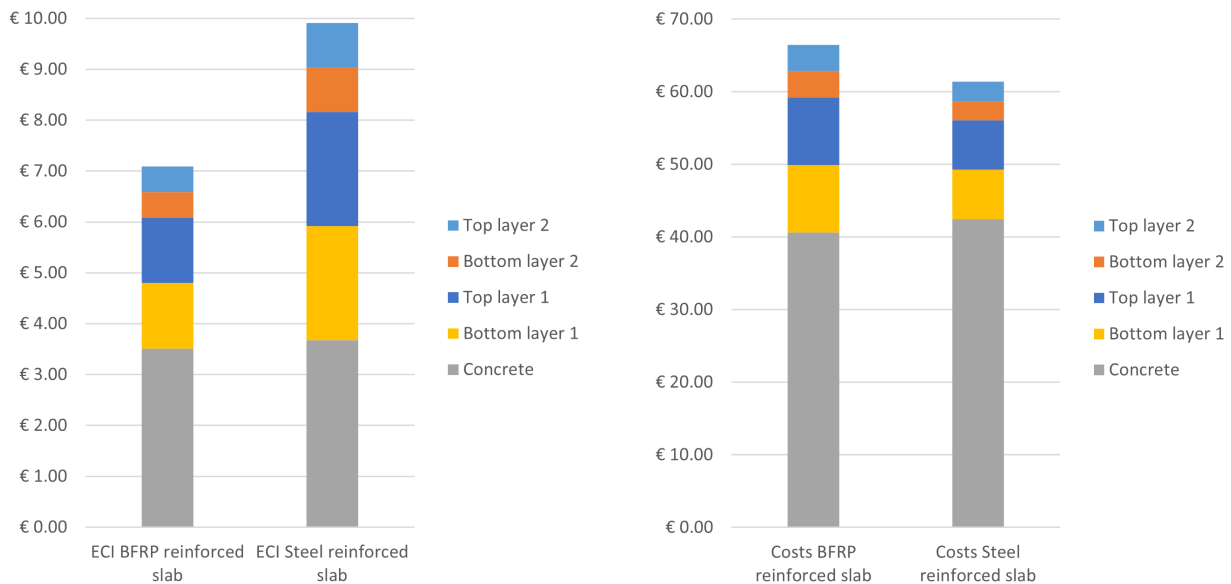
Table A.3: Adjusted ECI-score after adjusted for serviceability limit state

Reinforcement	Bottom layer 1	Bottom layer 2	Top layer 1	Top layer 2	Concrete	Total
ECI-score BFRP-bars BRL0513	€2.47	€0.50	€2.47	€0.50	€3.68	€9.63
ECI-score BFRP-bars ACI440	€3.06	€0.50	€3.06	€0.50	€3.68	€10.81
ECI-score Reinforcement steel	€2.24	€0.88	€2.24	€0.88	€3.68	€9.91

After adjusting for crack width control, the advantage in the ECI-score becomes minimal or even disappears. This however is based on a crack width limit of 0.5 for BFRP-bars. If a larger crack width limit for BFRP-bars is allowed, the advantage in ECI-score could increase as less reinforcement (e.g. a larger centre-to-centre distance) is then required for the BFRP-reinforced slab.

Reduction of concrete cover

The deterioration resistance of BFRP eliminates the necessity for determining concrete cover based on durability factors such as deflection and cracking, as outlined in the SLS criteria according to ACI440. By reducing the concrete cover to 1.5 times the diameter of the BFRP-bars (24 mm as per forthcoming Eurocode 2 informative Annex R), the bending moment capacity of the slab is preserved while necessitating less concrete. This reduction specifically targets the bottom cover to uphold the lever arm, enabling a comparative analysis using the same slab in figures A.6a and A.6b.



(a) ECI comparison, slab t=250 mm (t=239 mm for BFRP-reinforced slab) (b) Cost comparison, slab t=250 mm (t=239 mm for BFRP-reinforced slab)

Figure A.6: Costs and ECI comparison square metre slab t=250 mm, b=1000 mm, equal geometry with reduced cover of BFRP-reinforced slab

Table A.4: Components of total ECI-score and costs per square metre slab $t=250$ mm ($t=239$ mm for BFRP-reinforced slab), $b=1000$ mm, equal geometry

Reinforcement	Bottom layer 1	Bottom layer 2	Top layer 1	Top layer 2	Concrete	Total
ECI-score BFRP-bars	€1.29	€0.50	€1.29	€0.50	€3.51	€7.09
ECI-score Reinforcement steel	€2.24	€0.88	€2.24	€0.88	€3.68	€9.91
ECI-score difference						€2.82
Costs BFRP-bars	€9,29	€3.63	€9,29	€3.63	€40.63	€66.47
Cost Reinforcement steel	€6.79	€2.65	€6.79	€2.65	€42,50	€61.36
Cost difference						€5.11

This reduced the concrete part of the ECI and the costs significantly. the ECI-value is further reduced from €7.25 to €7.09, which is €0.16 reduction over a square metre of the slab. This increases the ECI-value difference between a steel-reinforced slab and a BFRP-reinforced slab from 23.8% to 26.8%. The costs due to the reduction of concrete cover are from €68.34 to €66.47 per square metre of slab. This reduction in costs reduced the difference to €5.11 per square metre of the slab.

Figure A.7 presents the crack width development curves according to the models in the codes. for this slab, the crack width development of the BFRP-reinforced slab also exceeds that of the steel-reinforced slab.

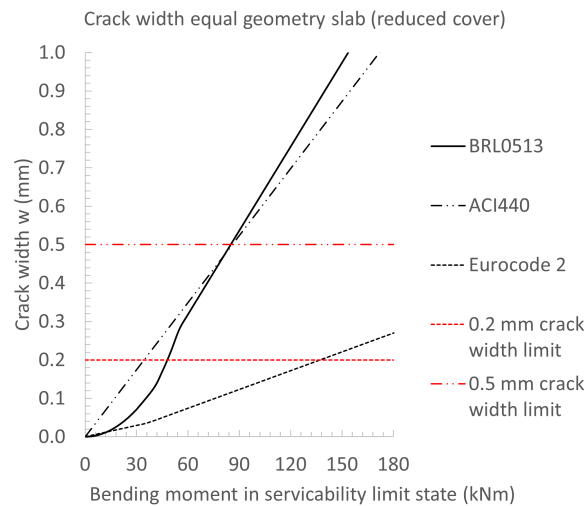


Figure A.7: Crack width development for slab equal geometry (reduced cover for BFRP-reinforced slab)

To adjust for this, the centre-to-centre distance needs to be altered. For this slab type, the required centre-to-centre distance is 66 mm according to BRL0513 and 61 mm according to ACI440. The centre-to-centre distance for a slab with reduced cover is therefore allowed to be larger. figure A.8 and table A.5 present the adjusted crack width curves for ad reduced cover as well as the subsequent ECI-score calculations.

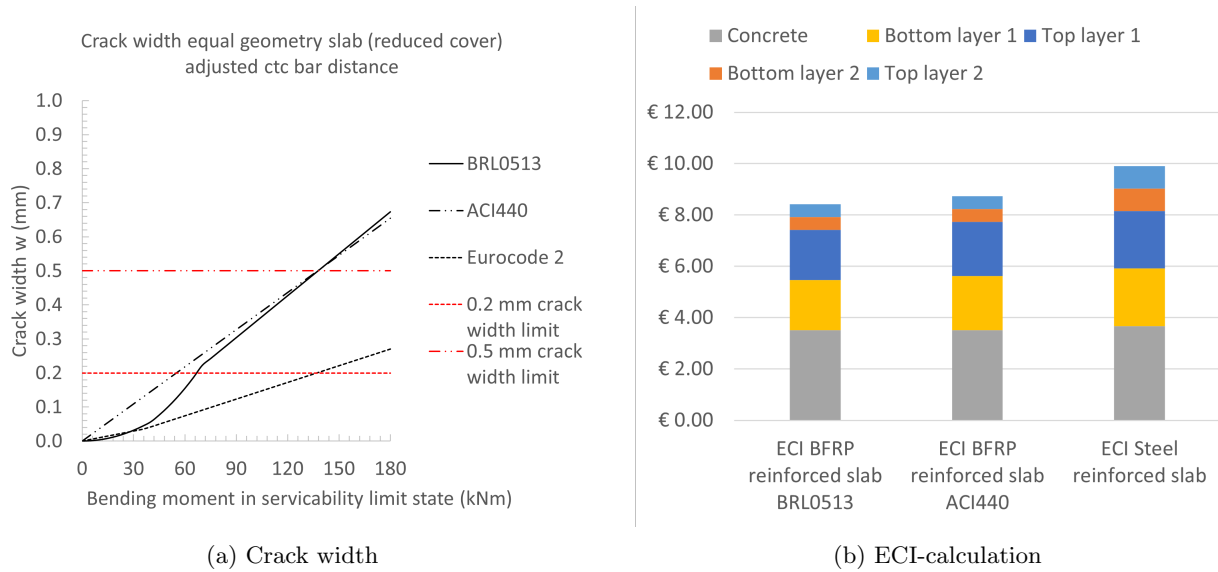


Figure A.8: Crack width curves and ECI-score for adjusted for serviceability limit state, slab with reduced concrete cover

Table A.5: Adjusted ECI-score after adjusted for serviceability limit state

Reinforcement	Bottom layer 1	Bottom layer 2	Top layer 1	Top layer 2	Concrete	Total
ECI-score BFRP-bars BRL0513	€1.95	€0.50	€1.95	€0.50	€3.51	€8.42
ECI-score BFRP-bars ACI440	€2.11	€0.50	€1.95	€0.50	€3.51	€8.74
ECI-score Reinforcement steel	€2.24	€0.88	€2.24	€0.88	€3.68	€9.91

After adjusting for crack width control, the advantage in ECI-score is still there if both the BRL0513 and ACI440 crack width are applied. The reduced slab thickness, as well as the larger required centre-to-centre distance compared to a slab with constant thickness, ensures a slight ECI-score advantage.

Non-structural slabs

For slabs where structural parameters are not dominant, the slab can be kept as thin as possible. Examples of these types of structures are interior walls, fire barriers, sound screens and cosmetic concrete elements. In these elements, only a single reinforcement mesh in the centre of the slab is sufficient to resist small loads and forces from its self-weight as well as a small wind load.

When an element of such type is designed to be exposed to exterior influences such as freeze-thaw cycles, wetting and drying cycles and chloride attacks either from seawater or not, the required concrete cover to protect the reinforcement plays a dominant factor in the required slab thickness. Because of the absence of forces, the reinforcement can be kept to a minimum. The smallest possible thickness (t_{min}) can be determined by using equation A.1

$$t_{\min} = c + \varnothing_1 + \varnothing_2 + c \quad (\text{A.1})$$

Where \varnothing_1 and \varnothing_2 represent the diameters of the reinforcement bars applied in the mesh. According to the effectual Eurocode 2, concrete cover requirements for steel-reinforced concrete are dependent on the exposure class (e.g. XC3/XS3) and the structural classes. For example, a slab of a sound barrier next to a highway is subjected to freezing-thawing cycles (XF4), chlorides from the traffic (XD3) and carbonation due to cyclic wet and drying cycles (XC4). For replaceable parts of a structure, a cover of 35 mm is required since XD3 is the dominant exposure class. In the forthcoming Eurocode 2, for concrete elements reinforced with BFRP-bars, the required concrete cover is equal to $1.5\varnothing$. The cover for concrete structures does not depend on the exposure class but is determined by bond properties. Figure A.9 shows the reinforcement configuration of a slab with a single mesh. For comparison, a mesh of $\varnothing 10-100$ in both directions is implemented. A concrete class of C30/37 is assumed.

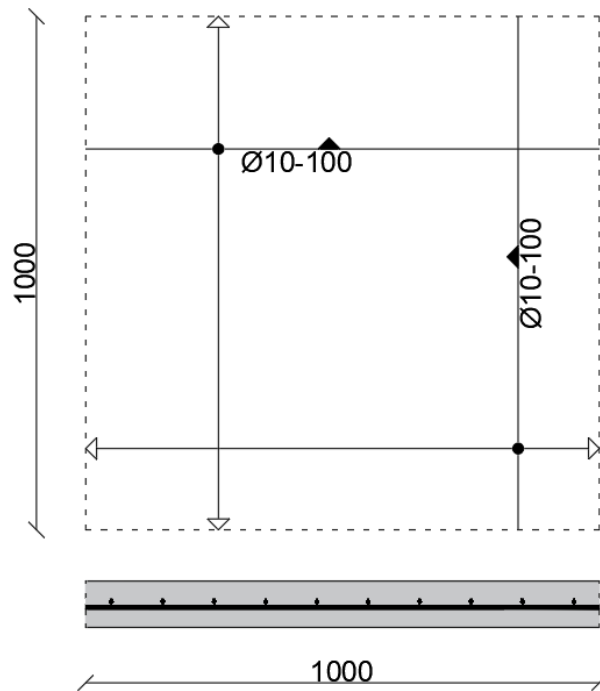


Figure A.9: Single reinforcement mesh slab reinforcement drawing

By using equation A.1, and the bar diameter of 10 mm, the reinforced concrete slab would have a minimum thickness of 90 mm. For an element reinforced with BFRP-bars of the same diameter, the required cover would be 15 mm, which is significantly smaller. Therefore, according to equation A.1 the minimum thickness is 50 mm. The ECI-calculation and the cost analysis for these elements are shown in figure A.10a and figure A.10b respectively. Note that in some cases, it is more appropriate to design elements thicker than the minimum thickness described in this section. Even though the structural demands are met, other factors that influence the element thickness could still apply.

Table A.6: Components of total ECI-score per square metre slab minimum required thickness, b=1000 mm

Reinforcement	Bottom layer	Top layer	Concrete	Total
ECI-score BFRP-bars	€0,50	€0,50	€0,74	€1,74
ECI-score Reinforcement steel	€0.88	€0.88	€1.32	€3.07
ECI-score difference				€1.33
Costs BFRP-bars	€3.63	€3.63	€8.50	€15.76
Costs Reinforcement steel	€2.65	€2.65	€15.30	€20.60
Costs difference				€4.84

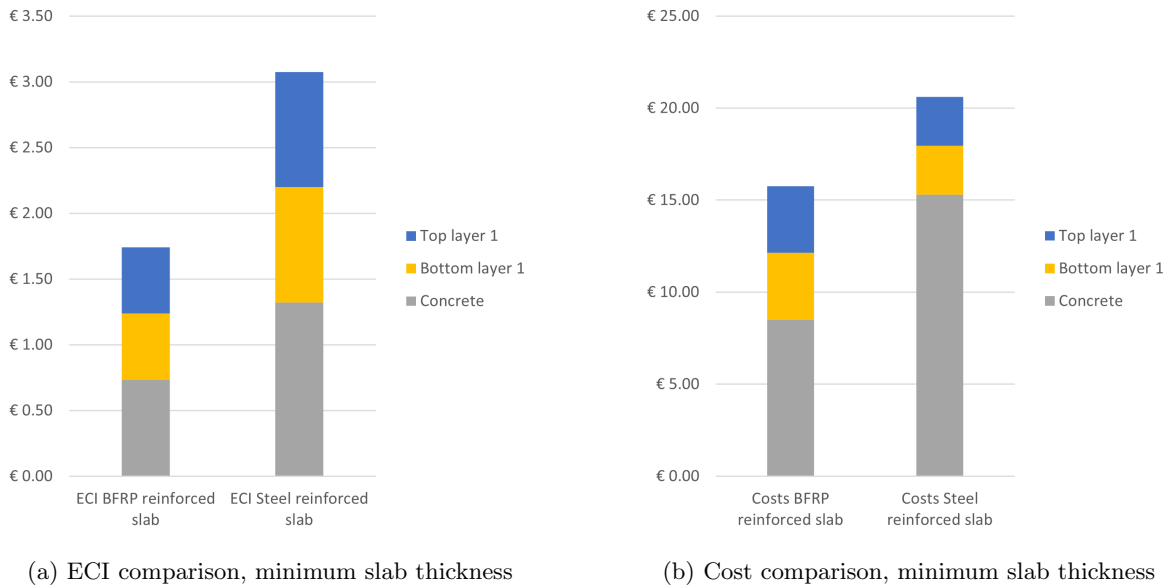


Figure A.10: Costs and ECI comparison square metre slab t=250 mm, b=1000 mm, equal geometry with reduced cover of BFRP-reinforced slab

The ECI-scores and costs are presented in table A.6 and figure A.10. The ECI-value for the slab with steel reinforcement is €3.07 for a square metre of slab, whereas the ECI-value for a slab with reinforced with BFRP-bars is €1.74. This is a reduction of €1.33 if BFRP-bars were to be applied. In the previous examples, the costs of a BFRP-bar reinforced slab turned out to be higher, even with a reduced concrete cover. However, a thickness difference of 40 mm is significant. In this example, a slab with a thickness of 50 mm with BFRP-bars is €15.76, compared to a cost of €20.60 for a steel reinforced concrete slab. This is a cost reduction of €4.84.

Upon adding serviceability to the equation (figure A.11), it is shown that a crack width of 0.2 mm is reached at a bending moment of 12.5 kNm. The crack width development of this slab with BFRP-bars according to the models in BRL0513 and ACI440 is exceeded if 0.5 mm is applied.

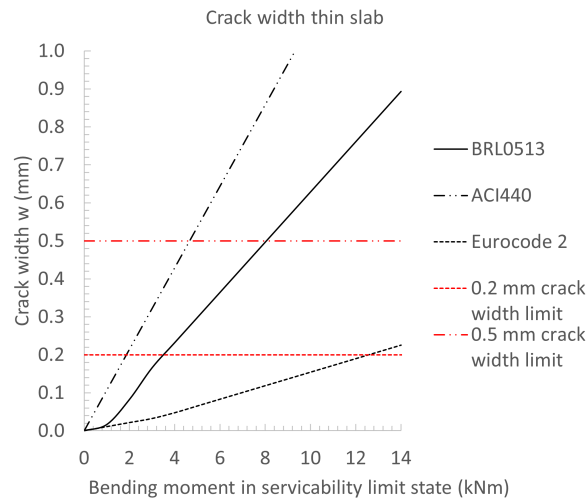


Figure A.11: Crack width development for a thin slab

To adapt to this, the centre-to-centre distance is adjusted to 69 mm and 56 mm for BRL0513 and ACI440 respectively. The results of this are presented in figure A.12 and table A.7 concerning the crack width development and the subsequent ECI-scores. Although the advantage in the ECI-score is still there with respect to a steel-reinforced slab, the adjustment for the serviceability limit state has increased the ECI-score compared to a configuration with a centre-to-centre distance of 100 mm. The advantage does increase as a larger crack width is allowed, as subsequently, the required minimum centre-to-centre distance is larger as well. This in turn reduces the ECI-score.

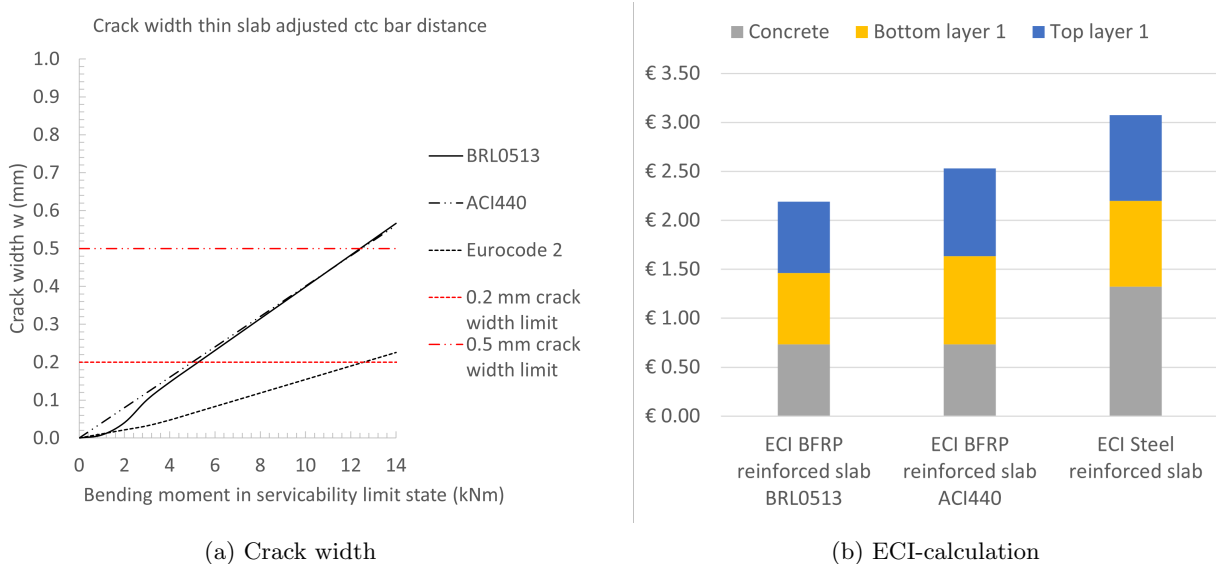


Figure A.12: Crack width curves and ECI-score for adjusted for serviceability limit state, thin slab

Table A.7: Components of total ECI-score per square metre slab minimum required thickness, b=1000 mm

Reinforcement	Bottom layer	Top layer	Concrete	Total
ECI-score BFRP-bars BRL0513	€0.73	€0.73	€0.74	€2.20
ECI-score BFRP-bars ACI440	€0.90	€0.90	€0.74	€2.54
ECI-score Reinforcement steel	€0.88	€0.88	€1.32	€3.07

A.4 Structural parameters

In the structural parameter comparison, the bending moment capacity, bond behaviour subsequently cracking are subject to research. The bending moment capacity calculations vary among different design guidelines. Slabs and beams are parametrically designed according to the Dutch BRL0513 [CvD, 2015] code and the American ACI440 [Busel, 2006] code for reinforced concrete flexural structures. These codes are chosen since the Dutch BRL0513 is closest to the Dutch concrete market for concrete structures with embedded FRP-reinforcement bars, whereas the ACI440 is mostly applied internationally in structural design. A comparison with a slab or beam with reinforcement steel according to the effectual Eurocode 2 [European Committee for Standardization, 2022] is made.

The cracking behaviour of structures reinforced with BFRP-bars is subject to debate in the thesis. As a consequence of this, the bond behaviour of the reinforcement bar is subject to research. The crack width models used in the design guides and the parameters that influence the cracking according to these models are compared.

Assumptions

The BFRP-bars used in the structural parameter analyses are assumed to have a characteristic tensile strength of 1000 MPa. The Young's modulus is assumed to 50 GPa. The rupture strain is assumed to be 2.60% These minimum values are guaranteed by technical approval for the BFRP-bars from manufacturer Orlitech, which in reality might be higher. Furthermore, the bond factor ζ_{bf} used in the cracking is assumed to be 1.5, however, this factor differs from the surface deformation of the BFRP-bars, as rougher sand-coatings are likely to provide better bond strength than fine sand coatings [S. Solyom, 2017] [Sólyom, 2017].

Ultimate bending moment resistance

The determination of the bending moment resistance of a concrete structure differs from guideline to guideline. As the ACI440 [Busel, 2006] is most used globally and the BRL0513 [CvD, 2015] is a Dutch standard applied for the design of concrete structures reinforced with embedded FRP-bars, these design codes are scrutinized. To draw a comparison with concrete reinforced with steel bars, the design codes in the Eurocode 2 [European Committee for Standardization, 2022] are examined as well.

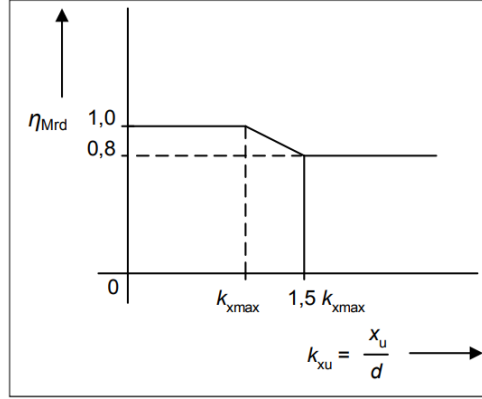
Ultimate bending moment resistance BRL0513 (BFRP)

The formula's for the bending moment resistance provided in the BRL0513 depends on a factor k_{xu} , which is determined in equation A.2.

$$k_{xu} = \frac{x_u}{d} \leq k_{x_{max}} = \frac{0.0025E_{bfrp}}{0.0025E_{bfrp} + f_{bfrp}} \quad (A.2)$$

If this prerequisite cannot be met, the bending moment has to be multiplied with η_{Mrd} according to figure A.13. If k_{xu} oversteps $k_{x_{max}}$ by a factor 1.5, the reduction factor remains limit at 0.8.

For the calculation of the bending moment resistance, 2 formula's are provided by the BRL0513. The applicability of the formula's depends on the value of k_{xu} . These formulas and its prerequisites for applying are shown in equations A.3 to A.6.


 Figure A.13: Determination reduction factor η_{Mrd} according to BRL0513 [CvD, 2015]

 for $k_{xu} \leq 1.3k_{xmax}$:

$$M_{Rd,bfrp} = \eta_{Mrd} A_{bfrp} f_{bfrp} \left(d - 0.6 \frac{A_{bfrp} f_{bfrp}}{b f_{cd}} \right) \quad (A.3)$$

 for $k_{xu} > 1.3k_{xmax}$:

$$M_{Rd,bfrp} = \left(\frac{\mu_1 \mu_2}{1040000 f_{cd}} - \frac{\mu_1^2}{400000 f_{cd}} - \frac{\mu_1}{402} + \frac{\mu_2}{1890} \right) b d^2 \quad (A.4)$$

Where:

$$\mu_1 = E_{bfrp} \rho_{bfrp} \quad (A.5)$$

$$\mu_2 = \sqrt{7\mu_1^2 + 6000 f_{cd} \mu_1} \quad (A.6)$$

By varying the reinforcement A_{bfrp} in the cross-section from 300 mm² to 3000 mm², the force per metre width of slab in the reinforcement bars increases. By differing the effective height of the slab, the lever arm increases of the reinforcement bars, therefore the ultimate bending moment resistance increases as well. In figure A.14, the ultimate bending moment resistances according to the BRL0513 for concrete classes C20/25, C30/37 and C40/50 with effective heights deviating from 150 mm to 450 mm with 50 mm increments and varying reinforcement amounts in the cross-section for a 1000 mm wide slab are shown.

The curves for the bending moment resistance show a steep increment in bending moment resistance as A_{bfrp} increases. For this part of the curve, the bending moment resistance is located in the first regime of the bending moment resistance determination (for $k_{xu} \leq 1.3k_{xmax}$), for which equation A.3 is utilized. For this part of the curve, the increment is almost linear.

Appendix A – Parameter Study

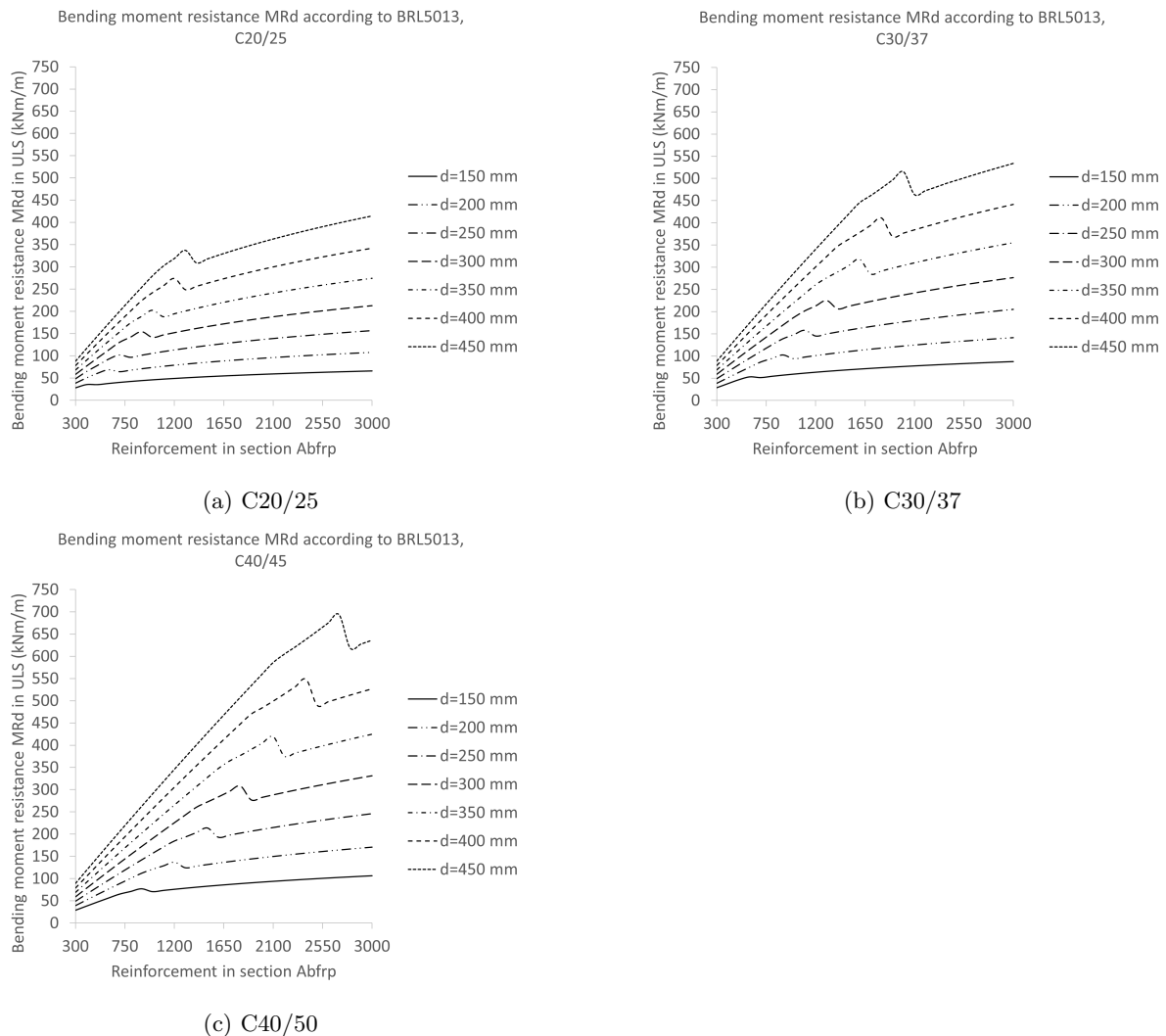


Figure A.14: Bending moment diagrams for parameter A_{bfrp} for concrete classes C20/25, C30/37, C40/50 according to BRL0513

When the height of the concrete compression zone in ULS x_u and the parameter k_{xu} surpass $k_{x_{max}}$ by 1.3 times, the curve transitions into its second phase. This is dependent on the area of reinforcement in the cross-section. In practice, this means that the cross-section switches from under-reinforced to over-reinforced and the failure mode switches from tensile failure in the reinforcement to crushing of the concrete compression zone. In the second phase, the formula used leads to a brief increase in the bending moment along the curve. The second phase initiates at the initial deviation in the slope of the curves depicted in figure A.14. Following this decline, the bending moment resistance sees a subsequent increase, albeit not at the same rate observed in the initial part of the curve.

Ultimate bending moment resistance ACI440 (BFRP)

The provisions in the American ACI440 design code for the ultimate bending moment resistance are distinguished into three zones depending on the reinforcement ratio. figure A.15 shows these three zones for concrete sections. The section is either tension-controlled, in a transition zone or compression-controlled. A reduction factor ϕ is multiplied with the nominal flexural strength M_n which has to be greater or equal to the bending moment on the structure M_u (equation A.7). This reduction factor is utilized to provide a conservative value for the bending moment resistance to account for the non-ductile behaviour of the reinforcement material but also takes into account long-term effects.

$$\phi M_n \geq M_u \quad (A.7)$$

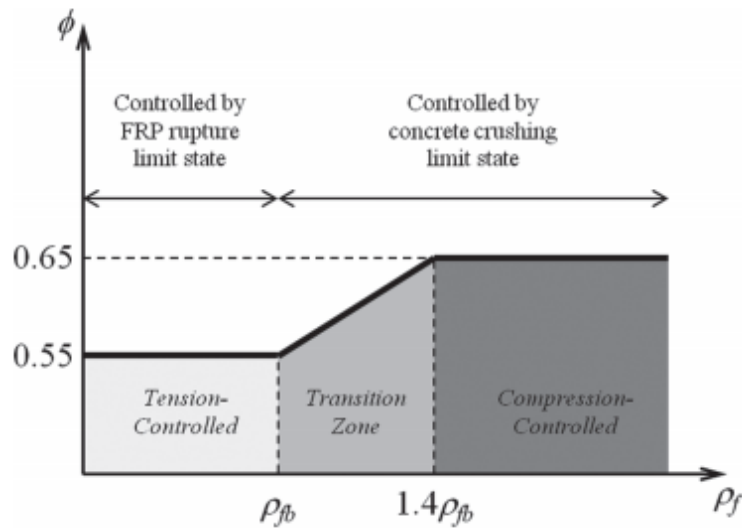


Figure A.15: Strength reduction factor according to ACI440 [Busel, 2006]

The strength reduction factor ϕ is determined using a threshold for the reinforcement ratio which is noted as ρ_{fb} . If the reinforcement ratio ρ_f of the reinforced concrete structure is below ρ_{fb} , the section is tension controlled. In this case, the rupture strength of the BFRP reinforcement is governed in the section. The reinforcement ratio is determined according to equation A.8.

$$\rho_f = \frac{A_f}{bd} \quad (A.8)$$

The balanced reinforcement ratio ρ_{fb} is determined according to equation A.9

$$\rho_{fb} = 0.85\beta_1 \frac{f'_c}{f_{fu}} \frac{E_f \varepsilon_{cu}}{E_f \varepsilon_{cu} + f_{fu}} \quad (A.9)$$

for $\rho_f \leq \rho_{fb}$, a reduction factor of 0.55 is applied and the section is classified as tension controlled. For $\rho_{fb} \leq \rho_f \leq 1.4\rho_{fb}$, the value for ϕ is determined according to equation A.10. For $\rho_f \geq 1.4\rho_{fb}$, the value for ϕ is 0.65.

$$\phi = 0.3 + 0.25 \frac{\rho_b}{\rho_{fb}} \quad (\text{A.10})$$

The parameters β_1 , the design tensile strength of the reinforcement bars f_{fu} and f'_c in equation A.9 are determined by using equations A.11 and A.12. The value for β_1 may be taken as 0.85 for design concrete compressive strengths f'_c up to 28 MPa. For concrete classes with higher design compressive strengths, the value is reduced with a rate of 0.05 for every 7 MPa above 28 MPa, with a minimum value of 0.65. The design tensile strength of the reinforcement bars f_{fu} is determined according to equation A.11.

$$f_{fu} = C_e f_{fu}^* \quad (\text{A.11})$$

Where C_e is an environmental reduction factor. For concrete structures exposed to weather influences, this value should be taken as 0.8 [Busel, 2006]. f_{fu}^* is the guaranteed tensile strength. This value is defined as the mean tensile strength of test samples minus three times the standard deviation (according to equation A.12).

$$f_{fu}^* = f_{fu,ave} - 3\sigma \quad (\text{A.12})$$

When ρ_f exceeds ρ_{fb} , the section falls into either compression control or the transition zone, with the concrete's crushing as the governing limit state. Consequently, it necessitates a reduction in the full design tensile strength f_{fu} of the reinforcement material. This specific limit state is illustrated in figure A.16. Instead of employing f_{fu} , a reduced design tensile strength, denoted as f_f , is determined using equation A.13

$$f_f = \sqrt{\frac{(E_f \varepsilon_{cu})^2}{4} + \frac{0.85 \beta_1 f'_c}{\rho_f} E_f \varepsilon_{cu}} - 0.5 E_f \varepsilon_{cu} \leq f_{fu} \quad (\text{A.13})$$

The nominal flexural strength M_n can be determined by the height of the concrete compression zone and subsequently the nominal flexural strength using equations A.14 and A.15.

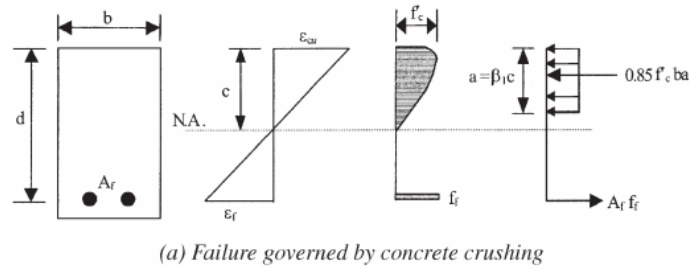


Figure A.16: Stress and strain distribution at ultimate conditions, Failure governed by concrete crushing failure (compression controlled) [Busel, 2006]

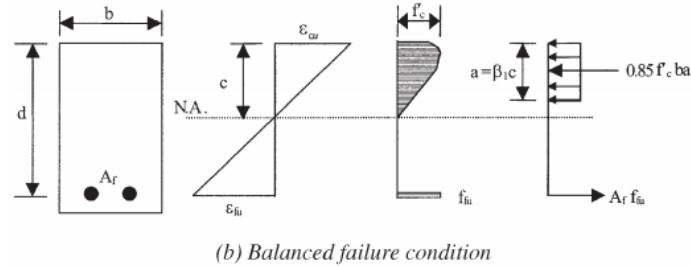


Figure A.17: Stress and strain distribution at ultimate conditions, balanced failure (Transition zone) [Busel, 2006]

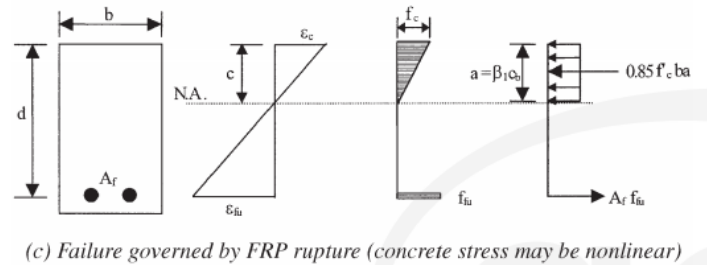


Figure A.18: Stress and strain distribution at ultimate conditions, Failure governed by FRP rupture (tension controlled) [Busel, 2006]

$$M_n = A_f f_f \left(d - \frac{a}{2} \right) \quad (\text{A.14})$$

Where:

$$a = \frac{A_f f_f}{0.85 f'_c b} \quad (\text{A.15})$$

For cross-sections classified as compression controlled or within the transition zone according to figure A.15 en equations A.8 and A.9, ACI440 does not require the minimum reinforcement in the cross-section to be checked.

For $\rho_f < \rho_{fb}$, the controlling limit state is the design rupture strength of the FRP reinforcement material. In this case, the section is tension controlled and the stress in the concrete compression zone is assumed to be linear, which is presented in figure A.18. Based on the ultimate strain in the concrete, the height of the concrete compression zone c_b is determined using equation A.17. As the design rupture strength of the reinforcement material is the determining factor, f_{fu} may be used. The nominal flexural strength M_n is determined using equation A.16

$$M_n = A_f f_{fu} \left(d - \frac{\beta_1 c_b}{2} \right) \quad (\text{A.16})$$

Where the concrete compression zone height c_b is determined as follows:

$$c_b = \frac{\varepsilon_{cu}}{\varepsilon_{cu} + \varepsilon_{fu}} d \tag{A.17}$$

For a tension-controlled section, the minimum reinforcement is required to be checked using equation A.18.

$$A_{f,\min} = \frac{0.41\sqrt{f'_c}}{f_{fu}} b_w d \geq \frac{2.3}{f_{fu}} b_w d \tag{A.18}$$

Figure A.19 shows the bending moment resistances for the same concrete strength classes and the differing effective heights with the reinforcement in the section A_{bfrp} varying from 300 mm²/m to 3000 mm²/m.

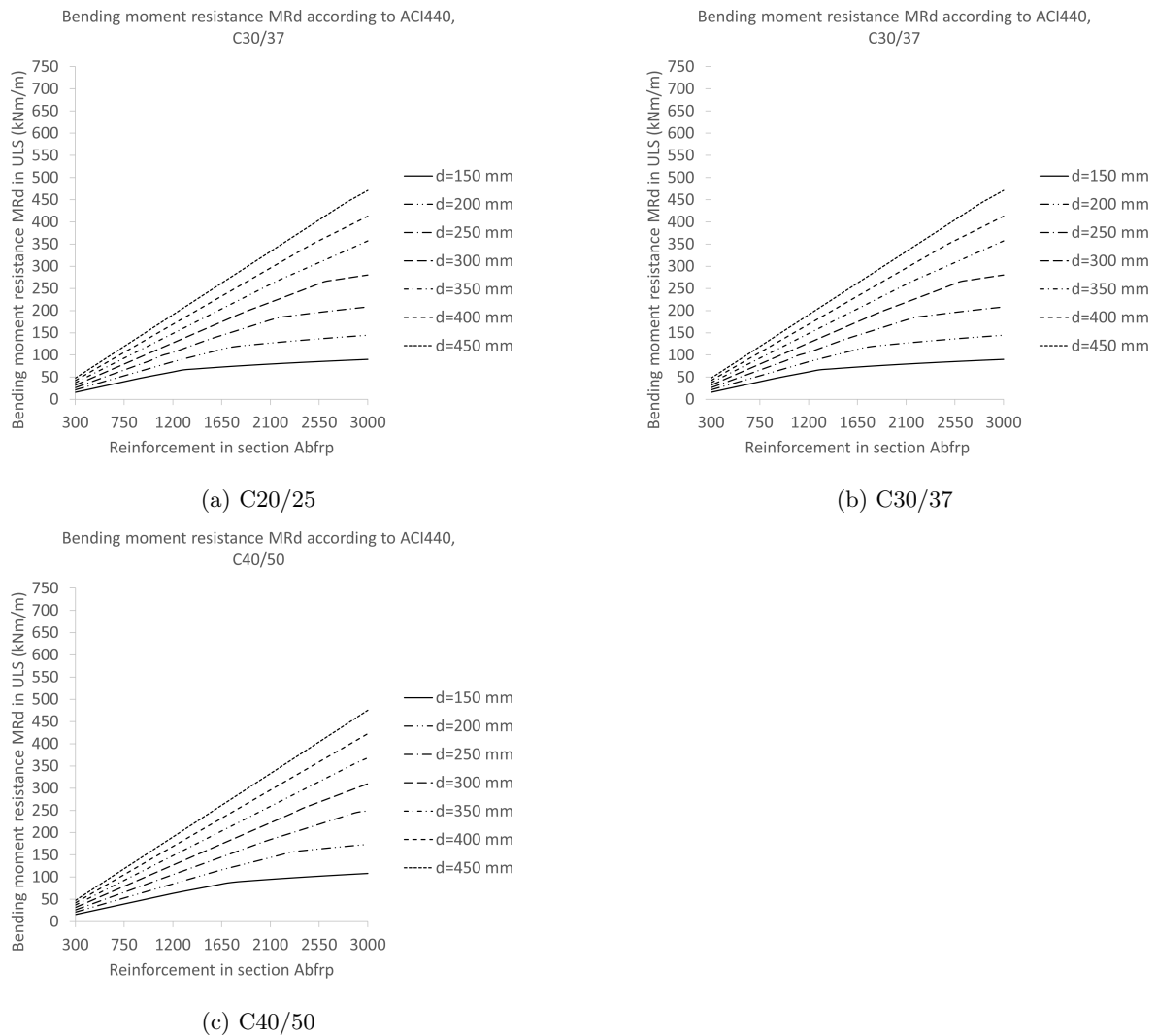


Figure A.19: Bending moment diagrams for parameter A_{bfrp} for concrete classes C20/25, C30/37, C40/50 according to ACI440

Ultimate bending moment resistance Eurocode 2 (Reinforcement steel)

To draw a comparison of the ultimate bending moment capacities of slabs reinforced with BFRP-bars according to the Dutch BRL0513 and American ACI440, a concrete slab reinforced with reinforcement steel B500B is designed with the same boundary conditions. The results are shown in figure A.20.

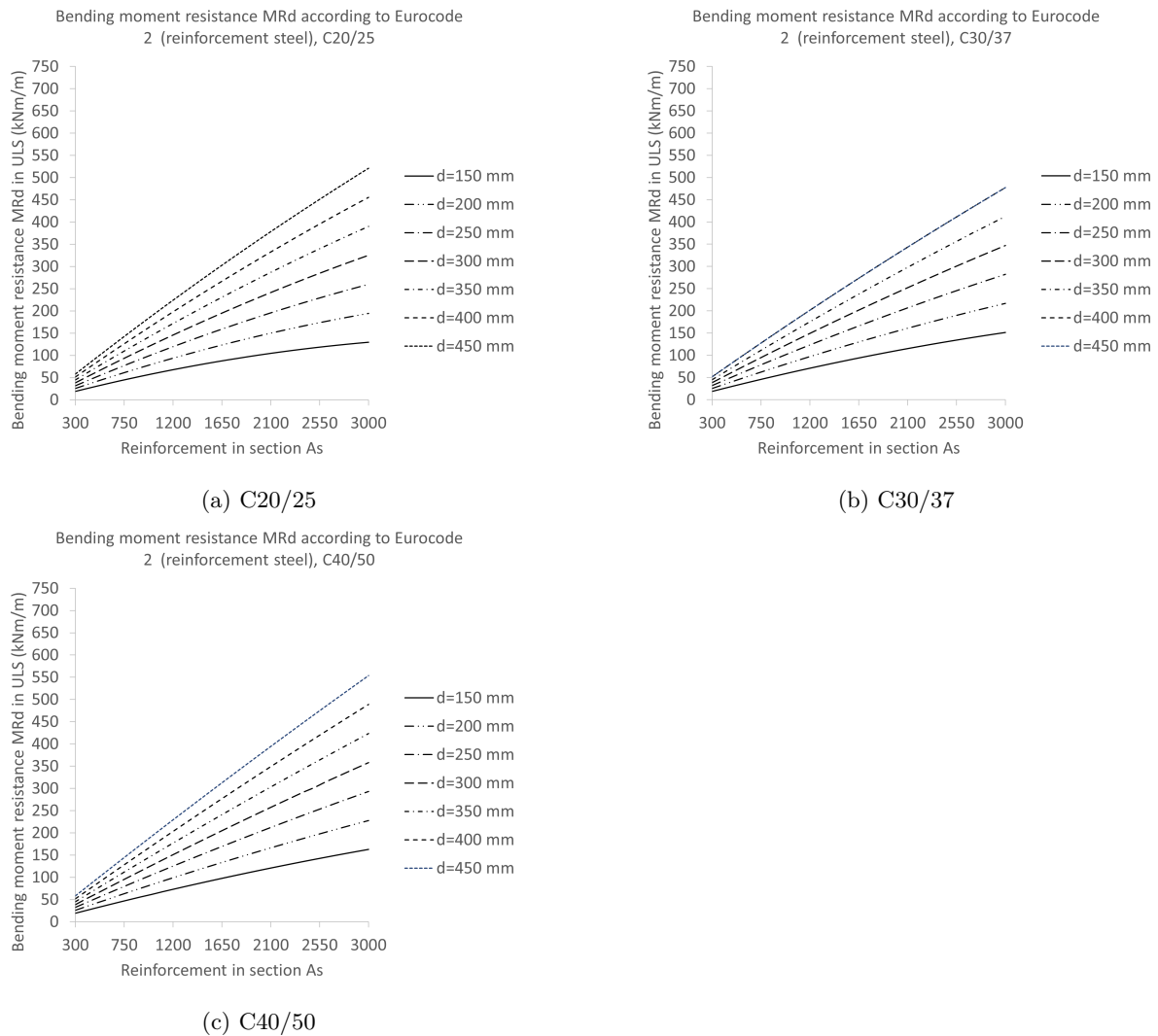


Figure A.20: Ultimate bending moment diagrams for parameter A_s for concrete classes C20/25, C30/37, C40/50 according to Eurocode 2

Ultimate bending moment resistance comparison

The bending moment resistance of a slab with an effective height of 250 mm and concrete strength class C30/37 is illustrated in Figure A.21. The curves representing the analysis from the selected design codes are juxtaposed for comparative purposes. Notably, a significant similarity emerges between the ACI440 curve during the

transition phase of analysis and the second phase of the BRL0513 analysis. These curves show substantial correspondence, with the second phase of the BRL0513 curves following a similar trajectory. Subsequent graphs pertaining to these analyses can be found in Appendix B, figure B.1a to figure B.1u.

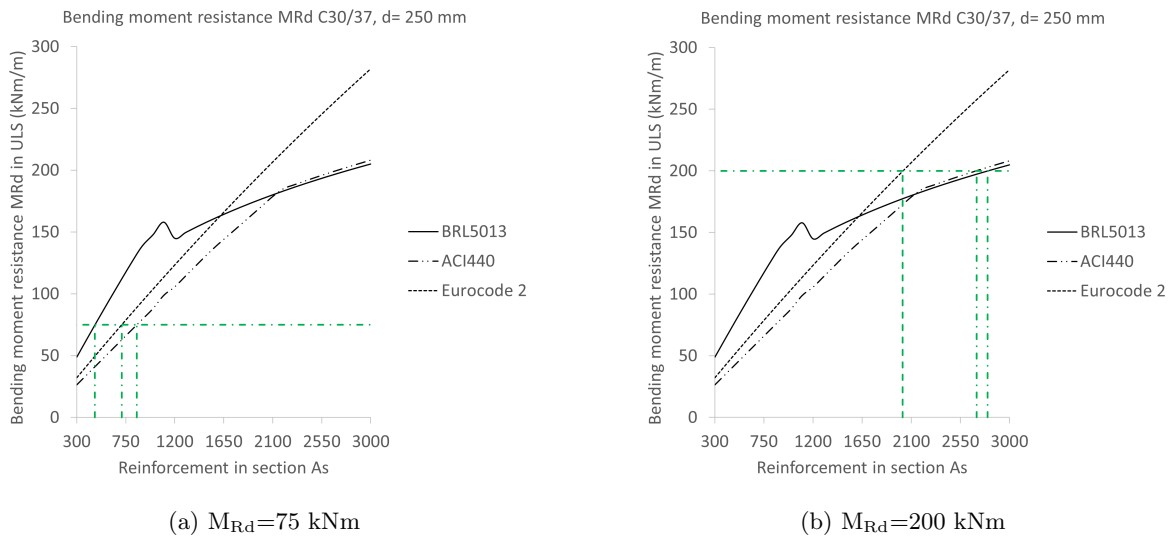


Figure A.21: Comparison bending moment resistance BRL0513, ACI440 and EC2 for C30/37, d=250 mm

In subfigure A.21a, a line is drawn at 75 kNm. The required amount of reinforcement required for a bending moment resistance of 75 kNm is $467 \text{ mm}^2/\text{m}$ according to the BRL0513 code. An analysis according to the ACI440 requires $852 \text{ mm}^2/\text{m}$ to reach the same bending moment resistance. The ACI440 analysis is more conservative than the Eurocode 2 as its curve does not reach greater values than a slab reinforced with steel bars for this slab design. A slab reinforced with reinforcement steel bars requires $713 \text{ mm}^2/\text{m}$.

Shown in subfigure A.21b, to achieve a bending moment resistance of 200 kNm, the BRL0513 code requires the reinforcement amount to be $2800 \text{ mm}^2/\text{m}$, which approximately coincides with the required amount of $2700 \text{ mm}^2/\text{m}$. A concrete slab reinforced with reinforcement steel however only requires $2022 \text{ mm}^2/\text{m}$ to achieve a bending moment capacity of 200 kNm. In this example, the cross-over point of favourability between the BFRP-bars and the reinforcement steel at approximately 161 kNm. This point is located at the intersection of the BRL0513 and EC2 curves. Figure A.22 shows curves that indicate the favourability depending on the required bending moment capacity, the effectual height and the concrete strength class.

For each analysis, for which the resulting curves are shown in Appendix B, figure B.1a to figure B.1u, the ACI440 for concrete structures reinforced with BFRP-bars curves never reaches greater values than EC2 curves for reinforcement steel.

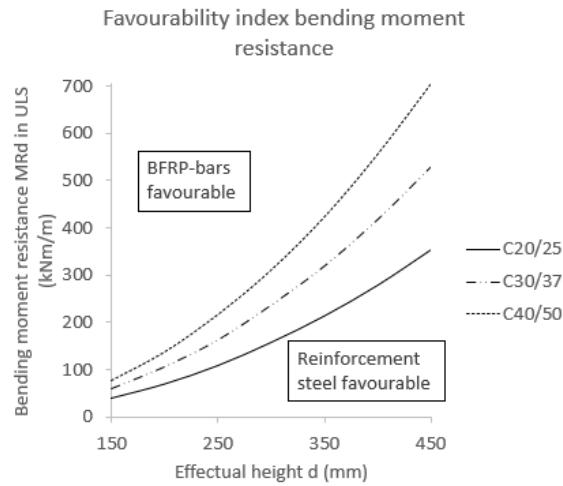


Figure A.22: Favourability index BFRP according to BRL0513 and reinforcement steel according to Eurocode 2

At $m_{Rd}=75$ kNm, the ECI-value for the required reinforcement according to the BRL0513 is considerably more favourable than the ECI-value for the required reinforcement steel to achieve the same bending moment capacity with €0.30 for BFRP versus €0.79 for reinforcement steel. Although significantly more reinforcement is required to reach a bending moment capacity of 200 kNm when applying BFRP-bars, the ECI-value remains lower than that of reinforcement steel, as shown in figure A.24.

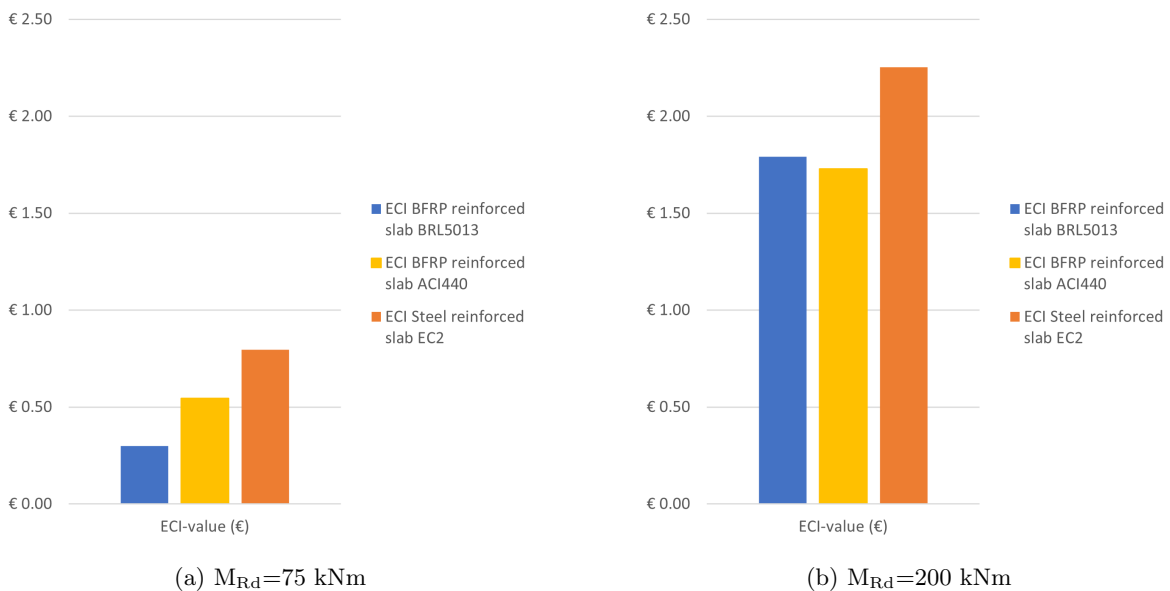


Figure A.23: Comparison ECI-value for BRL0513, ACI440 and EC2 for C30/37, bottom reinforcement first layer, $d=250$ mm, C30/37

Appendix A – Parameter Study

The costs however generally remain in favour of the reinforcement steel, except for the required reinforcement according to the BRL0513 at 75 kNm. As the required bending moment capacity exceeds the cross-over point of the BRL0513 and the EC2 curves, the cost advantage of the reinforcement steel becomes apparent, which is presented in figure A.24. The costs for the required reinforcement steel to reach a 200 kNm bending moment resistance is €6.83, which is considerably less than €12.94 and €12.47 according to the BRL0513 and ACI440 respectively.

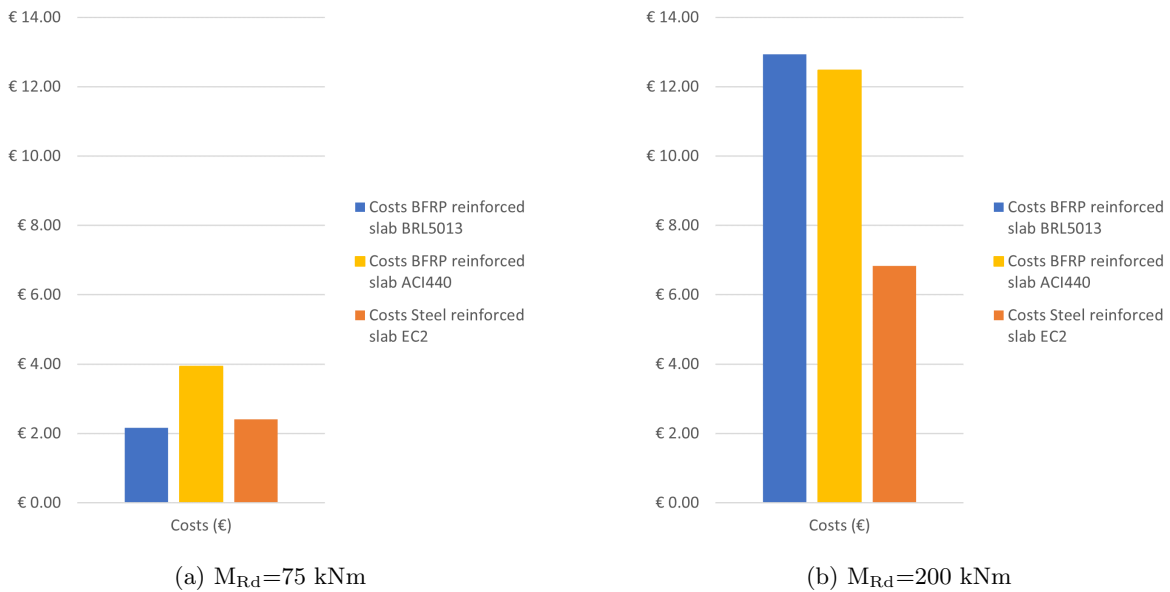


Figure A.24: Comparison ECI-value for BRL0513, ACI440 and EC2 for C30/37, bottom reinforcement first layer, $d=250$ mm, C30/37

The results for the required reinforcement, the ECI-values and costs are compiled in table A.8. Note that these results only account for the structural reinforcement in the bottom layer. In relation to the required reinforcement, the ECI-score of a slab reinforced with BFRP-bars is consistently lower than a steel-reinforced slab. However, the production cost remains higher. As table A.8 only outlines tensile reinforcement in bottom layer 1, these differences will only widen if the distribution reinforcement and the top reinforcement layers are taken into account.

Table A.8: Required reinforcement and corresponding ECI-values and Costs slab $d=250$ mm for $M_{Rd}=75$ kNm and $M_{Rd}=200$ kNm

Code	$M_{Rd}=75$ kNm			$M_{Rd}=200$ kNm		
	A_{bfrp}	ECI	Costs	A_{bfrp}	ECI	Costs
BRL0513 (BFRP)	467 mm ²	€0.30	€2.16	2800 mm ²	€1.79	€12.94
ACI440 (BFRP)	852 mm ²	€0.55	€3.94	2700 mm ²	€1.73	€12.94
EC2 (Reinf. steel)	713 mm ²	€0.79	€2.41	2022 mm ²	€2.25	€6.83

Serviceability, crack width

The serviceability limit state of reinforced concrete from a standpoint of durability is often the determining factor in reinforced concrete structural elements. One of these aspects of the SLS-analysis is the crack width control. According to Eurocode 2, the crack width cannot exceed a certain threshold to ensure the durability of the concrete structure and prevent the deterioration of the reinforcement steel. As the deterioration of the reinforcement is less of a problem, a larger crack width is allowed up to 0.70 mm according to the ACI440. This limit requirement does not stem from a durability requirement, but rather from aesthetics.

Crack width BRL0513 (BFRP)

The approach to crack width control the BRL0513 has is largely identical to the Eurocode 2 except for a bond factor ξ_{bf} , which influences the crack spacing, as well as the limiting factor for the crack spacing. The formulae used in crack width control according to BRL0513 are shown in equations A.19, A.20 and A.21.

$$w_k = s_{r,max,bf}(\varepsilon_{bf} - \varepsilon_{cm}) \quad (A.19)$$

Where:

$$\varepsilon_{bf} - \varepsilon_{cm} = \frac{\sigma_{bf} - k_t \frac{f_{ct,eff}}{\rho_{p,eff}} (1 + \alpha_{bf} \rho_{p,eff})}{E_{bf}} \geq 0.6 \frac{\sigma_{bf}}{E_{bf}} \quad (A.20)$$

$$s_{r,max,bf} = k_3 c + \frac{k_1 k_2 k_4 \varnothing_{bf}}{\rho_{p,eff}} < \frac{\sigma_{bf} \varnothing_{bf}}{3.6 \xi_{bf} f_{ctm}} \quad (A.21)$$

Where:

$$k_1 = \frac{0.8}{\xi_{bf}} \quad (A.22)$$

In Eurocode 2, the value for k_1 is to be taken as 0.8 for bonded bars. In the BRL0513, this parameter in the crack spacing formula is adapted by means of bond factor ξ_{bf} to account for the difference in bond strength.

Parameters of note are the tensile strength of the concrete $f_{ct,eff}$, the effective reinforcement percentage $\rho_{p,eff}$, the bar diameter \varnothing_{bf} , the concrete cover c and the tensile stress σ_{bf} in the reinforcement in SLS. The effects of these parameters are researched in this section.

Figure A.25 shows the crack width curves for concrete cover $c=15$ mm up to $c=45$ mm with increments of 5 mm for a concrete slab with a concrete strength class of C20/25, a set effective height of $d=250$ mm and a reinforcement of $A_{bfrp}=1500$ mm²/m. The running variable is the bending moment in the serviceability state, which drives the tensile stress in the reinforcement. The curves show an exponential increase in crack width development until a limit value for which the crack spacing does not increase anymore. This causes the crack width development to increase linearly according to the model used in the BRL0513.

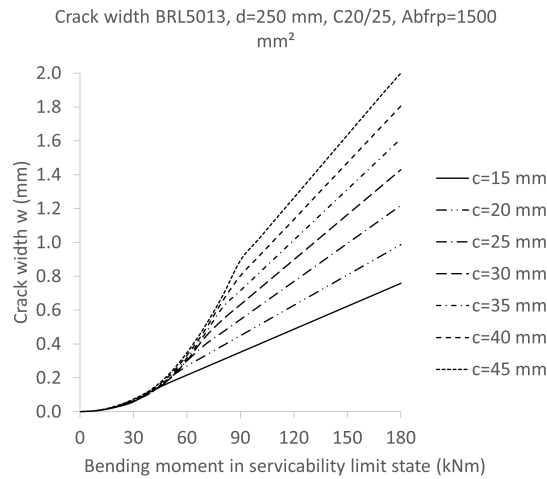


Figure A.25: Crack width development curves according to BRL0513 for various concrete cover c values, C20/25, $d=250$ mm, $A_{bfrp}=1500$ mm²/m

The relevance of crack width control becomes apparent when the maximum bending moment is limited by the maximum allowable crack width w_{max} . According to the curve for concrete cover $c=30$ mm in figure A.25, the maximum bending moment is 76.70 kNm in SLS for the maximum allowable crack width of 0.50 mm. For comparison, the ultimate bending moment resistance in ULS for this slab design is 135.38 kNm, which is a factor of 1.77 difference. This renders the influence of crack width control significant, where this aspect is regularly the decisive factor in the design of concrete structures reinforced with BFRP-bars. By increasing the reinforcement from 1500 mm²/m to 2500 mm²/m, the reinforcement percentage is increased significantly. Crack width curves for this slab design are shown in figure A.26a. The maximum bending moment in SLS corresponding to a crack width of 0.50 mm is 128 kNm. For comparison, the ultimate bending moment according to the BRL0513 guideline is 166.67 kNm. By increasing the reinforcement percentage, the factor between the maximum allowable bending moments in SLS and ULS is now reduced to 1.30 instead of 1.77.

Increasing the concrete strength class from C20/25 to C30/37 does not have a significant effect on the crack width development according to the BRL0513. The corresponding curves are shown in figure A.26. The increase in tensile strength of the concrete does not influence the crack width significantly. The bending moment in SLS corresponding to the maximum allowable crack width of 0.50 mm is 83.3 kNm, which is only slightly higher than the same slab with C20/25. The increase in concrete strength however does influence the ultimate bending moment in ULS. The ultimate bending moment is increased to 173.79 kNm.

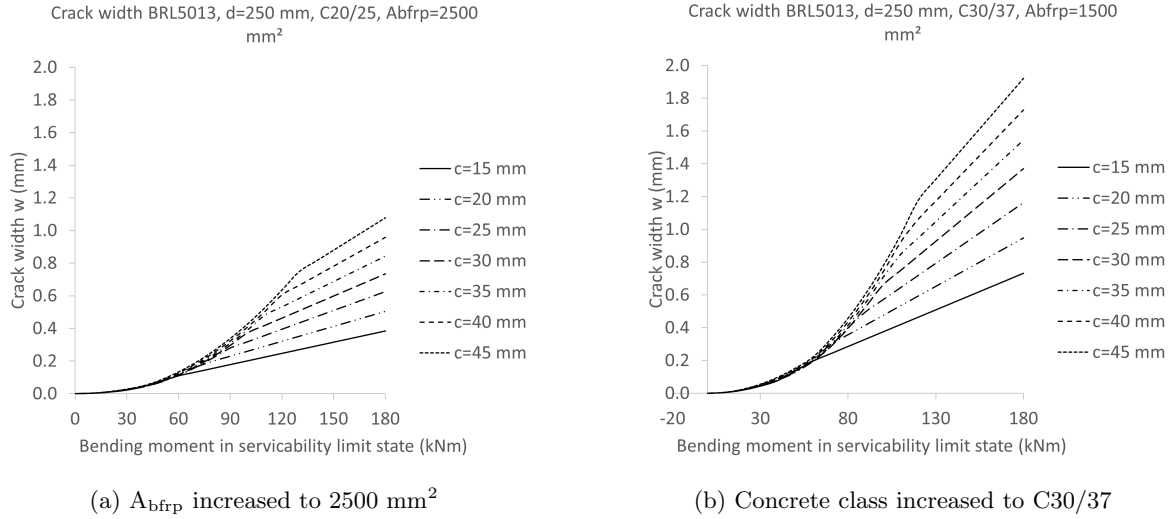


Figure A.26: Crack width development curves according to BRL0513 for various concrete cover c values with increased properties

Crack width ACI440 (BFRP)

Whereas the BRL0513 limits the crack width to 0.50 mm, the ACI440 allows a crack width of 0.7 mm if not subjected to aggressive environments, otherwise, the maximum allowable crack width is 0.50 mm. The crack width analysis according to the ACI440 is relatively less elaborate than the BRL0513 and Eurocode 2. The formula used for the crack width control is based on the maximum concrete cover from the bottom of the concrete to the centre of the tensile reinforcement bar, denoted as d_c . Equation A.23 is used to determine the upper bound of the parameter d_c .

$$d_c \leq \frac{E_f w_{\max}}{f_{fs} \beta k_b} \quad (\text{A.23})$$

Note that this formula is based on the maximum allowable crack width. By rearranging equation A.23, the crack width can be noted as the unknown as a function of the tensile stress in the reinforcement f_{fs} . The formula is rearranged in equation A.24.

$$w = \frac{f_{fs} \beta d_c k_b}{E_f} \leq w_{\max} \quad (\text{A.24})$$

The parameters in equation A.24 are determined in equation A.25 to A.31

$$\beta = \frac{h - kd}{d - kd} \quad (\text{A.25})$$

$$f_{fs} = M_s \frac{n_f d (1 - k)}{I_{cr}} \quad (\text{A.26})$$

Where:

$$k = \sqrt{2\rho_f n_f + (\rho_f n_f)^2} - \rho_f n_f \quad (\text{A.27})$$

$$d_c = h - d \quad (\text{A.28})$$

$$\rho_f = \frac{A_f}{bd} \quad (\text{A.29})$$

$$n_f = \frac{E_f}{E_c} \quad (\text{A.30})$$

$$I_{cr} = \frac{bd^3}{3} k^3 + n_f A_f d^2 (1 - k)^2 \quad (\text{A.31})$$

The computation of the other parameters has been established previously. The parameter M_s represents the bending moment at serviceability level, which is required to determine the tensile stress in the reinforcement f_{tu} . The parameter n_f is the factor of the Young's modulus of the BFRP-bar over that of the concrete. The parameter d_c represents the thickness of the concrete cover measured from extreme tension fibre to the centre of the bar. I_{cr} is the moment of inertia of a cracked section. Lastly, the parameter k represents the ratio of the depth of the neutral axis to the reinforcement depth.

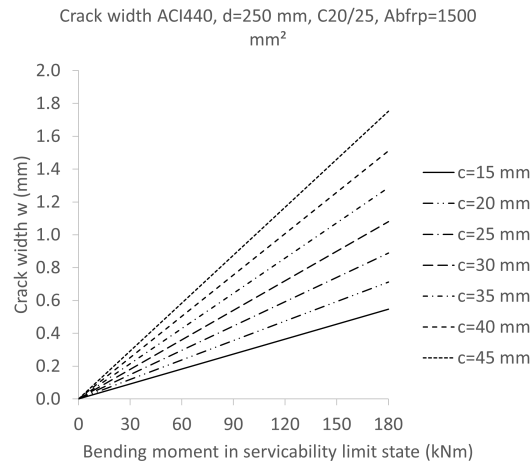


Figure A.27: Crack width development curves according to ACI440 for various concrete cover c values, C20/25, $d=250$ mm, $A_f=1500$ mm²/m

Figure A.27 shows the crack width curves of the various concrete covers as described previously. Due to the simple formula for crack width, crack width development according to this model is linear, contrary to the BRL0513 curves. For a w_{max} of 0.50 mm, a slab with a concrete cover of 30 mm, has a maximum serviceability bending moment of 83.33 kNm, which is comparable to the result of the BRL0513 analysis (76.70 kNm). The ultimate bending moment for this slab is 135.24 kNm, which again is comparable to the bending moment capacity

in ULS according to the BRL0513 analysis (135.35 kNm). The bending moment capacity in serviceability is a factor of 1.62 lower than the bending moment capacity.

The advantage of the ACI440 is the permission of a maximum crack width of 0.70 mm, provided there is no aggressive environment. The serviceability bending moment for this slab limited by crack width is 116.67 kNm, which is only a factor 1.16 lower than the ultimate bending moment capacity of 135.24 kNm. Therefore, crack width is less likely to be governing in the design.

By increasing the properties similar to the previous section, the same trends are noticeable. By increasing the reinforcement in the cross-section A_f to 2500 mm², the crack width development is significantly smaller, shown in figure A.28a. An increase in concrete strength class to C30/37 (figure A.28b) only marginally reduced the crack width development, however, these differences are negligible. Both options provide higher bending moment capacities, however, only the increase of the reinforcement ensures a more favourable crack development.

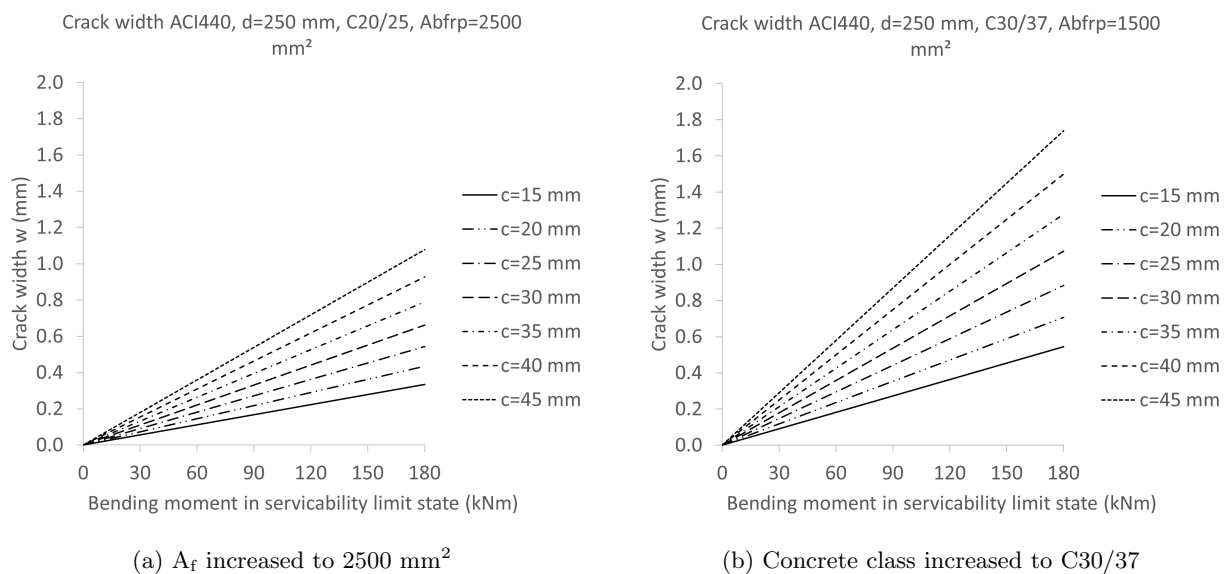


Figure A.28: Crack width development curves according to ACI440 for various concrete cover c values with increased properties

Crack width Eurocode 2 (Reinforcement steel)

The Young's modulus of the reinforcement bars significantly influences crack width development, typically resulting in smaller crack widths for steel-reinforced structures compared to those reinforced with BFRP-bars in concrete. Given that BFRP-bars exhibit a Young's modulus approximately one-fourth of that of reinforcement steel, the curves in Figure A.29, depicting various concrete covers c , are expected to reveal smaller crack widths.

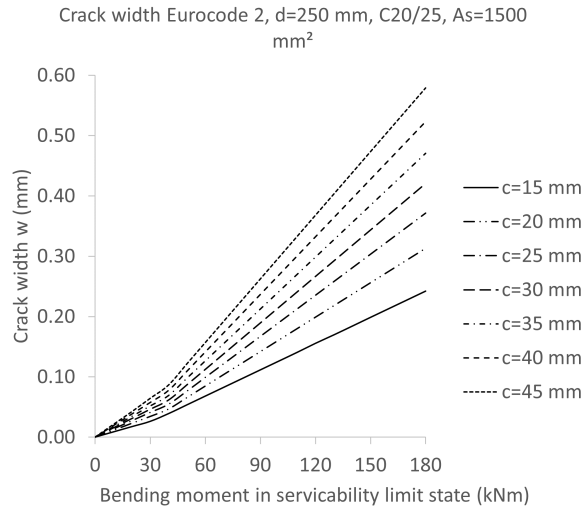
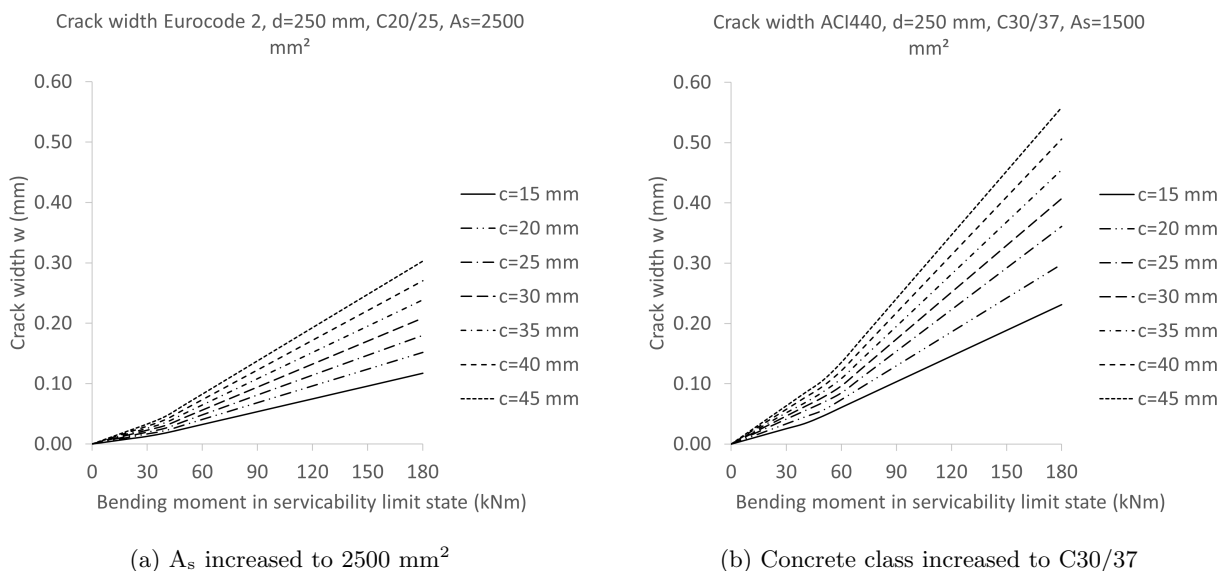


Figure A.29: Crack width development curves according to Eurocode 2 for various concrete cover c values, C20/25, $d=250$ mm, $A_f=1500$ mm²/m

For example, a slab with a concrete cover $c=30$ mm as described previously has a maximum bending moment in SLS of 85.88 kNm for a w_{max} of 0.2 mm. The ultimate bending moment capacity in ULS is 161,80 kNm, which is a factor of 1.88 higher. Therefore, the crack width is likely to be a governing and limiting aspect in the general design. Figure A.30 outlines the same trends as previous analyses with increased parameters. To effectively reduce the crack width development, adding reinforcement seems the most effective rather than increasing the concrete strength class.



(a) A_s increased to 2500 mm²

(b) Concrete class increased to C30/37

Figure A.30: Crack width development curves according to ACI440 for various concrete cover c values with increased properties

Crack width comparison

All graphs pertaining to comparing the crack width development are shown in Appendix C, figures C.1a to C.1u. The Eurocode 2 curves consistently remain below both ACI440 and BRL0513 curves. The BRL0513 starts at approximately the same slope as the Eurocode 2 curves but increases exponentially up to a point of a constant slope which is larger than the ACI440 curve slopes. The BRL0513 curve is more favourable until the exponential section of the curve intersects the ACI440 curve, which is roughly at the crossover point of the BRL0513 curve entering its linear section. After this crossover point, the BRL0513 crack width model is more conservative than the ACI440 model. Figure A.31 shows a comparison of the aforementioned slab design for both the most and least strict crack width limits in the researched codes. For concrete structures reinforced with BFRP-bars, this ranges from 0.5 mm to 0.7 mm. For steel-reinforced concrete structures, 0.2 mm to 0.4 mm is the interval for crack width.

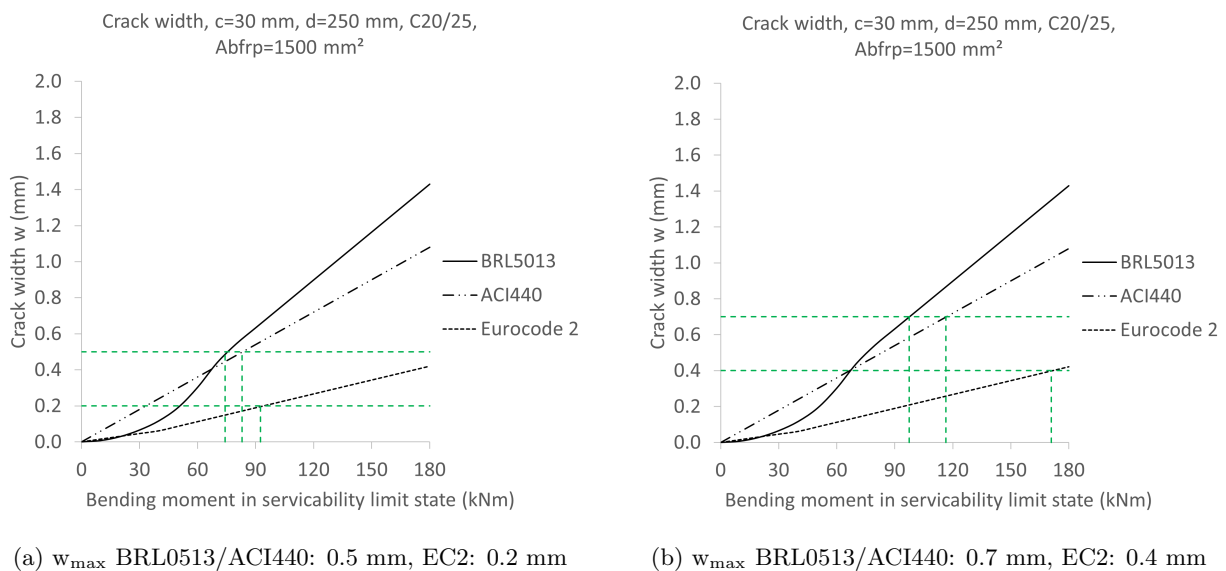


Figure A.31: Crack width comparison with code limits

The favourability of the ACI440 curves rapidly declines as the concrete cover increases, and the intersection moves further to the right. The exponential section of the BRL0513 curves becomes relatively larger, increasing its favourability.

In terms of favourability towards reinforcement steel, the greater maximum allowable crack width for the BFRP-bars ensures comparability in bending moments in permissible serviceability bending moments. The most strict maximum allowable crack width of 0.5 mm is reached for concrete structures reinforced with BFRP-bars is reached earlier than the 0.2 mm limit for steel-reinforced structures according to Eurocode. As this trend is visible in all comparative graphs in Appendix C (figures C.1a to C.1u), a larger maximum allowable crack width does not necessarily grant favourability towards concrete structures reinforced with BFRP-bars. However, the differences are still relatively small. For the upper boundaries of the allowable crack width (0.4 and 0.7 mm respectively) the difference becomes more apparent. Despite the greater maximum allowable crack width for BFRP-bars ensuring comparability in bending moments, the earlier attainment of the most restrictive crack width limit in BFRP-reinforced concrete challenges the presumed favorability, emphasizing the importance of thoughtful material selection for concrete structures.

Serviceability, bond factor

According to the provisions in the BRL0513, the crack width in the serviceability limit state is determined using equation A.21. The equation is a convolution of the crack spacing and the strain difference in the basalt fibre and the concrete. The crack spacing (equation A.21) is dependent on the bond factor ξ_{bf} , the effective reinforcement percentage $\rho_{p,eff}$, the bar diameter \varnothing_{bf} and the cover c .

By varying these parameters between certain boundaries, the significance of the individual parameters on the crack spacing can be visualized. These visualisations are shown in Appendix D, figures D.1a to D.1o. Figure A.32 shows one of these graphs. This graph shows the relation between the crack spacing and the bond factor for various effective reinforcement percentages.

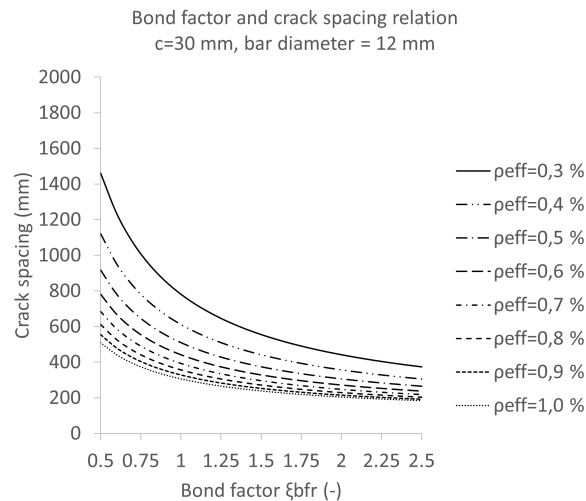


Figure A.32: Bond factor crack spacing relation for $\varnothing_{bf}=12$ mm, $c=30$ mm

As the bond factor increases, the crack spacing decreases. However, the curves for the crack spacing seem to be converging to a bottom limit depending on the curve and its input parameters. For a bond factor smaller than 1.0, the crack spacing grows exponentially.

A.5 Conclusions

The comparison between steel reinforcement and basalt fibre reinforcement in slabs of equal geometry and various cover thicknesses reveals intriguing trends. When substituting steel with BFRP-bars in slabs, BFRP exhibits a consistently lower Environmental Cost Indicator across different configurations. Despite the initial higher construction costs associated with BFRP, the reduced environmental impact, particularly in terms of concrete usage and global warming potential, is noteworthy. The adjustment of cover thickness significantly impacts both the ECI and costs of BFRP-reinforced slabs. Reducing the cover to 1.5 times the BFRP bar diameter amplifies the ECI advantage and narrows the cost disparity between BFRP and steel reinforcement. Notably, in slabs requiring minimum thickness for non-structural purposes, BFRP demonstrates a clear advantage in both ECI and potential cost savings. These findings highlight the potential environmental benefits of BFRP, especially in minimizing concrete usage and lessening environmental impact, despite initial higher costs. The

adaptability of BFRP in thinner, non-structural slabs underscores its promising role in sustainable construction practices.

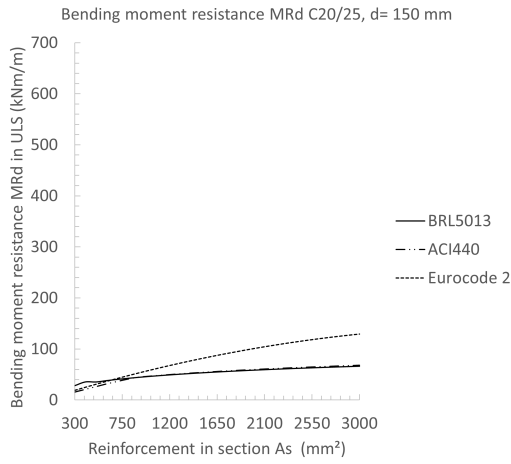
The crack width analysis across the assessed design codes shows varied crack width approaches. Eurocode 2 sets strict limits, while ACI440 allows wider cracks for aesthetics. BRL0513 aligns with Eurocode 2 but adapts for BFRP reinforcement using a bond factor and allows for a larger maximum crack width. The impact of parameters like concrete cover and reinforcement percentage on crack widths is evident. Increasing reinforcement significantly reduces crack widths, affecting serviceability bending moments. Changes in concrete strength minimally affect crack width in BRL0513 but substantially impact ultimate bending moments.

While the greater maximum allowable crack width for BFRP-bars ensures comparability in bending moments in permissible serviceability bending moments, the earlier attainment of the most restrictive crack width limit in BFRP-reinforced concrete challenges the presumed favorability over steel reinforcement according to Eurocode standards. The observed trend, illustrated in all comparative graphs in Appendix C, indicates that a larger maximum crack width does not necessarily grant an advantage to concrete structures reinforced with BFRP-bars. Thus, careful consideration of material selection is crucial for optimizing the performance and durability of concrete structures. ACI440 allows wider cracks initially but becomes more conservative than BRL0513 after a certain point. The higher the applied concrete strength of a concrete structure reinforced with BFRP-bars, the more likely it is for the SLS-analysis to be decisive. If the crack width has to be reduced, according to the graphs in figure A.26, it is more effective to increase the reinforcement percentage $\rho_{p,eff}$, rather than the concrete strength class.

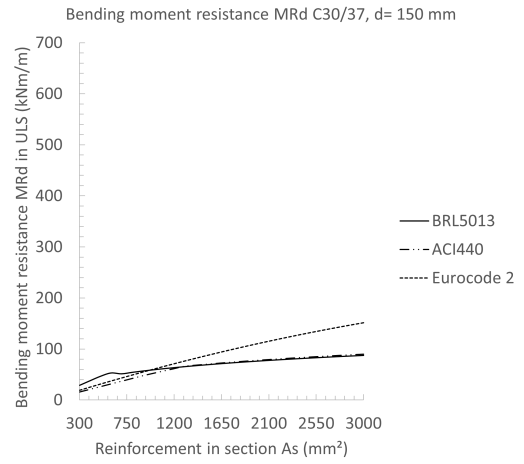
Appendix B

Graphs bending moment resistance parameter study

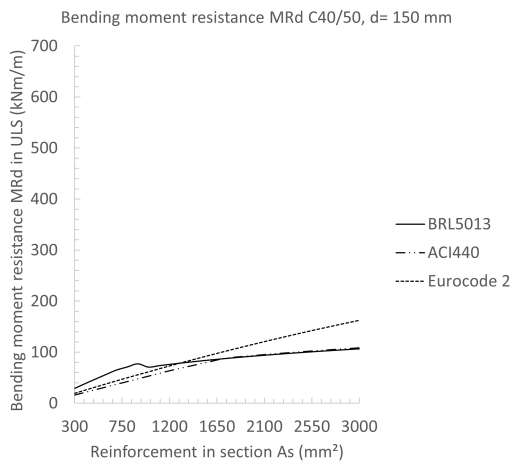
Appendix B – Graphs bending moment resistance parameter study



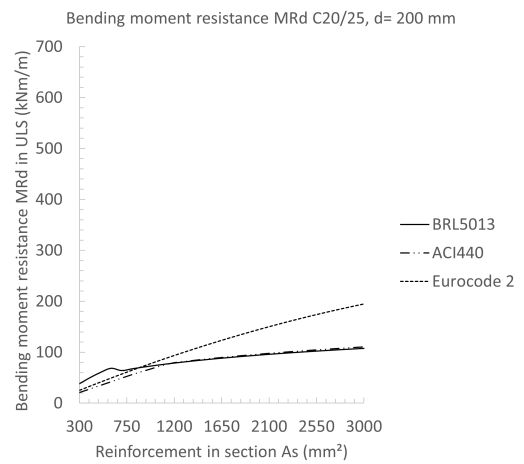
(a) d=150 mm, C20/25



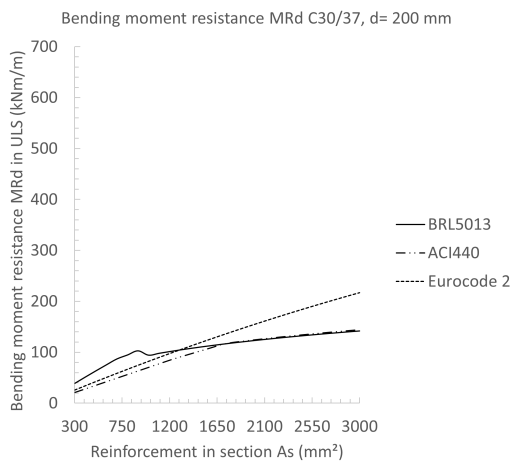
(b) d=150 mm, C30/37



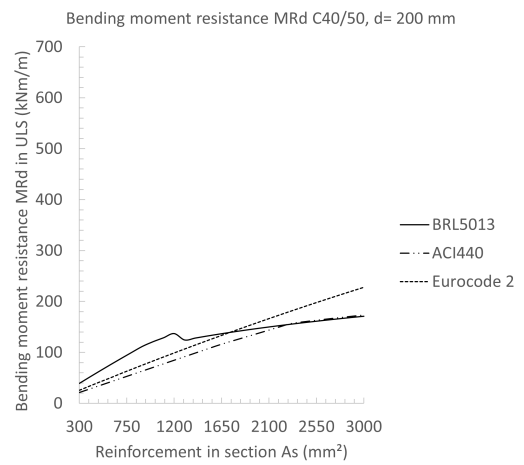
(c) d=150 mm, C40/50



(d) d=200 mm, C20/25

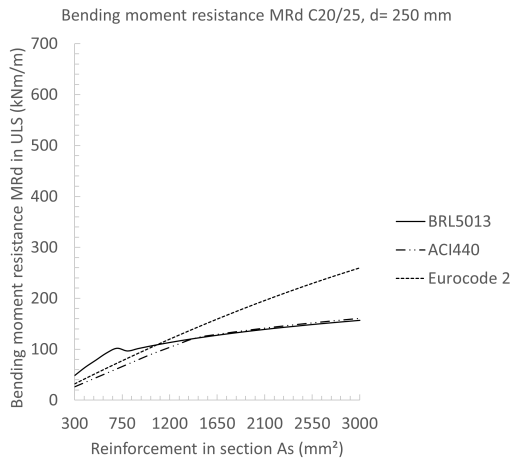


(e) d=200 mm, C30/37

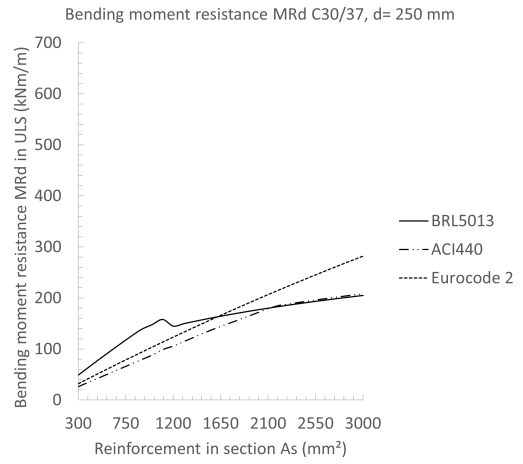


(f) d=200 mm, C40/50

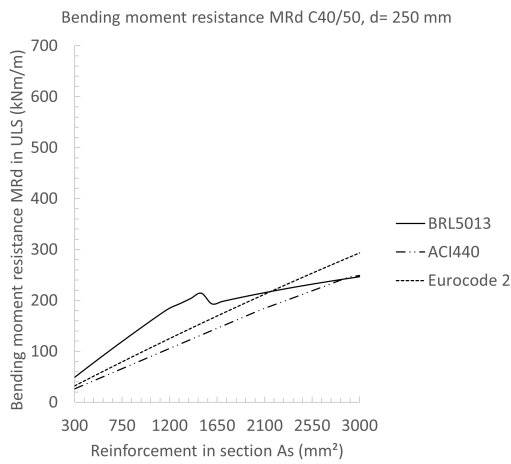
Appendix B – Graphs bending moment resistance parameter study



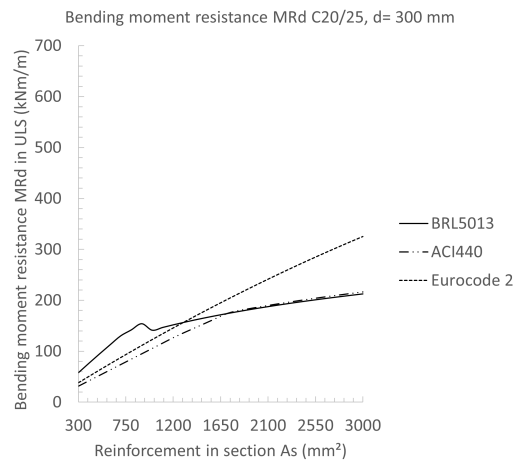
(g) d=250 mm, C20/25



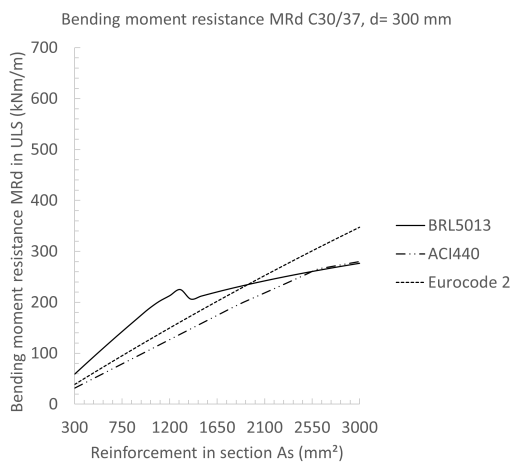
(h) d=250 mm, C30/37



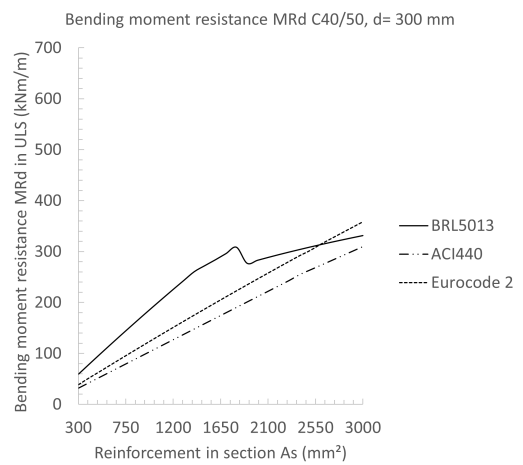
(i) d=250 mm, C40/50



(j) d=300 mm, C20/25

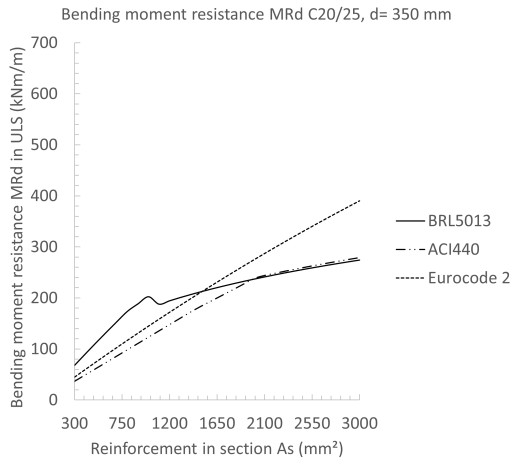


(k) d=300 mm, C30/37

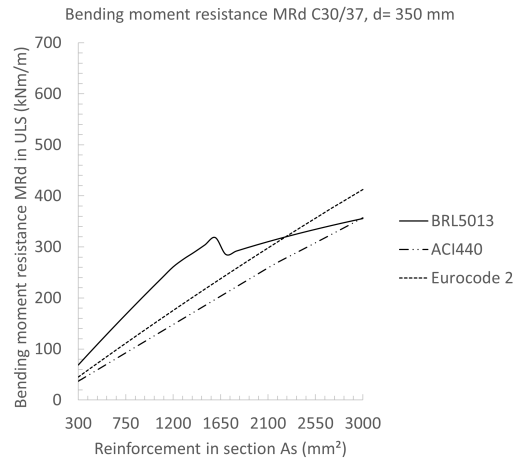


(l) d=300 mm, C40/50

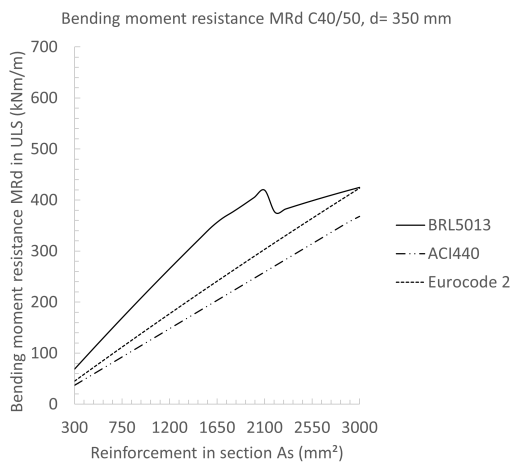
Appendix B – Graphs bending moment resistance parameter study



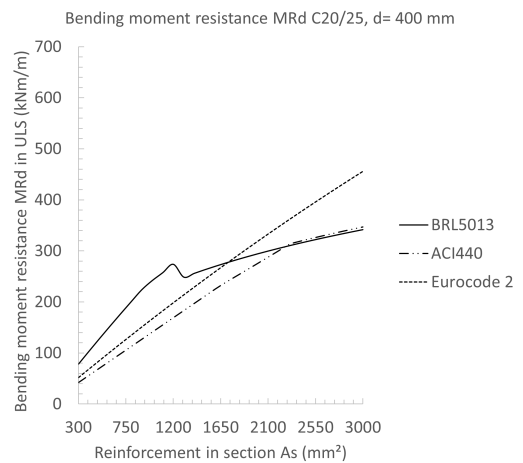
(m) d=350 mm, C20/25



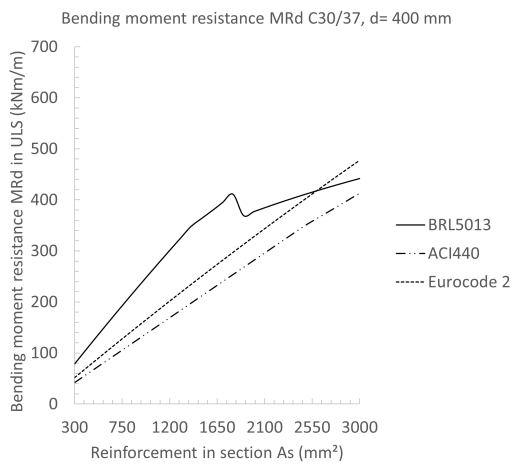
(n) d=350 mm, C30/37



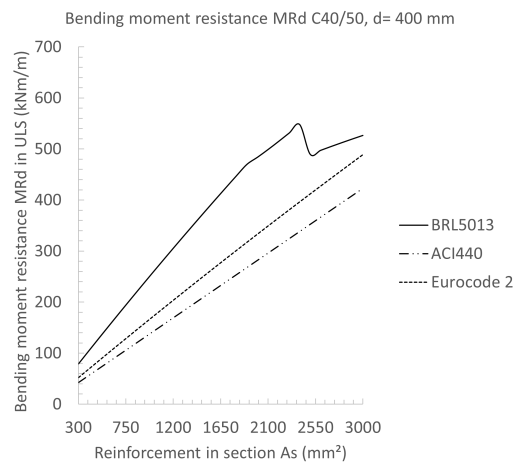
(o) d=350 mm, C40/50



(p) d=400 mm, C20/25

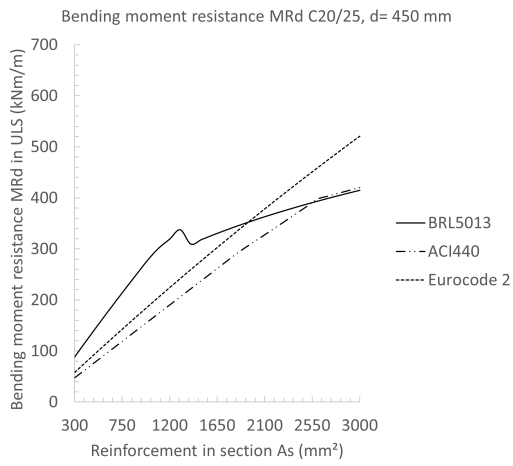


(q) d=400 mm, C30/37

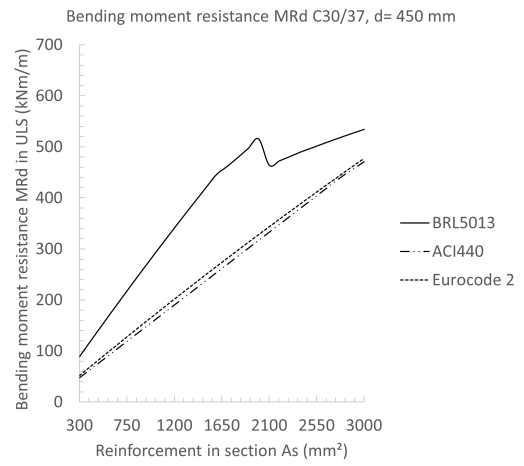


(r) d=400 mm, C40/50

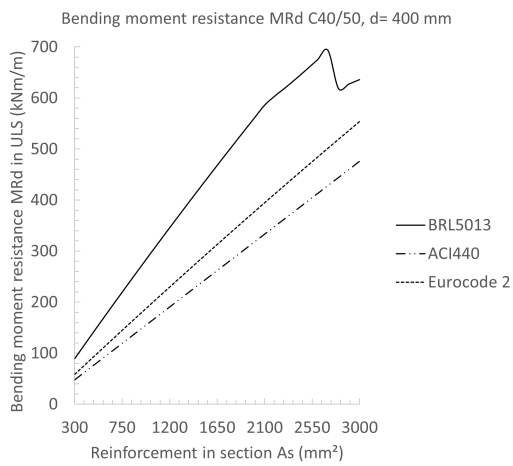
Appendix B – Graphs bending moment resistance parameter study



(s) d=450 mm, C20/25



(t) d=450 mm, C30/37



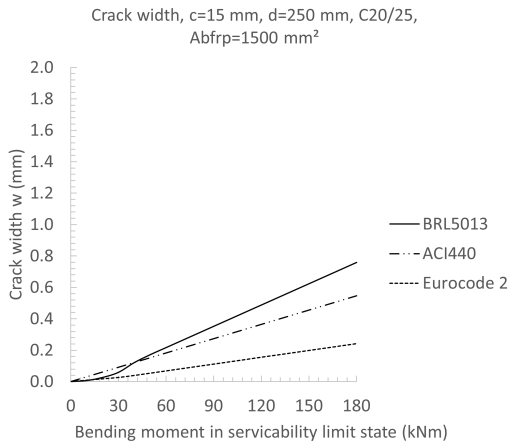
(u) d=450 mm, C40/50

Figure B.1: Bending moment diagrams comparison for varying effective heights and concrete strength classes

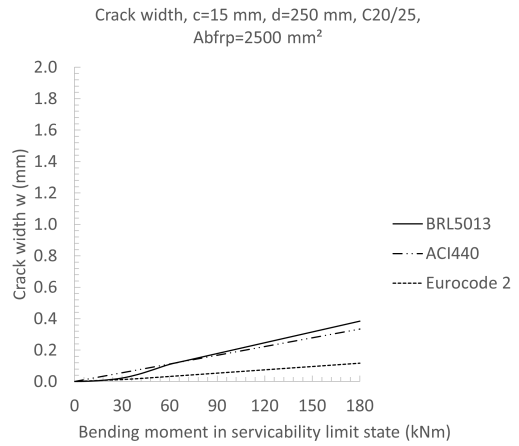
Appendix C

Graphs Crack width parameter study

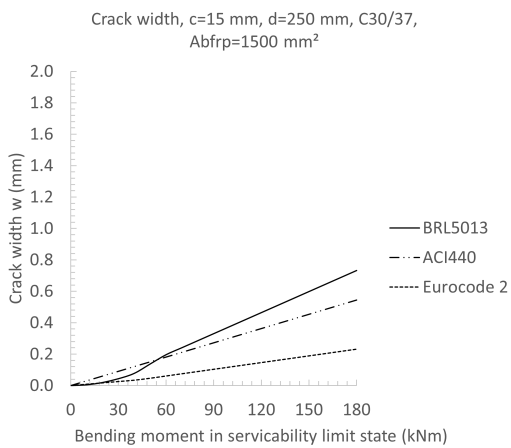
Appendix C – Graphs Crack width parameter study



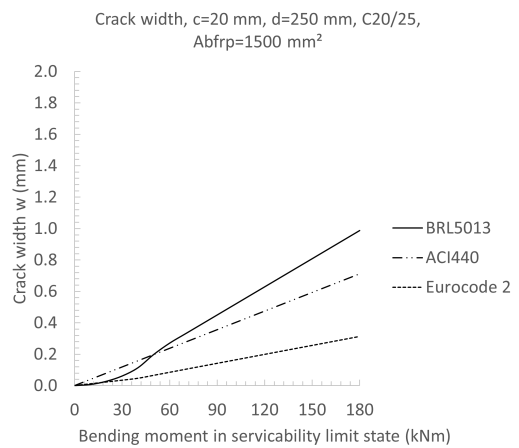
(a) $c=15$ mm, C20/25, $A_{bfrp}=1500$ mm²



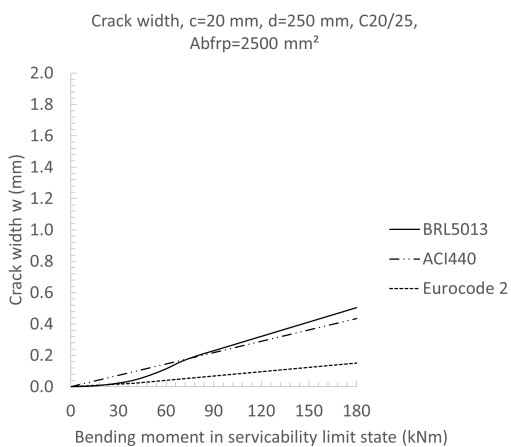
(b) $c=15$ mm, C20/25, $A_{bfrp}=2500$ mm²



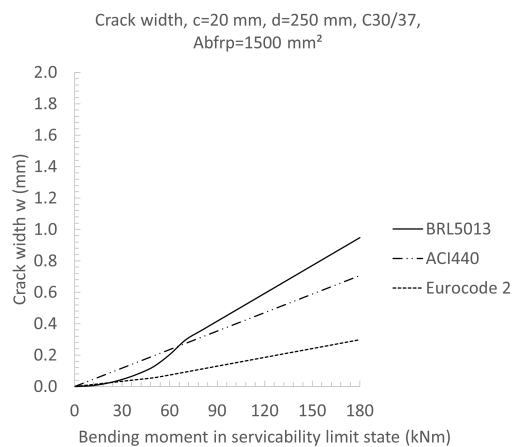
(c) $c=15$ mm, C30/37, $A_{bfrp}=1500$ mm²



(d) $c=20$ mm, C20/25, $A_{bfrp}=1500$ mm²

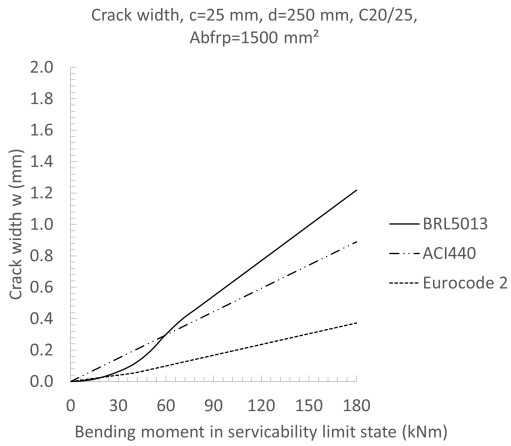


(e) $c=20$ mm, C20/25, $A_{bfrp}=2500$ mm²

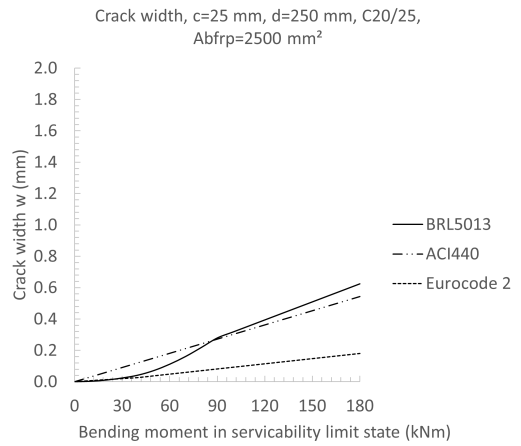


(f) $c=20$ mm, C30/37, $A_{bfrp}=1500$ mm²

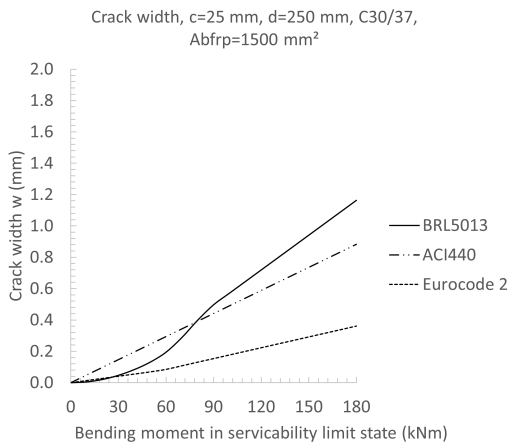
Appendix C – Graphs Crack width parameter study



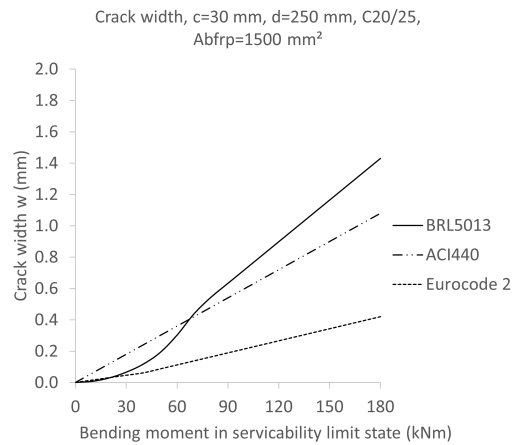
(g) $c=25$ mm, C20/25, $A_{bfrp}=1500$ mm²



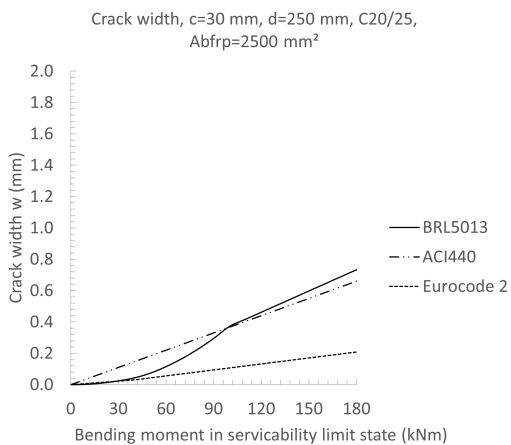
(h) $c=25$ mm, C20/25, $A_{bfrp}=2500$ mm²



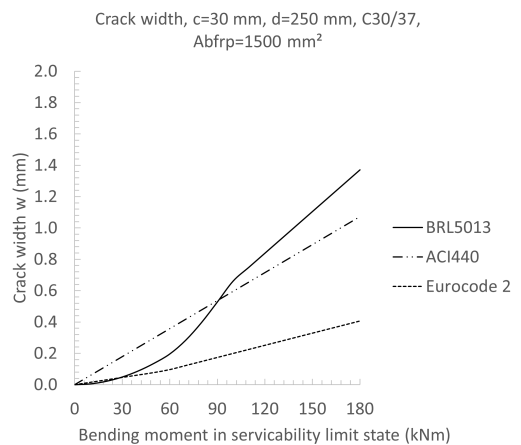
(i) $c=25$ mm, C30/37, $A_{bfrp}=1500$ mm²



(j) $c=30$ mm, C20/25, $A_{bfrp}=1500$ mm²

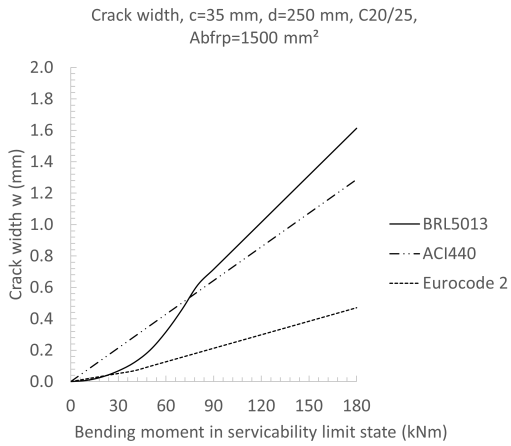


(k) $c=30$ mm, C20/25, $A_{bfrp}=2500$ mm²

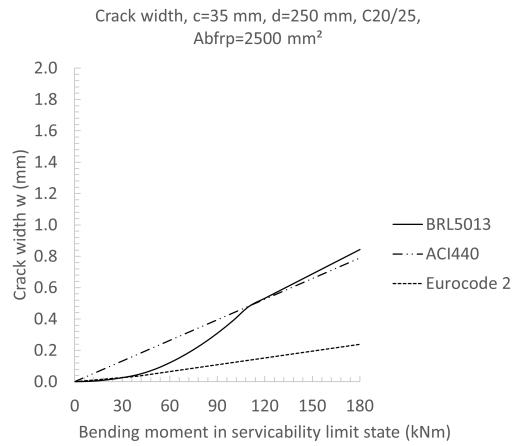


(l) $c=30$ mm, C30/37, $A_{bfrp}=1500$ mm²

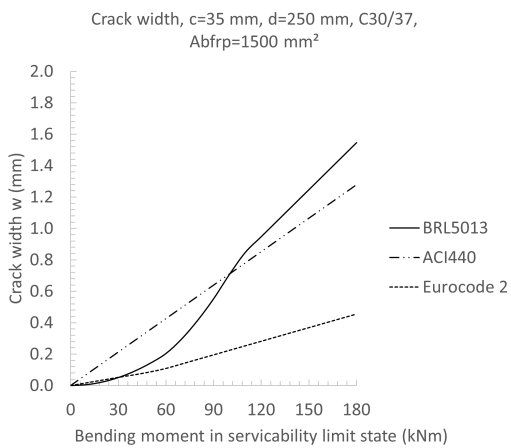
Appendix C – Graphs Crack width parameter study



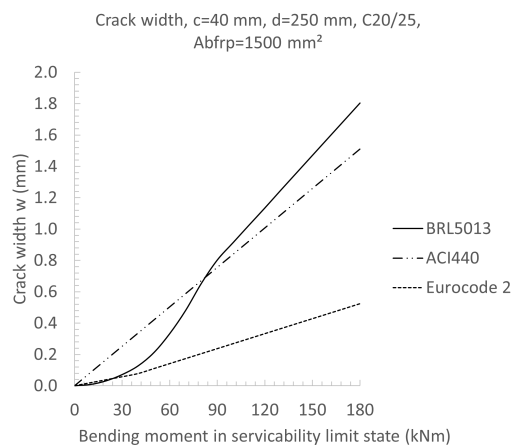
(m) $c=35$ mm, C20/25, $A_{bfrp}=1500$ mm²



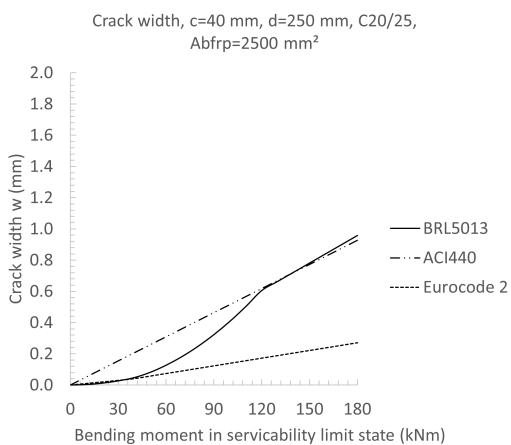
(n) $c=35$ mm, C20/25, $A_{bfrp}=2500$ mm²



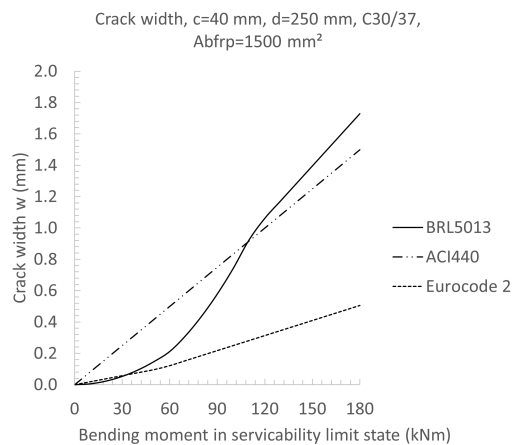
(o) $c=35$ mm, C30/37, $A_{bfrp}=1500$ mm²



(p) $c=40$ mm, C20/25, $A_{bfrp}=1500$ mm²

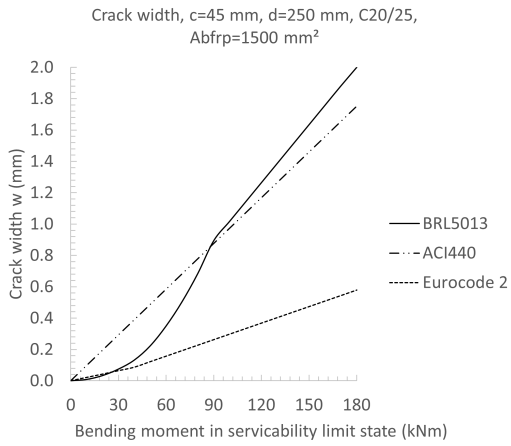


(q) $c=40$ mm, C20/25, $A_{bfrp}=2500$ mm²

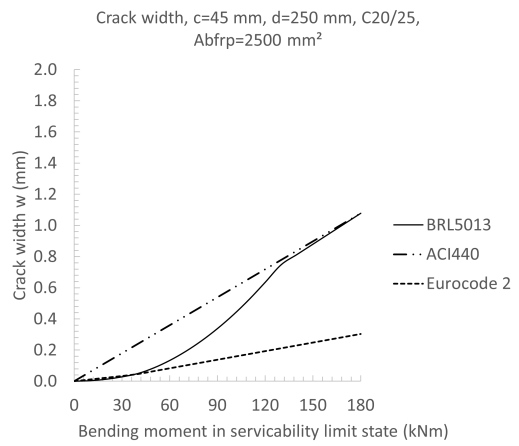


(r) $c=40$ mm, C30/37, $A_{bfrp}=1500$ mm²

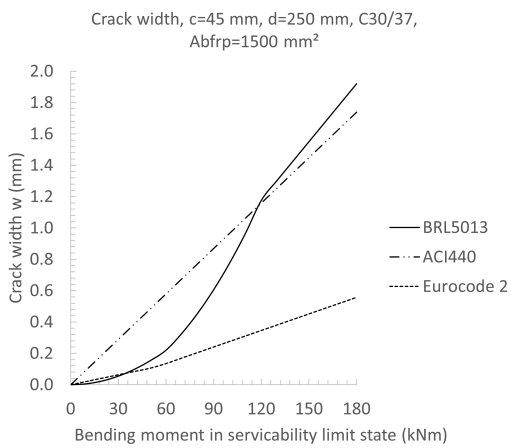
Appendix C – Graphs Crack width parameter study



(s) $c=45$ mm, C20/25, $A_{bfrp}=1500$ mm²



(t) $c=45$ mm, C20/25, $A_{bfrp}=2500$ mm²



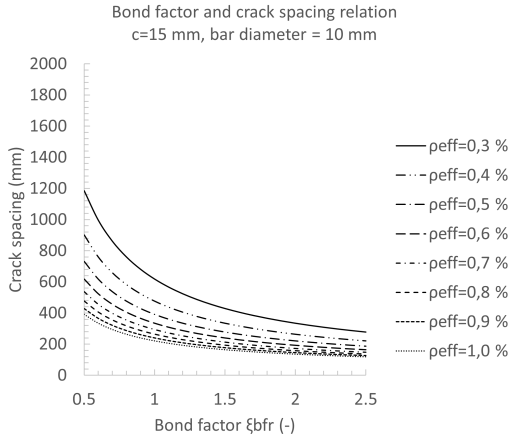
(u) $c=45$ mm, C30/37, $A_{bfrp}=1500$ mm²

Figure C.1: Crack width diagram comparison for various concrete covers, cross-sectional reinforcement area and concrete strength classes

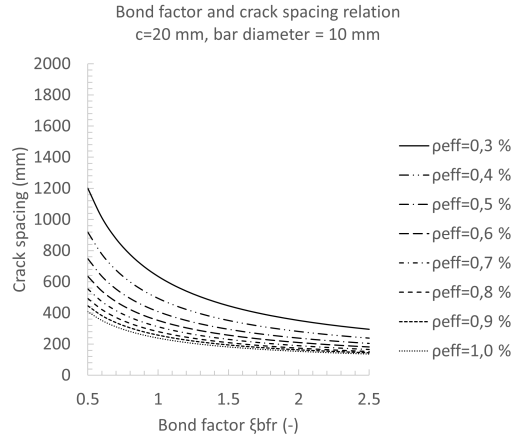
Appendix D

Graphs crack spacing parameter study

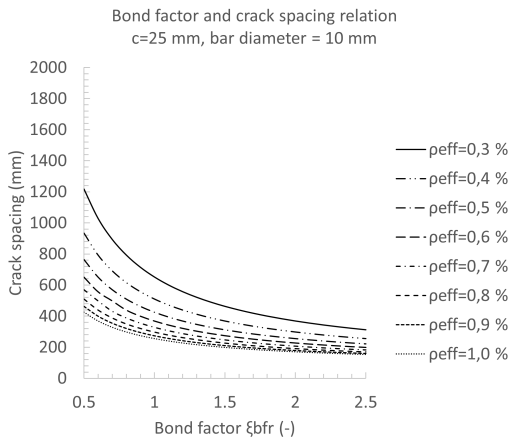
Appendix D – Graphs crack spacing parameter study



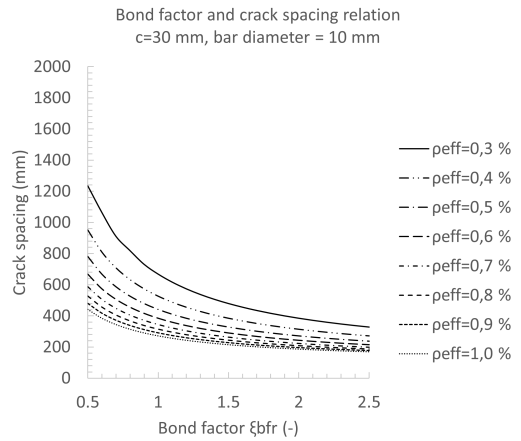
(a) c=15 mm, \varnothing_{bf} =10 mm



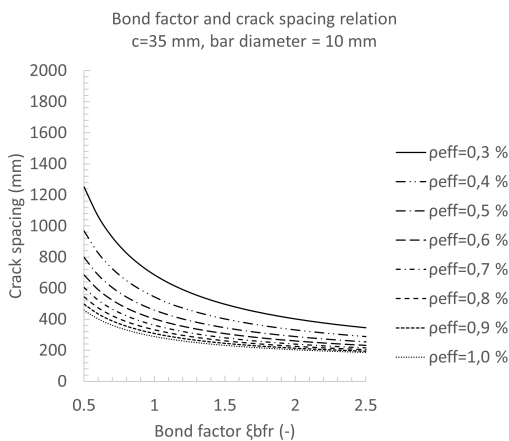
(b) c=20 mm, \varnothing_{bf} =10 mm



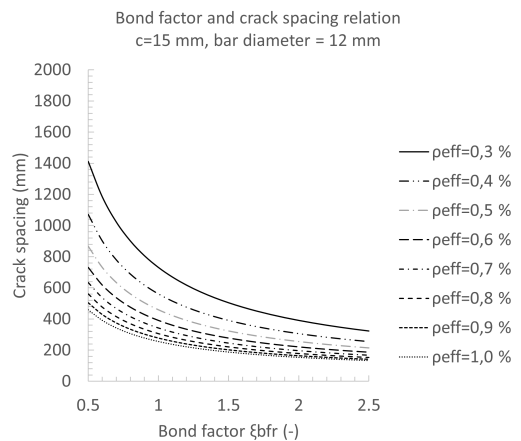
(c) c=25 mm, \varnothing_{bf} =10 mm



(d) c=30 mm, \varnothing_{bf} =10 mm

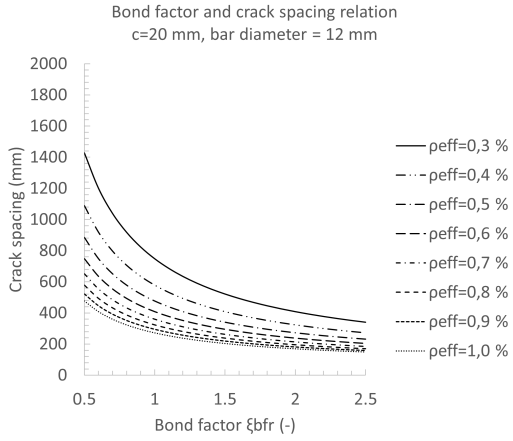


(e) c=35 mm, \varnothing_{bf} =10 mm

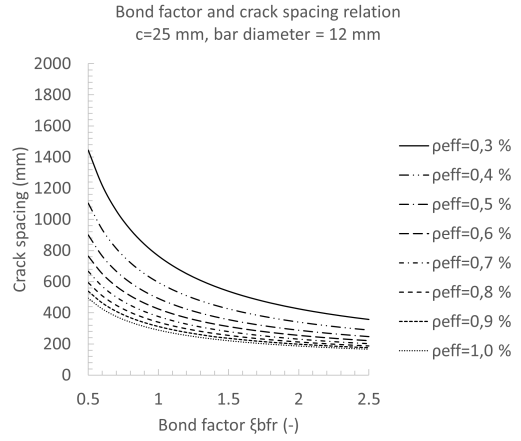


(f) c=15 mm, \varnothing_{bf} =12 mm

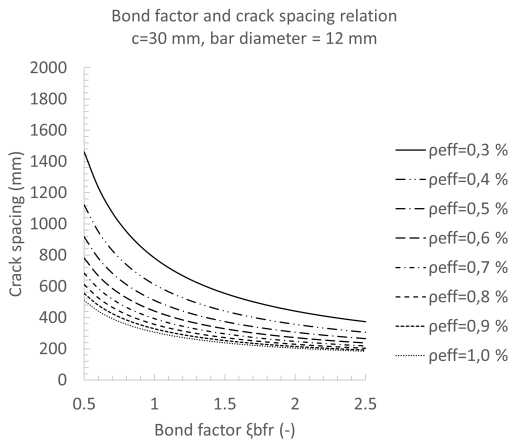
Appendix D – Graphs crack spacing parameter study



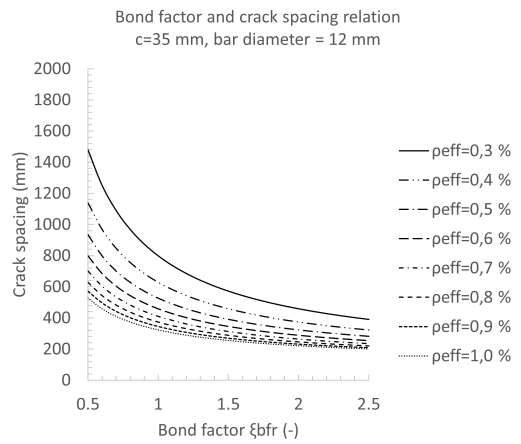
(g) c=20 mm, \varnothing_{bf} =12 mm



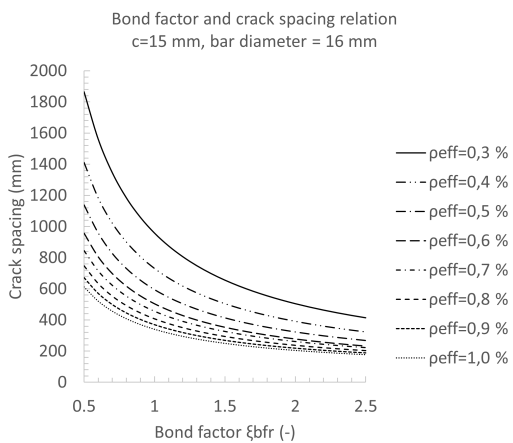
(h) c=25 mm, \varnothing_{bf} =12 mm



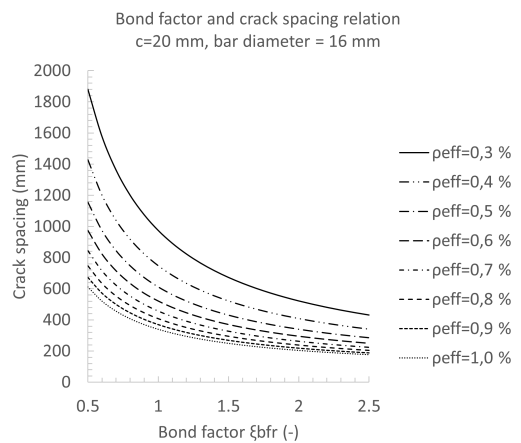
(i) c=30 mm, \varnothing_{bf} =12 mm



(j) c=35 mm, \varnothing_{bf} =12 mm



(k) c=15 mm, \varnothing_{bf} =16 mm



(l) c=20 mm, \varnothing_{bf} =16 mm

Appendix D – Graphs crack spacing parameter study

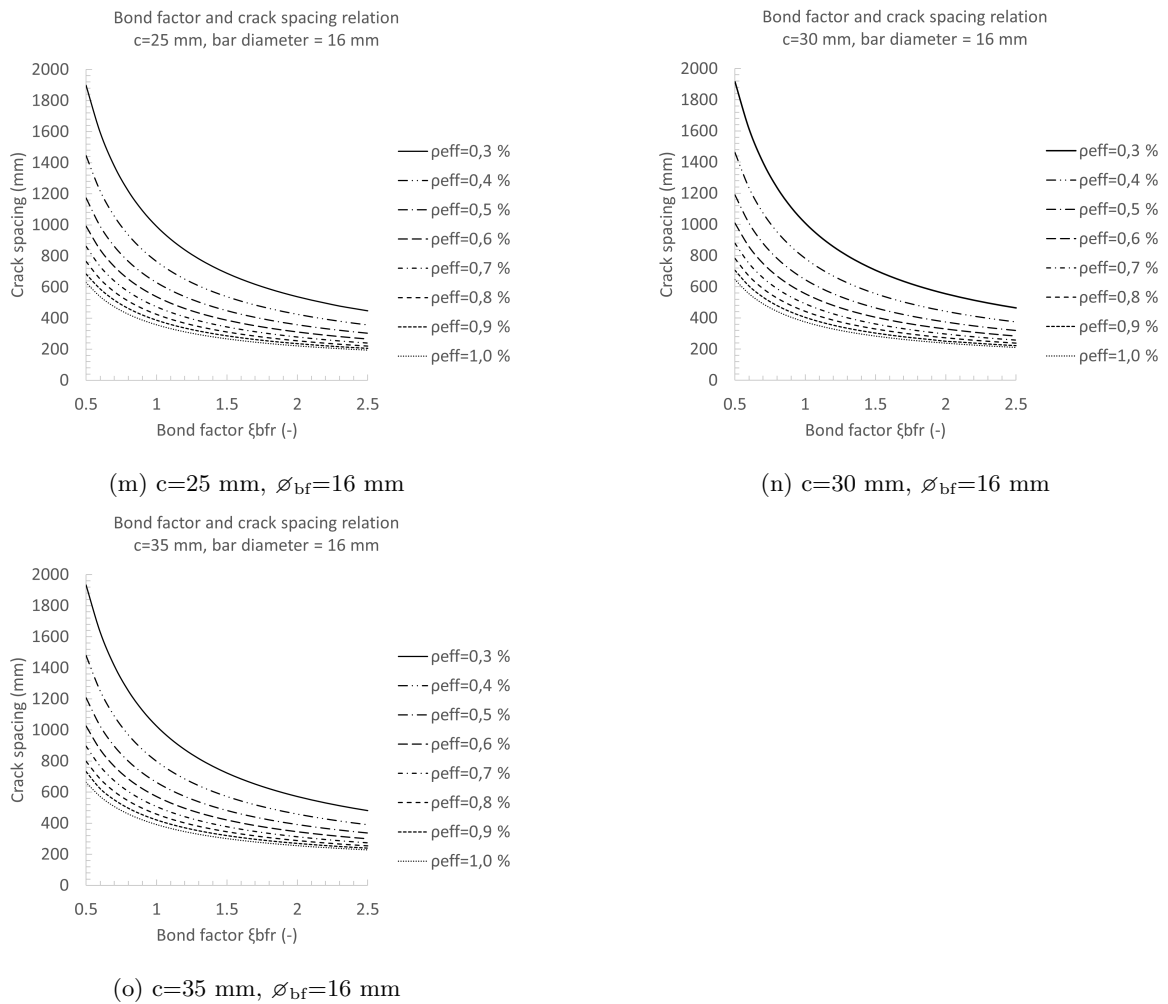


Figure D.1: Bond factor crack spacing relation for varying diameter, concrete cover, and bar diameter

Appendix E

Results cube compression test

Table E.1: Concrete batch 1 cubes results

Cube number	Loading speed (kN/s)	Load (kN)	Stress (MPa)	Concrete age (days)
C1.1	13.50	898.2	39.9	29
C1.2	13.50	1049.6	46.6	29
C1.3	13.50	1054.4	46.9	29

Average stress: 44.5 MPa
Standard deviation: 3.9 MPa
Coefficient of variation: 8.88%

Casting date: 05/07/2023
Testing date: 03/08/2023

Table E.2: Concrete batch 2 cubes results

Cube number	Loading speed (kN/s)	Load (kN)	Stress (MPa)	Concrete age (days)
C2.1	13.50	1135.7	50.5	29
C2.2	13.50	1219.1	54.2	29
C2.3	13.50	1119.1	49.7	29

Average stress: 51.5 MPa
Standard deviation: 2.4 MPa
Coefficient of variation: 4.63%

Casting date: 10/07/2023
Testing date: 08/08/2023

Table E.3: Concrete batch 3 cubes results

Cube number	Loading speed (kN/s)	Load (kN)	Stress (MPa)	Concrete age (days)
C3.1	13.50	1193.7	53.1	29
C3.2	13.50	1095.2	48.7	29
C3.3	13.50	1169.8	52.0	29

Average stress: 51.2 MPa

Standard deviation: 2.3 MPa

Coefficient of variation: 4.46%

Casting date: 17/07/2023

Testing date: 15/08/2023

Appendix F

Results cubes tensile splitting test

Table F.1: Concrete batch 2 cubes tensile splitting results

Cube number	Loading speed (kN/s)	Load (kN)	Tensile splitting strength (MPa)	Concrete age (days)
C2.4	2.12	1135.7	3.98	29
C2.5	2.12	1219.1	3.73	29
C2.6	2.12	1119.1	4.13	29

Average tensile splitting strength: 3.94 MPa

Standard deviation: 0,201 MPa

Coefficient of variation: 5.10%

Casting date: 10/07/2023

Testing date: 08/08/2023

Table F.2: Concrete batch 3 cubes tensile splitting results

Cube number	Loading speed (kN/s)	Load (kN)	Tensile splitting strength (MPa)	Concrete age (days)
C3.4	2.12	131.1 3	3.71	29
C3.5	2.12	135.6	3.84	29
C3.6	2.12	134.7	3.81	29

Average tensile splitting strength: 3.94 MPa

Standard deviation: 0.067 MPa

Coefficient of variation: 1.780%

Casting date: 17/07/2023

Testing date: 15/08/2023

Appendix G

Results prisms compression test

Table G.1: Concrete batch 1 prisms results

Prism number	Loading (L) and unloading(U) speed (kN/s)	Prisms strength (kN)	Young's modulus (MPa)	Concrete age (days)
P1.1	1.0(L)/ 2.0(U)	429.92	37727	29
P1.2	1.0(L)/ 2.0(U)	434.91	39950	29
P1.3	1.0(L)/ 2.0(U)	453.48	40390	29

Average Young's modulus: 39355 MPa
 Standard deviation: 1684.58 MPa
 Coefficient of variation: 4.28%

Casting date: 05/07/2023
 Testing date: 03/08/2023

Table G.2: Concrete batch 2 prisms results

Prism number	Loading (L) and unloading(U) speed (kN/s)	Prisms strength (kN)	Young's modulus (MPa)	Concrete age (days)
P2.1	1.0(L)/ 2.0(U)	431.99	36681	29
P2.2	1.0(L)/ 2.0(U)	407.55	36818	29
P3.2	1.0(L)/ 2.0(U)	407.33	35232	29

Average Young's modulus: 36244 MPa
 Standard deviation: 878.34 MPa
 Coefficient of variation: 2.42%

Casting date: 10/07/2023
 Testing date: 08/08/2023

Table G.3: Concrete batch 3 prisms results

Prism number	Loading (L) and unloading(U) speed (kN/s)	Prisms strength (kN)	Young's modulus (MPa)	Concrete age (days)
P3.1	1.0(L)/ 2.0(U)	388.98	38426	29
P3.2	1.0(L)/ 2.0(U)	393.73	37686	29
P3.3	1.0(L)/ 2.0(U)	422.19	38716	29

Average Young's modulus: 38276 MPa

Standard deviation: 531 MPa

Coefficient of variation: 1.39%

Casting date: 17/07/2023

Testing date: 15/08/2023

Appendix H

Crack width development DIC-data

H.1 Results B-3r8-c31

The load-deflection curve for beam B-3r8-c31 is shown in figure H.1. In the same figure, a curve containing the maximum crack width measured from DIC-data is presented. Table H.1 indicates the performance of the beam. The chronological crack pattern propagation from the DIC-data is presented in figure H.2.

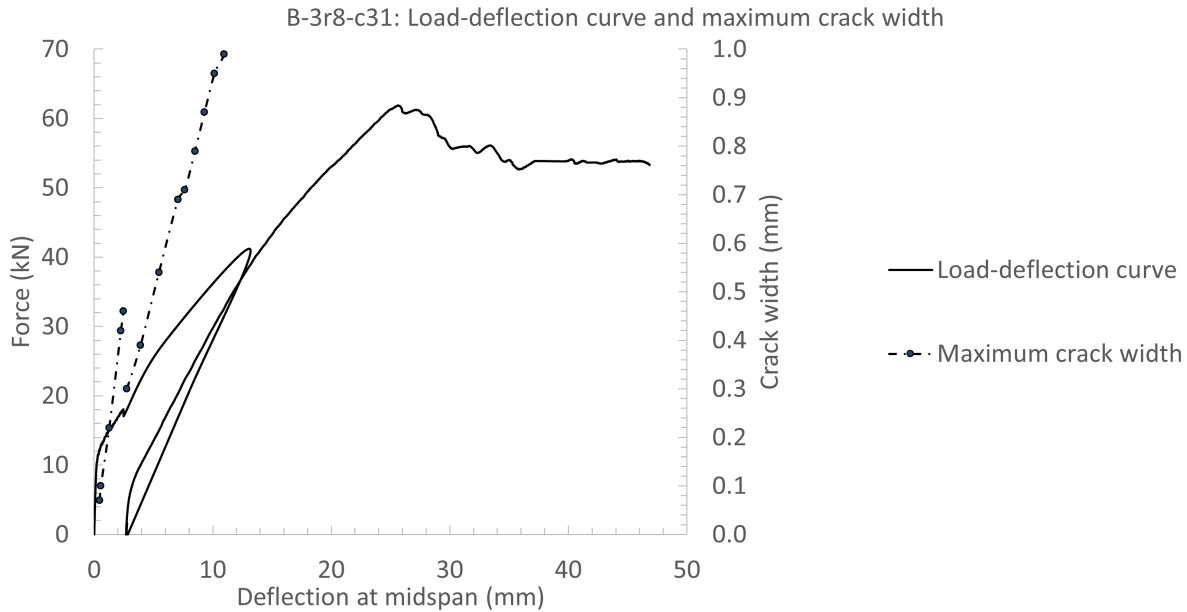
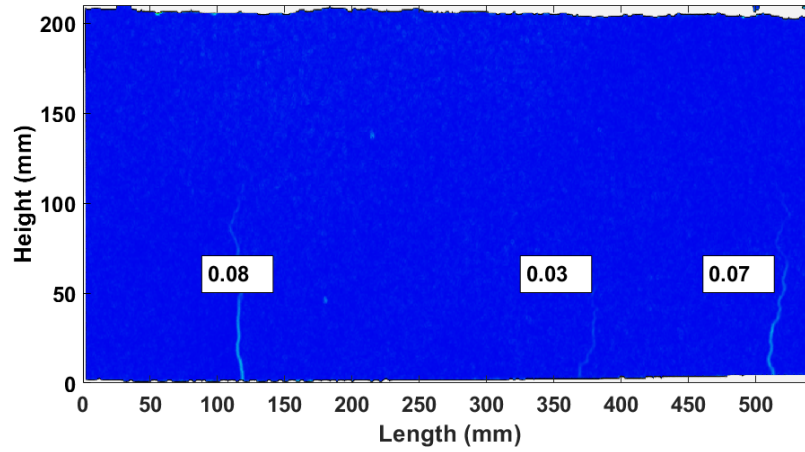


Figure H.1: B-3r8-c31, load-deflection curve versus maximum crack width measured from DIC-data

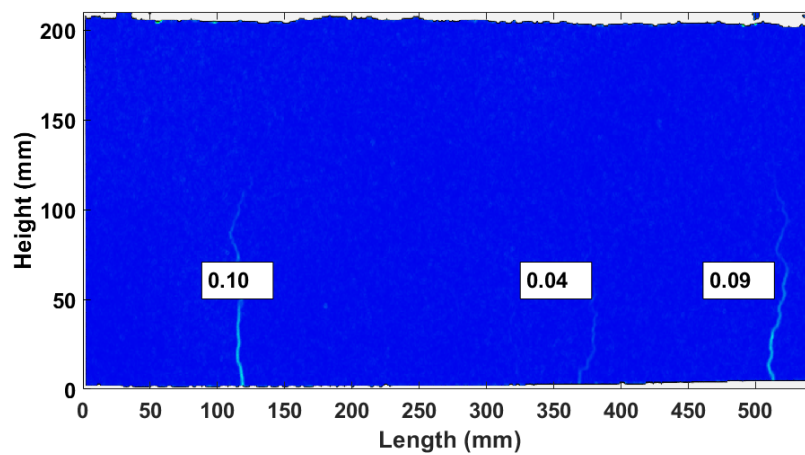
Table H.1: B-3r8-c31, summarized performance parameters

Performance parameters	
Maximum load	61.89 kN
Mid-span vertical deflection at maximum load	25.64 mm
Maximum vertical deflection at mid-span	46.83 mm
Number of cracks in constant bending moment zone	7
Average crack spacing	71.43 mm

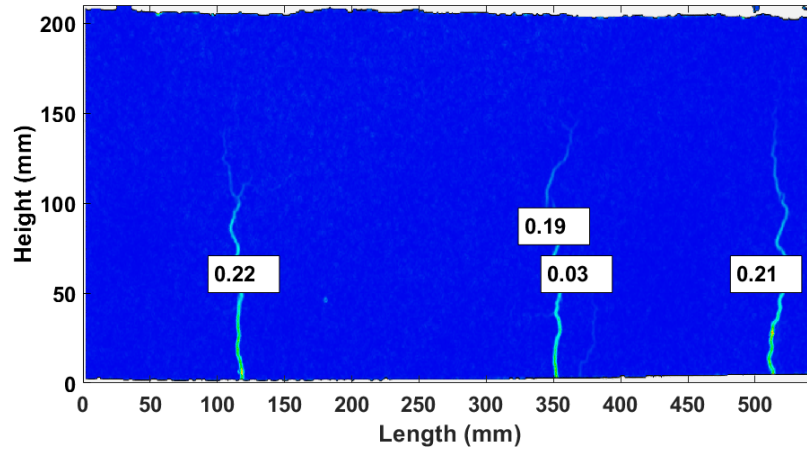
The crack width development in beam B-3r8-c31 is displayed using a Von Mises contour plot from the DIC-data. The base colour is dark blue indicating no strain. Ranging from turquoise to red, strain concentrations are indicated from the DIC-data, which indicates cracks in the concrete. The first cracks appear at 12.11 kN as presented in figure H.2a. At a load of 17.49 kN, horizontal cracks also emerge at the depth of the reinforcement (figure H.2d). As the load increases, more cracks start to emerge and develop in the constant bending moment zone of the beam. Eventually, 7 primary cracks develop, however, more secondary cracks appear at mid-height, where the cracking is not limited by reinforcement (figure H.2f). The beam failed in the concrete compression zone, near one of the points of load application.



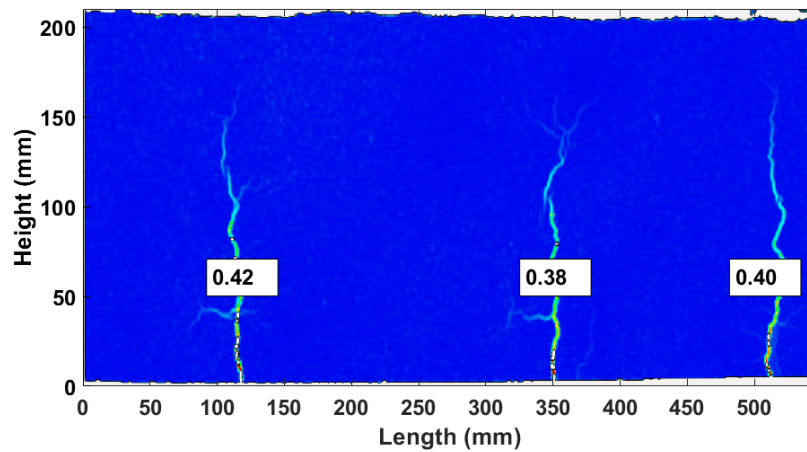
(a) CB-3r8-c31: $F=12.11$ kN



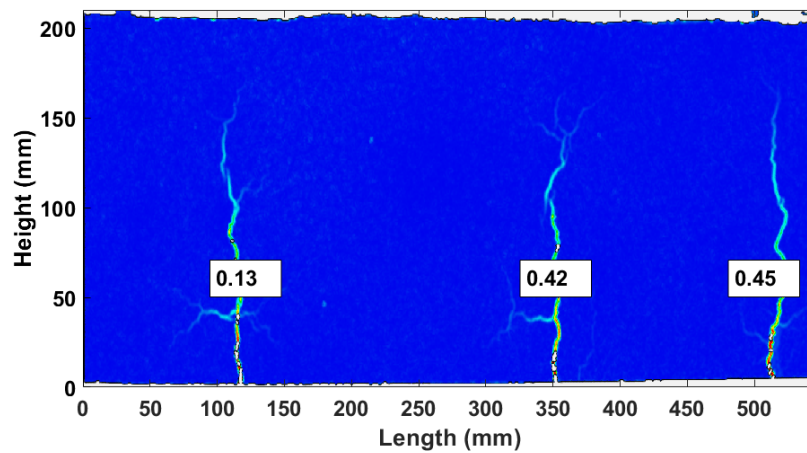
(b) CB-3r8-c31: $F=12.91$ kN



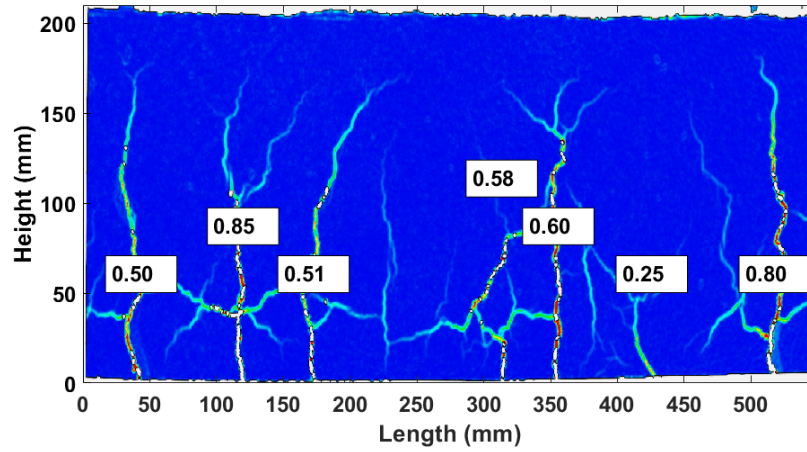
(c) CB-3r8-c31: F=15.04 kN



(d) CB-3r8-c31: F=17.49 kN

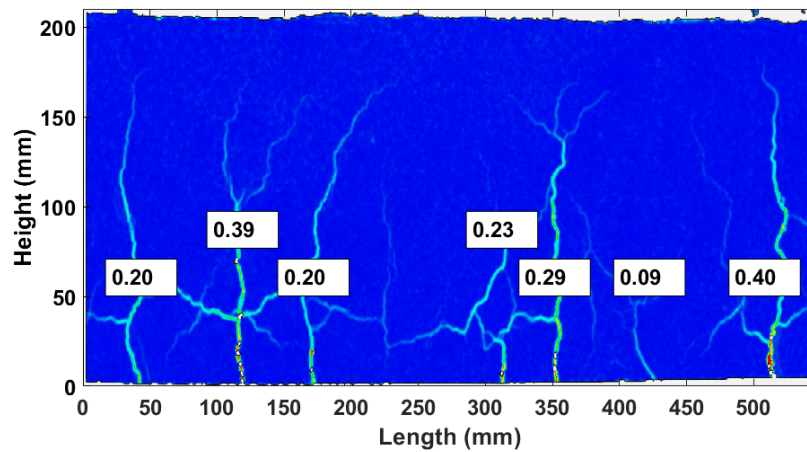


(e) CB-3r8-c31: F=18.12 kN

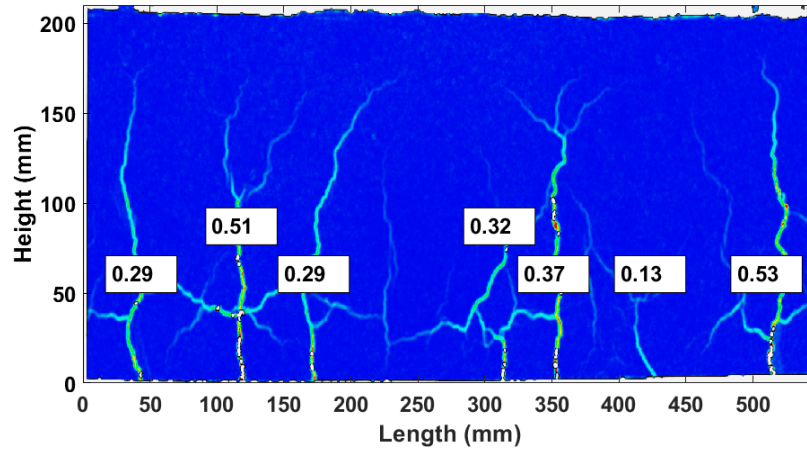


(f) CB-3r8-c31: $F=26.37$ kN

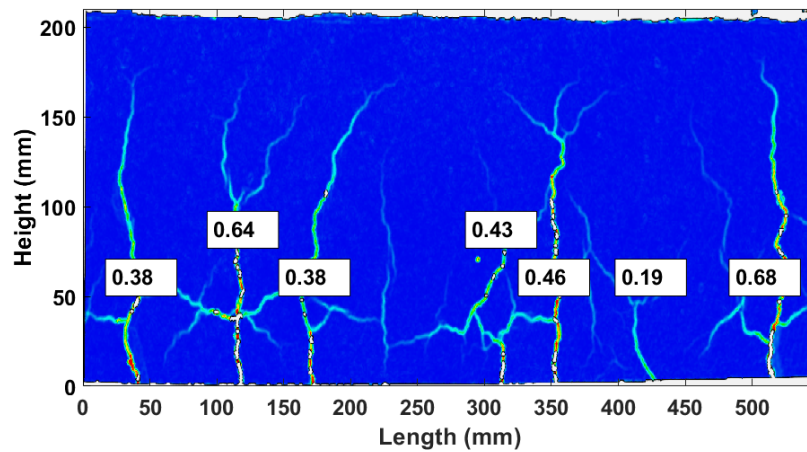
Note that during the test, the test was stopped and resumed as the jack increased force from approximately 20 kN to 40 kN within seconds, which is visible in the load-deflection curve (figure H.1) as well as the DIC-images. After the test was resumed, the trajectory of the load-deflection curve resumed in accordance with the initial curve.



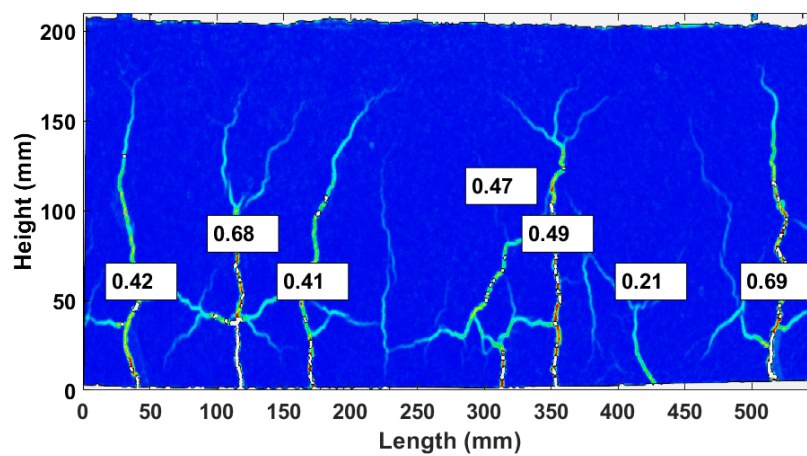
(g) CB-3r8-c31: $F=10.02$ kN



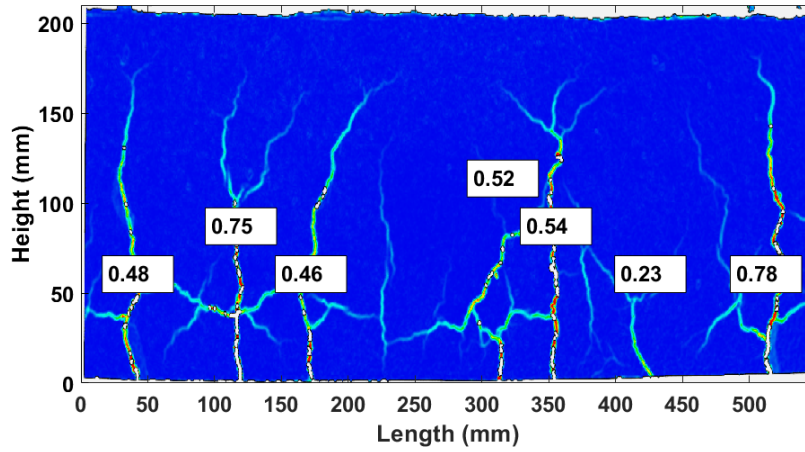
(h) CB-3r8-c31: F=15.00 kN



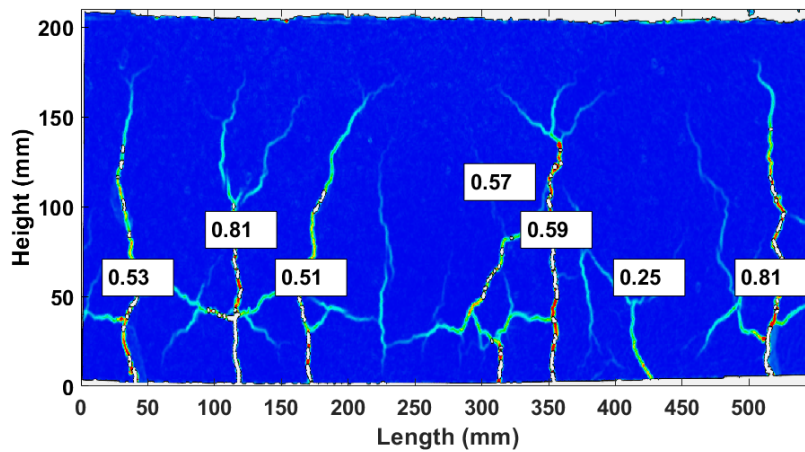
(i) CB-3r8-c31: F=20.34 kN



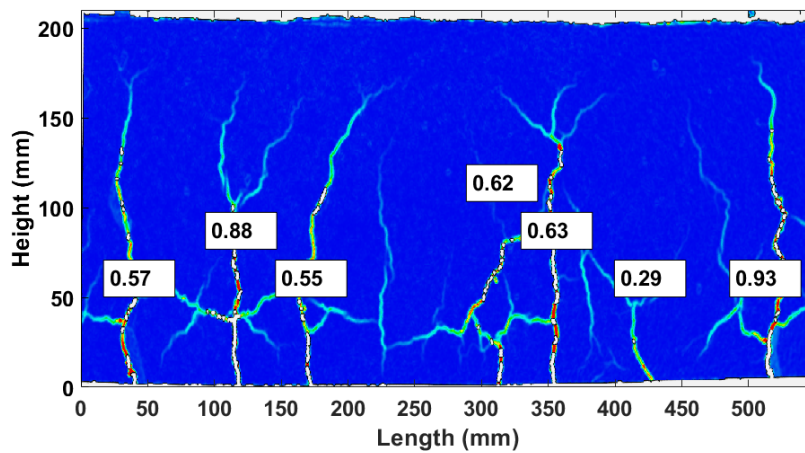
(j) CB-3r8-c31: F=22.38 kN



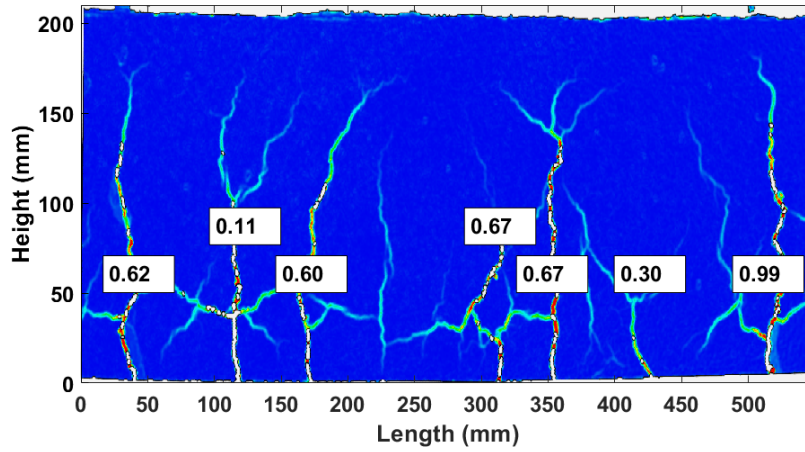
(k) CB-3r8-c31: F=25.07 kN



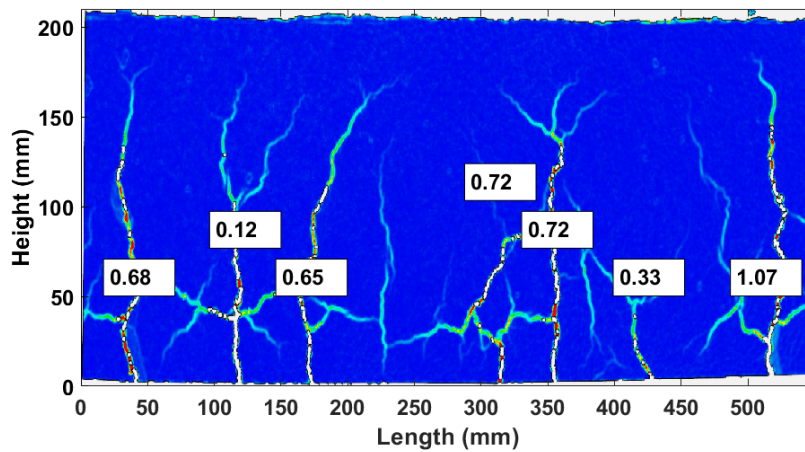
(l) CB-3r8-c31: F=27.59 kN



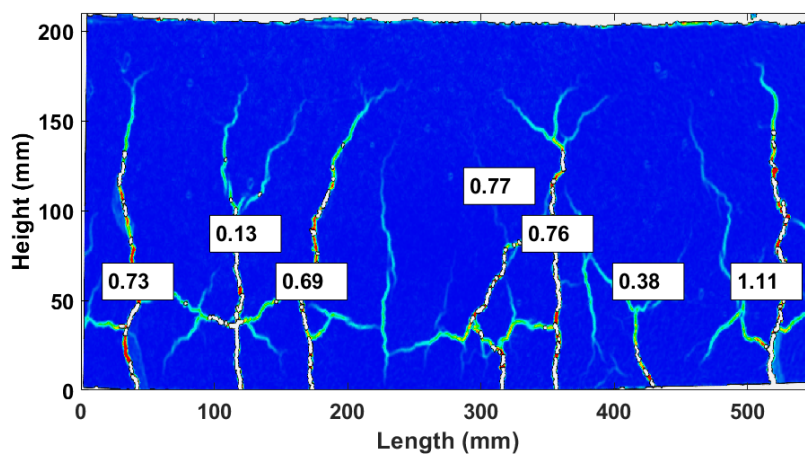
(m) CB-3r8-c31: F=30.26 kN



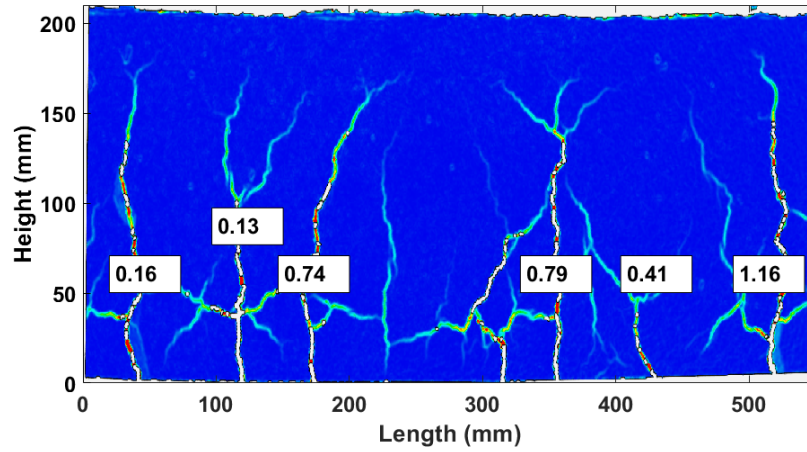
(n) CB-3r8-c31: $F=32.62$ kN



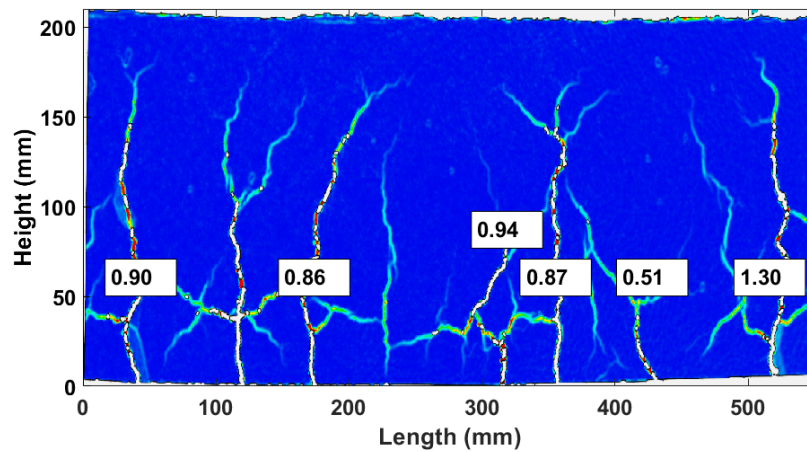
(o) CB-3r8-c31: $F=35.05$ kN



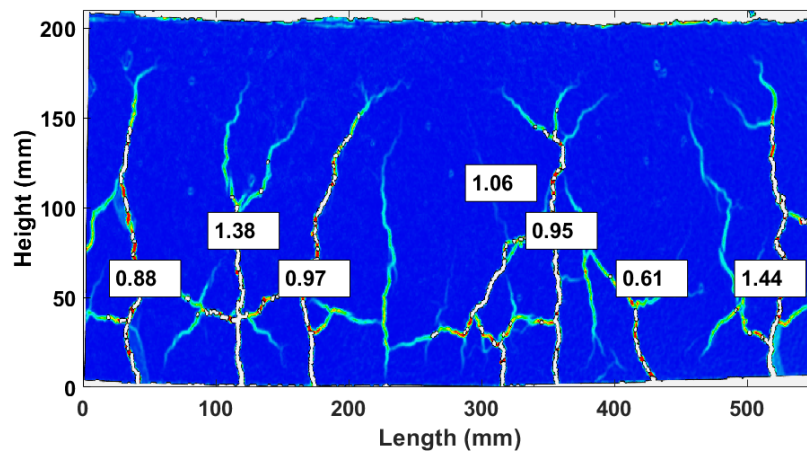
(p) CB-3r8-c31: $F=37.60$ kN



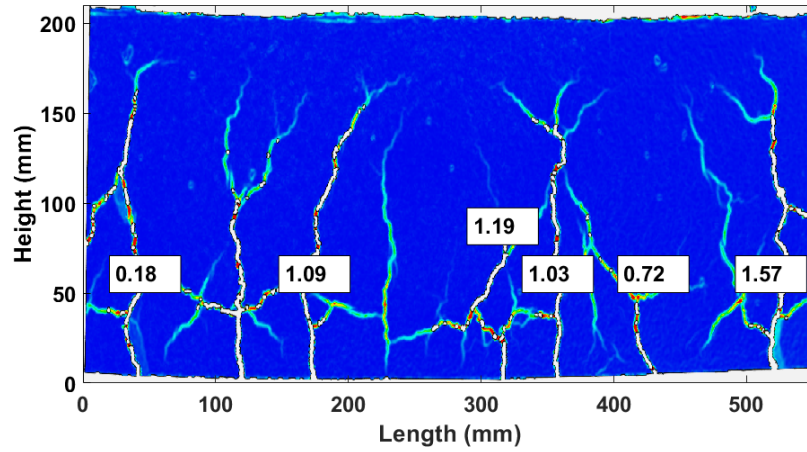
(q) CB-3r8-c31: F=39.99 kN



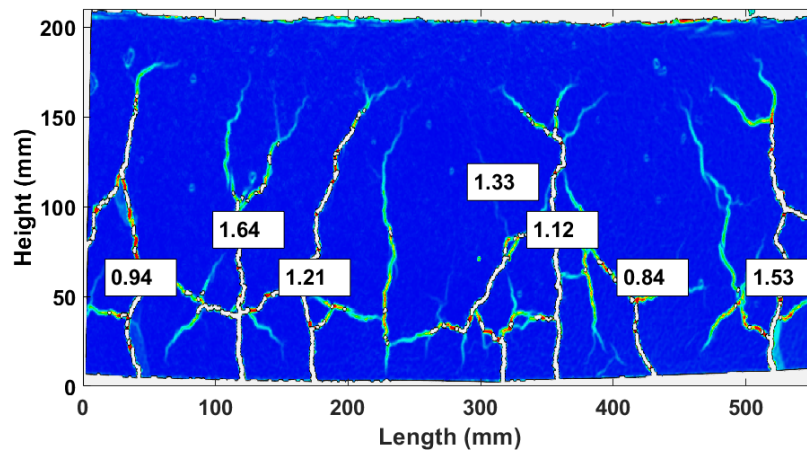
(r) CB-3r8-c31: F=45.07 kN



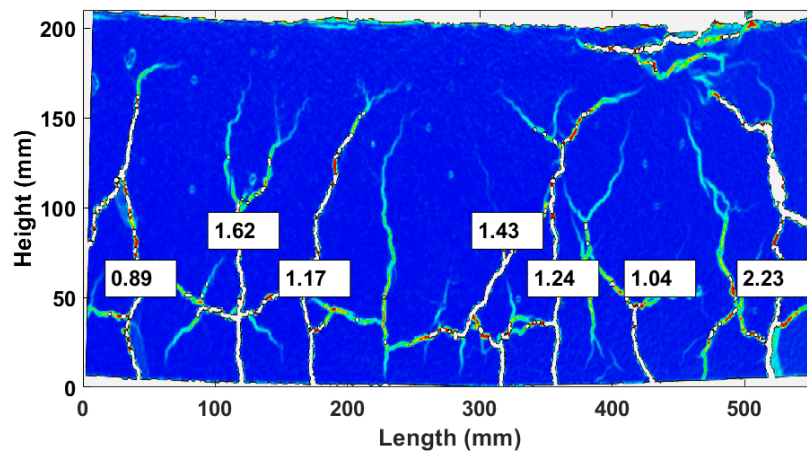
(s) CB-3r8-c31: F=49.93 kN



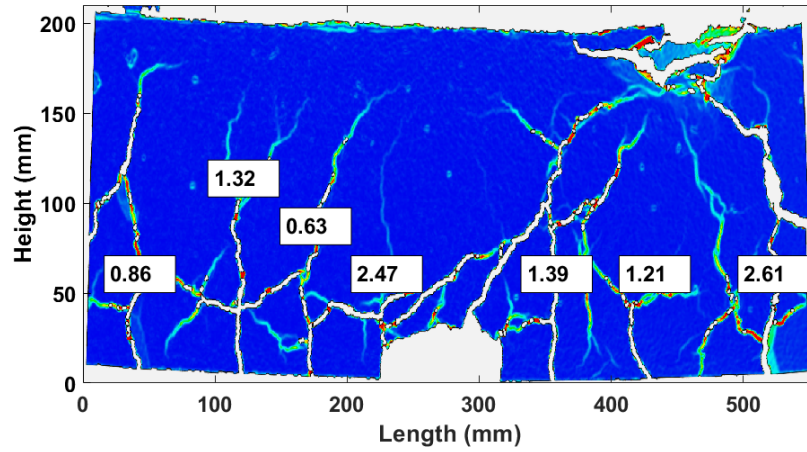
(t) CB-3r8-c31: F=54.94 kN



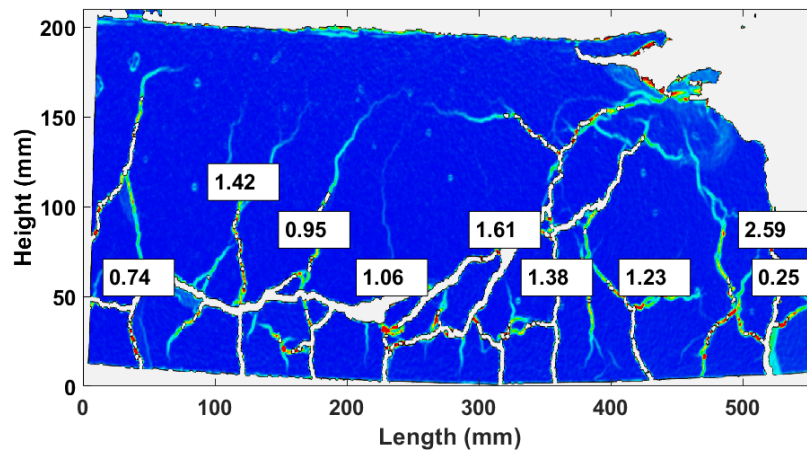
(u) CB-3r8-c31: F=60.01 kN



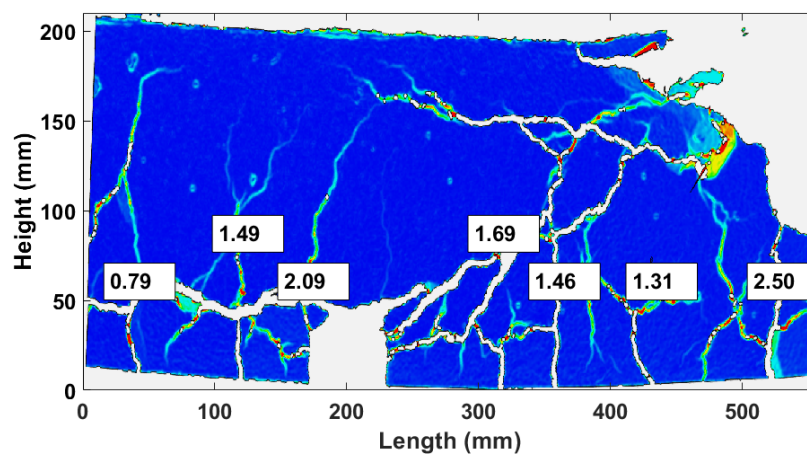
(v) CB-3r8-c31: F=57.50 kN



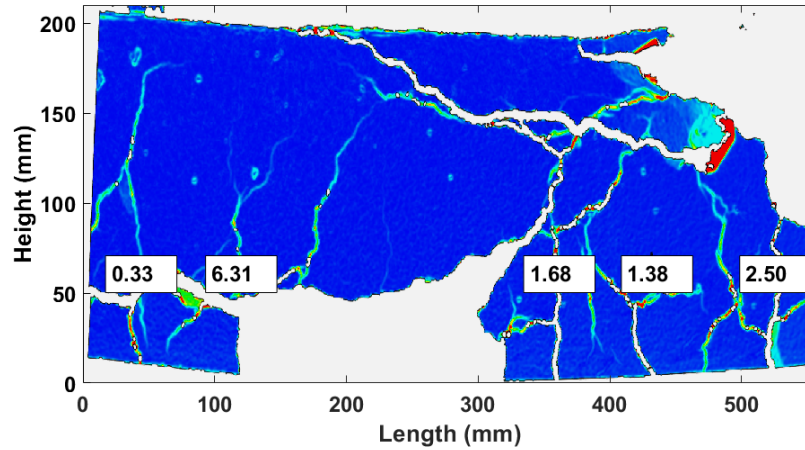
(w) CB-3r8-c31: F=55.97 kN



(x) CB-3r8-c31: F=54.00 kN



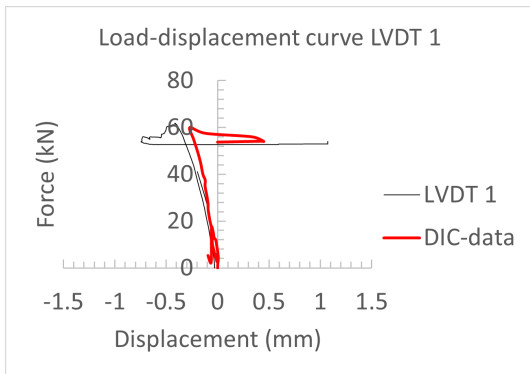
(y) CB-3r8-c31: F=54.10 kN



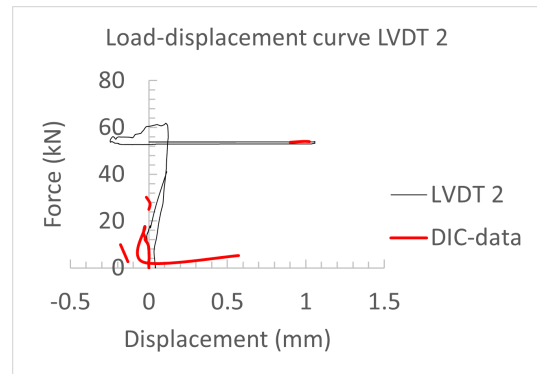
(z) CB-3r8-c31: $F=53.72$ kN

Figure H.2: Crack widths contour plots B-3r8-c31 from DIC-data

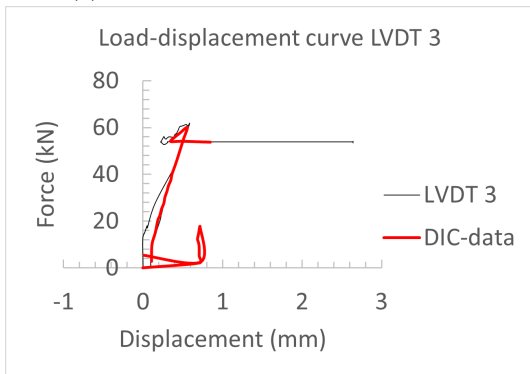
By comparing the DIC-data to the data from the LVDT's used during the test, some significant differences can be noticed. This is likely due to the loading history of the beam. As the DIC-data relies on images taken every 5 seconds, the data gathered during the vastly increased loading speed part of the cycle is not accurate. As the compression zone started to fail, LVDT 3 failed as well and overstepped its reach. After the reach of an LVDT is exceeded, the curve flat-lines, which is noticeable in subfigure H.3c. Upon inspecting the DIC-data for LVDT 2, limited data of sufficient accuracy could be gathered to make a sound comparison. In general, the data gathered from the first loading cycle is usable up to a load level of 17.10 kN, as the sudden acceleration of the load has not occurred at this point yet. The data from the second load cycle is generally accurate except for LVDT 2, which is located in the concrete compressive zone at 30 mm from the top edge of the beam. As LVDT's 1 and 3 are located in the compression zone as well at 10 mm and 50 mm from the top edge respectively, valid data about the concrete compression zone can still be used. The DIC-data is therefore accepted with the exception of the aforementioned parts.



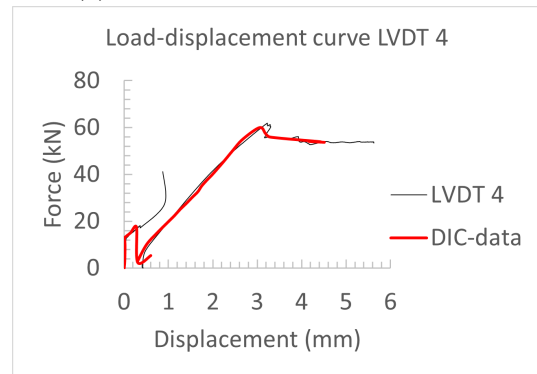
(a) Load-displacement curve LVDT 1



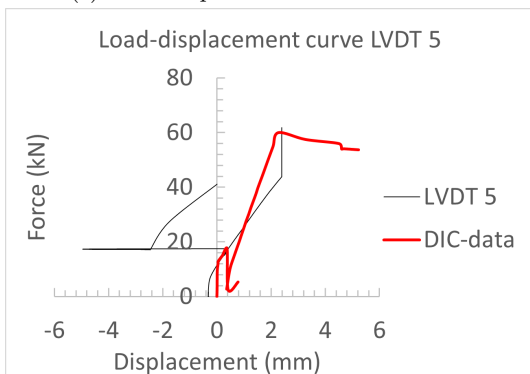
(b) Load-displacement curve LVDT 2



(c) Load-displacement curve LVDT 3



(d) Load-displacement curve LVDT 4



(e) Load-displacement curve LVDT 5

Figure H.3: B-3r8-c31: Load-displacement curves LVDT's and comparison with DIC-data

H.2 Results B-2r10-c31

The load-deflection curve for beam B-2r10-c31 is shown in figure H.4, as well as the maximum crack width curve. The maximum crack width according to the ACI440 and BRL0513 are shown as well. The chronological crack pattern propagation from the DIC-data is presented in figure H.5.

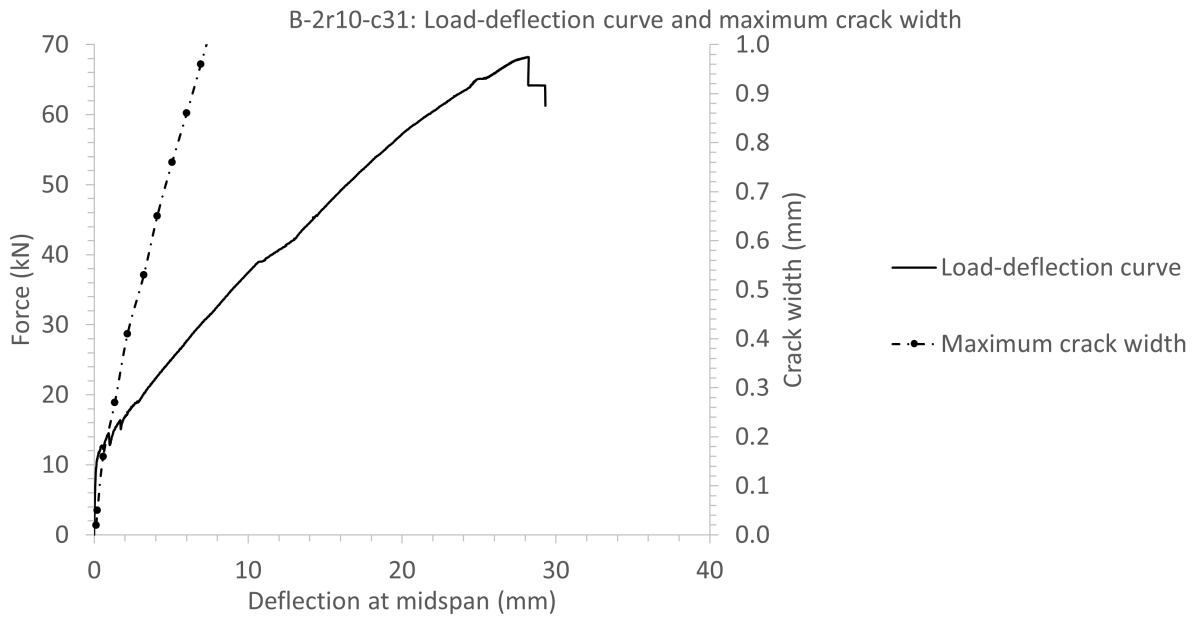
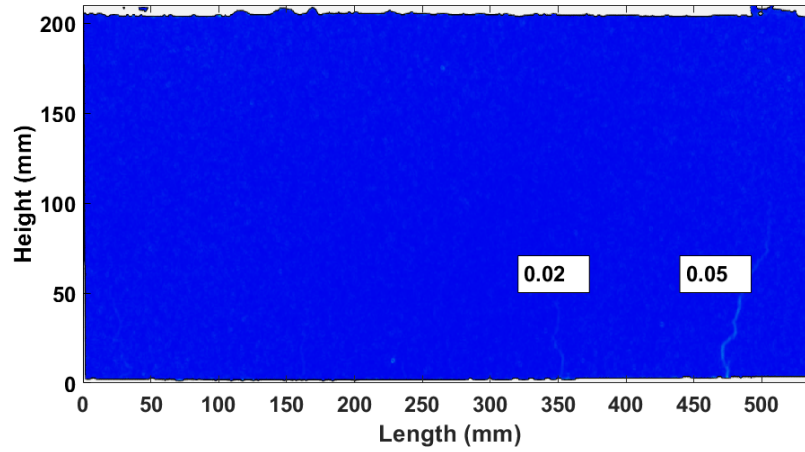


Figure H.4: B-2r10-c31, load-deflection curve versus maximum crack width measured from DIC-data

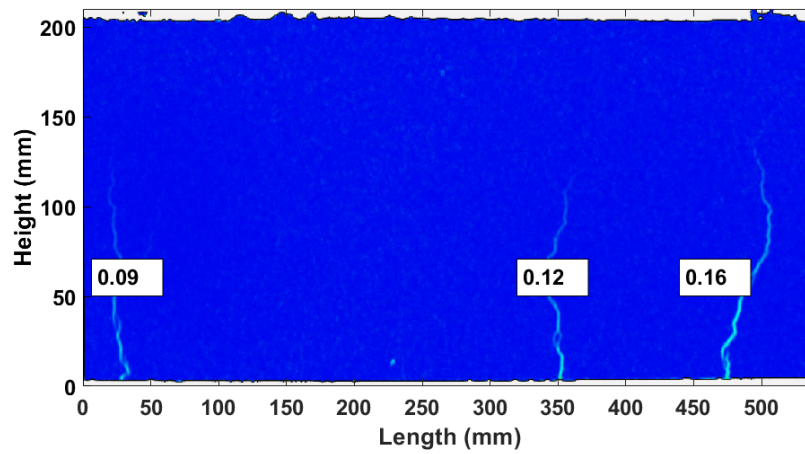
Table H.2: B-2r10-c31, summarized performance parameters

Performance parameters	
Maximum load	65.17 kN
Mid-span vertical deflection at maximum load	25.47 mm
Maximum vertical deflection at mid-span	25.47 mm
Number of cracks in constant bending moment zone	7
Average crack spacing	71.43 mm

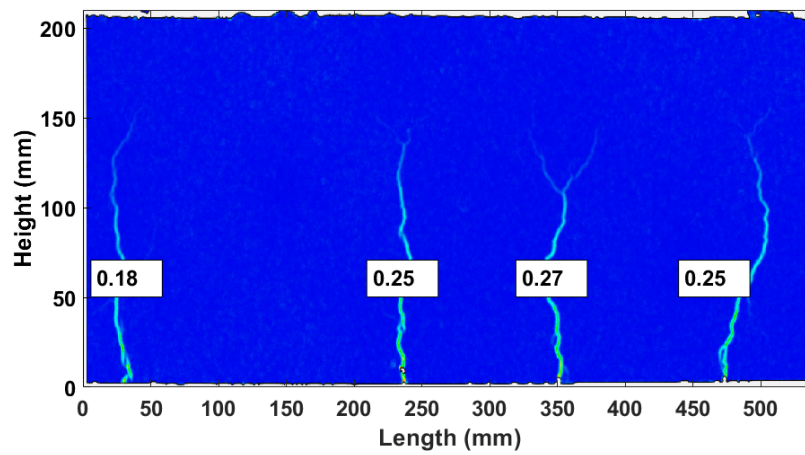
Beam B-2r8-c31 failed in the shear zone of the beam due to a faulty stirrup. Although the failure mode was not as expected, the force at which B-2r8-c31 failed is comparable to the beams that failed in compression. Initial cracks emerged at 10.90 kN (figure H.5a). Similar to beam B-3r8-c31, it exhibited horizontal cracks at the depth of reinforcement (figure H.5d), suggesting tensile splitting.



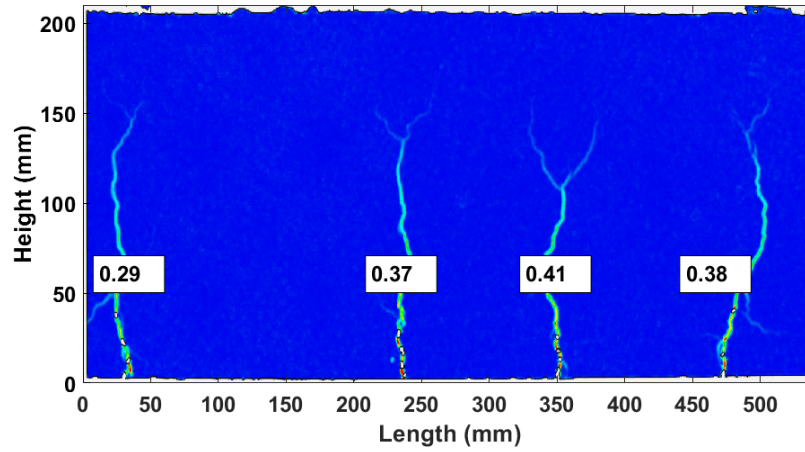
(a) B-2r10-c31: $F=10.90$ kN



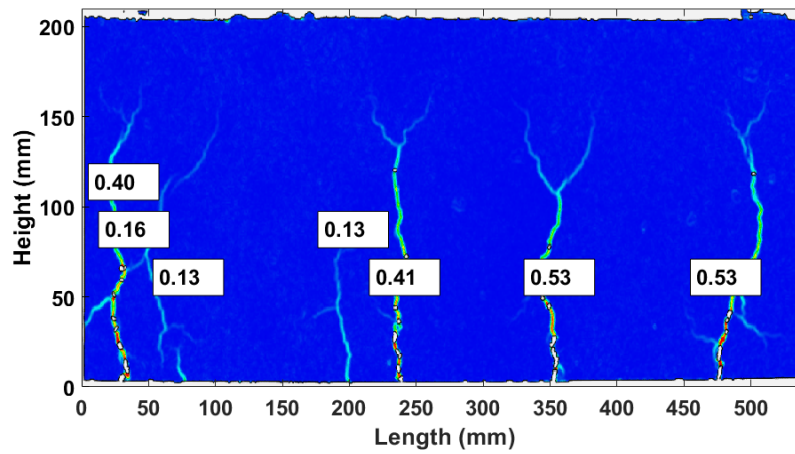
(b) B-2r10-c31: $F=12.27$ kN



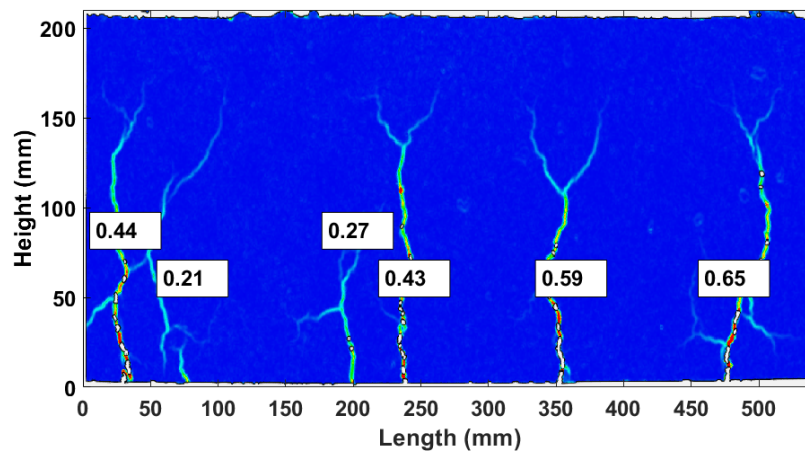
(c) B-2r10-c31: $F=15.05$ kN



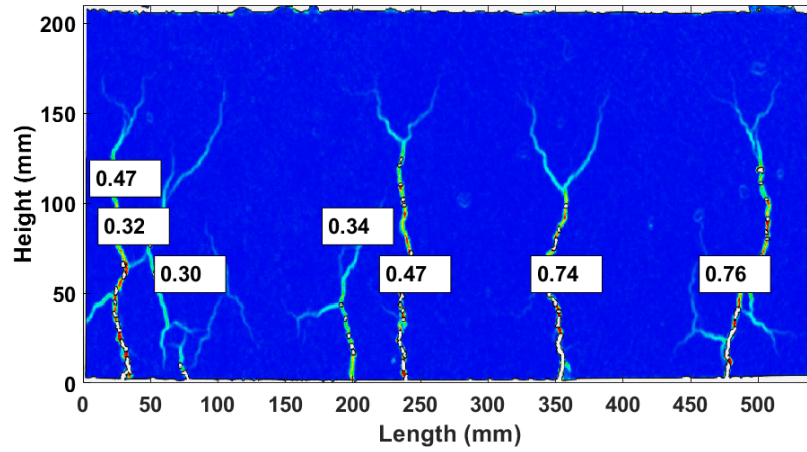
(d) B-2r10-c31: $F=17.20$ kN



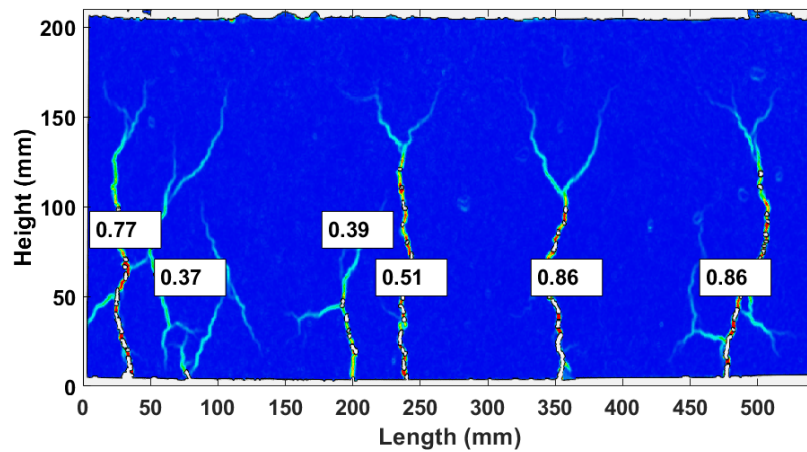
(e) B-2r10-c31: $F=20.13$ kN



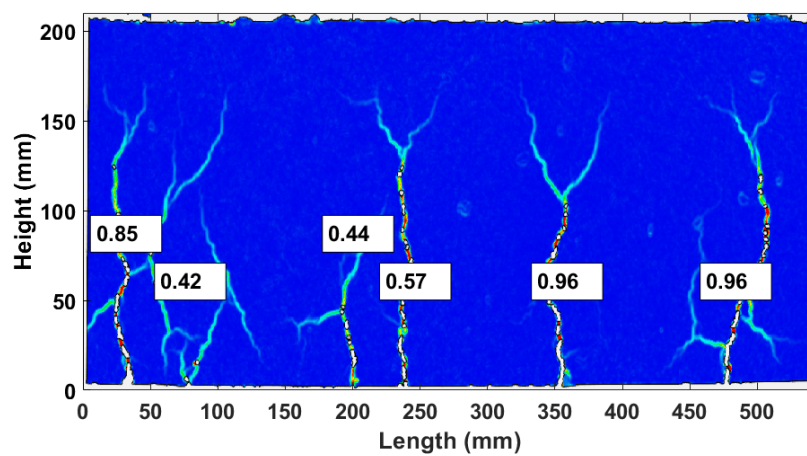
(f) B-2r10-c31: $F=22.60$ kN



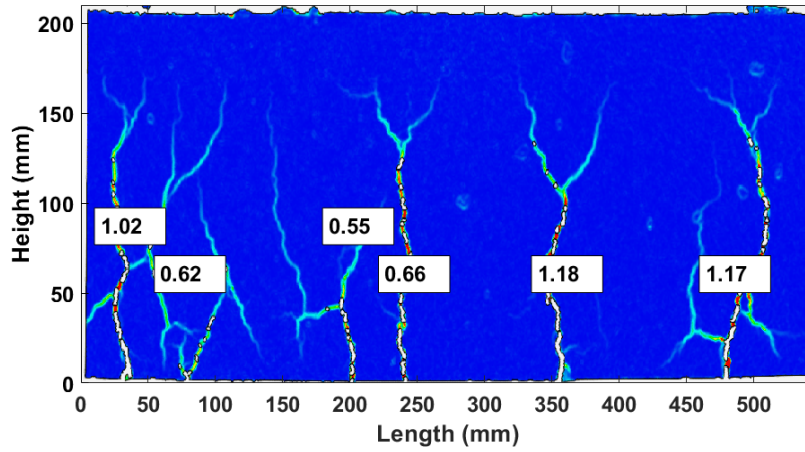
(g) B-2r10-c31: F=25.20 kN



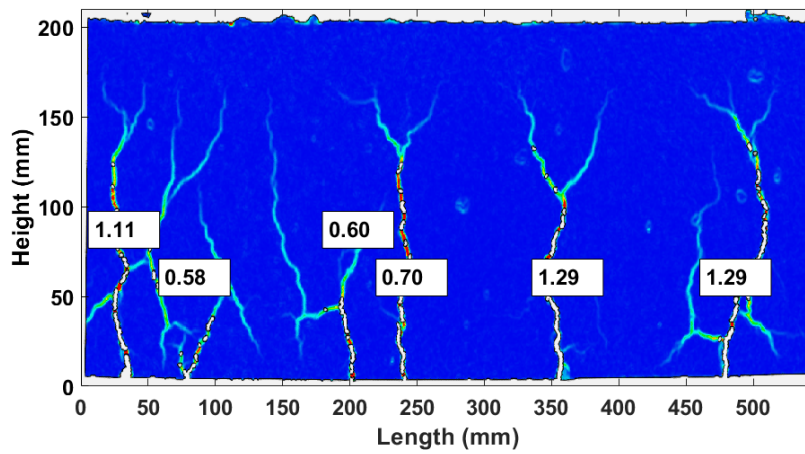
(h) B-2r10-c31: F=27.72 kN



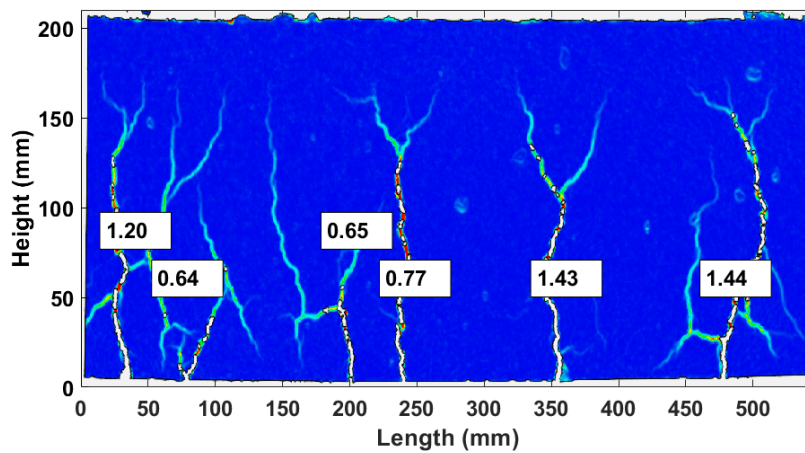
(i) B-2r10-c31: F=30.05 kN



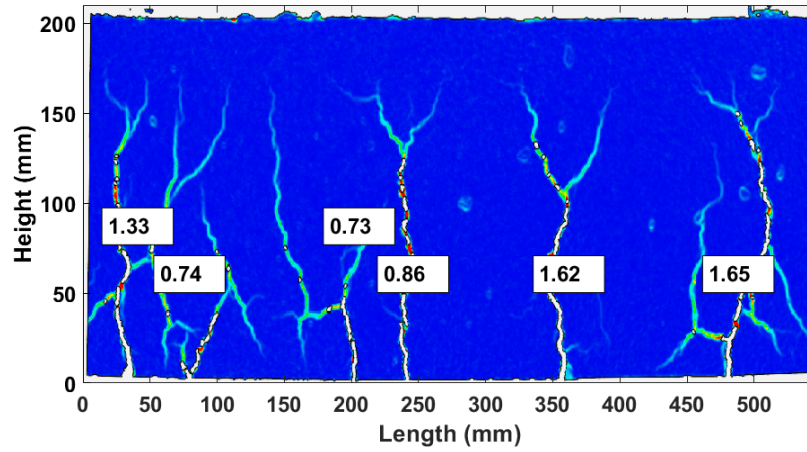
(j) B-2r10-c31: F=35.05 kN



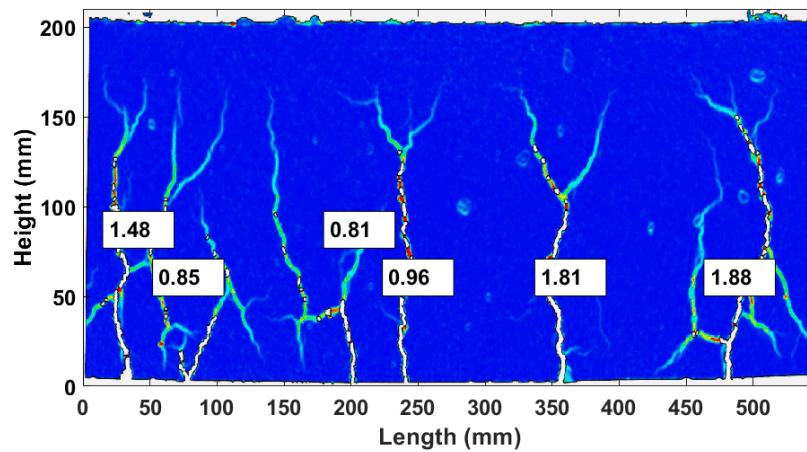
(k) B-2r10-c31: F=37.60 kN



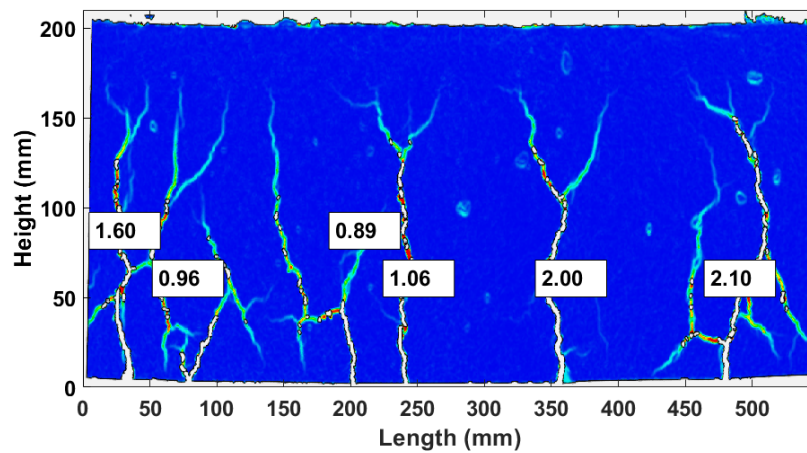
(l) B-2r10-c31: F=40.06 kN



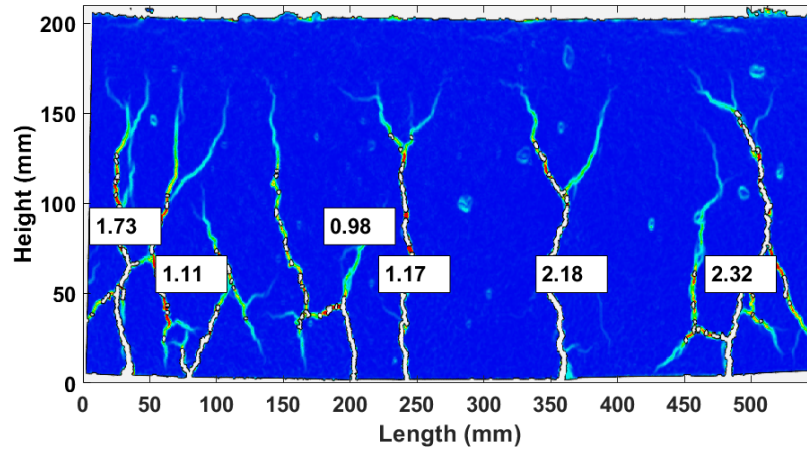
(m) B-2r10-c31: $F=45.06$ kN



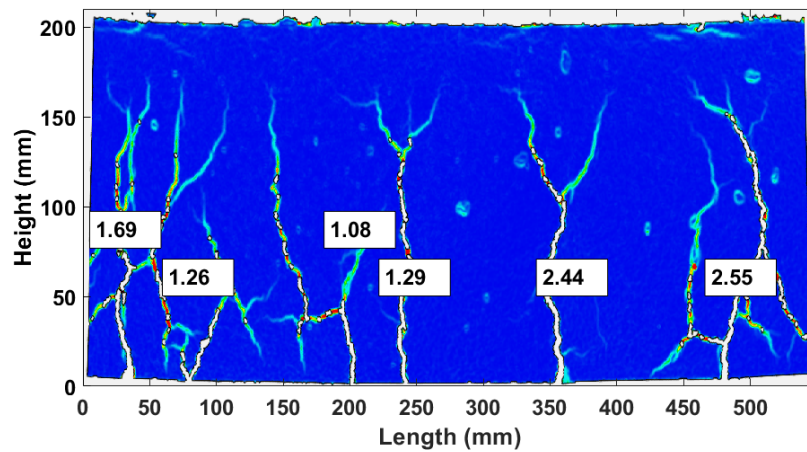
(n) B-2r10-c31: $F=50.01$ kN



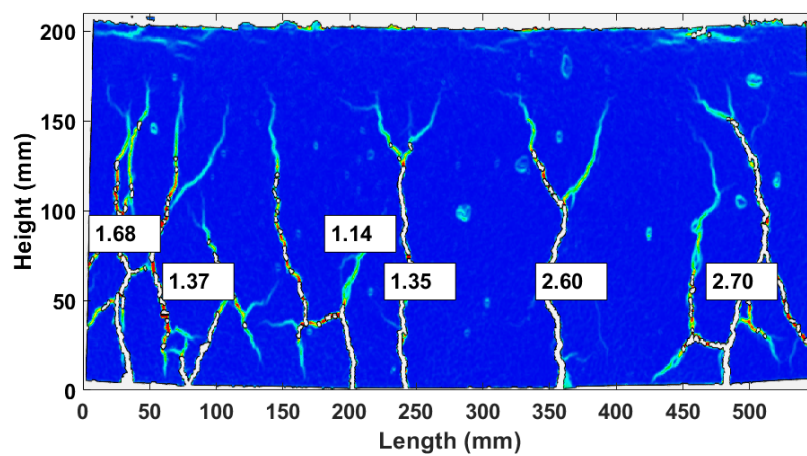
(o) B-2r10-c31: $F=55.02$ kN



(p) B-2r10-c31: $F=60.12$ kN



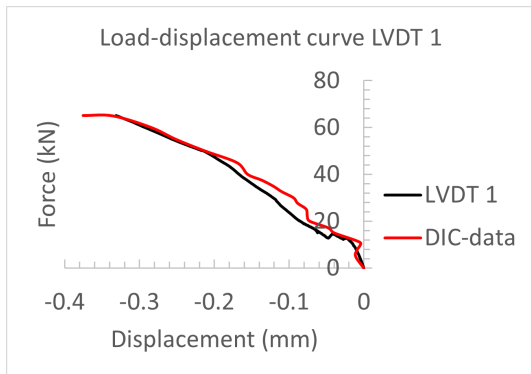
(q) B-2r10-c31: $F=65.01$ kN



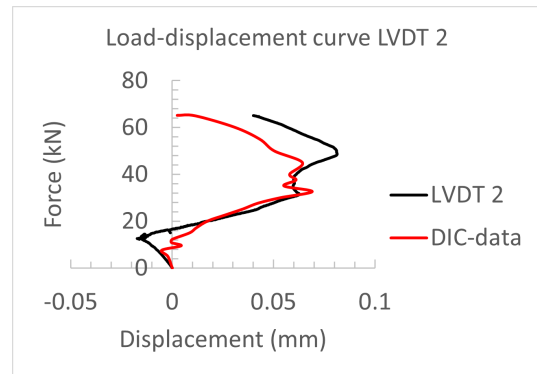
(r) B-2r10-c31: $F=65.17$ kN

Figure H.5: Crack widths contour plots B-2r10-c31 from DIC-data

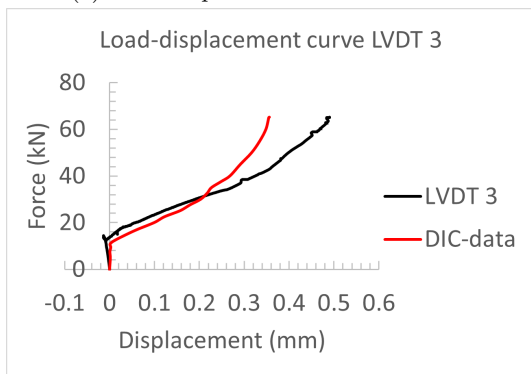
By comparing the DIC-data (figure H.6) to the data of the LVDT's, small differences are found between the DIC-data and the LVDT-data. The largest difference is found in LVDT 2 which is located in the concrete compression zone. As the force reached the load level of concrete crushing, DIC-data could become less accurate. The differences can be explained as the LVDT's are placed on the opposite side of the beam as the DIC-data is taken. The DIC-data is accepted as it is generally accurate.



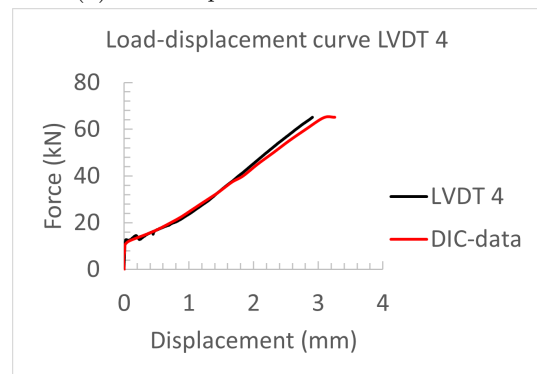
(a) Load-displacement curve LVDT 1



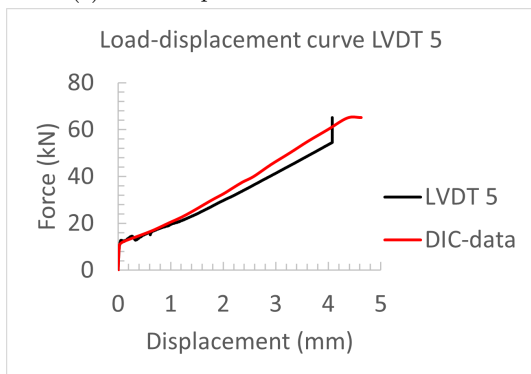
(b) Load-displacement curve LVDT 2



(c) Load-displacement curve LVDT 3



(d) Load-displacement curve LVDT 4



(e) Load-displacement curve LVDT 5

Figure H.6: B-2r10-c31: Load-displacement curves LVDT's and comparison with DIC-data

H.3 Results B-2r8-c31

Figure H.7 presents the load-deflection curve as well as the cracking curve of beam B-2r8-c31. Some performance indicators are noted in table H.3. The beam failed in the compression zone. The chronological crack pattern propagation from the DIC-data is presented in figure H.8.

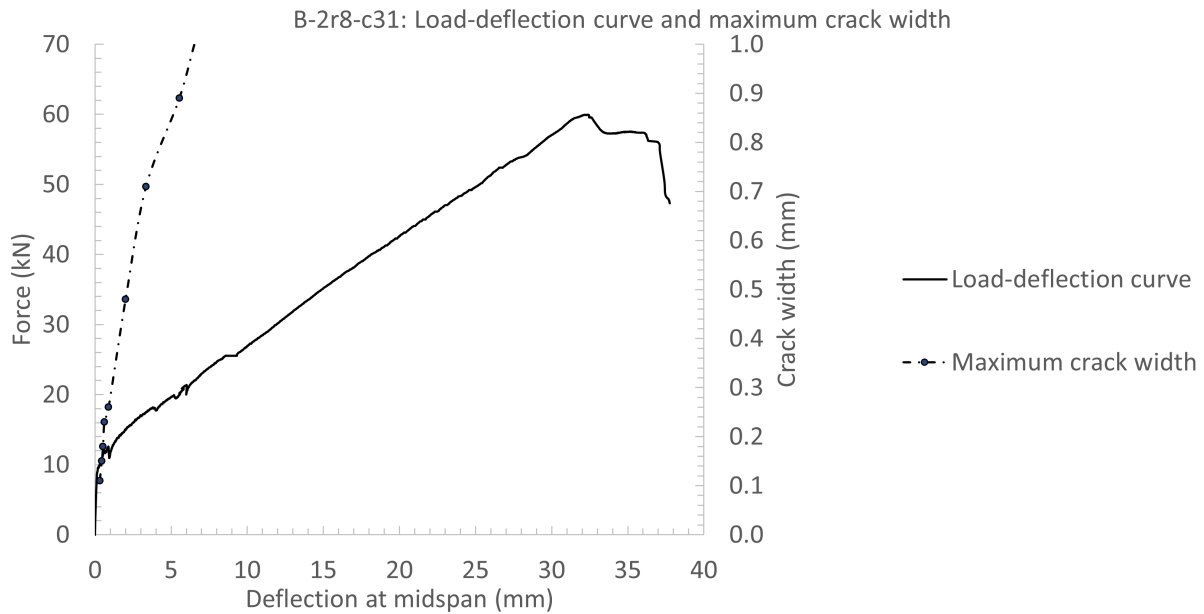


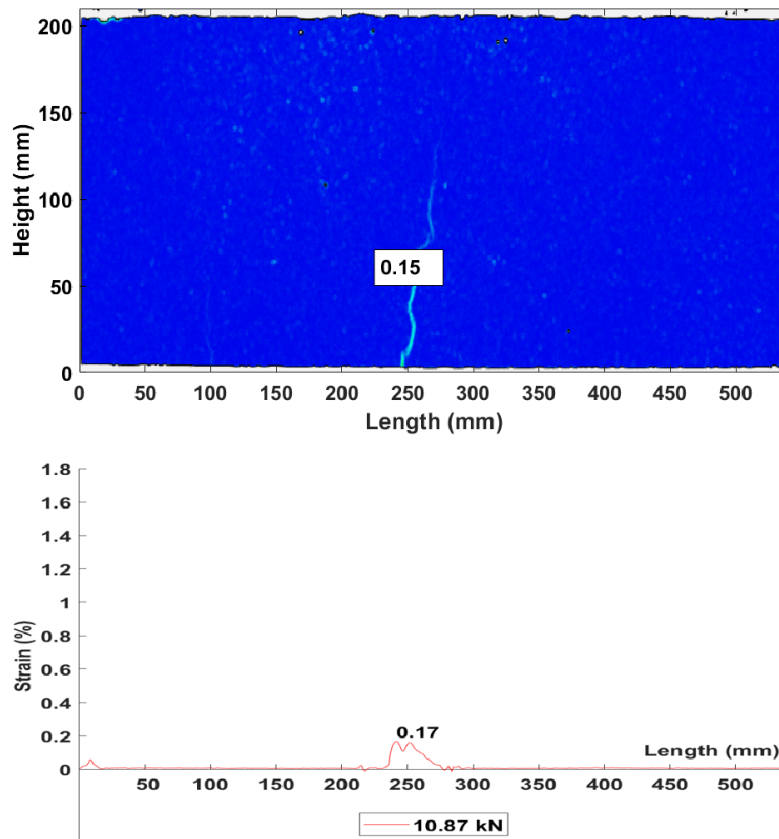
Figure H.7: B-2r8-c31, load-deflection curve versus maximum crack width measured from DIC-data

Table H.3: B-2r8-c31, summarized performance parameters

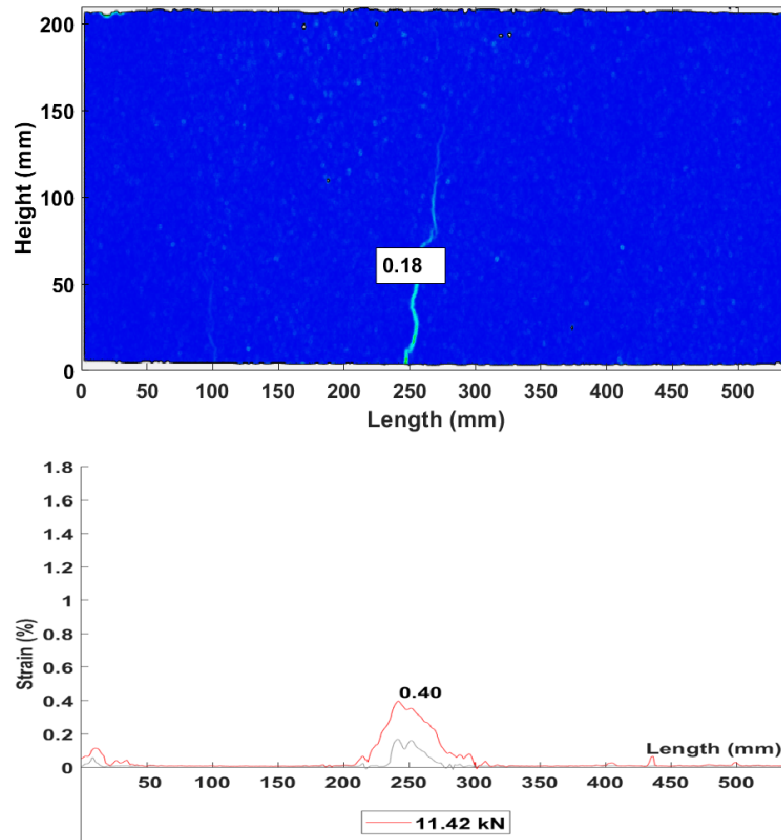
Performance parameters	
Maximum load	59.96 kN
Mid-span vertical deflection at maximum load	32.16 mm
Maximum vertical deflection at mid-span	37.76 mm
Number of cracks in constant bending moment zone	7
Average crack spacing	71.43 mm

As this beam specimen contains the least amount of reinforcement cross-section area of the 4 BFRP-reinforced beam specimens, this beam has the lowest stiffness, expecting the deflection to be comparatively larger at the same load levels after cracking. Figures H.8a to H.8t present the crack width propagation and pattern development in the constant bending moment zone of beam B-2r8-c31, combined with strain measurements from the optical strain fibre. The strain development in the reinforcement measured with the optical fibre is aligned below the contour plots. A peak in the strain development indicates the location of a crack, which aligns with the DIC-images. At higher load levels, the deformation of the beam causes the curves to be constantly above zero.

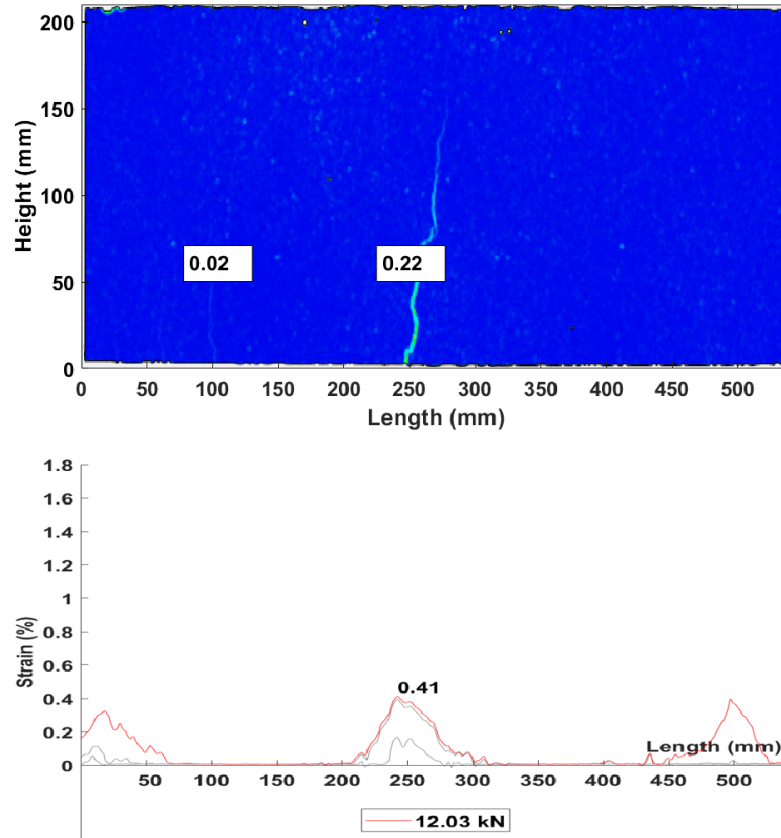
The first crack starts to appear at a load level of 10.87 kN, which is located approximately in the centre of the beam zone of constant bending moment. At the next load level of approximately 15 kN, 3 more flexural cracks have now developed where tensile splitting cracks emerge at the depth of the reinforcement. The crack width development is expected to be the largest as the reinforcement in the bottom is the least in terms of cross-sectional area, and therefore provides the least crack width control.



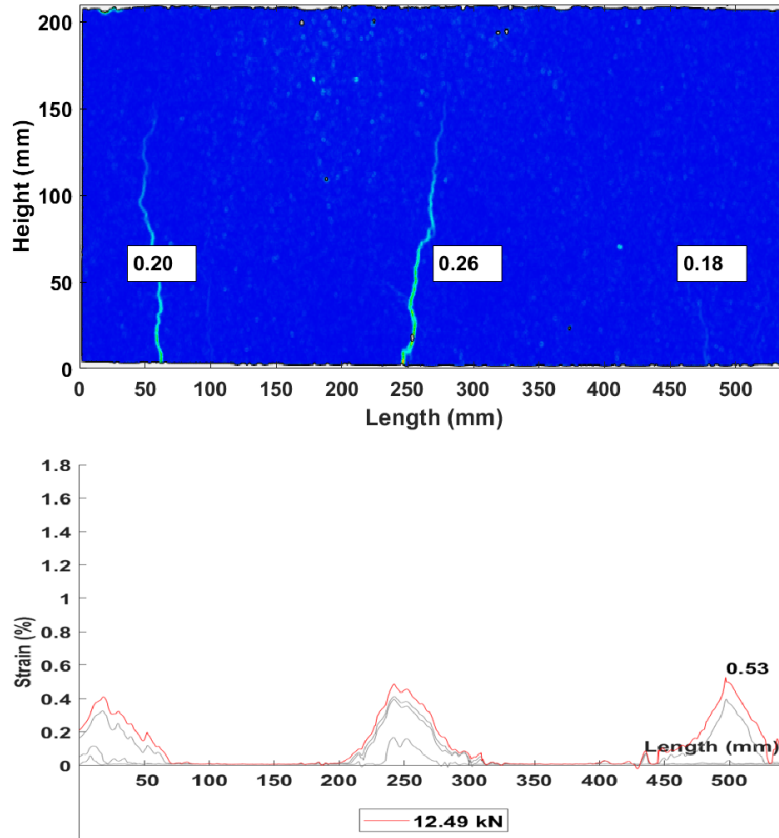
(a) B-2r8-c31: F=10.87 kN



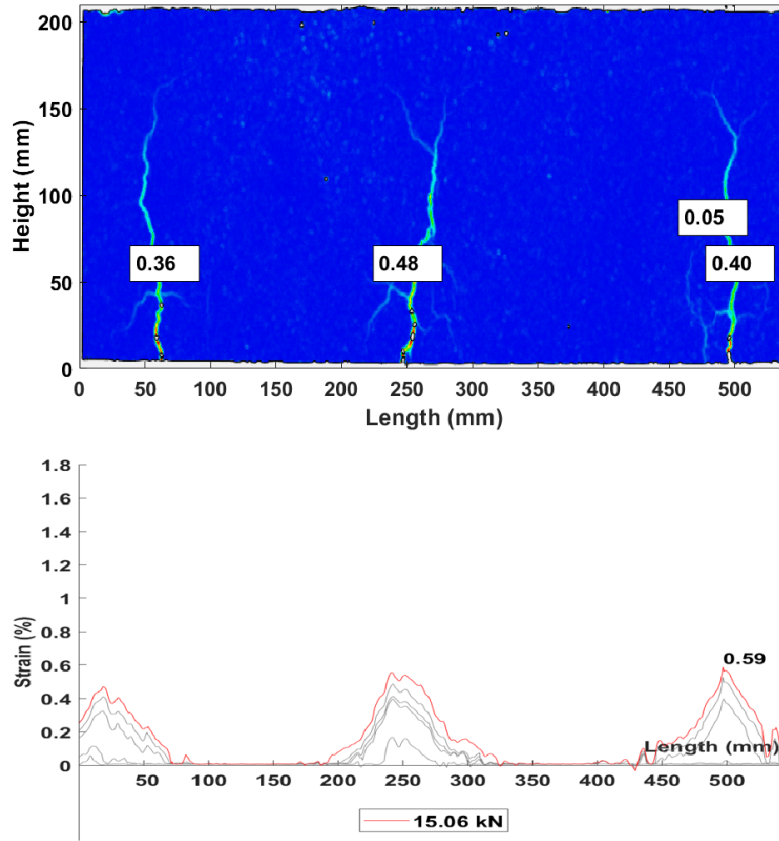
(b) B-2r8-c31: F=11.42 kN



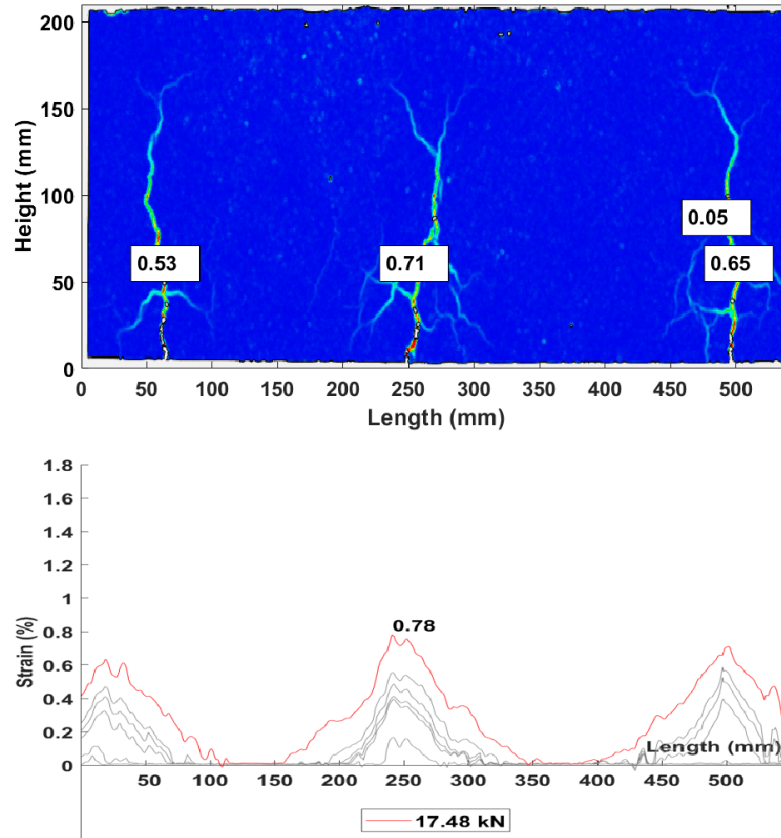
(c) B-2r8-c31: F=12.03 kN



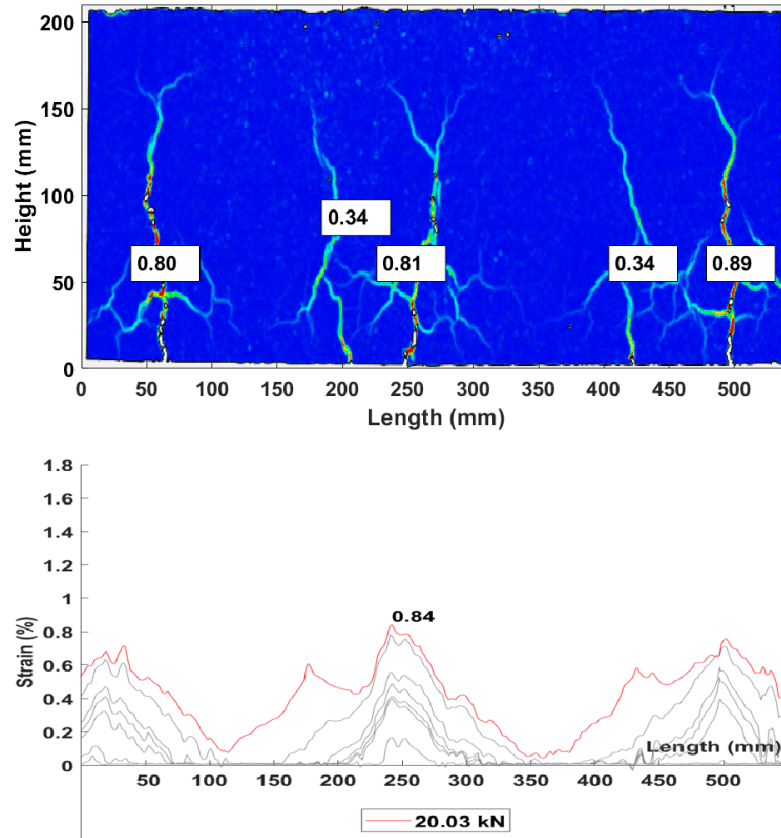
(d) B-2r8-c31: F=12.49 kN



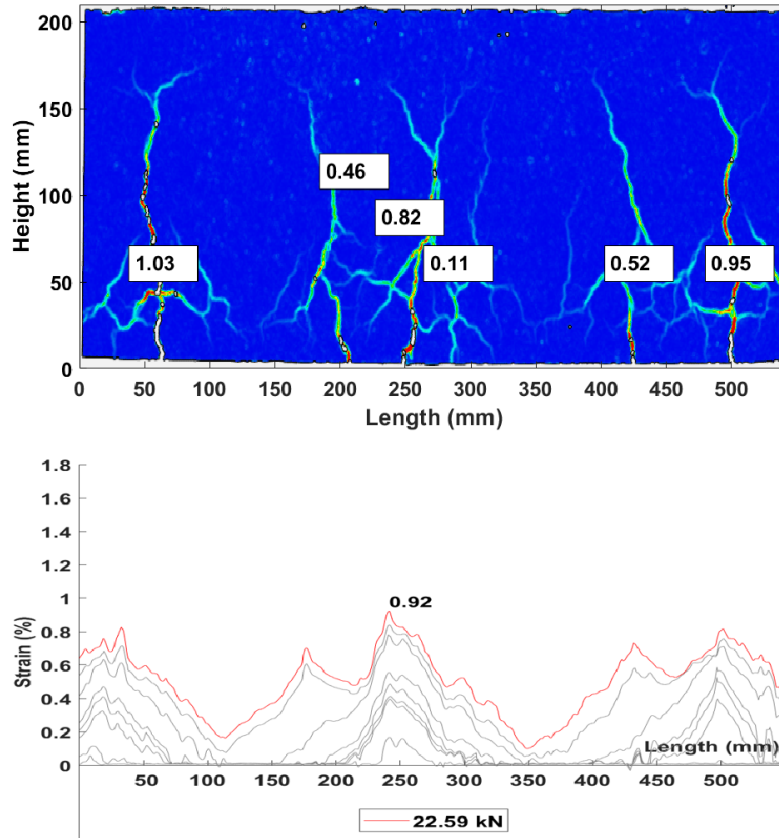
(e) B-2r8-c31: F=15.06 kN



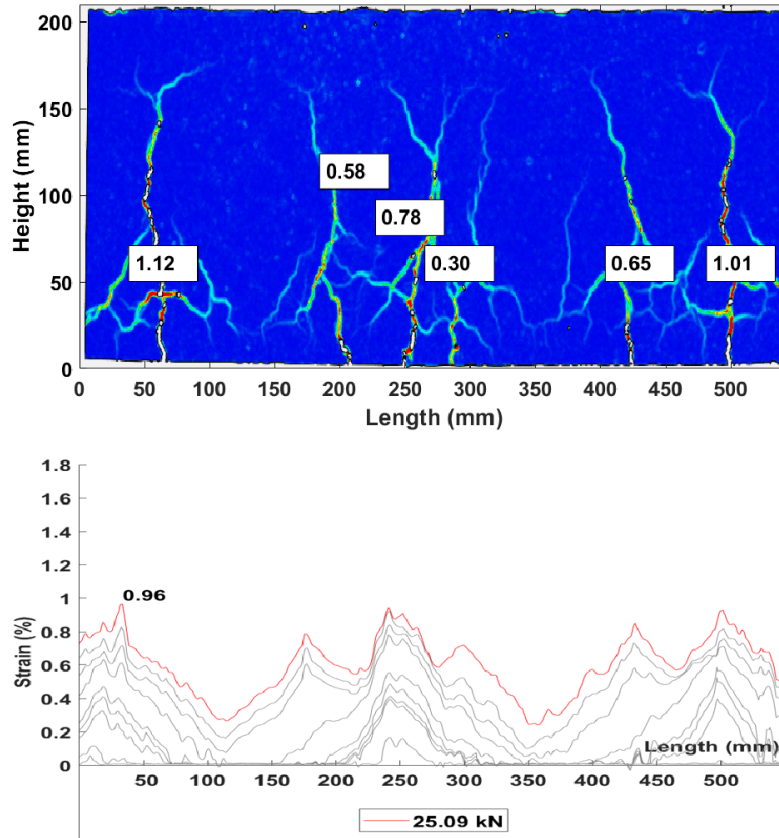
(f) B-2r8-c31: F=17.48 kN



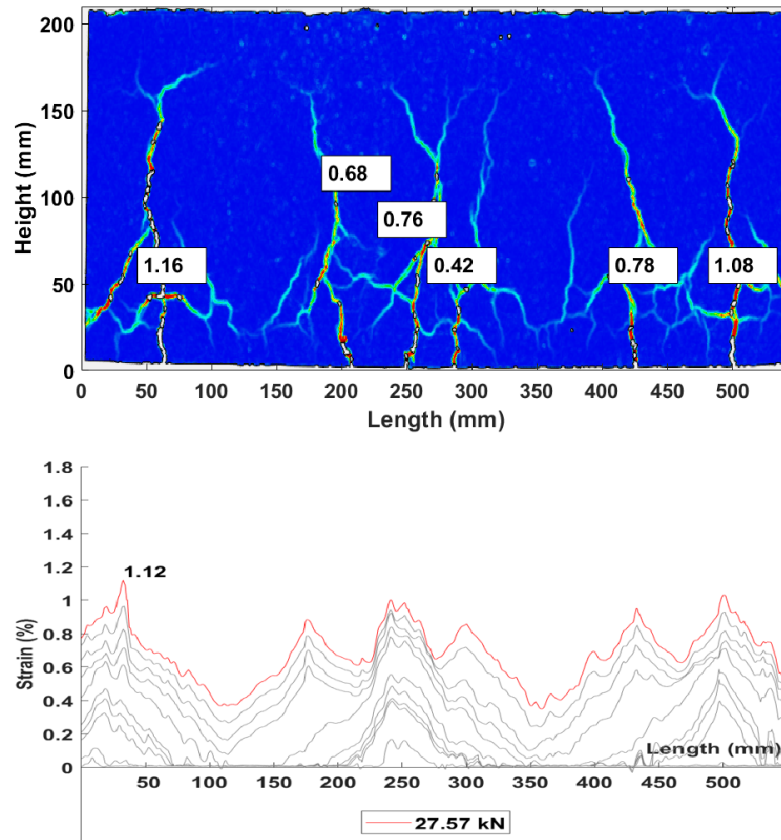
(g) B-2r8-c31: F=20.03 kN



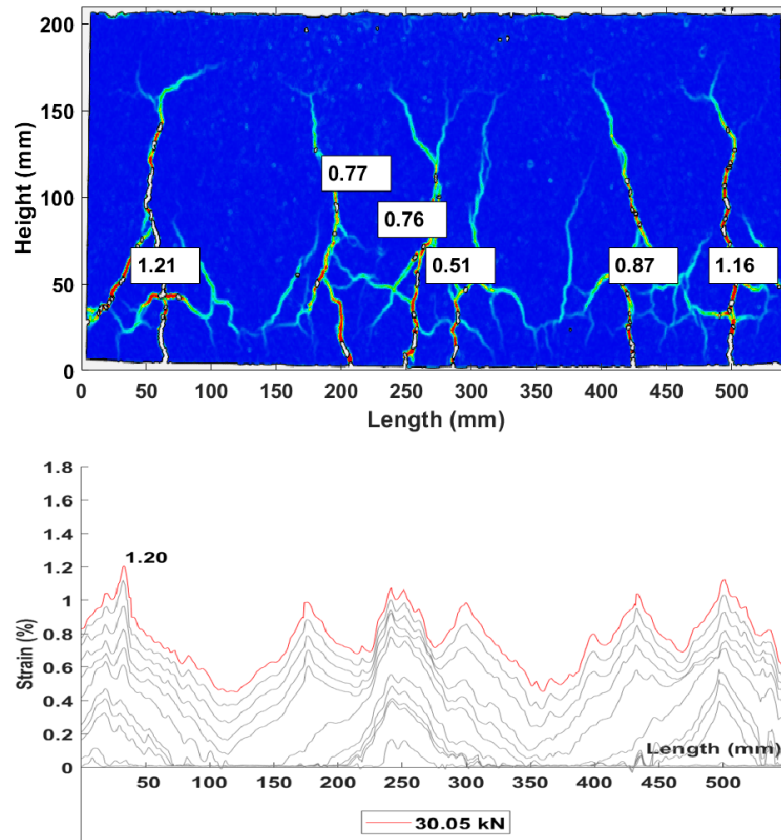
(h) B-2r8-c31: F=22.59 kN



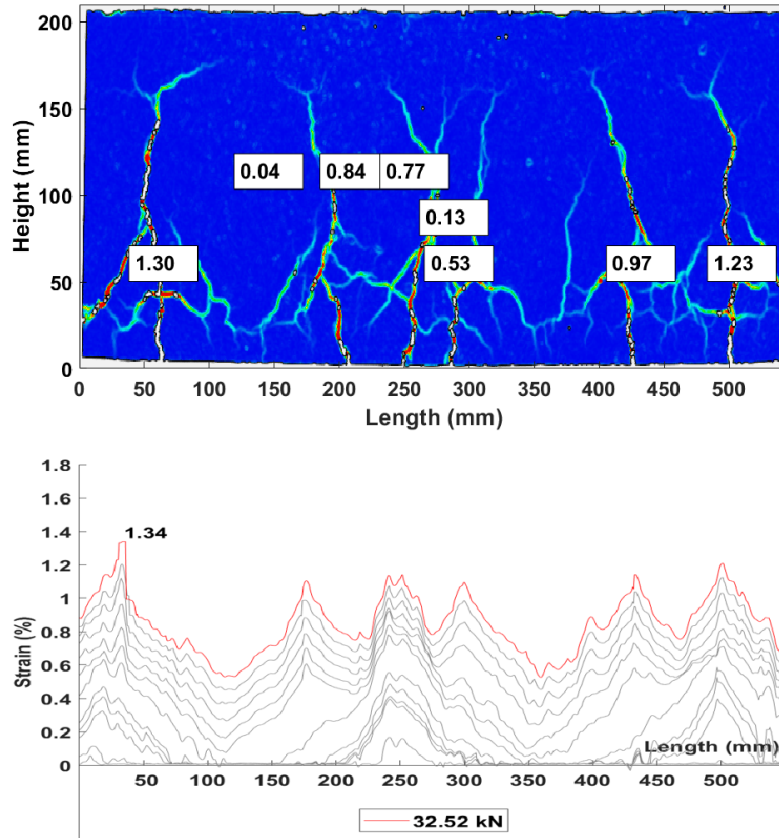
(i) B-2r8-c31: F=25.09 kN



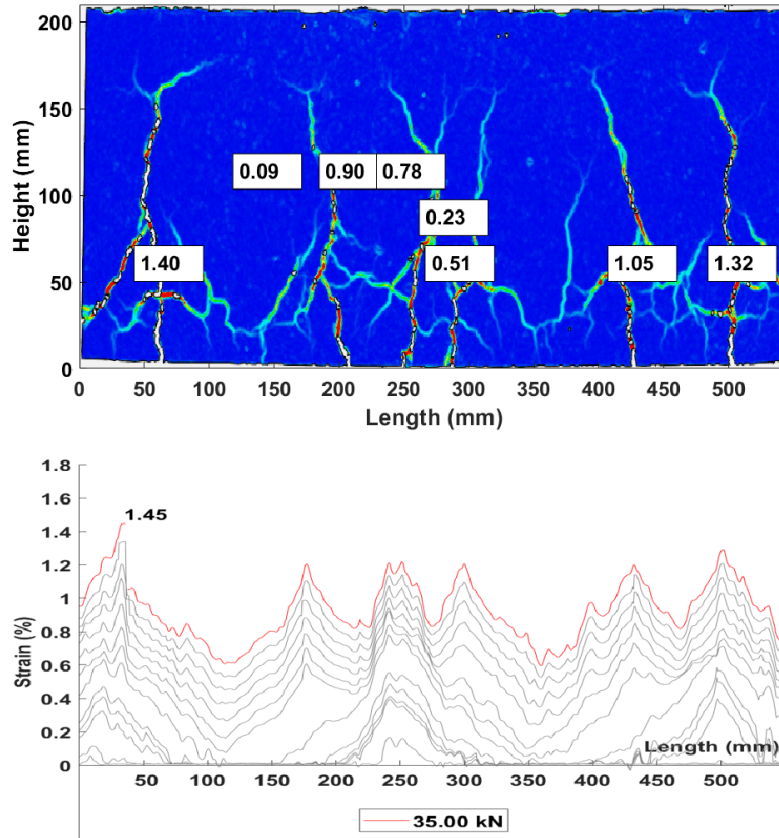
(j) B-2r8-c31: F=27.57 kN



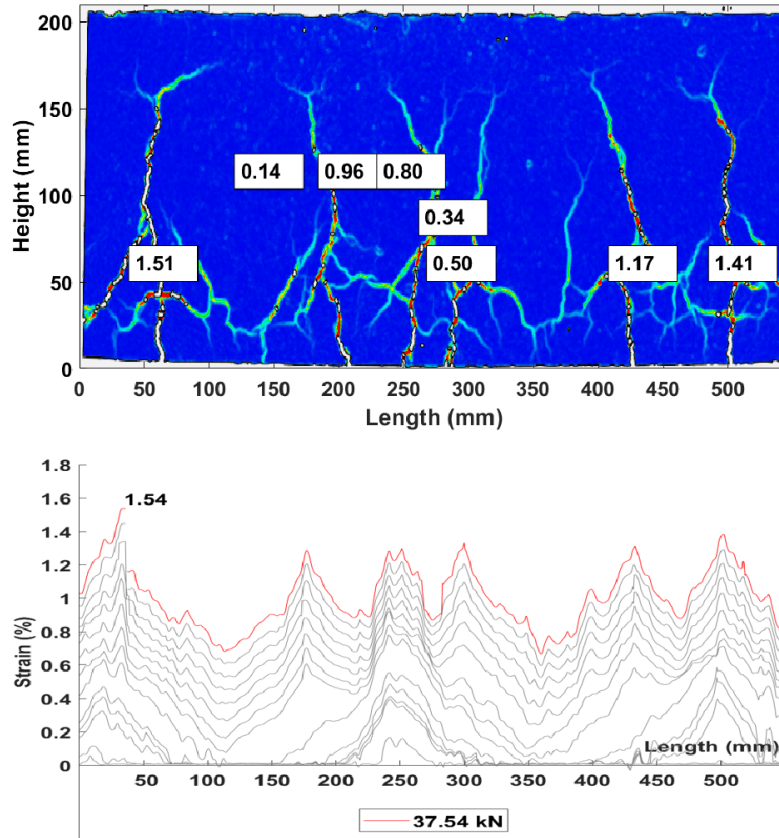
(k) B-2r8-c31: F=30.05 kN



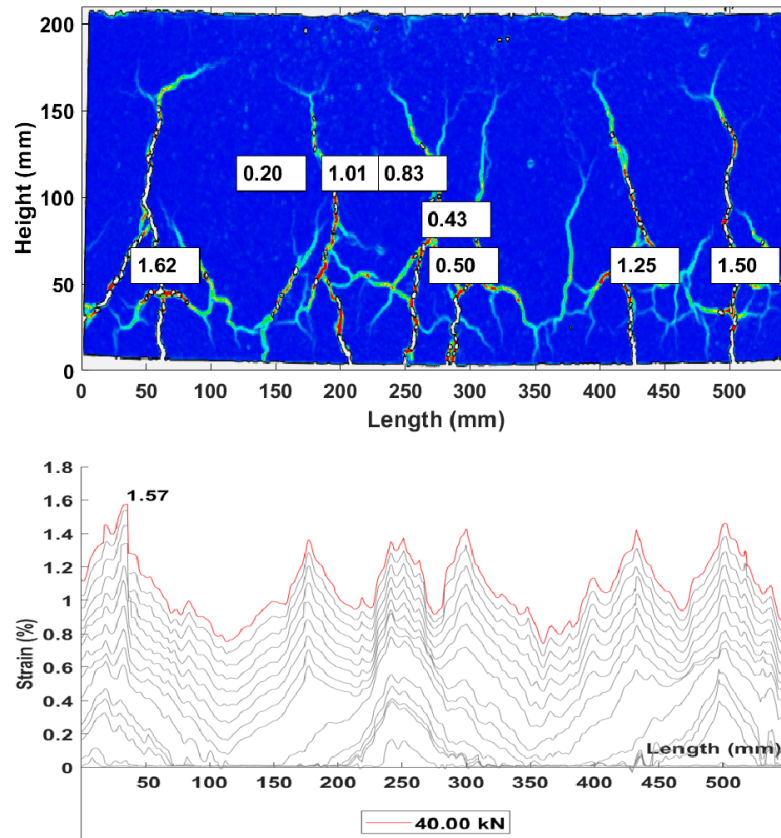
(1) B-2r8-c31: F=32.52 kN



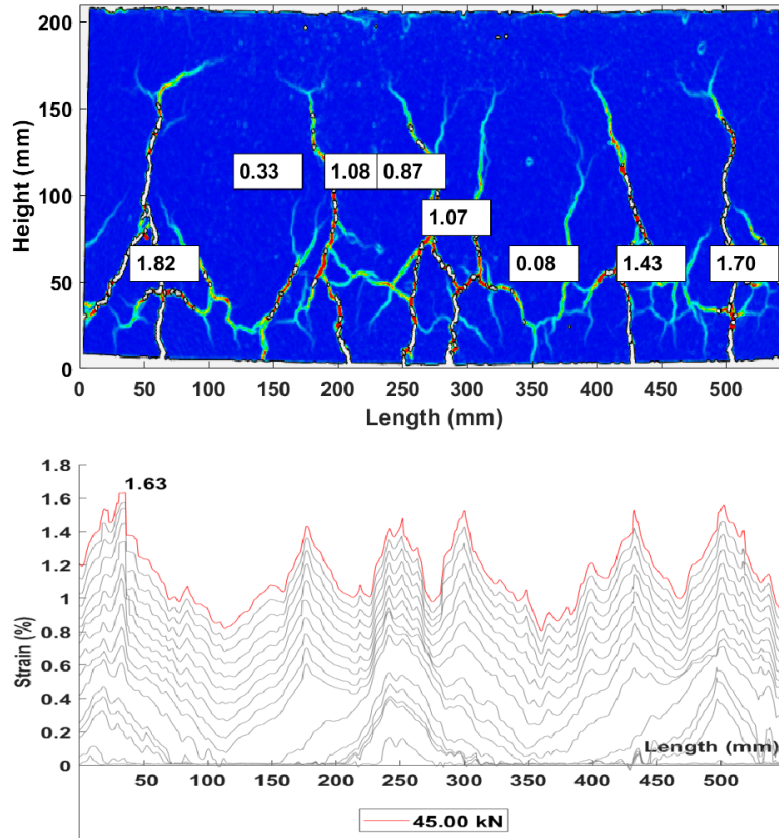
(m) B-2r8-c31: F=35.00 kN



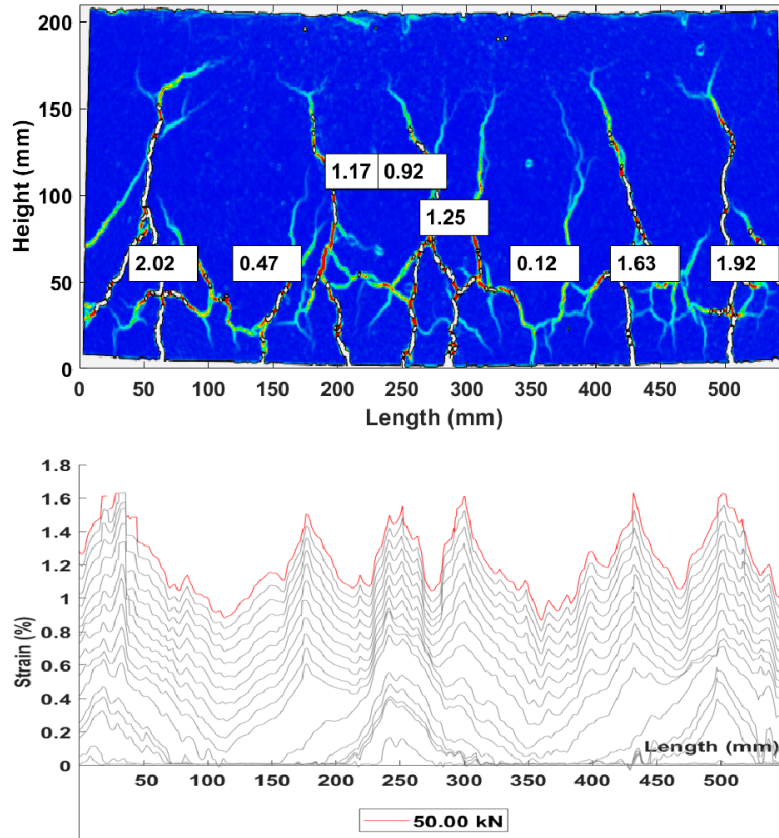
(n) B-2r8-c31: F=37.54 kN



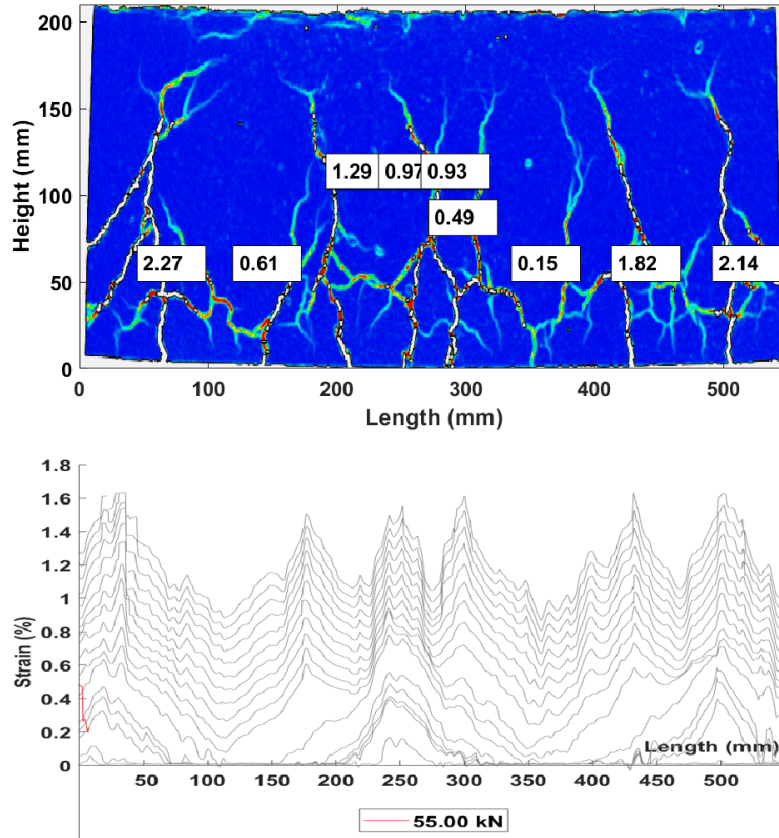
(o) B-2r8-c31: F=40.00 kN



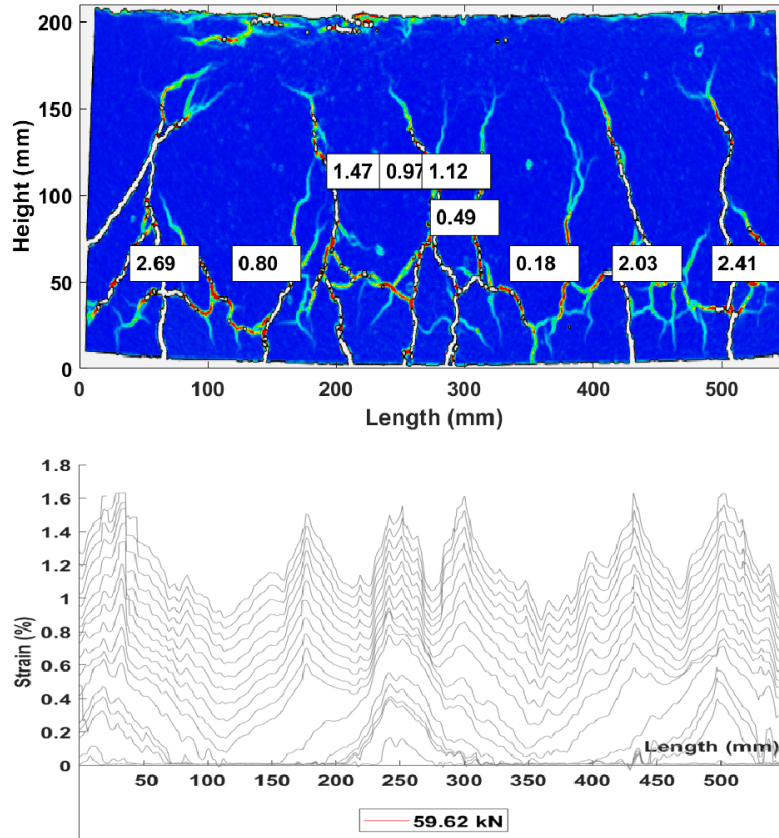
(p) B-2r8-c31: F=45.00 kN



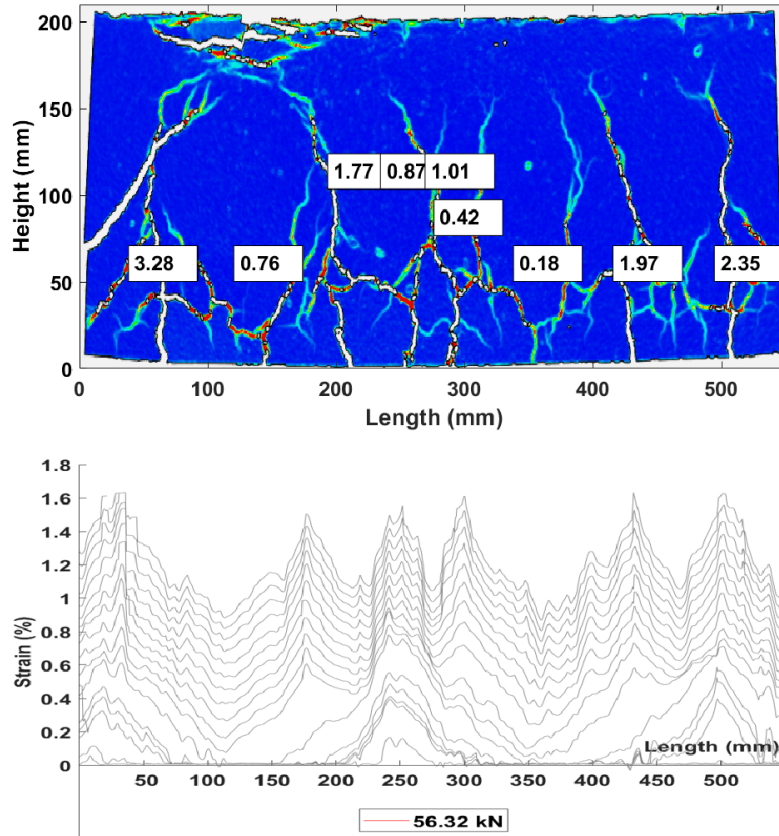
(q) B-2r8-c31: F=50.00 kN



(r) B-2r8-c31: F=55.00 kN



(s) B-2r8-c31: F=59.62 kN



(t) B-2r8-c31: F=56.32 kN

Figure H.8: Combined crack widths contour plots B-2r8-c31 from DIC-data and corresponding strain graphs optical fibre from optical fibre data

At load levels 59.62 kN and 56.32 kN, the data from the optical fibre does not provide strain development at the constant bending moment zone of the beam. This is likely due to the excessive elongation, causing the breaking of the fibre.

Upon inspecting the data of the optical fibre, the fibre broke at a load level of approximately 55 kN. Figure H.9 presents the strain development over the full length of the fibre. The constant bending moment zone begins at 0 mm in this figure. At load level 59.62 kN, and -150 mm at load level 56.31 kN, the optical fibre does not convey data anymore for strain measuring. Probable causes for this are breaking of the fibre or extensive slip with respect to either its coating or the adhesive.

The highest strain measured in the gauge is equal to 1.65%, which is located at approximately 600 mm, which is located outside the constant bending moment zone. The real maximum strain is likely higher if the is not the maximum load level. For the higher load levels, the strain gauge did not capture any useful data.

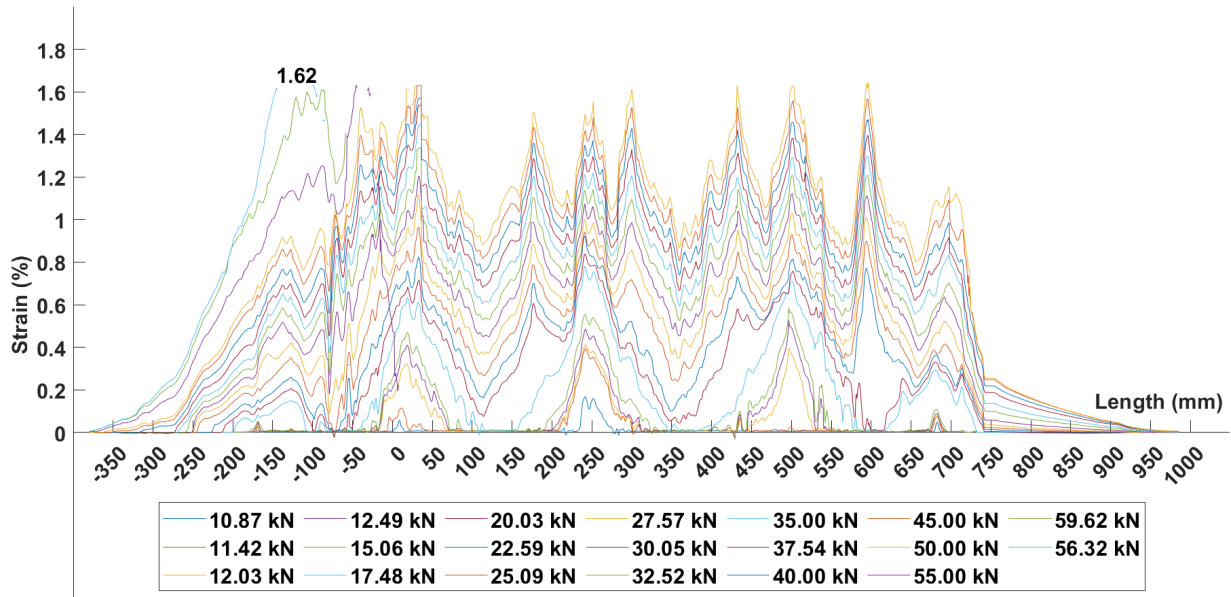


Figure H.9: Full optical fibre gauge length strain development beam B-2r8-c31

Figure H.10 present the stress development over the length of the strain gauge. As the stress-strain behaviour of the BFRP-bars is linear-elastic, the stress in the reinforcement is determined by multiplying the strain with the Young's modulus. Therefore, the measured maximum stress in the tensile reinforcement is equal to 880.95 MPa.

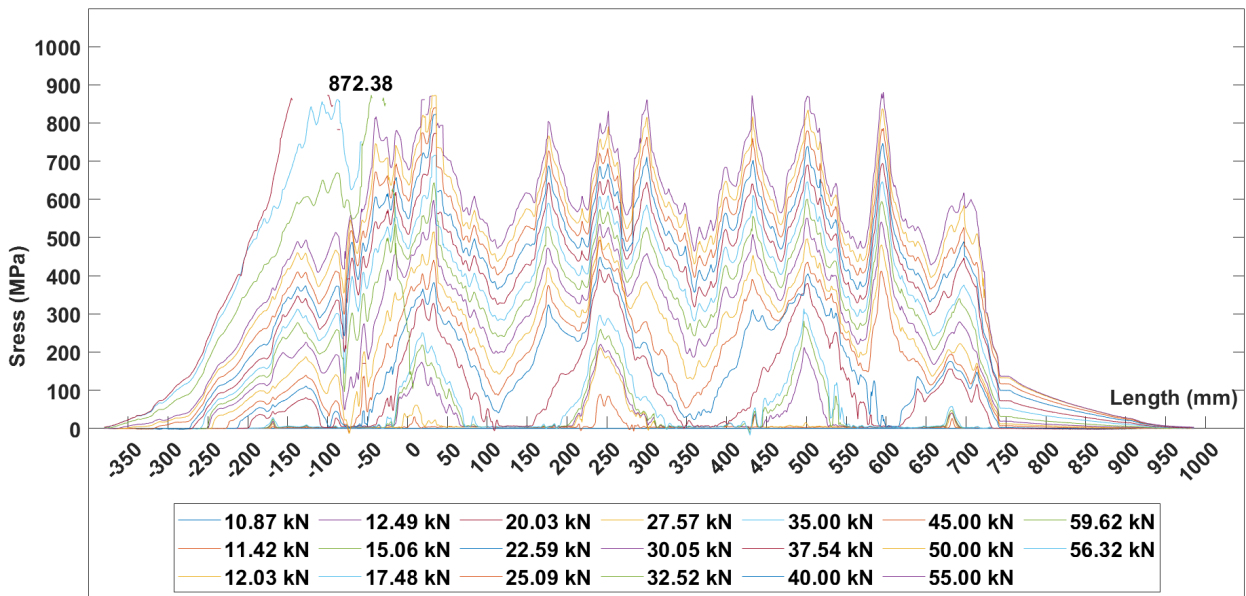
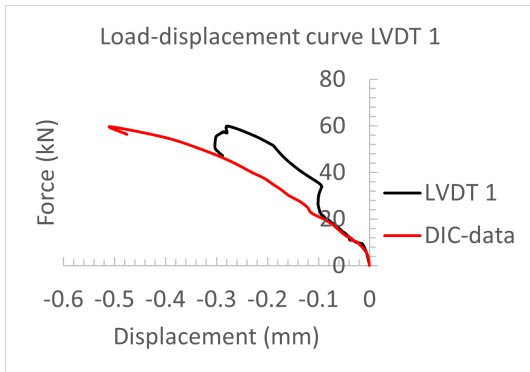
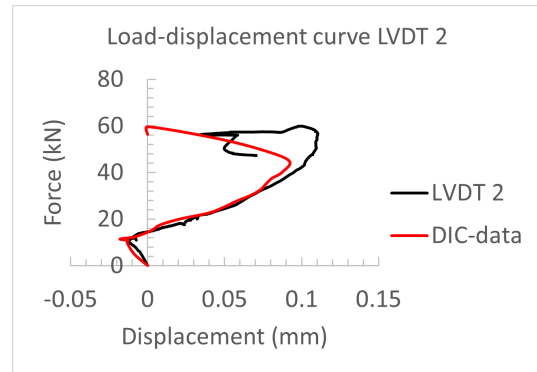


Figure H.10: Full optical fibre gauge length stress development beam B-2r8-c31

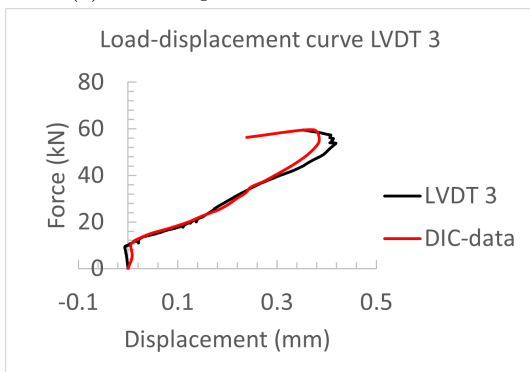
By comparing the DIC-data (figure H.11) to the data of the LVDT's, small differences are found between the DIC-data and the LVDT-data. The differences can be explained as the LVDT's are placed on the opposite side of the beam as the DIC-data is taken. The DIC-data is accepted as it is generally accurate.



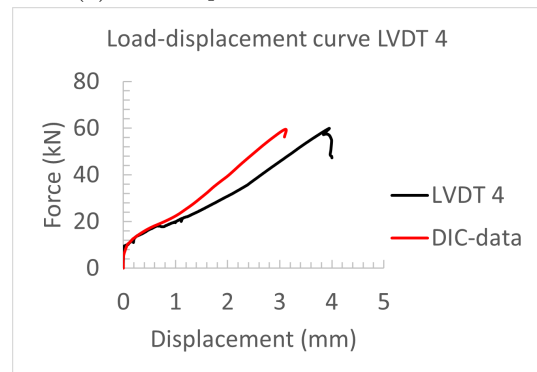
(a) Load-displacement curve LVDT 1



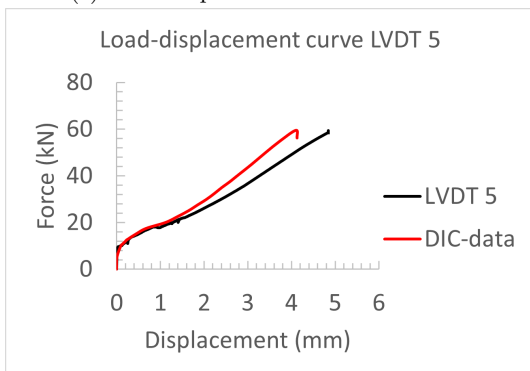
(b) Load-displacement curve LVDT 2



(c) Load-displacement curve LVDT 3



(d) Load-displacement curve LVDT 4



(e) Load-displacement curve LVDT 5

Figure H.11: B-2r8-c31: Load-displacement curves LVDT's and comparison with DIC-data

H.4 Results B-3r8-c11

Figure H.12 presents the load-deflection curve for beam B-3r8-c11. This graph includes the maximum crack width curve for which the corresponding load level can be determined. The chronological crack pattern propagation from the DIC-data is presented in figure H.13. The beam failed as one of the reinforcement bars failed in tension at a load of 71.05 kN.

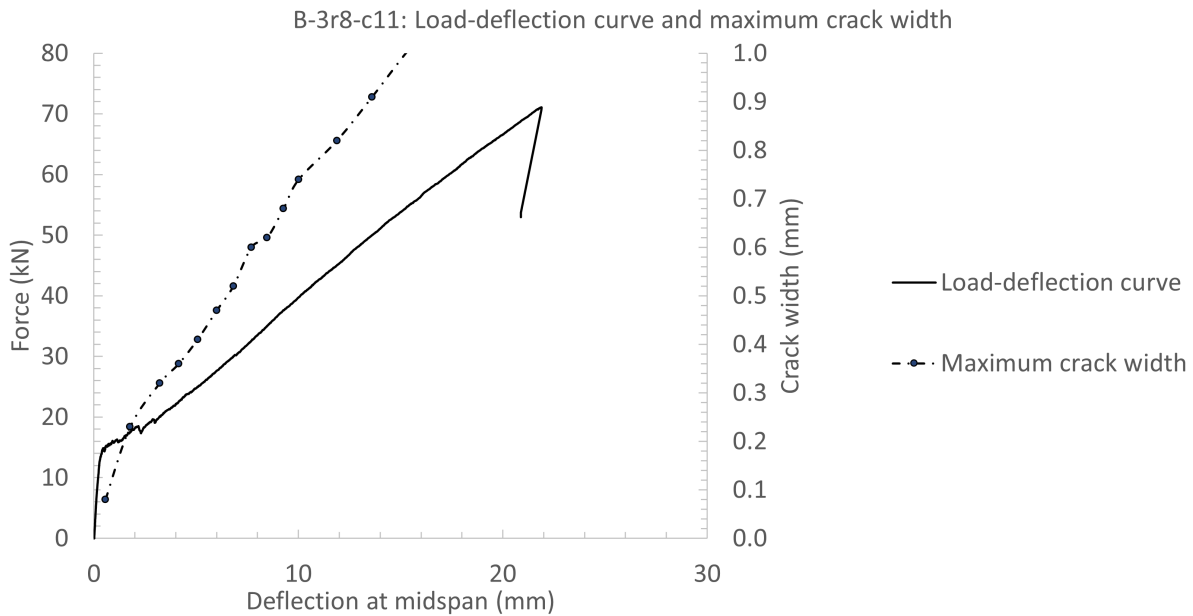
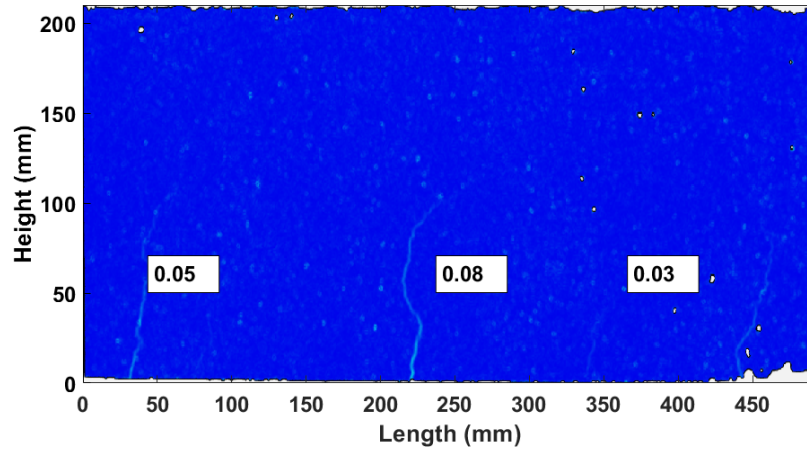


Figure H.12: B-3r8-c11, load-deflection curve versus maximum crack width measured from DIC-data

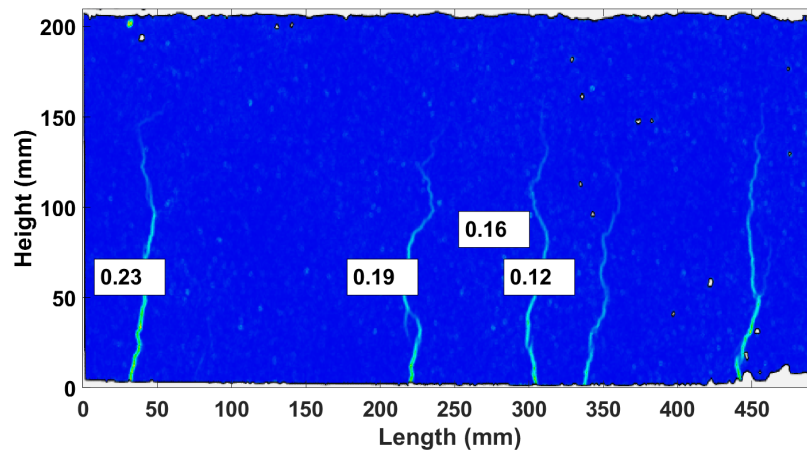
Table H.4: B-3r8-c11, summarized performance parameters

Performance parameters	
Maximum load	71.05 kN
Mid-span vertical deflection at maximum load	21.90 mm
Maximum vertical deflection at mid-span	21.90 mm
Number of cracks in constant bending moment zone	8
Average crack spacing	62.5 mm

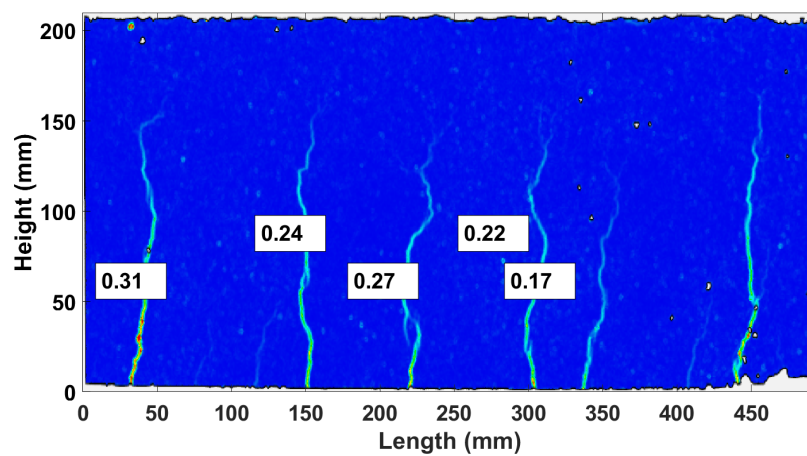
Some performance indicators are noted in table H.4. From the contour plots from the DIC-data, it is shown that the first cracks appear at 15.08 kN (figure H.13a).



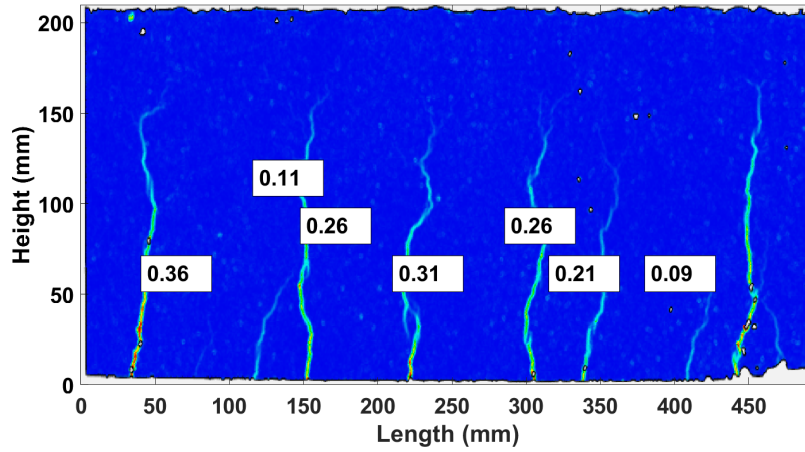
(a) B-3r8-c11: F=15.08 kN



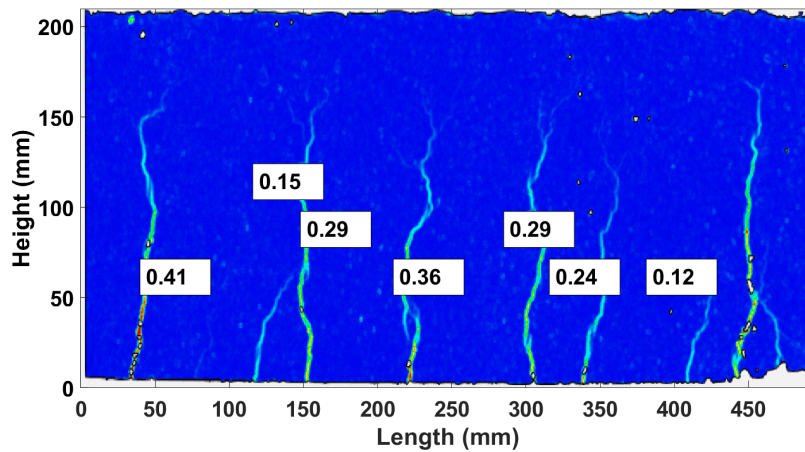
(b) B-3r8-c11: F=17.56 kN



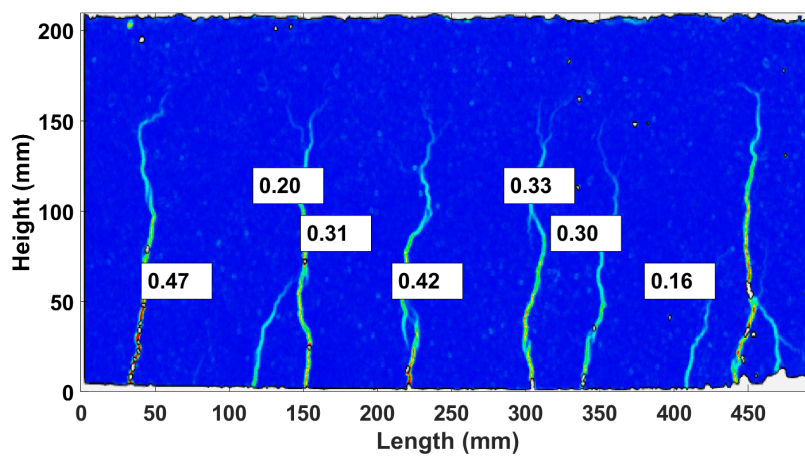
(c) B-3r8-c11: F=20.14 kN



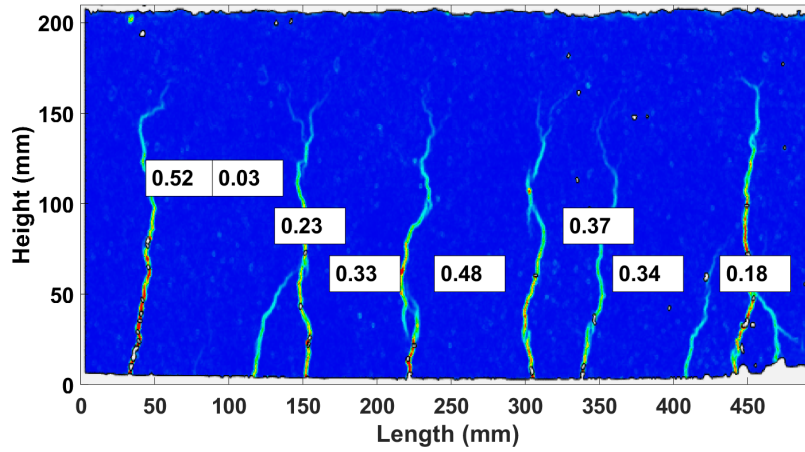
(d) B-3r8-c11: F=22.57 kN



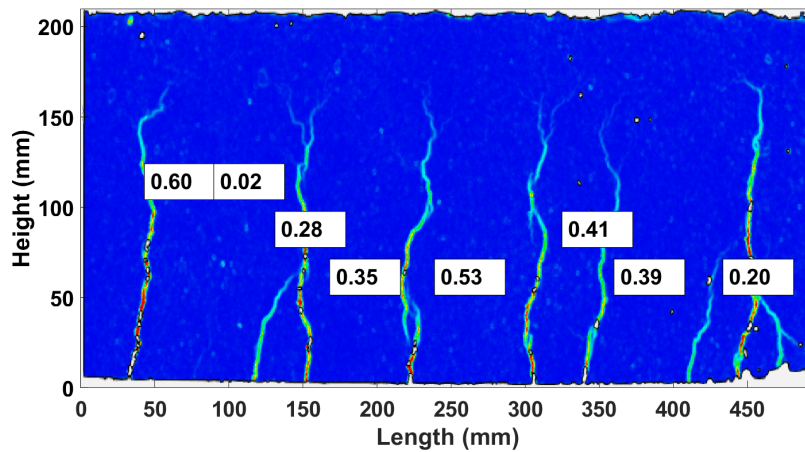
(e) B-3r8-c11: F=25.02 kN



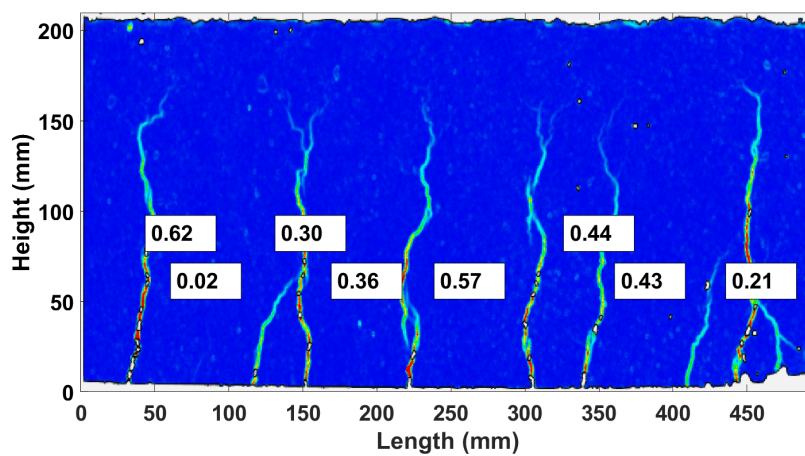
(f) B-3r8-c11: F=27.66 kN



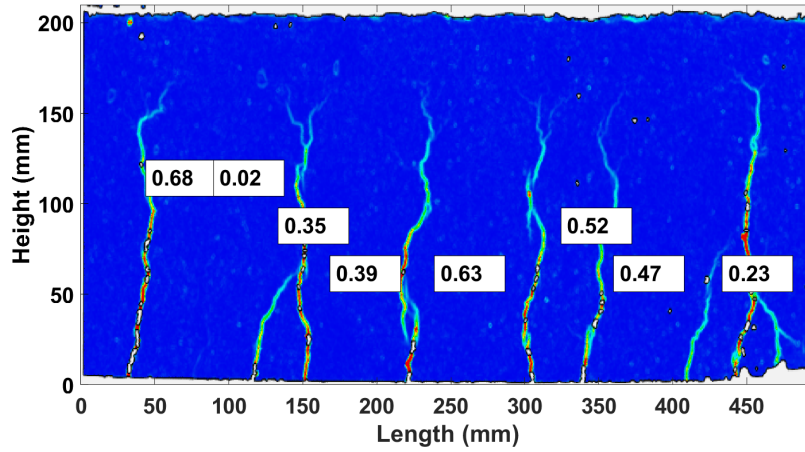
(g) B-3r8-c11: $F=30.02$ kN



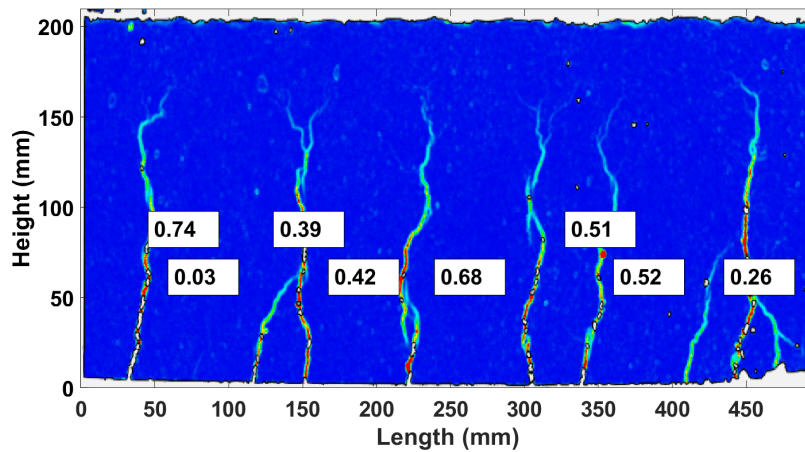
(h) B-3r8-c11: $F=32.60$ kN



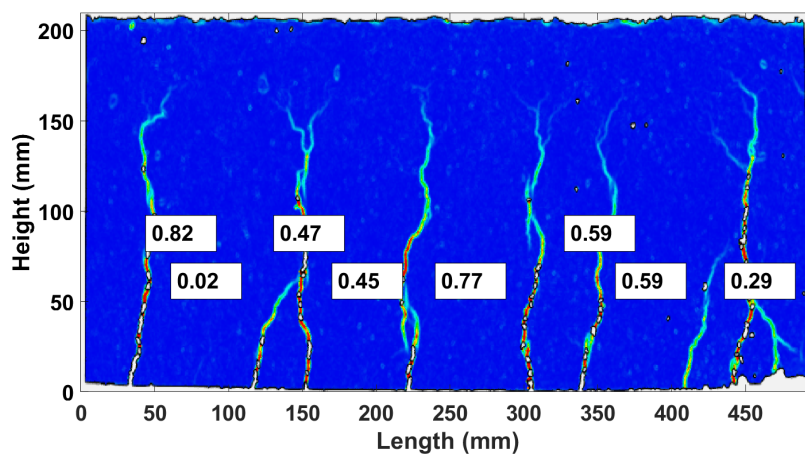
(i) B-3r8-c11: $F=35.04$ kN



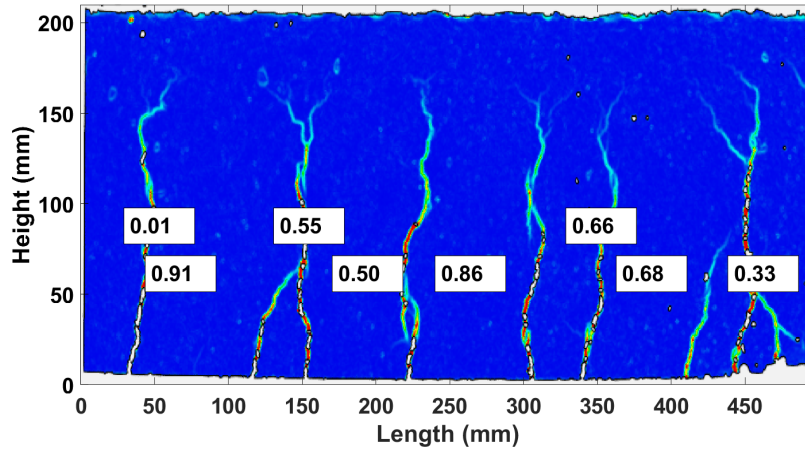
(j) B-3r8-c11: $F=37.61$ kN



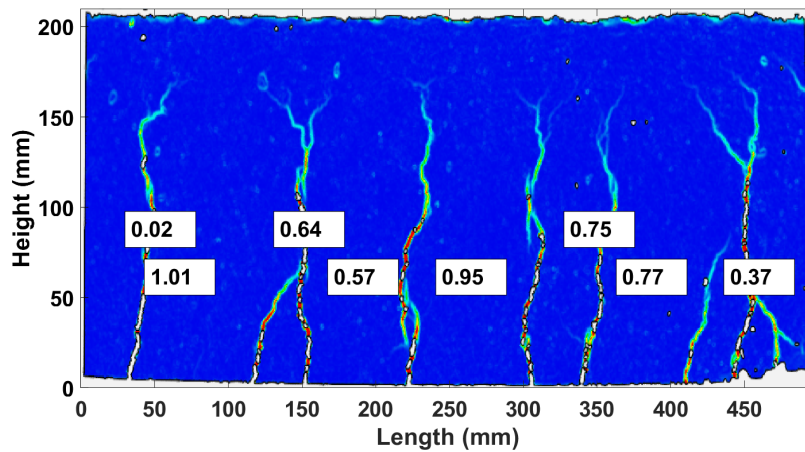
(k) B-3r8-c11: $F=39.76$ kN



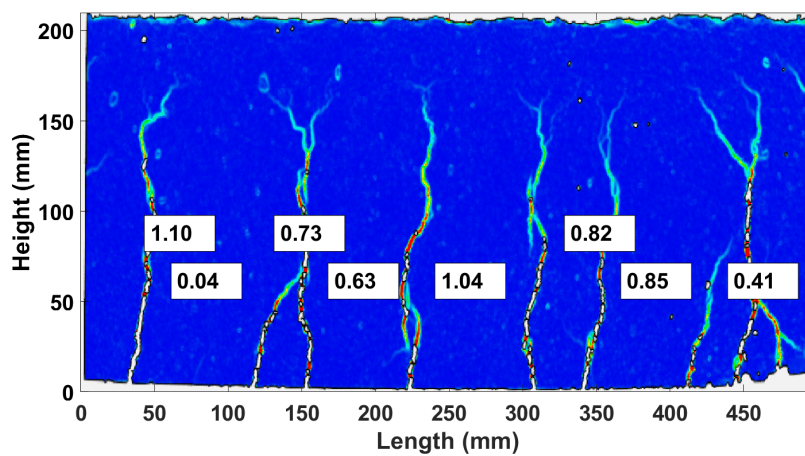
(l) B-3r8-c11: $F=45.06$ kN



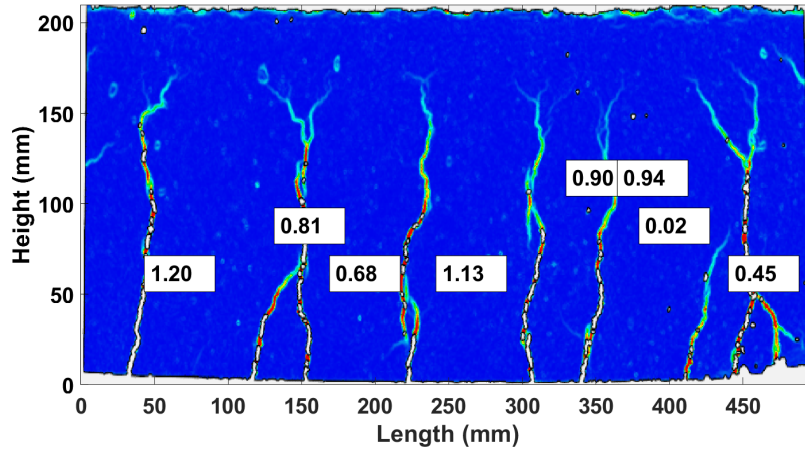
(m) B-3r8-c11: $F=50.02$ kN



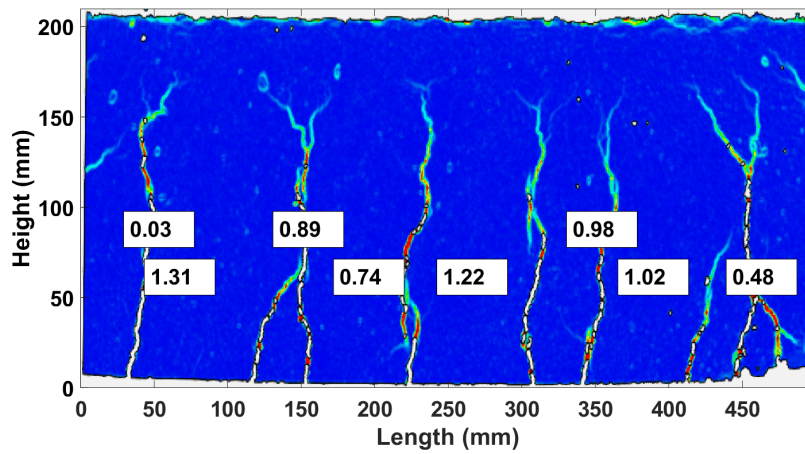
(n) B-3r8-c11: $F=55.00$ kN



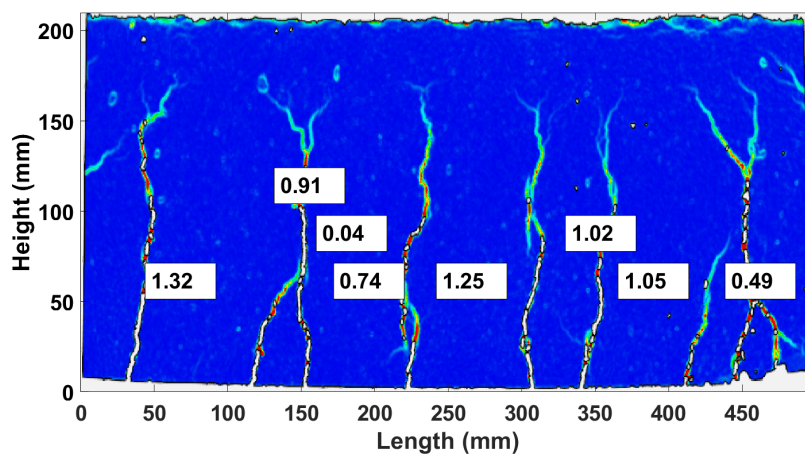
(o) B-3r8-c11: $F=60.02$ kN



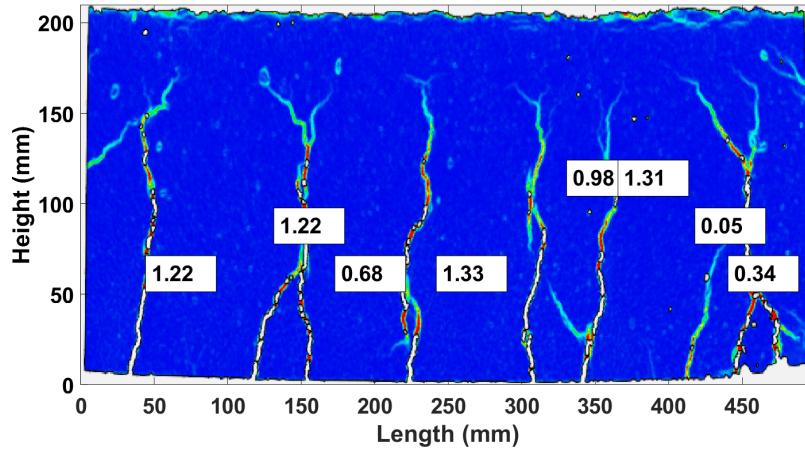
(p) B-3r8-c11: $F=65.05$ kN



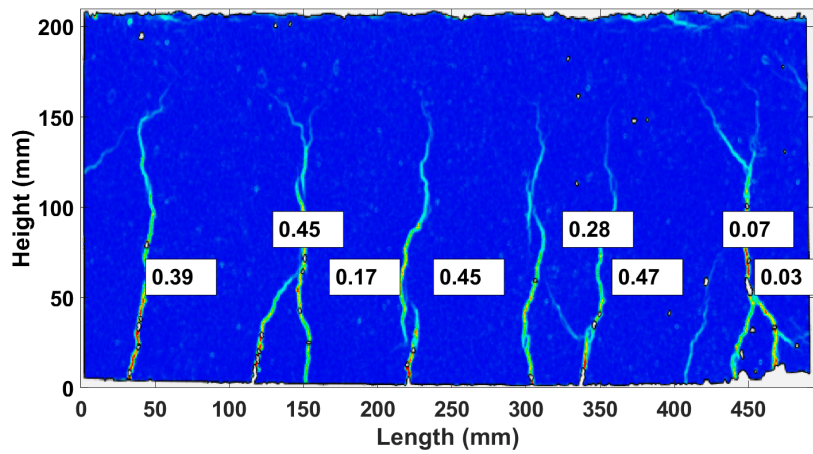
(q) B-3r8-c11: $F=70.03$ kN



(r) B-3r8-c11: $F=71.03$ kN



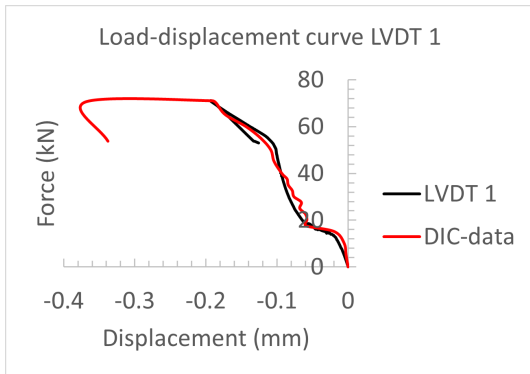
(s) B-3r8-c11: F=70.48 kN



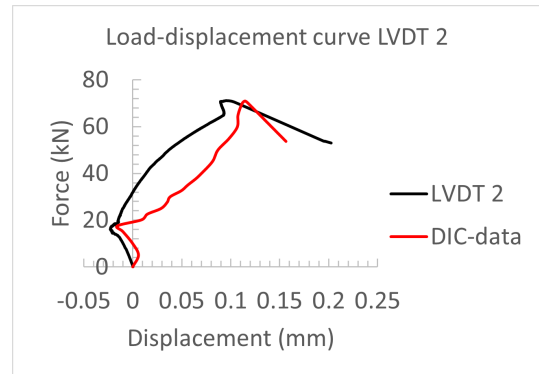
(t) B-3r8-c11: F=53.74 kN

Figure H.13: Crack widths contour plots B-3r8-c11 from DIC-data

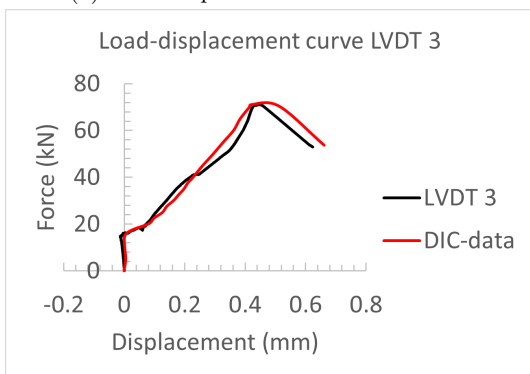
By comparing the DIC-data (figure H.14) to the data of the LVDT's, small differences are found between the DIC-data and the LVDT-data. The differences can be explained as the LVDT's are placed on the opposite side of the beam as the DIC-data is taken. The DIC-data is accepted as it is generally accurate.



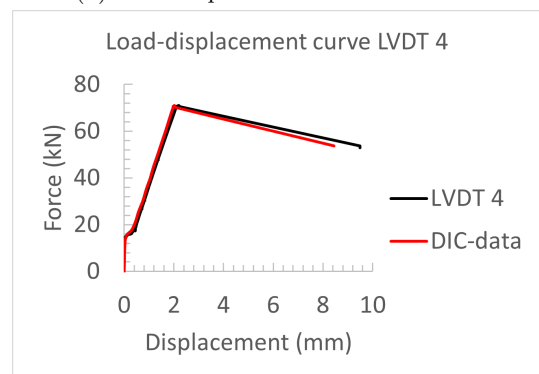
(a) Load-displacement curve LVDT 1



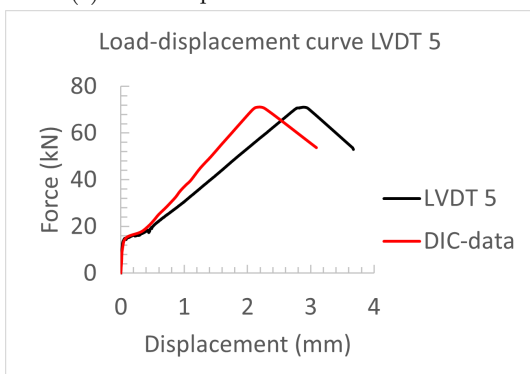
(b) Load-displacement curve LVDT 2



(c) Load-displacement curve LVDT 3



(d) Load-displacement curve LVDT 4



(e) Load-displacement curve LVDT 5

Figure H.14: B-3r8-c11: Load-displacement curves LVDT's and comparison with DIC-data

H.5 Results S-3r8-c31

Beam specimen S-3r8-c31 serves as a comparison beam for its counterpart reinforced with BFRP-bars (B-3r8-c31), as it contains the same reinforcement configuration and concrete cover. Figure H.15 presents the load-deflection curve for this beam and also includes the maximum crack width curve. The chronological crack pattern propagation from the DIC-data is presented in figure H.16.

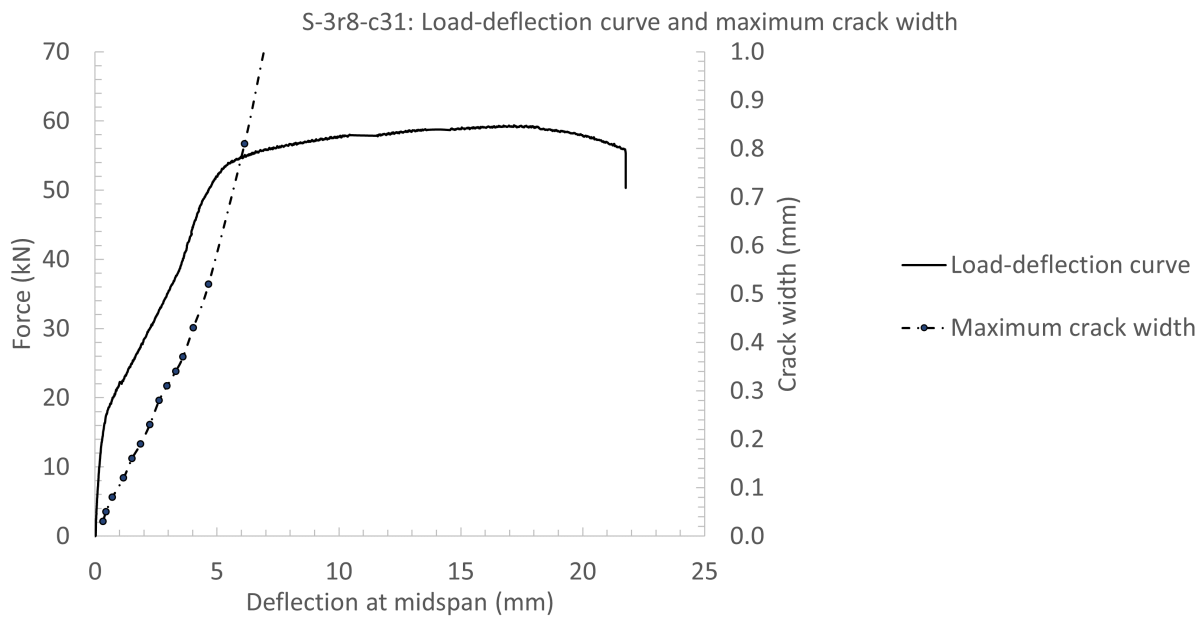
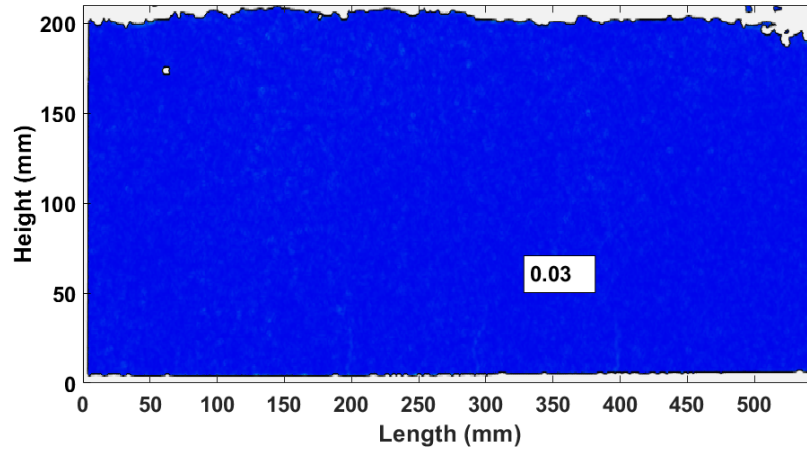


Figure H.15: S-3r8-c31, load-deflection curve versus maximum crack width measured from DIC-data

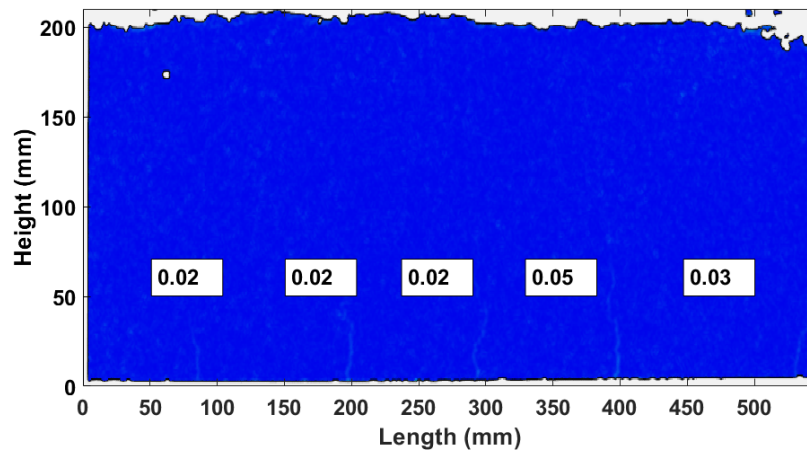
Table H.5: S-3r8-c31, summarized performance parameters

Performance parameters	
Maximum load	59.38 kN
Mid-span vertical deflection at maximum load	17.17 mm
Maximum vertical deflection at mid-span	21.76 mm
Number of cracks in constant bending moment zone	5
Average crack spacing	100 mm

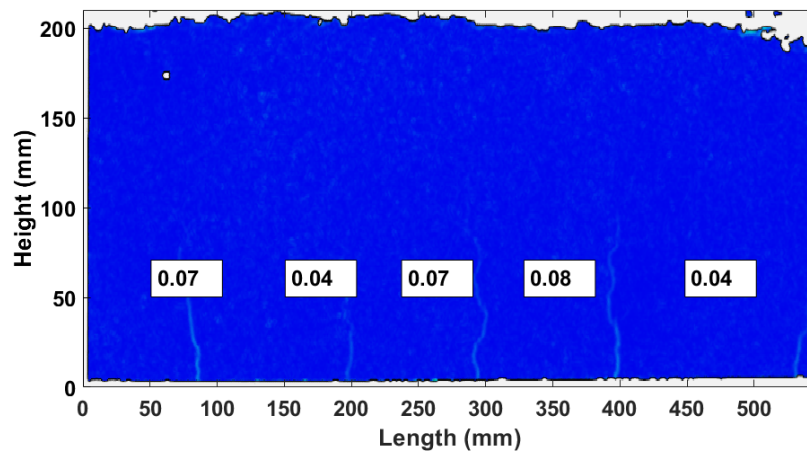
Table H.5 presents performance indicators of the beam. The beam specimen failed in the compression zone with a maximum force of 59.38 kN. The first cracks emerge at 15.11 kN as displayed in figure H.16a. At a load of 17.49 kN, all 5 cracks have already formed and proceed to propagate. These 5 cracks are the ones that have emerged in the 500 mm constant bending moment zone, however, another crack formed just outside of this zone and entered the zone from the left. This is visible in figure H.16g from a load level of 30.04 kN.



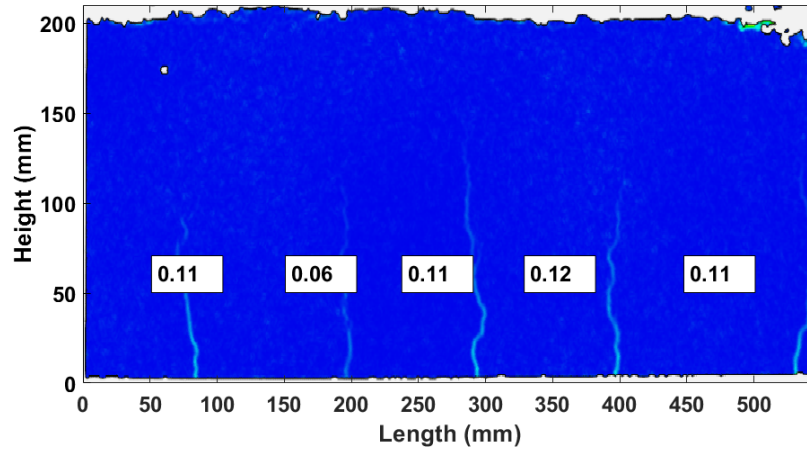
(a) S-3r8-c31: F=15.11 kN



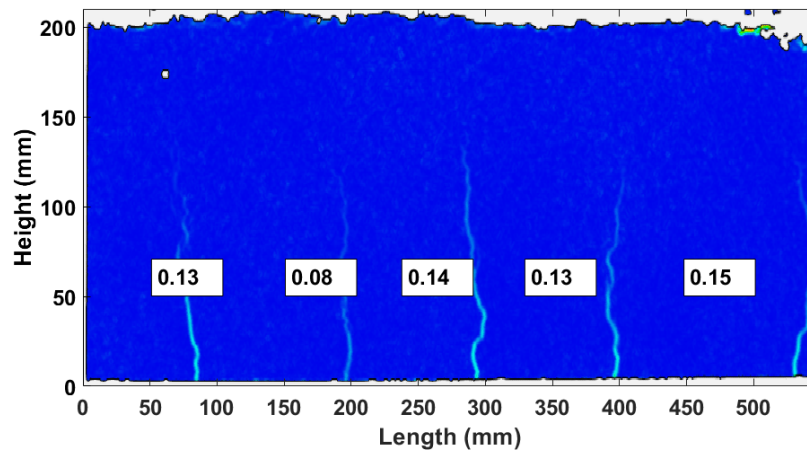
(b) S-3r8-c31: F=17.49 kN



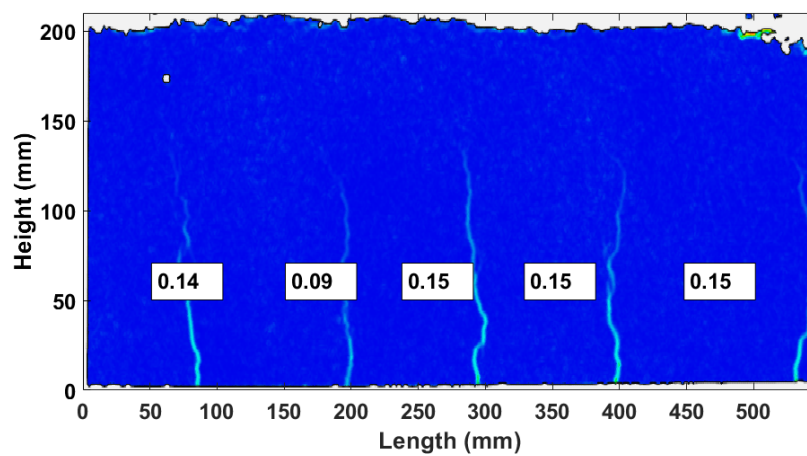
(c) S-3r8-c31: F=20.01 kN



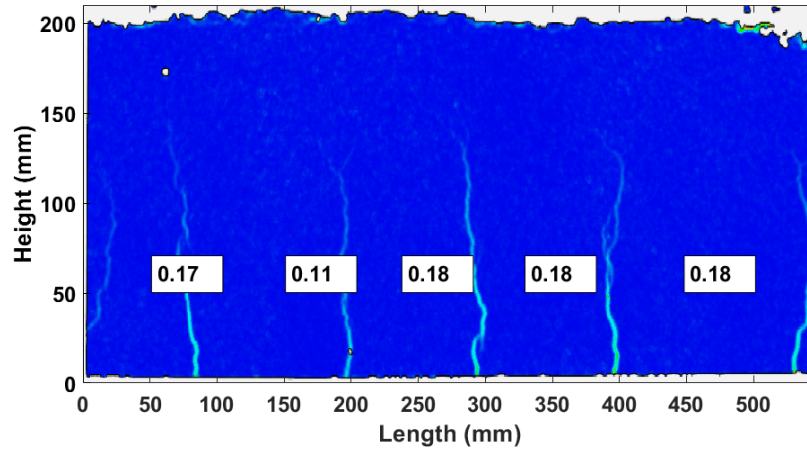
(d) S-3r8-c31: F=22.71 kN



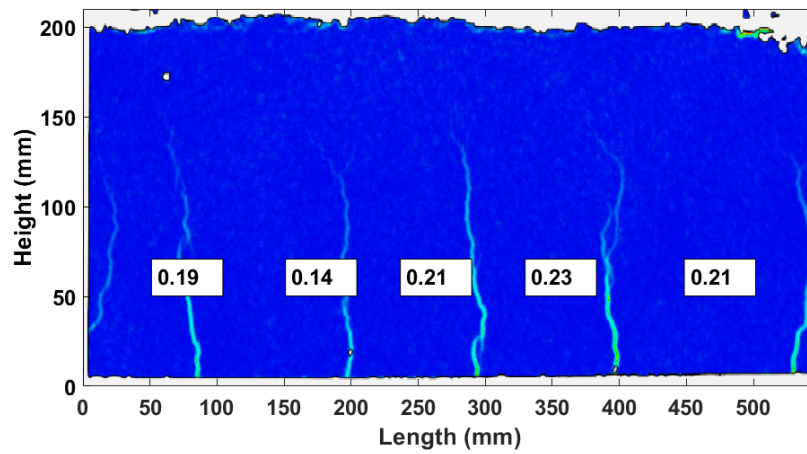
(e) S-3r8-c31: F=25.10 kN



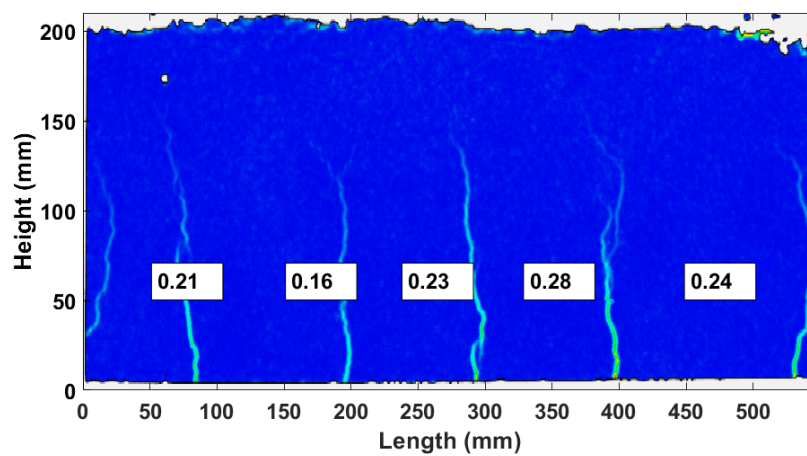
(f) S-3r8-c31: F=27.47 kN



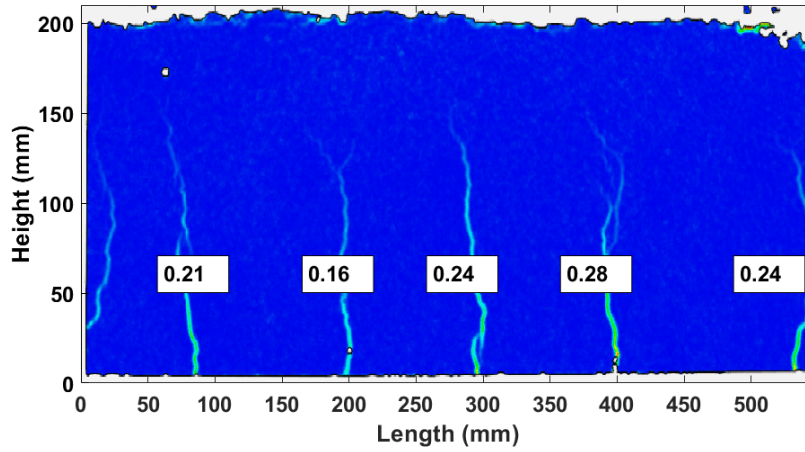
(g) S-3r8-c31: F=30.04 kN



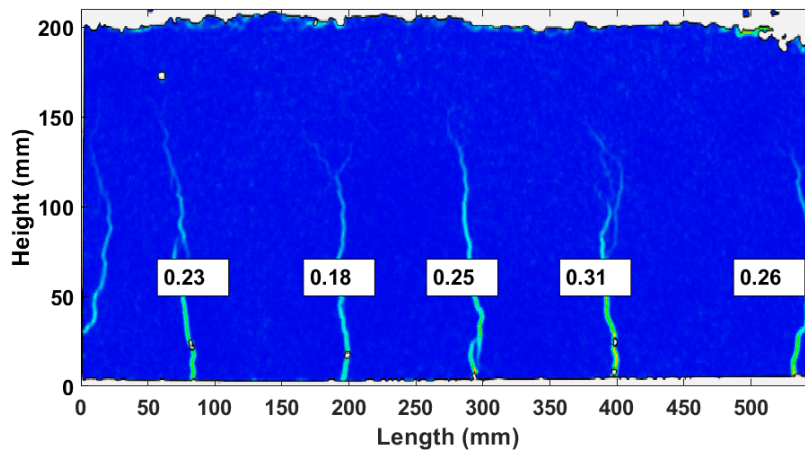
(h) S-3r8-c31: F=32.77 kN



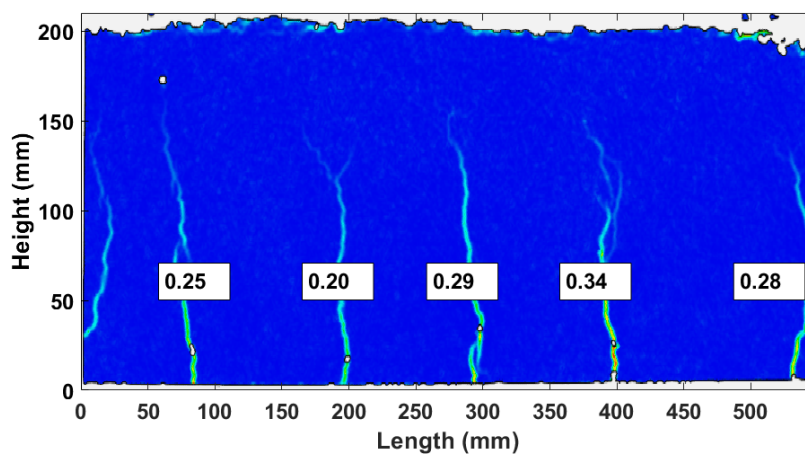
(i) S-3r8-c31: F=35.07 kN



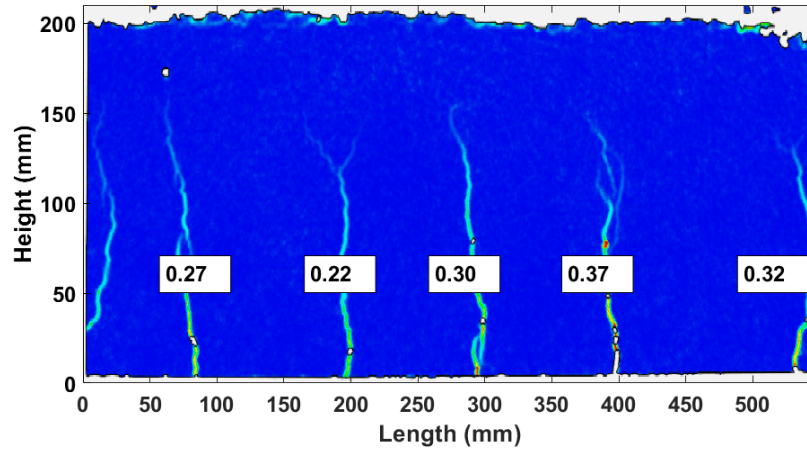
(j) S-3r8-c31: F=37.58 kN



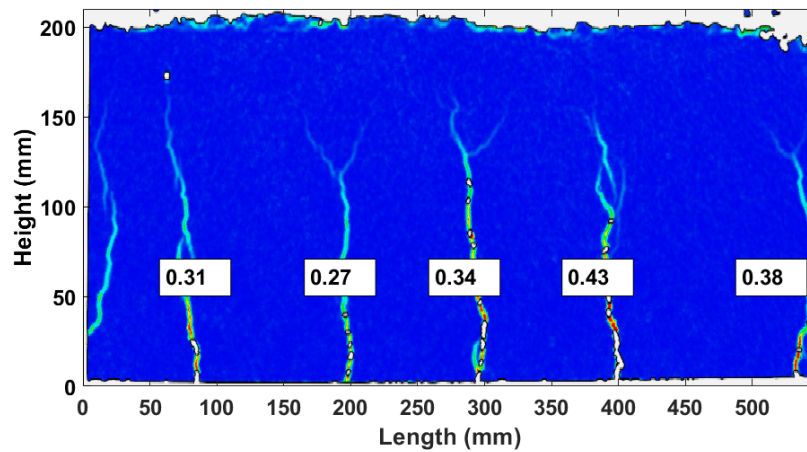
(k) S-3r8-c31: F=40.16 kN



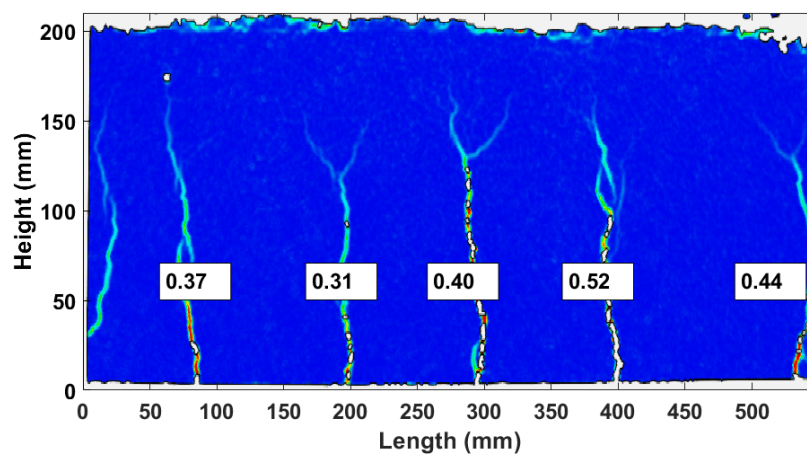
(l) S-3r8-c31: F=45.02 kN



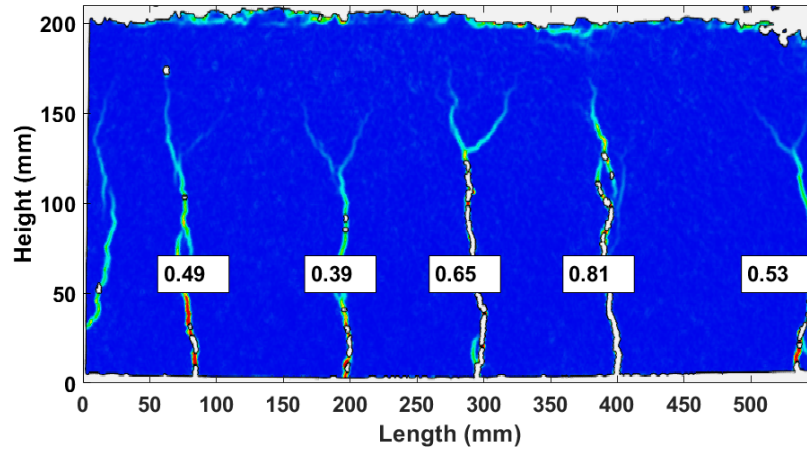
(m) S-3r8-c31: F=50.14 kN



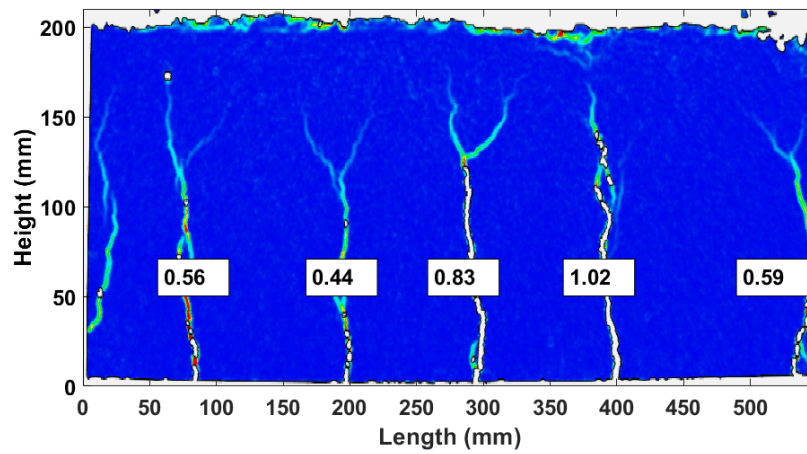
(n) S-3r8-c31: F=55.10 kN



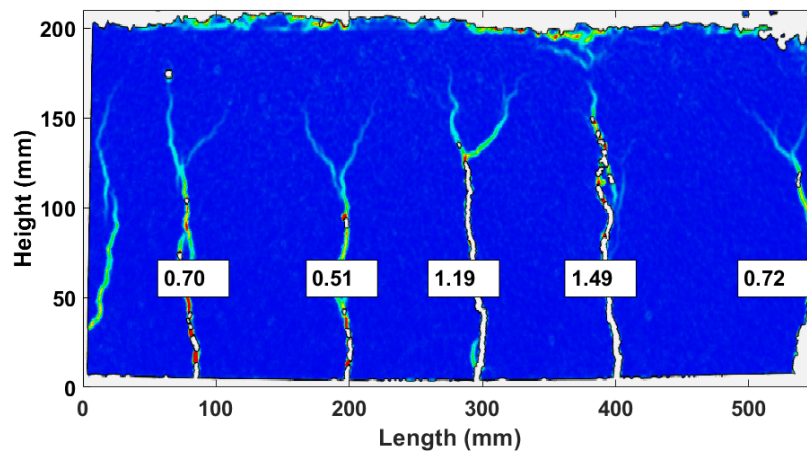
(o) S-3r8-c31: F=55.87 kN



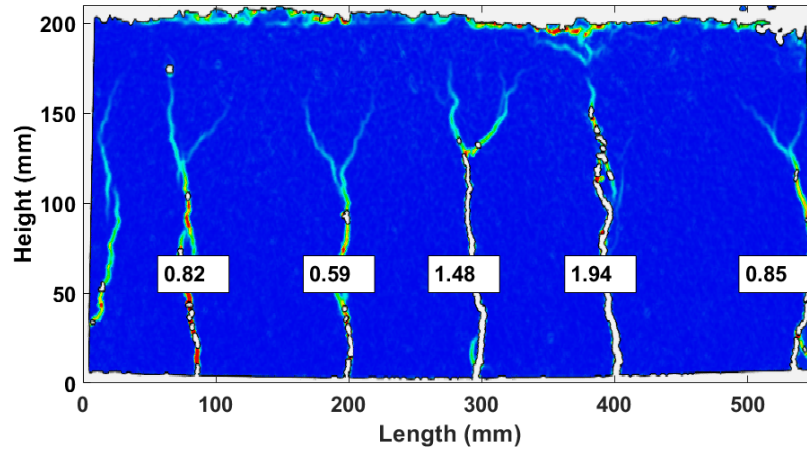
(p) S-3r8-c31: F=57.26 kN



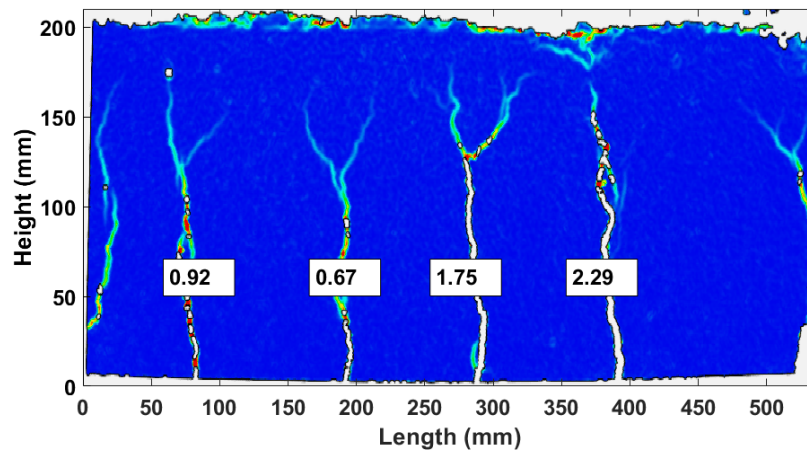
(q) S-3r8-c31: F=58.24 kN



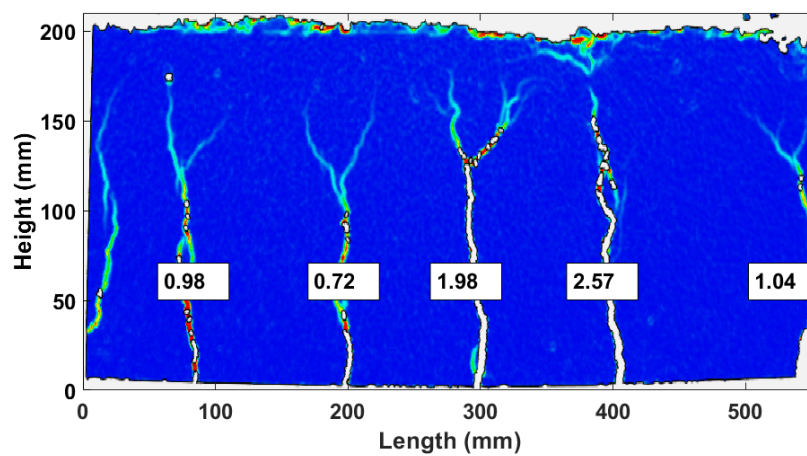
(r) S-3r8-c31: F=58.90 kN



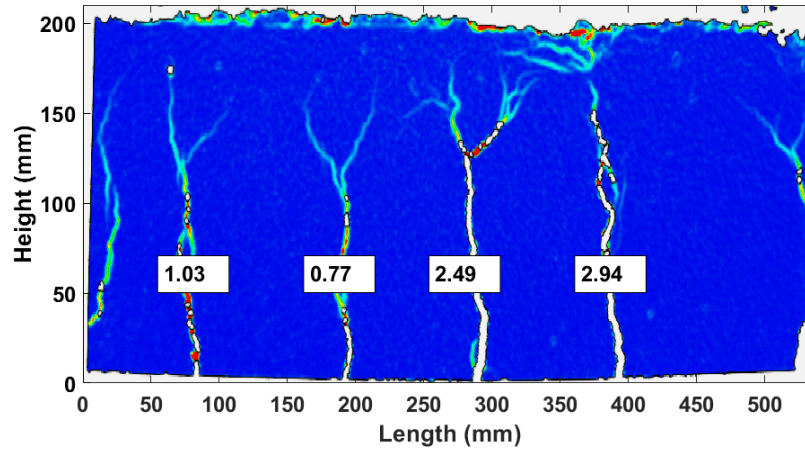
(s) S-3r8-c31: F=59.03 kN



(t) S-3r8-c31: F=59.05 kN



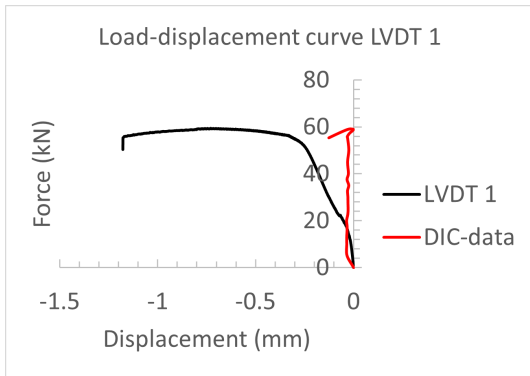
(u) S-3r8-c31: F=58.81 kN



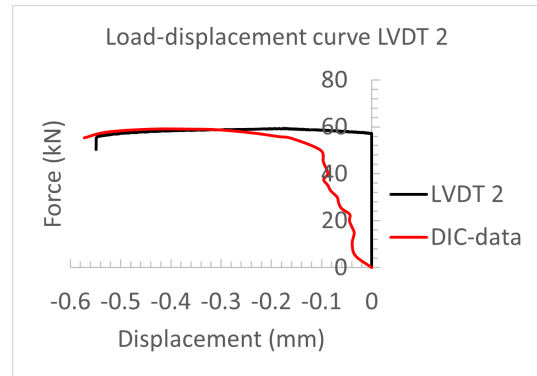
(v) S-3r8-c31: F=55.35 kN

Figure H.16: Crack widths contour plots S-3r8-c31 from DIC-data

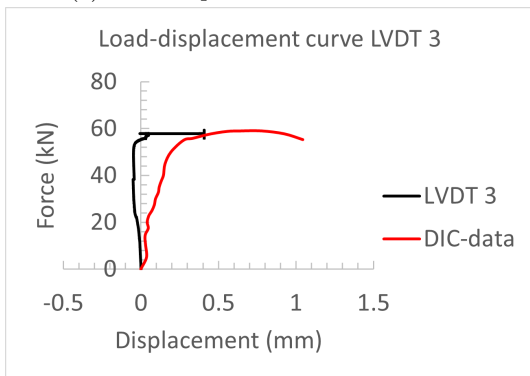
By comparing the DIC-data (figure H.17) to the data of the LVDT's, small differences are found between the DIC-data and the LVDT-data. The differences can be explained as the LVDT's are placed on the opposite side of the beam as the DIC-data is taken. The DIC-data is accepted as it is generally accurate.



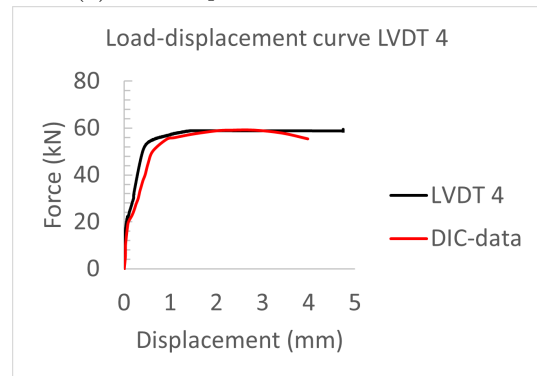
(a) Load-displacement curve LVDT 1



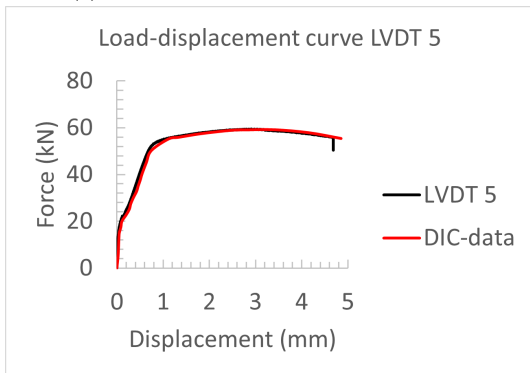
(b) Load-displacement curve LVDT 2



(c) Load-displacement curve LVDT 3



(d) Load-displacement curve LVDT 4



(e) Load-displacement curve LVDT 5

Figure H.17: S-3r8-c31: Load-displacement curves LVDT's and comparison with DIC-data

H.6 Results S-3r8-c11

Beam specimen S-3r8-c11 serves as a comparison beam for its counterpart reinforced with BFRP-bars (B-3r8-c11), as it contains the same reinforcement configuration and concrete cover. Figure H.18 presents the load-deflection curve for this beam and also includes the maximum crack width curve. The chronological crack pattern propagation from the DIC-data is presented in figure H.19.

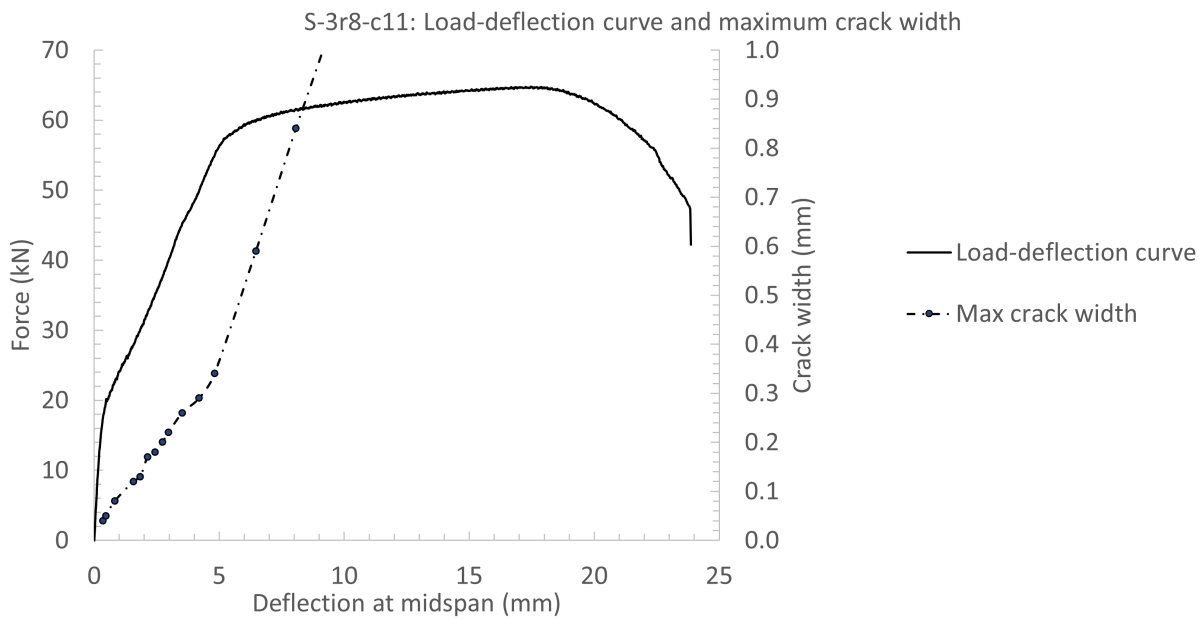
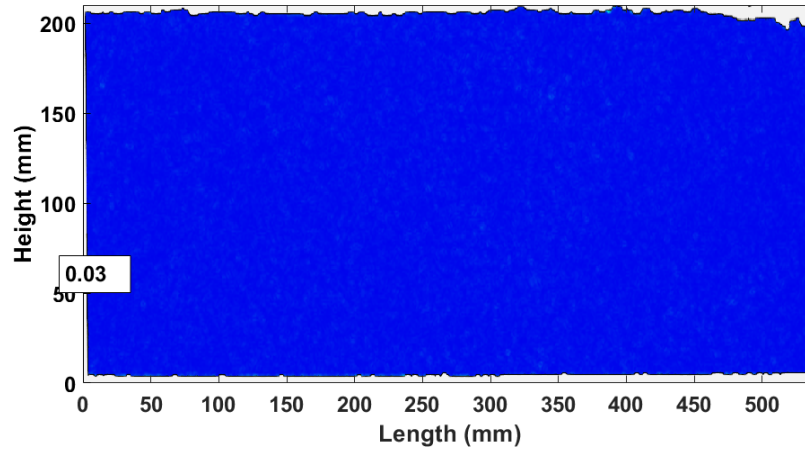


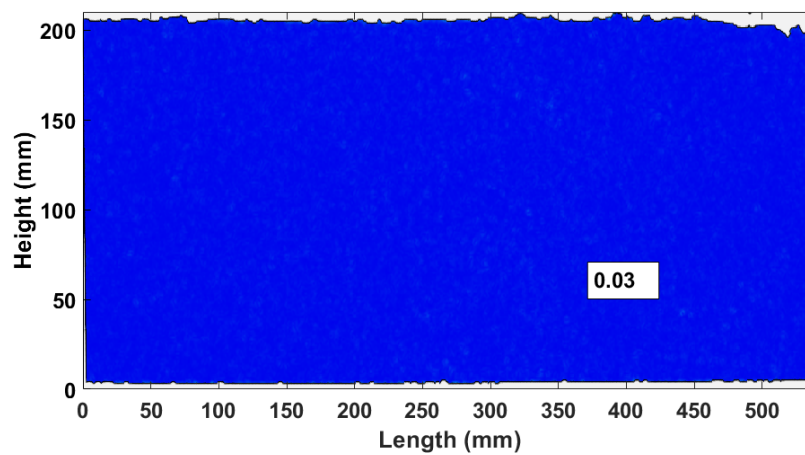
Figure H.18: S-3r8-c11, load-deflection curve versus maximum crack width measured from DIC-data

Table H.6: S-3r8-c11, summarized performance parameters

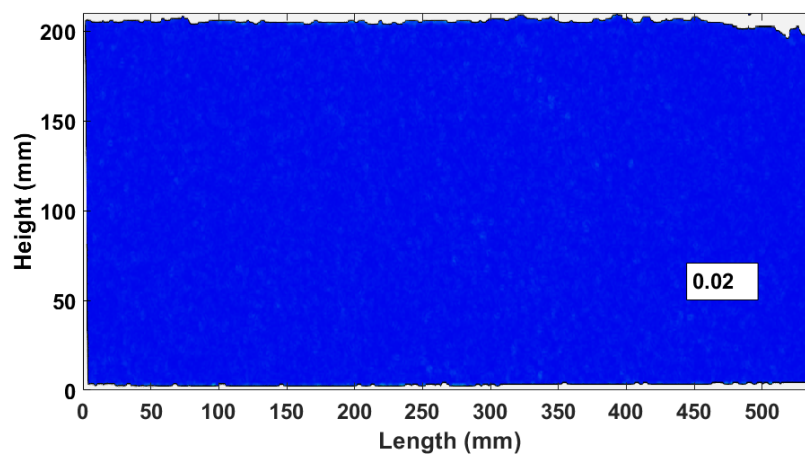
Performance parameters	
Maximum load	64.77 kN
Mid-span vertical deflection at maximum load	17.47 mm
Maximum vertical deflection at mid-span	23.87 mm
Number of cracks in constant bending moment zone	7
Average crack spacing	71.43 mm



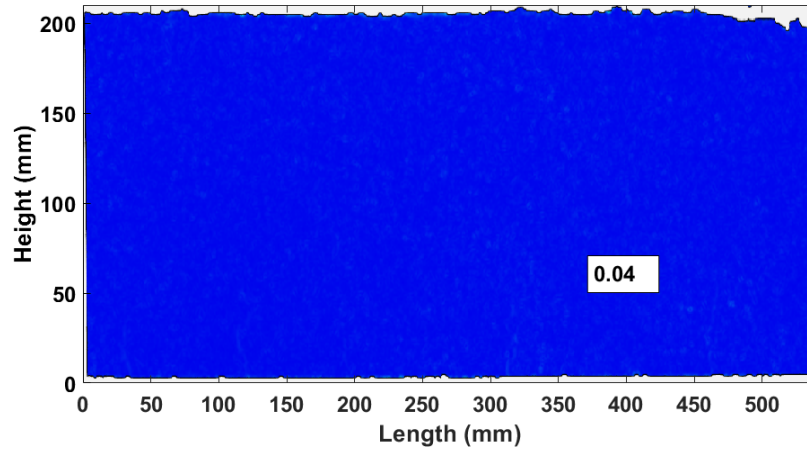
(a) S-3r8-c11: F=5.28 kN



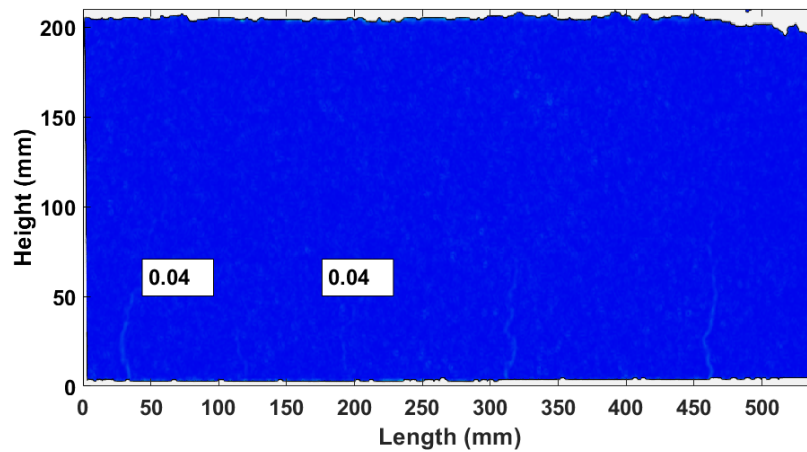
(b) S-3r8-c11: F=10.24 kN



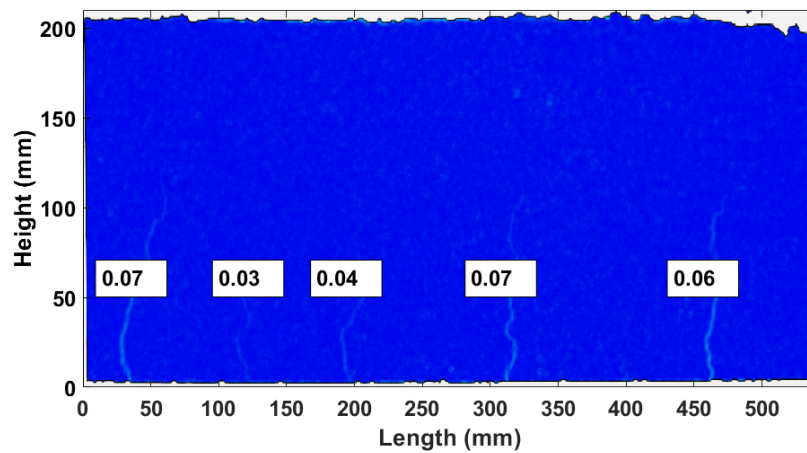
(c) S-3r8-c11: F=15.10 kN



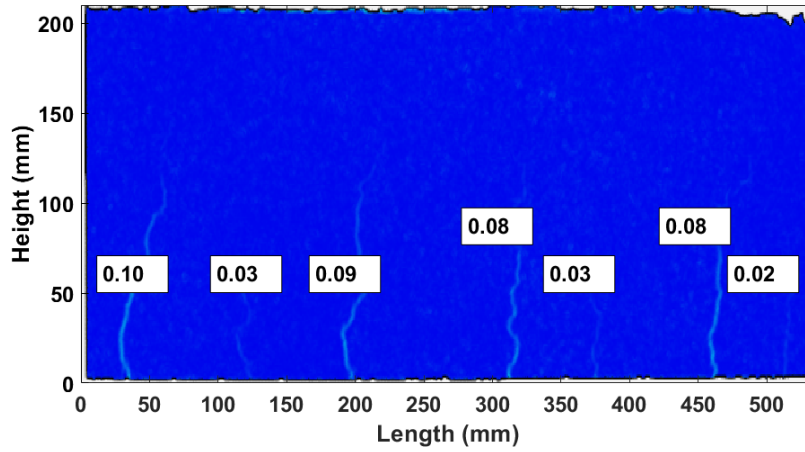
(d) S-3r8-c11: F=17.69 kN



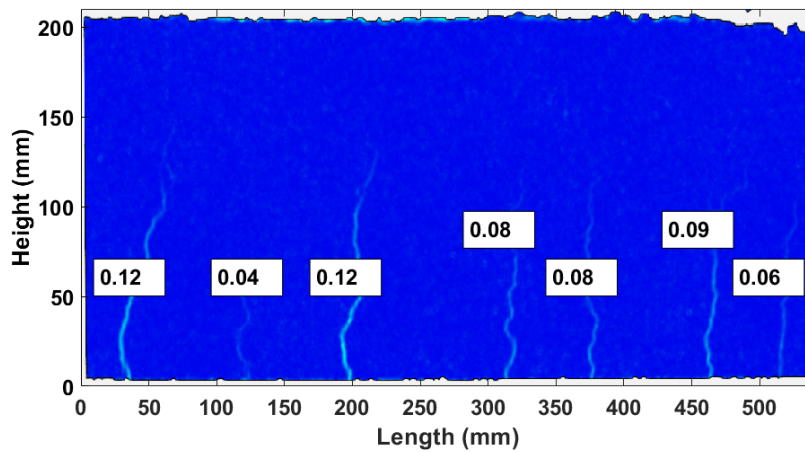
(e) S-3r8-c11: F=20.18 kN



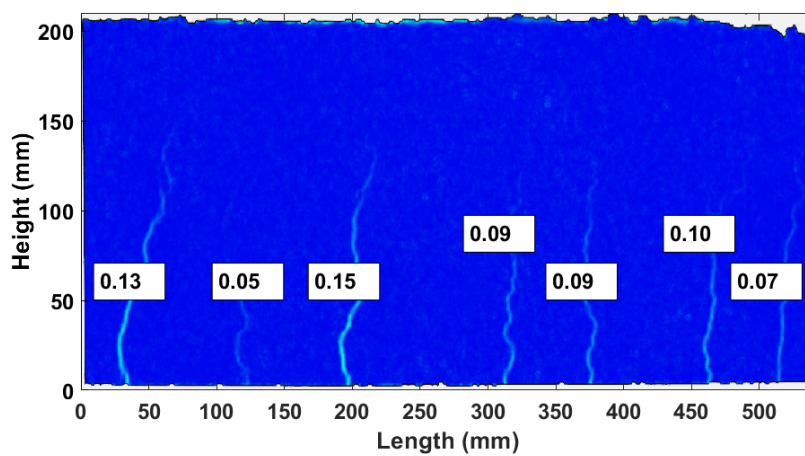
(f) S-3r8-c11: F=22.57 kN



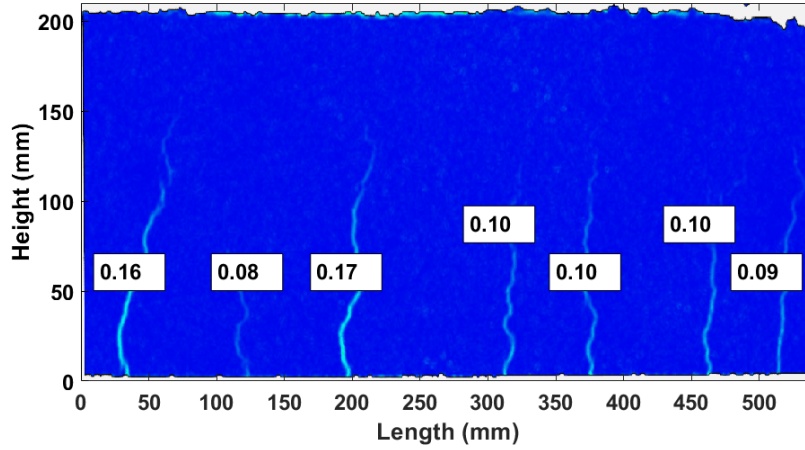
(g) S-3r8-c11: F=25.13 kN



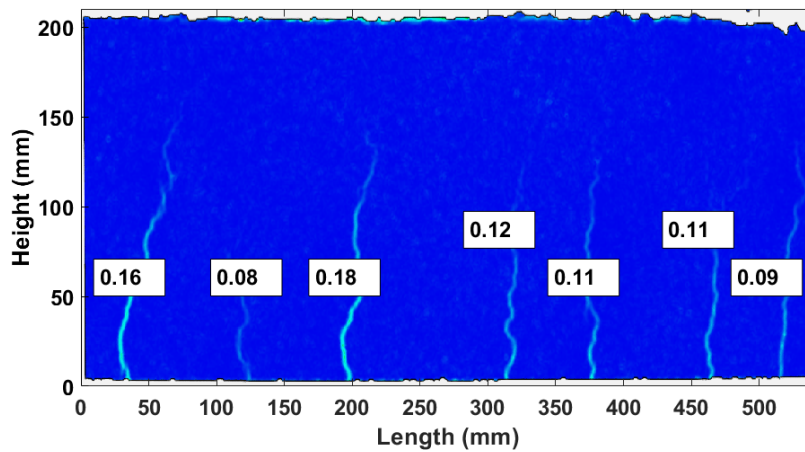
(h) S-3r8-c11: F=27.91 kN



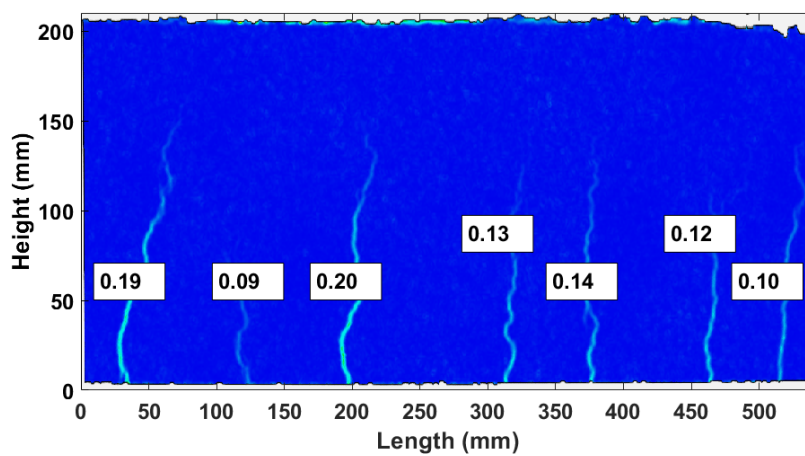
(i) S-3r8-c11: F=30.20 kN



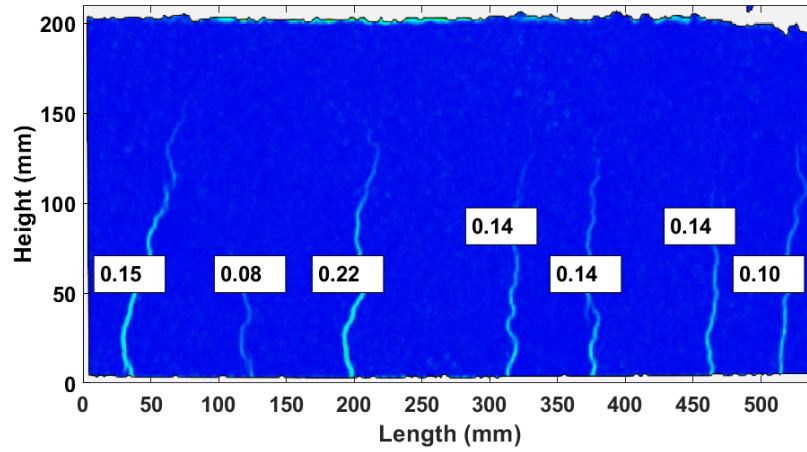
(j) S-3r8-c11: F=32.62 kN



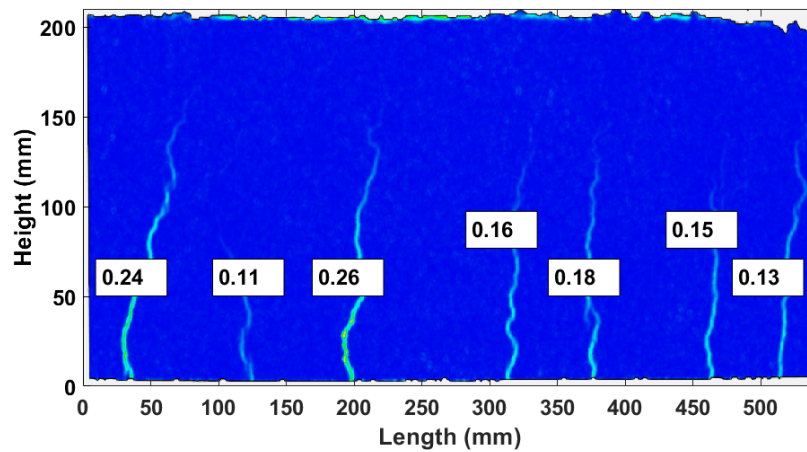
(k) S-3r8-c11: F=35.12 kN



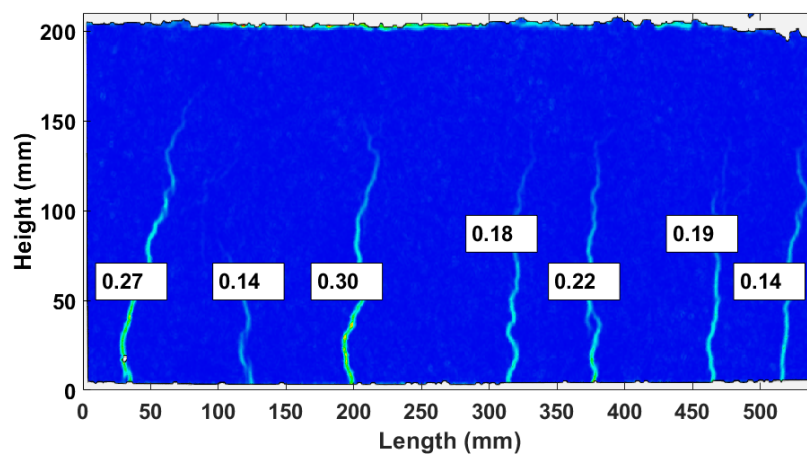
(l) S-3r8-c11: F=37.57 kN



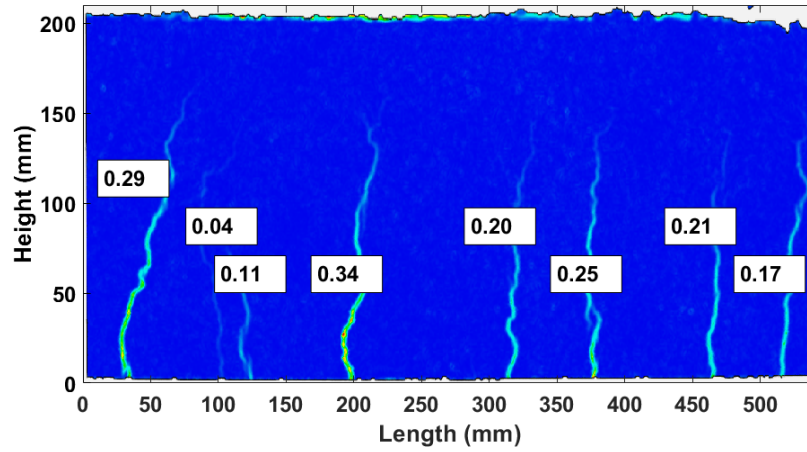
(m) S-3r8-c11: F=40.00 kN



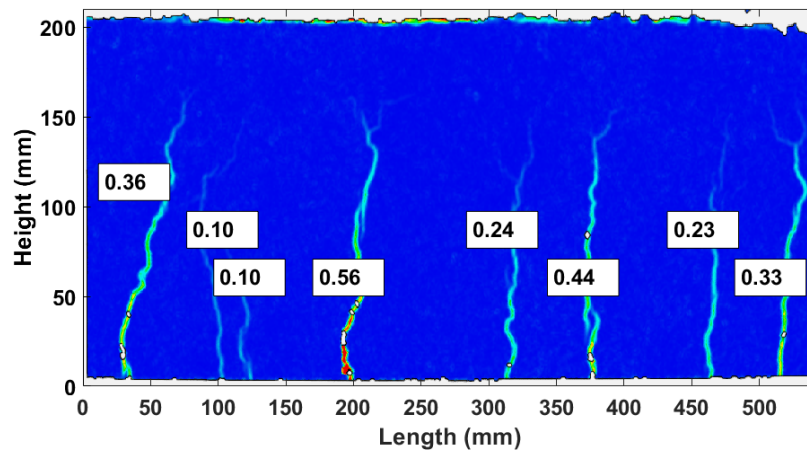
(n) S-3r8-c11: F=45.33 kN



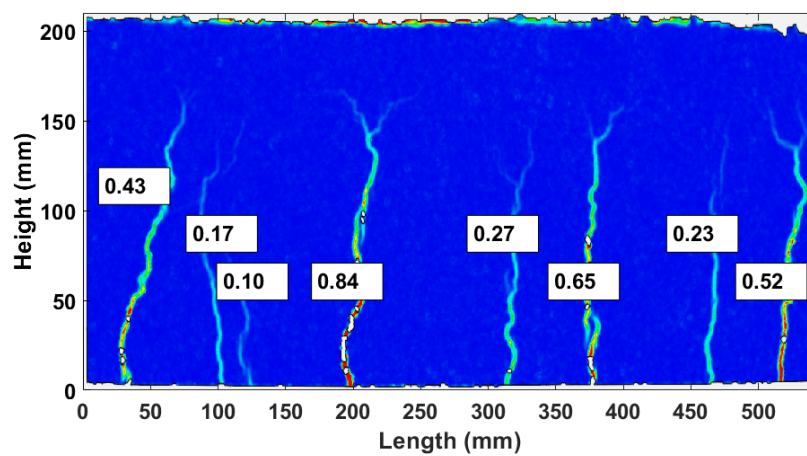
(o) S-3r8-c11: F=50.02 kN



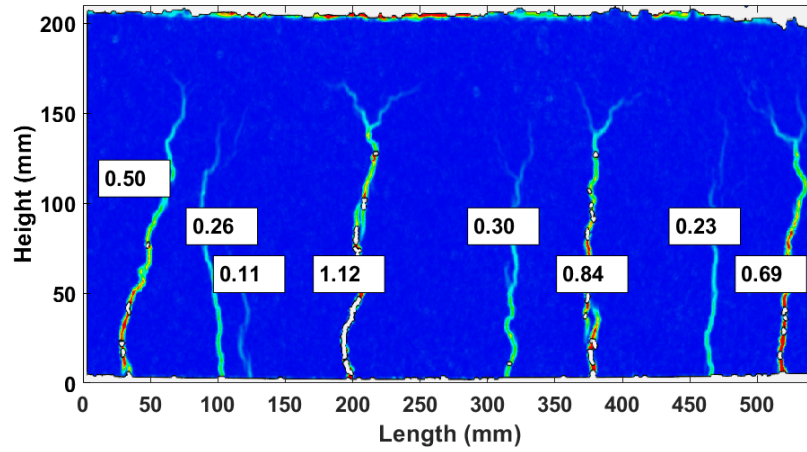
(p) S-3r8-c11: F=55.03 kN



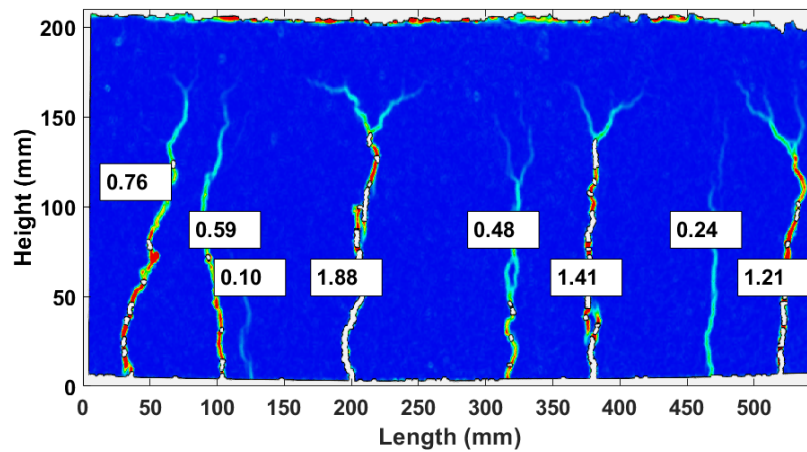
(q) S-3r8-c11: F=60.02 kN



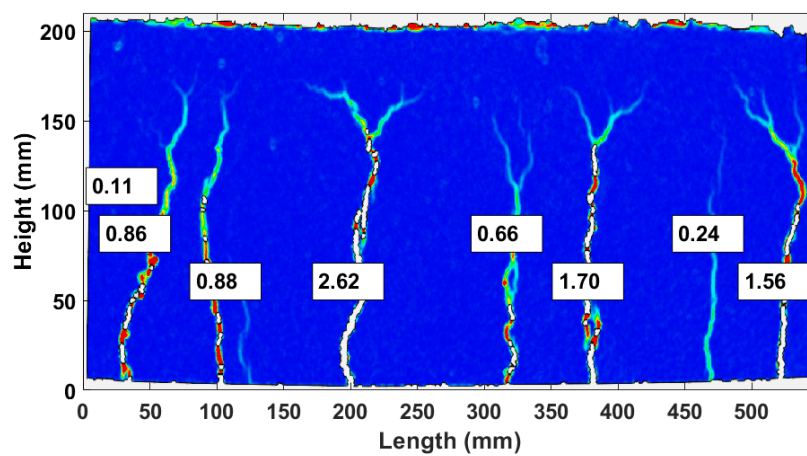
(r) S-3r8-c11: F=61.58 kN



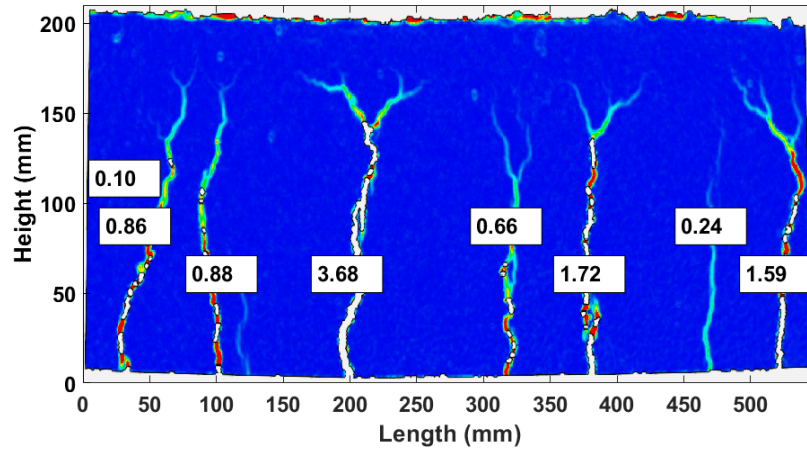
(s) S-3r8-c11: F=62.56 kN



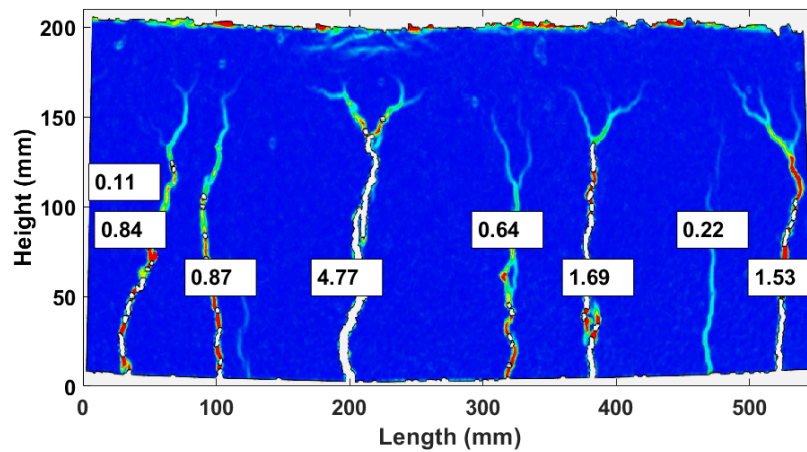
(t) S-3r8-c11: F=64.05 kN



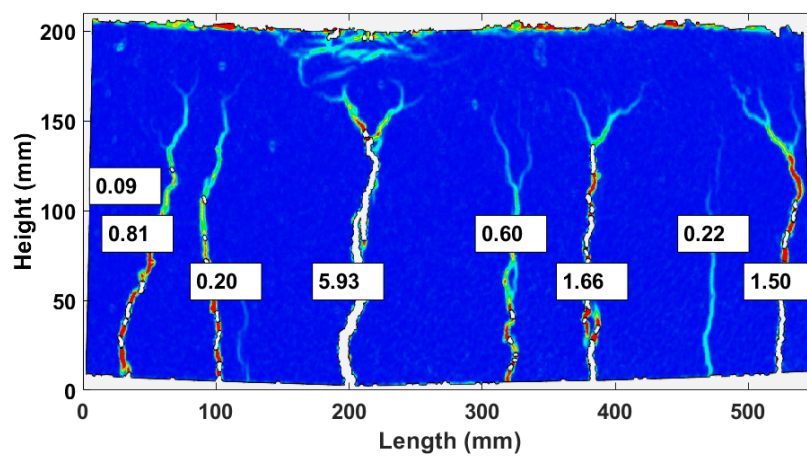
(u) S-3r8-c11: F=64.71 kN



(v) S-3r8-c11: F=62.29 kN



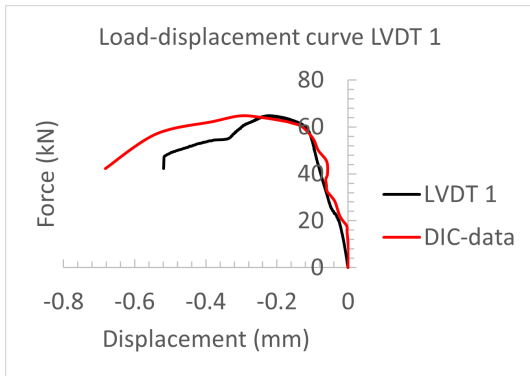
(w) S-3r8-c11: F=56.99 kN



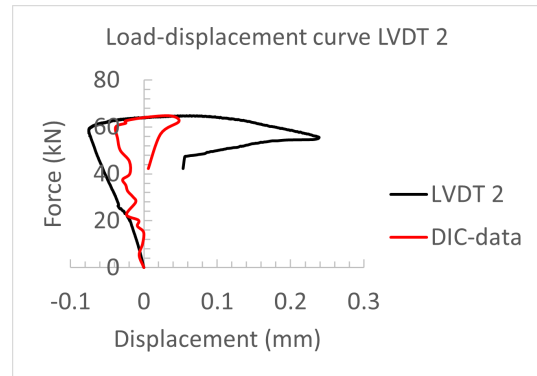
(x) S-3r8-c11: F=42.22 kN

Figure H.19: Crack widths contour plots S-3r8-c11 from DIC-data

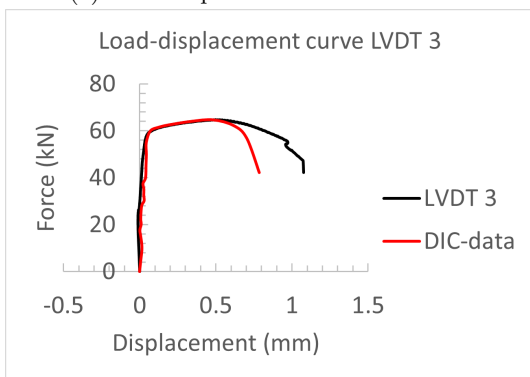
By comparing the DIC-data (figure H.20) to the data of the LVDT's, small differences are found between the DIC-data and the LVDT-data. The differences can be explained as the LVDT's are placed on the opposite side of the beam as the DIC-data is taken. The DIC-data is accepted as it is generally accurate.



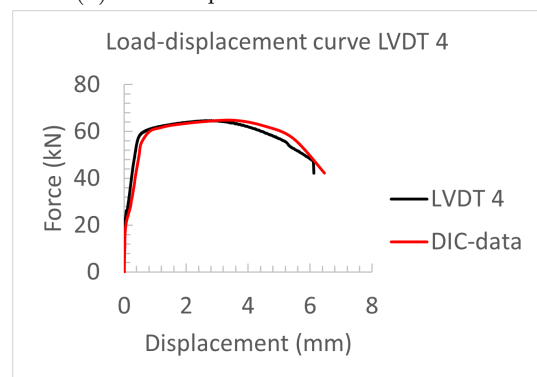
(a) Load-displacement curve LVDT 1



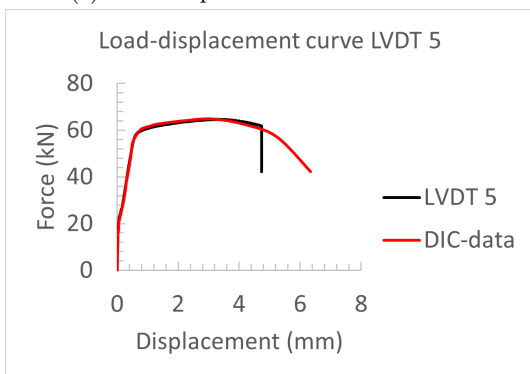
(b) Load-displacement curve LVDT 2



(c) Load-displacement curve LVDT 3



(d) Load-displacement curve LVDT 4



(e) Load-displacement curve LVDT 5

Figure H.20: S-3r8-c11: Load-displacement curves LVDT's and comparison with DIC-data

 **TU Delft**

 **Van Hattum en Blankevoort**

een VolkerWessels onderneming